IEKP-KA/2008-16

Measurement of the Mass and the Quantum Numbers J^{PC} of the $X(3872)$ State

Zur Erlangung des akademischen Grades eines
DOKTORS DER NATURWISSENSCHAFTEN
von der Fakultät für Physik der
Universität Karlsruhe (TH)

genehmigte

DISSERTATION

von

Dipl.-Phys. Joachim Heuser
aus Pforzheim

Tag der mündlichen Prüfung: 20.06.2008

Referent: Prof. Dr. M. Feindt, Institut für Experimentelle Kernphysik

Korreferent: Prof. Dr. G. Quast, Institut für Experimentelle Kernphysik

Contents

1 The $X(3872)$ 1

1.1 History of the Understanding of Matter 1

1.2 The Standard Model of Elementary Particle Physics 2

1.3 The Discovery of the $X(3872)$ 5

1.4 The $X(3872)$: Early Measurements 6

1.5 The $X(3872)$: Possible Interpretations 10

1.5.1 Charmonium Hypothesis 10

1.5.2 Molecular Hypothesis 14

1.5.3 Multiquark Hypotheses 16

1.5.4 Alternate Hypotheses 17

1.5.5 Summary of Hypotheses 18

1.6 Recent Experimental Developments 18

1.7 Summary and Outline 23

2 The CDF II Experiment 25

2.1 The Tevatron 25

2.1.1 The Accelerator Chain 25

2.1.2 Luminosity 28

2.2 The CDF II Detector 31

2.2.1 General Overview 31

2.2.2 Tracking System 31

2.2.3 Muon Detection System 35

2.2.4 Other Detector Systems 37

2.2.5 Trigger System 39

3 Determination of the Quantum Numbers J^{PC} 41

3.1 Decay Topology and Amplitude Construction 41

3.1.1 Conservation Rules in the $X(3872)$ Decay 44

3.1.2 Construction of a Vertex Decay Matrix Element 47

3.1.3 Construction of the Full Decay Matrix Element 50

3.1.4 Matrix Element for the $\psi(2S)$ Decay 54

3.2 Data Reconstruction 56

3.2.1 Preselection Cuts 57

3.2.2 $X(3872)$ Candidate Reconstruction 57

3.2.3 Final Cut Optimization 59

3.2.4 Measurement of Data Distributions 63

3.3 Monte Carlo Simulation Sample 64

3.3.1 Event Generation 64

3.3.2 Detector Acceptance 65

3.3.3 Event Reweighting 67

3.3.4 Simulation Verification with $\psi(2S)$ Measurements 68

3.4 Measurement and Comparison of Angular Distributions 74

3.4.1 Measurement of Angular Distributions 75

3.4.2 Comparison of Measured Distributions to Predictions 76

3.5 Systematic Uncertainties 82

3.5.1 Determination of the Quantum Numbers J^{PC} of the $\psi(2S)$ . . 82

3.5.2 Selection Effects 84

3.5.3 $X(3872)$ Polarization Effects 85

3.5.4 Further Cross-Checks 88

3.5.5 Measurement and Simulation Effects 89

4 Measurement of the $X(3872)$ Mass 97

4.1 Sample Selection 97

4.1.1 Preselection of the Measured Data Sample 98

4.1.2 Signal Selection Procedure 98

4.1.3 Simulation Sample Generation 104

4.1.4 Final Reweighting of the Simulated Samples 106

4.2 Analysis of the $X(3872)$ Mass Shape 107

4.2.1 Hypothesis Test Procedure 110
4.2.2 Fit Model and Test Quantity 110
4.2.3 Width Scale Measurement 112
4.2.4 Ensemble Creation 112
4.2.5 Ensemble Test Evaluation 117
4.3 Measurement of the $X(3872)$ Mass 118
4.3.1 Fit to the Mass Spectrum 120
4.3.2 Evaluation of Systematic Uncertainties 121

5 Discussion and Outlook 127
5.1 Summary 127
5.2 Discussion 128
5.2.1 Comparison to Previous Results 128
5.2.2 Impact on $X(3872)$ Models 130
5.3 Outlook 131
5.4 Conclusion 132

A Reference Distributions for the J^{PC} Analysis 135
A.1 Angular Distributions of All Tested J^{PC} Hypotheses 135
A.2 Fits to the $J/\psi\pi\pi$ Mass Spectrum 142
A.3 Angular Comparison for All Tested J^{PC} Hypotheses 149

Chapter 1

The $X(3872)$

The understanding of matter is one of the most compelling topics in science. Because of this, it has been studied through the ages. What is matter composed of? Can one understand the behavior of things by identifying their building blocks?

After revolutionary discoveries in the last century, our current understanding of matter is contained in the standard model of particle physics. It describes all the building blocks of matter as we know them today. Theoretically there is a wide range of possibilities to form combinations of these elementary building blocks. In nature, however, only very basic combinations have been observed.

In 2003, a new particle was discovered with the name $X(3872)$. Its observed properties are not in good agreement with the expectations for the 'traditional' forms of matter. At the same time, the properties are partly in exceptional agreement with exotic forms. Does the $X(3872)$ proof the existence of a new form of matter? To help answer this question this thesis will measure properties of the $X(3872)$.

This introductory chapter presents a short history of our understanding of matter, the discovery of the $X(3872)$, and the reason why it is considered as a candidate for exotic matter. Both the early experimental findings and the interpretations developed to explain them are covered. Also discussed are further experimental developments that started to constrain theoretical models.

1.1 History of the Understanding of Matter

The discussion of the fundamentals of matter can be dated back to the Greek philosophers. Some, like Democritus, believed that matter was made up from solid basic elements of different shape and size that could not be further divided ('atomos', indestructible particle). These atoms could be arranged and combined differently in empty space to form all sorts of known matter. This approach was however rejected later by Aristotle. As a consequence, the more spiritual view of explaining all things as a combination of air, earth, fire, and water prevailed. This view remained very popular, lasting through the Middle Ages and the Renaissance till the 17th century.

Only the advances in chemistry in the 17th century made apparent that there had to be more than four elements. Next to the different chemical properties of these elements it was observed that the ratio of elements involved in a chemical reaction followed simple rules. This reintroduced the concept of atoms of different types — elementary, not further divisible building blocks. More and more elements were discovered which allowed to group them by their chemical properties — this was the birth of the periodic table of elements.

At the threshold of the 19th century, radiation experiments lead to a major step forward in the understanding of the atom. The discovery of the electron showed that atoms were not the most basic building blocks of matter. Surprisingly it was found that an atom is made up of a heavy, very tiny nucleus, surrounded by a cloud of electrons. In 1932, the discovery of the neutron marked an important intermediate point in our understanding of matter — matter as a combination of different atoms, which in turn are made up of three basic constituents: electrons, protons and neutrons.

Starting from the 1940s, unexpected observations of unknown particles in cosmic rays pronounced the birth of particle physics. The muon and the pion could not be explained as new elements, but proved to be completely new particles. These discoveries were followed subsequently by the observation of a lot of new particles. In order to explain these new states, the quark model was introduced in the 1960s. This model proposed the existence of so-called quarks as constituents of the new particles, where different quark combinations result in different particles.

The quark model was however not very popular, since quarks could not be experimentally observed. The wide acceptance of the quark model began with the discovery of the J/ψ in 1974. While other theories could not accommodate this particle, it was easily explained within the quark model. Further experimental evidence and progress in the theoretical understanding culminated in the development of the standard model of particle physics.

The standard model contains our current understanding of the structure of matter. In short it says that matter as we know it is composed out of two basic components: quarks and leptons. The electron, one of the leptons, is still considered to be an elementary particle. However, the proton and neutron proved to be composites out of three quarks.

1.2 The Standard Model of Elementary Particle Physics

The standard model of elementary particle physics (abbreviated as SM) is a theory that describes all the constituents of observed matter as we know them today. Furthermore it describes the fundamental forces that act between these constituents of matter. This section concentrates on the aspect of matter within the standard model and only briefly mentions the interactions between the matter particles.

particle name	symbol	mediated force	couples to
photon	γ	electromagnetic force	electric charge
Z boson	Z^0	weak force	weak charge
W bosons	$W^\pm$	weak force	weak charge
gluon	g	strong force	color charge

Table 1.1: List of the gauge bosons, the particles responsible for the mediation of the forces.

The particles in the standard model can be ordered into three different groups: gauge bosons, leptons, and quarks. Gauge bosons are responsible for the mediation of the forces. Table 1.1 lists the gauge bosons, the force they mediate and the property they couple to. As the name already states, gauge bosons are bosons, which means that they follow Bose statistics and have integer spin. The gauge boson responsible for transmitting the electromagnetic force is the photon, which couples to the electric charge. Because the photon is massless, the range of the electromagnetic interaction is infinite. The weak interaction is transmitted by the Z and W bosons. They are extremely massive, making the weak interaction a short-range interaction. The high mass is also the reason for the fact that weak interaction effects usually can be neglected in the presence of other interactions. This effect becomes less pronounced with higher available energies. At energies of the order of the W/Z boson masses the strength of the weak interaction becomes comparable to that of the electromagnetic interaction. The last interaction is the strong interaction. It is transmitted by massless gluons which couple very strongly to the so-called color charge. This color charge is carried by quarks (see below) and by the gluons themselves. This has the unique effect that gluons can couple among themselves. Because of color confinement gluons cannot exist as independent particles. As a consequence the strong interaction has a very short range. It should be noted that gravity is not included in the standard model, so that there is also no corresponding boson in the standard model which would be responsible for the gravitational force.

The group of particles which only couples to the weak and the electromagnetic interaction and not to the strong interaction is called leptons. They are grouped in three generations, listed in table 1.2. Leptons are fermions, obeying Fermi-Dirac statistics. This is a crucial feature, since the Pauli exclusion principle forbids two fermions to be in the same quantum state. This leads to countless effects in atomic and solid state physics, which all have their origin in the fact that a system of electrons — the only stable lepton — are not all allowed to occupy the state of lowest energy. Each charged lepton has its corresponding neutral partner, the neutrinos. Although they were postulated in the standard model with zero mass, the observation of neutrino-oscillations — neutrinos changing their flavor over time and distance — has proven this postulation wrong. Neutrinos can only interact weakly, possessing no electric charge or color charge, which makes them extremely difficult to study.

	particle name	symbol
first generation	electron	e
	electron neutrino	ν_e
second generation	muon	μ
	muon neutrino	ν_μ
third generation	tau	τ
	tau neutrino	ν_τ

Table 1.2: List of the leptons within the standard model.

	particle name	symbol
first generation	up quark	u
	down quark	d
second generation	charm quark	c
	strange quark	s
third generation	top quark	t
	bottom quark	b

Table 1.3: List of the quarks within the standard model.

The last group of elementary particles in the standard model are referred to as 'quarks'. Quarks are the only particles which couple to all of the forces, since quarks carry electric charge, weak charge and color charge. As is the case for leptons, they can be arranged in three generations (see table 1.3). The properties of the strong interaction are described by the theory of 'Quantum Chromodynamics' (QCD). One of the most surprising properties of the theory is the fact, that the strength of the interaction between two quarks increases with their distance. The reason is the already mentioned fact, that the gluons as the carriers of the strong interaction possess color charge themselves, which leads to self-coupling. As a result it is not possible to observe free quarks. The energy required to separate quarks would result in the creation of new quark pairs, always preventing the existence of separated quarks. Quarks are only observable in composites, called 'hadrons', which are color-neutral.

In addition, each fermionic particle, i.e. every quark and lepton, has its corresponding anti-particle with identical mass and spin, but opposite charge. Antimatter behaves completely symmetrical to matter, following the same physical rules.

The standard model proves to be a theory that is in exceptional agreement with many experimental facts. However, it is not without limitations. Concentrating on the subject of matter, we know from cosmology that there are unknown sources of gravitational forces, 'Dark Matter' and 'Dark Energy', which cannot be explained

by the matter that we know about.

There is a different aspect where the standard model does not give a definitive answer. While the standard model contains all the elementary particles we know of, it does at the moment not firmly predict how these particles can be combined. This is not a theoretical but a practical issue, because current methods to calculate QCD processes are not able to perform calculations with acceptable uncertainties at the low energies of the particle masses.

From a purely phenomenological point of view it is however known that all observed particles can either be interpreted as a lepton or, for the vast majority, as a so-called 'hadron'. Two types of hadrons are known: baryons and mesons. Whereas baryons consist of a combination of three quarks, mesons are made up from a quark and an anti-quark. Examples for baryons are the proton with quark combination uud or the neutron with combination udd. Pions (e.g. π^+ as $u\bar{d}$) or kaons (e.g. K^+ as $u\bar{s}$) are examples for mesons. Baryons and mesons are the only hadronic combinations known to be realized in nature. The quark model classifies baryons and mesons according to their quark content. It is however known that the true structure of a hadron is more complicated than a simple composition of two or three quarks. Virtual quark pairs as well as virtual gluons that are constantly produced and annihilated also add to the picture.

One can also imagine that other possibilities to form matter, other than mesons and baryons, could exist. Combinations of four valence quarks, five valence quarks, quarks and gluons, or only gluons have been hypothesized. All of them are possible within QCD — however experiment did not yield convincing evidence for them yet.

1.3 The Discovery of the $X(3872)$

In 2003 the Belle collaboration announced the discovery of a new state [1] with a measured mass of

$$m = 3872.0 \pm 0.6 \text{ (stat)} \pm 0.5 \text{ (syst) MeV}/c^2.$$

Because the nature of the state was not clear, its mass was used to label the state $X(3872)$. It was reconstructed in the exclusive decay

$$B^\pm \to K^\pm X(3872) \to K^\pm (J/\psi \pi^+ \pi^-).$$

35.7±6.8 events were observed, with a statistical significance of 10.3σ (see figure 1.1).

The observation of the $X(3872)$ was quickly confirmed by the CDF collaboration [2]. A significant excess of 730 ± 90 candidates was found in the invariant $J/\psi\pi^+\pi^-$ mass spectrum (see figure 1.1). Also DØ [3] and *BABAR* [4] were soon able to confirm the state in the decay to $J/\psi\pi^+\pi^-$.

However, despite four independent observations, it turned out to be very difficult to answer the question 'What is the $X(3872)$?'. The most natural answer was to

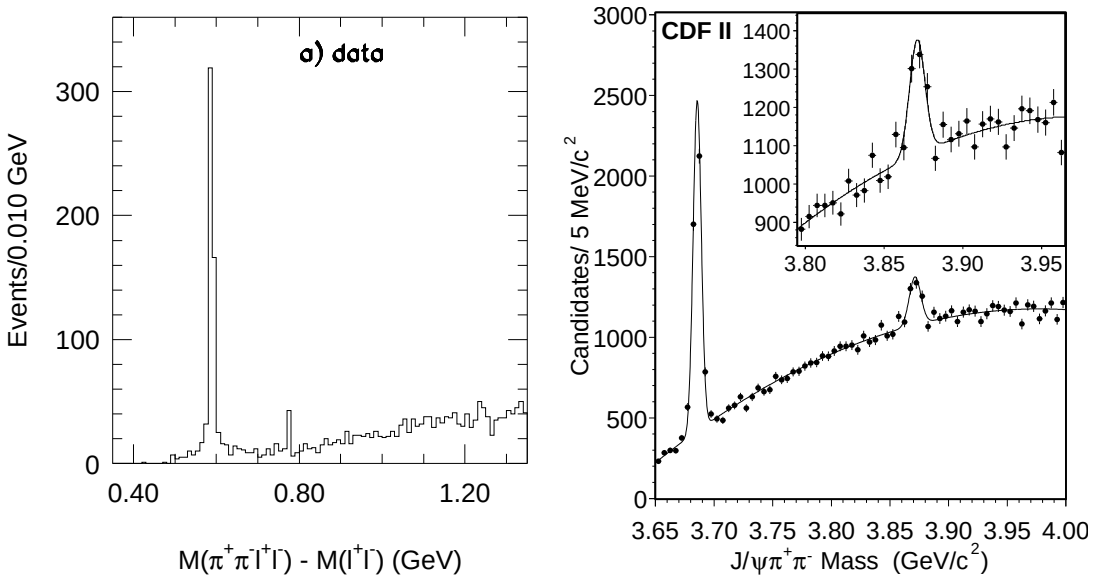

Figure 1.1: Observed spectrum of $m(J/\psi\pi^+\pi^-) - m(J/\psi)$ by Belle (left plot). The new $X(3872)$ state can be seen at $\approx 0.8\,\mathrm{GeV}/c^2$. The prominent signal at $\approx 0.6\,\mathrm{GeV}/c^2$ is the long-known charmonium state $\psi(2S)$. The right plot shows the observed spectrum of $m(J/\psi\pi^+\pi^-)$ by CDF with a clear signal peak at $\approx 3.87\,\mathrm{GeV}/c^2$.

assume that the $X(3872)$ is a charmonium state — a quark model meson state which contains a charm quark and a charm anti-quark. However, none of the possible states could be matched with expectations as will be explained in chapter 1.5.1. The intense search for alternative hypotheses and to some extent the eagerness to abandon the conventional paths would have been much less pronounced, if there had not existed a very interesting fact: the mass of the $X(3872)$ is within the errors identical to the combined mass of the D^0 and the D^{0*} mesons. This gave rise to a further, exotic hypothesis: could the $X(3872)$ be a bound state of those two mesons? And if not, could it be something else? Anything different than a charmonium state would be unprecedented in high energy physics and would open the window for a completely new spectroscopy.

1.4 The $X(3872)$: Early Measurements

After the discovery of the $X(3872)$ in 2003, the amount of experimental knowledge about this mysterious particle has steadily increased.

Information about its mass and width was already determined quite precisely in the observation and confirmation publications. The Belle collaboration observed [1] the $X(3872)$ in the decay mode[1] $B^+ \to K^+X(3872)$, $X(3872) \to J/\psi\pi^+\pi^-$. A

[1]In this thesis the charge conjugate mode is always implied, unless explicitly stated otherwise. This means that the decay $B^+ \to K^+X(3872)$ also addresses the charge conjugate decay $B^- \to K^-X(3872)$.

measurement of the mass resulted in

$$m = 3872.0 \pm 0.6 \text{ (stat)} \pm 0.5 \text{ (syst) MeV}/c^2,$$

giving the particle its name. The signal peak, very narrow and compatible with detector resolution effects, contained 35.7 ± 6.8 signal events (see figure 1.1). Belle set an upper limit on the $X(3872)$ width of

$$\Gamma < 2.3 \,\text{MeV (90\% C.L.)}$$

at 90% confidence level (C.L.).

The decay of the $X(3872)$ into the final state $J/\psi\pi^+\pi^-$ proved to be quickly observable by other experiments as well. The first confirmation was reported by the CDF collaboration [2], observing 730 ± 90 signal events (see figure 1.1). Their measured mass was

$$m = 3871.3 \pm 0.7 \text{ (stat)} \pm 0.4 \text{ (syst) MeV}/c^2.$$

The DØ collaboration observed 522 ± 100 events [3] and measured the mass difference between the J/ψ and the $X(3872)$ to be

$$\Delta m = 774.9 \pm 3.1 \text{ (stat)} \pm 3.0 \text{ (syst) MeV}/c^2,$$

translating[2] into a $X(3872)$ mass of $m = 3871.8 \text{ MeV}/c^2$. Finally, the *BABAR* collaboration was able to confirm the $X(3872)$ [4] and measured the mass

$$m = 3873.4 \pm 1.4 \,\text{MeV}/c^2.$$

The mass and the width proved to be two extraordinary pieces of information. First, the mass measurement puts the $X(3872)$ mass right on top of the sum of the D^0 and D^{0*} masses. The mass is also in the midst of the mass range, where according to the quark model, only charmonium states should exist. Second, the $X(3872)$ is very narrow. This immediately suggests that the $X(3872)$ cannot decay into two D-mesons, because this would be a strong decay, only requiring the exchange of one gluon and resulting in a broad resonance.

Belle measured the branching ratio of the B^+-decay into the $X(3872)$ in the $J/\psi\pi^+\pi^-$ mode, relative to the one into the long-known $\psi(2S)$ [1]

$$\frac{\mathcal{B}(B^+ \to K^+X(3872), X(3872) \to J/\psi\pi^+\pi^-)}{\mathcal{B}(B^+ \to K^+\psi(2S), \psi(2S) \to J/\psi\pi^+\pi^-)} = 0.063 \pm 0.012 \text{ (stat)} \pm 0.007 \text{ (syst)}.$$

Using PDG values for the $\psi(2S)$ [6], one obtains the absolute branching fraction of the decay of a B meson into the final state $J/\psi\pi^+\pi^-$ via the $X(3872)$:

$$\mathcal{B}(B^+ \to K^+X(3872), X(3872) \to J/\psi\pi^+\pi^-) = (13.0 \pm 2.9 \text{ (stat)} \pm 0.7 \text{ (syst)}) \times 10^{-6}.$$

[2] Here the J/ψ world average mass from 2006, compiled by the Particle Data Group (PDG) [5], $m_{J/\psi,PDG} = 3096.9 \,\text{MeV}/c^2$ was simply added.

The absolute branching fraction was also measured by *BABAR* [7]. They obtain a compatible value of

$$\mathcal{B}(B^+ \to K^+X(3872), X(3872) \to J/\psi\pi^+\pi^-) = (8.4 \pm 1.5\ (\text{stat}) \pm 0.7\ (\text{syst})) \times 10^{-6}.$$

The search for other decay modes of the $X(3872)$ other than into $J/\psi\pi^+\pi^-$ did not yield positive results. Prime decay channel candidates were radiative decays into charmonium states, as one would expect for the $X(3872)$ if it were a charmonium state itself. Belle searched for $\chi_{c1}\gamma$ [1], a decay channel which would be one of the most probable decay channels for certain higher charmonium states. No signal was found and a relative limit to the $J/\psi\pi^+\pi^-$ mode was set to be

$$\frac{\Gamma(X(3872) \to \gamma\chi_{c1})}{\Gamma(X(3872) \to J/\psi\pi^+\pi^-)} < 0.89\ (90\%\ \text{C.L.}).$$

Consequently Belle also searched for the decay into χ_{c2} [8]. The result here was as well negative. The following relative limit was set:

$$\frac{\Gamma(X(3872) \to \gamma\chi_{c2})}{\Gamma(X(3872) \to J/\psi\pi^+\pi^-)} < 1.1\ (90\%\ \text{C.L.}).$$

Belle [9] searched for decays into charged or neutral D-mesons. If allowed, this strong decay would have a very high branching fraction — which already seemed unlikely because of the narrow $X(3872)$ width. Consequently, no signal was found and the limits were set to be

$$\begin{aligned} \mathcal{B}(B^+ \to K^+X(3872), X(3872) \to D^0\bar{D}^0) &< 6 \times 10^{-5}\ (90\%\ \text{C.L.}), \\ \mathcal{B}(B^+ \to K^+X(3872), X(3872) \to D^+D^-) &< 4 \times 10^{-5}\ (90\%\ \text{C.L.}), \end{aligned}$$

compared to the value of $\mathcal{B} \approx 10 \times 10^{-6}$ in the observation channel.

Of further interest were decay modes similar to the discovery mode. *BABAR* investigated the decay channel $X(3872) \to J/\psi\eta$ [10]. No signal was found and the limit was set to be

$$\mathcal{B}(B^+ \to K^+X(3872), X(3872) \to J/\psi\eta) < 7.7 \times 10^{-6}\ (90\%\ \text{C.L.}).$$

BABAR searched for charged partners of the $X(3872)$ [11] in decays involving a neutral and a charged pion. No signal was found and the following limits were set:

$$\begin{aligned} \mathcal{B}(B^0 \to K^+X^-, X^- \to J/\psi\pi^-\pi^0) &< 5.4 \times 10^{-6}\ (90\%\ \text{C.L.}), \\ \mathcal{B}(B^- \to K^0_SX^-, X^- \to J/\psi\pi^-\pi^0) &< 11 \times 10^{-6}\ (90\%\ \text{C.L.}). \end{aligned}$$

No traces of a signal were found as well in the decay to $J/\psi\pi^0\pi^0$ [12]. This mode probes the isospin of the dipion system in the decay to $J/\psi\pi\pi$. For isospin $I = 1$, one would expect to see no signal, while for $I = 0$ the ratio to the observation mode

would be expected to be $\approx 50\%$, as is the case for the $\psi(2S)$. As a result a limit for this mode was set to

$$\frac{\Gamma(X(3872) \to J/\psi\pi^0\pi^0)}{\Gamma(X(3872) \to J/\psi\pi^+\pi^-)} < 1.3 \times \frac{\Gamma(\psi(2S) \to J/\psi\pi^0\pi^0)}{\Gamma(\psi(2S) \to J/\psi\pi^+\pi^-)} \text{ (90\% C.L.)}.$$

This is however not stringent enough to make a firm statement about the dipion isospin. Information about the dipion isospin can also be obtained from the invariant dipion mass distribution. Belle measured [1] that the mass of the dipion system clusters at high masses, which suggests that the dipion system could be dominated by an intermediate ρ^0 resonance with isospin $I = 1$. However, the clustering at high masses is also predicted for some $I = 0$ hypotheses.

Not a different decay channel, but a different production channel was probed by the CLEO collaboration. They performed a search for the $X(3872)$ in untagged $\gamma\gamma$ fusion events and initial state radiation (ISR) e^+e^- annihilation [13]. No signal was found and the following limits were set: For an $X(3872)$ with positive C-parity and spins zero or two — the possible quantum numbers of two untagged photons — the limit is

$$(2J+1)\Gamma_{\gamma\gamma}(X(3872)) \times \mathcal{B}(X \to J/\psi\pi^+\pi^-) < 12.9\,\text{eV (90\% C.L.)}.$$

For an $X(3872)$ with quantum numbers $J^{PC} = 1^{--}$, the limit is

$$\Gamma_{ee}(X(3872)) \times \mathcal{B}(X \to J/\psi\pi^+\pi^-) < 8.3\,\text{eV (90\% C.L.)}.$$

Further searches in ISR events in e^+e^- annihilation also returned no signal. The BES collaboration obtained a limit [14] of

$$\Gamma_{ee}(X(3872)) \times \mathcal{B}(X(3872) \to J/\psi\pi^+\pi^-) < 10\,\text{eV (90\% C.L.)},$$

and *BABAR* [15] sets a limit of

$$\Gamma_{ee}(X(3872)) \times \mathcal{B}(X(3872) \to J/\psi\pi^+\pi^-) < 6.2\,\text{eV (90\% C.L.)}.$$

From these experiments it appears very unlikely that the $X(3872)$ is a vector particle. This is not surprising since otherwise the $X(3872)$ very likely would already have been observed much earlier in e^+e^--collision experiments.

At the Tevatron the $X(3872)$ can be both produced via B-meson decays, as is the case at Belle or *BABAR*, or in the fragmentation of the collision products. The production fraction of $X(3872)$ which stem from B decays is measured by CDF [16]. A value of

$$16.1 \pm 4.9\ \text{(stat)} \pm 1.0\ \text{(syst)}\ \%$$

was determined. So only a very small fraction of the observed $X(3872)$ particles at the Tevatron stems from B decays.

DØ compared multiple quantities of the $X(3872) \to J/\psi\pi^+\pi^-$ decay to those of the $\psi(2S) \to J/\psi\pi^+\pi^-$ decay [3]. Good agreement between the $X(3872)$ and the $\psi(2S)$

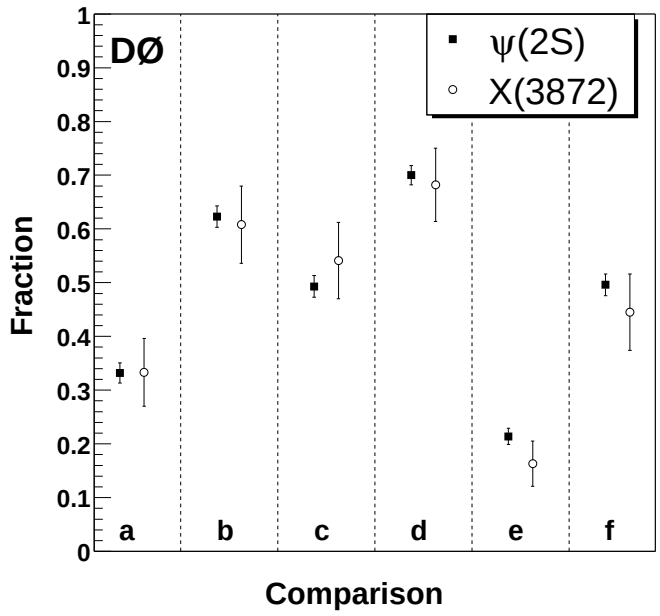

Figure 1.2: Comparison of various kinematic properties of the $\psi(2S)$ and the $X(3872)$ by DØ. Shown are the fraction of candidates with (a) transverse momentum $p_T > 15$ GeV/c, (b) rapidity $|y| < 1$, (c) helicity angle $\cos(\theta_\pi) < 0.4$, (d) decay length $L_{xy} < 0.01$, (e) isolation fulfillment, and (f) helicity angle $\cos(\theta_\mu) < 0.4$.

in the tested quantities was observed (see figure 1.2), indicating no major differences in the production and decay mechanisms between the $\psi(2S)$ and the $X(3872)$.

Finally, Belle performed an angular analysis for the quantum numbers $J^{PC} = 1^{+-}$. By comparing predictions to measurements Belle disfavors the assignment that the $X(3872)$ is a $h_c'(1^{+-})$ charmonium state [8].

1.5 The $X(3872)$: Possible Interpretations

Immediately after the discovery of the $X(3872)$ and the measurement of the first experimental properties the $X(3872)$ became a subject of discussion. The initial search by Belle was motivated by the search for new charmonium states. The properties of the $X(3872)$ did however not fit into charmonium model predictions, so that the initial plan to assign a charmonium state to the $X(3872)$ quickly changed from the question 'Which charmonium state can we assign to the $X(3872)$?' to 'Can we assign a charmonium state to the $X(3872)$ at all?'.

1.5.1 Charmonium Hypothesis

Since the final state of the decay mode $X(3872) \to J/\psi\pi^+\pi^-$ contains the J/ψ, a low-energetic charmonium state, it is natural to assume that also the higher-energetic

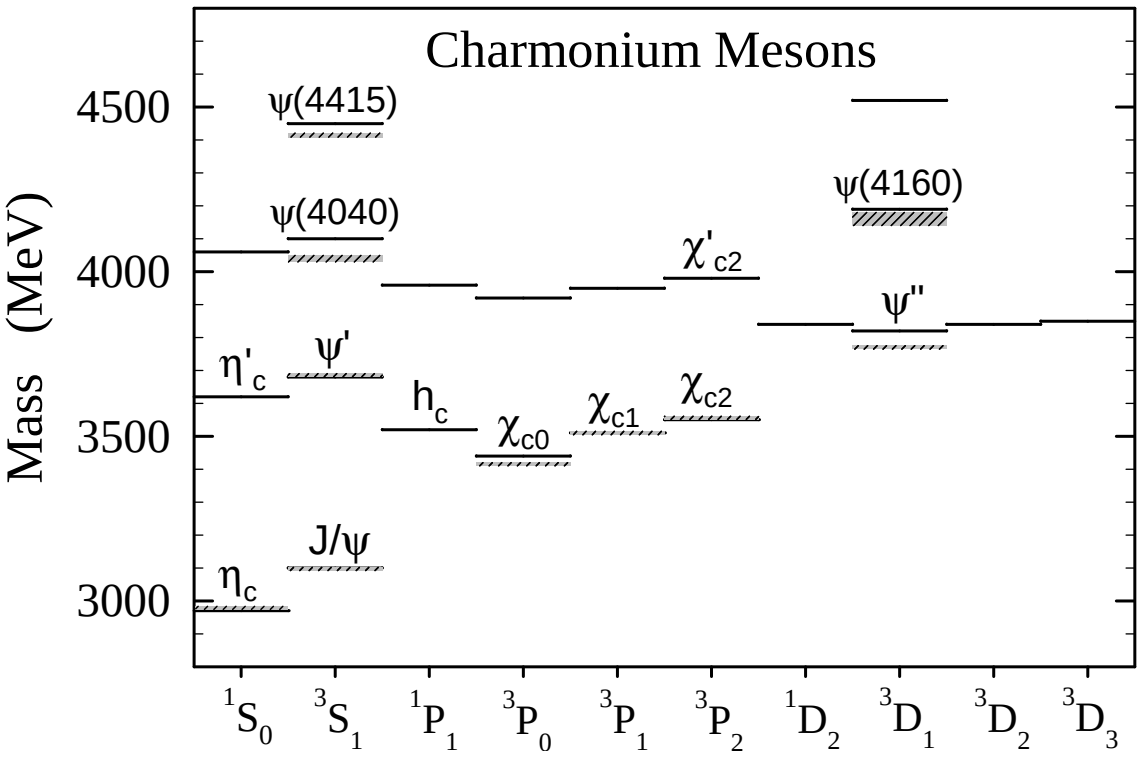

Figure 1.3: The charmonium spectrum [18]. Observed states are labelled, the naming scheme is explained in the text.

initial state contains a c-quark and an $\bar{c}$-quark. A charmonium state is the simplest configuration of a stable system containing those two quarks. Heavier quarks (e.g. a b-quark) in the initial state are very unlikely, since the known mesons containing a b-quark are much heavier than $3.87\,\mathrm{GeV}/c^2$. A charmonium state is the conservative quark model hypothesis for the $X(3872)$ and because of this the obvious place to start searching for candidates.

A charmonium system is a bound system of a c-quark and a $\bar{c}$-quark. The hydrogen atom is a rather close analogy. An even better analogy, taking into account the identical masses of the constituents, is the positronium. The dominating force at short-distances between the quarks is described by single-gluon-exchange, while at larger distances confinement becomes the dominant factor. The potential thus is commonly described by a Coulomb-like potential for small distances and a linear increase for larger distances. The energy levels of such a system can be found in analogy to the hydrogen atom by solving a non-relativistic Schrödinger equation [17].

The spectroscopy of charmonium state uses

- the quantum number for radial excitation n,
- the relative orbital angular momentum between the quarks $L = 0,1,2,\ldots$, denoted as $S,P,D,\ldots$,
- the combined spin $S = 0, 1$ of the two quarks,

- the total angular momentum $J = L \oplus S$

to define a state in the notation: $(n+1)^{2S+1}L_J$. Figure 1.3 shows the charmonium spectrum with emphasis on the observed states. However, there is also an alternative nomenclature for the known, low-lying states that assign the names after the convention of the Particle Data Group. For charmonia, it uses the symbols

- η for L-even singlet states (S=0),
- ψ for L-even triplet states (S=1),
- h for L-odd singlet states (S=0),
- χ for L-odd triplet states (S=1).

A very important physical aspect of the charmonium states are their quantum numbers P and C, which describe the behavior of the wave-function of the state under the parity operation and the charge-parity operation. Those quantum numbers define the physical behavior of the whole $c\bar{c}$-system, compared to n, L, and S which are important to describe the internal dynamics. They relate as follows:

$$\begin{aligned} P &= (-1)^{L+1}, \\ C &= (-1)^{L+S}. \end{aligned}$$

The lightest charmonium state is the η_c with $J^{PC} = 0^{-+}$. The two quark spins arrange to have total spin $S = 0$, the orbital angular momentum between the quarks is $L = 0$ as well, so that the total angular momentum is $J = 0$. This state thus is labelled 1^1S_0 in spectroscopic notation. The other state with $L = 0$ but with $S = 1$ is the most familiar charmonium state, the J/ψ (1^3S_1, $J^{PC} = 1^{--}$). The first radial excitations of those two states are the η_c' and the ψ', the second commonly referred to as $\psi(2S)$. In spectroscopic notation they are labelled 2^1S_0 and 2^3S_1, respectively.

The set of lightest charmonium states with $L = 1$ are called h_c (1^1P_1, $J^{PC} = 1^{+-}$) for the spin-singlet state with $S = 0$, and χ_c for the spin triplet states with $S = 1$: χ_{c0} (1^3P_0, $J^{PC} = 0^{++}$), χ_{c1} (1^3P_1, $J^{PC} = 1^{++}$), χ_{c2} (1^3P_2, $J^{PC} = 2^{++}$).

Those are all of the unambiguously known states. The main reason why no higher states are known is the fact that higher states mostly have masses above the $D\bar{D}$ thresholds:

- $D\bar{D}$ at a mass of $\approx 3730\,\mathrm{GeV}/c^2$,
- $D^*\bar{D}$ at a mass of $\approx 3875\,\mathrm{GeV}/c^2$,
- $D^*\bar{D}^*$ at a mass of $\approx 4015\,\mathrm{GeV}/c^2$.

These thresholds are important, because states with masses higher than those thresholds are kinematically allowed to decay into two D-mesons. If this decay is not suppressed for other reasons, it will become highly dominant since it is a strong decay involving only low-energetic (often called 'soft') gluons. The fast decay into $D\bar{D}$ translates to a broad state in mass, so that it is experimentally very difficult to isolate these states. This is not true for states which cannot decay to $D\bar{D}$ for other reasons, for example because of conservation of parity. These states can be narrow even above the $D\bar{D}$ threshold.

C-parity and isospin are important quantum numbers for the discussion of the possible charmonium assignments to the $X(3872)$. In the observation mode $X(3872) \to J/\psi\pi^+\pi^-$ the pions in the dipion system can be either in relative S-wave, forming the quantum numbers $J^{PC}_{\pi\pi} = 0^{++}$, or in relative P-wave ($J^{PC}_{\pi\pi} = 1^{--}$) — higher angular momenta are suppressed at the low dipion energies that are available in the $X(3872)$-decay. Because the J/ψ has $C = -1$, a C-even assignment of the $X(3872)$ translates into a C-odd (i.e. $J^{PC}_{\pi\pi} = 1^{--}$) assignment for the dipion system, and vice versa. In the $X(3872)$ decay, the C-parity is closely connected to the isospin. The isospin of a vector state dipion system is $I = 1$, since the ρ meson is the only dipion resonance which is kinematically allowed. However, a charmonium state always has isospin $I = 0$ (because it does not contain any light quarks), and can only decay into isospin $I = 0$ final states. An assignment which implies $C = +1$ for the charmonium state thus implies isospin violating effects in the decay.

In order to find good charmonium candidates, the expected spectrum is investigated. Good $X(3872)$ candidates are both the unobserved D-wave states, as well as higher radial excitations of the S- and P-wave states. F-wave states are neglected since they are expected to have masses higher than $4\,\mathrm{GeV}/c^2$ [19]. These possible states are:

- The 3^1S_0 state (η_c''): The η_c'' has quantum numbers $J^{PC} = 0^{-+}$. The main reason that disfavors the assignment to the $X(3872)$ is the predicted mass for the 3^1S_0, which is $\approx 4000 - 4100\,\mathrm{MeV}/c^2$ [19, 20] and thus too high. It is in addition very unlikely that the radially excited state has a smaller total decay width than the ground state, the η_c, with $\Gamma = 25.5 \pm 3.4\,\mathrm{MeV}/c^2$ [5]. (The limit on the $X(3872)$ width is smaller than $2.3\,\mathrm{MeV}/c^2$ at 90% C.L.)

- The 3^3S_1 state ($\psi(3S)$): This state with $J^{PC} = 1^{--}$ would be allowed to decay into $D\bar{D}$, leading to a large expected decay width. In addition, one would expect for any narrow, low-energetic, prominent vector state that it would have already been observed in electron-positron collisions.

- The 2^1P_1 state (h_c'): The h_c' is in most models expected to have masses higher than $3900\,\mathrm{MeV}/c^2$ [19, 20]. The assignment to a $J^{PC} = 1^{+-}$ state is also strongly disfavored from the comparison of the expected decay angular distribution to measured data [21].

- The 2^3P_0 state (χ_{c0}'): Since the χ_{c0}' can decay into $D\bar{D}$, the narrow observed width of the $X(3872)$ is a strong argument against this mode. In addition,

no signal was observed in ISR events, where states with $J^{PC} = 0^{++}$ can be produced.

- The 2^3P_1 state (χ'_{c1}): The mass of the χ'_{c1} with $J^{PC} = 1^{++}$ is expected to be $\approx 3930 - 4000\,\mathrm{MeV}/c^2$ [19, 20]. In addition, the expected width of this state is greater than $10\,\mathrm{MeV}/c^2$ [20].

- The 2^3P_2 state (χ'_{c2}): The assignment as a χ'_{c2}, a charmonium state with $J^{PC} = 2^{++}$, is improbable for various reasons. It can decay to $D\bar{D}$, leading to a large expected width, its expected mass is higher [19, 20], and no signal was observed in ISR events.

- The 1^1D_2 state (η_{c2}): This hypothesis would assign the quantum numbers $J^{PC} = 2^{-+}$. This decay is isospin-violating (as for every charmonium-state with C-parity $+1$) and one would thus expect a very tiny decay width into the final state $J/\psi\pi^+\pi^-$. Scenarios to explain the isospin breaking are possible, however this would require further assumptions.

- The 1^3D_1 state (ϕ_{c1}): This state has the quantum numbers $J^{PC} = 1^{--}$. The same arguments as for the 3^3S_1 apply.

- The 1^3D_2 state (ϕ_{c2}): For this state with $J^{PC} = 2^{--}$ a $\approx 70\,\mathrm{MeV}/c^2$ lower mass is expected [19, 20]. One should also observe a signal in the decay mode $X(3872) \to \chi_{c1}\gamma$, which yielded only experimental limits.

- The 1^3D_3 state (ϕ_{c3}): Similar arguments as for the 1^3D_2 apply for the 1^3D_3 with quantum numbers $J^{PC} = 3^{--}$. The expected, but unobserved decay is in this case $X(3872) \to \chi_{c2}\gamma$. Interestingly, the decay $1^3D_3 \to D\bar{D}$ is allowed, but still yields a small expected width. The reason is that in order to satisfy angular momentum conservation, a relative angular momentum of $L = 3$ between the two D-mesons would be required, which suppresses the strong decay.

No single state shows good agreement between theoretical model expectations and experimental observations. In order to match the $X(3872)$ to any of these states, changes are required for the charmonium models. Taking into account possible model variations, the unobserved D-wave states 1^1D_2, 1^3D_2, and 1^3D_3 are most likely to be explainable, because they have no gauge for mass splittings from experiment.

1.5.2 Molecular Hypothesis

In absence of a fitting charmonium hypothesis, attention soon focused on the peculiar mass of the $X(3872)$, which is in remarkable agreement with the sum of the D^0- and D^{0*}-masses. The measured masses [6, 22] are

$$m(X(3872)) = 3871.4 \pm 0.6\,\mathrm{MeV}/c^2$$

and

$$\begin{aligned} m(D^0) + m(D^{0*}) &= 1864.84 \pm 0.17\,\mathrm{MeV}/c^2 \quad + \quad 2006.97 \pm 0.19\,\mathrm{MeV}/c^2 \\ &= 3871.81 \pm 0.36\,\mathrm{MeV}/c^2. \end{aligned}$$

It can be seen that the mass of the $X(3872)$ is within the errors identical to the sum of the D^0- and D^{0*}-masses, so that the hypothesis of a bound state of these two mesons suggests itself. In addition, a molecular model also would explain the apparent breaking of isospin symmetry if the $X(3872)$ decays via $X(3872) \to J/\psi\rho^0$. The mass difference between the D^0D^{0*} and the D^+D^{-*} threshold is $\approx 8\,\mathrm{MeV}/c^2$. So the regular isospin $I = 0$ wave function, $(|D^0D^{0*}\rangle + |D^+D^{-*}\rangle)/\sqrt{2}$, shows severe isospin breaking because the contribution from D^+D^{-*} is above threshold and suppressed. This in turn means that the wave function of a molecular state is not an isospin eigenstate and that there is a significant $I = 1$ contribution.

The molecular hypothesis, like any of the alternative hypotheses, does not constitute 'new physics' in a sense of new fundamental matter particles — nothing in the theory of strong interactions (QCD) explicitly prevents such a molecular state. This being said, a positive identification would still be revolutionary for the understanding of matter. What other kinds of hadronic bound states could then exist? At which energies? How would they interact with the states we know?

The general idea of molecular hadronic states is nothing new, of course. A possible application of the idea was already tested for early known states as the $a_0(980)$ — as a possible candidate for a $K\bar{K}$-molecule [23]. However, no conclusive result could be obtained, mostly because states from the light-quark sector have large decay widths and overlap with nearby states. The possibility of the bound interaction of mesons with charm content can be traced back to works of Voloshin and Okun [24] in 1976. The charmonium state $\psi(4040)$, which initially did not fit well into the charmonium picture because of an unexpectedly high decay rate into $D\bar{D}^*$, was proposed to be a charmed molecule by De Rujula *et al.* [25]. Later the high $D\bar{D}^*$ rate was resolved differently and the $\psi(4040)$ could be assigned to the charmonium state 3^3S_1. So the idea of hadronic molecules has been around for quite some time, but no compelling evidence has yet been found.

The basic hypothesis of a bound state between D^0 and D^{0*} is suggested in different ways. Törnqvist [26] discusses a deuteron-like system ('deuson') where the D^0 and D^{0*} mesons are bound exclusively by long-range pion exchange. In this model only states with quantum numbers $J^{PC} = 1^{++}$ or $J^{PC} = 0^{-+}$ would be bound, for others pion exchange is repulsive or too weak to form bound states. This model can also be applied to the b-quark sector to predict b-deusons at masses of $\approx 10.55\,\mathrm{GeV}/c^2$, which are also more strongly bound. The question whether a system, only comprised of D^0 and D^{0*}, is able to form a bound state is challenged by Liu *et al.* [27].

Swanson [28] extends Törnqvist's model by adding short-range quark/gluon interactions to the long-range pion exchange. Assuming an S-wave coupling of D^0 and D^{0*} to be the main contribution to the state, the quantum numbers $J^{PC} = 1^{++}$ are predicted. Another refinement is the admixture of $J/\psi\rho^0$, $J/\psi\omega$ and D^+D^- to the

basic $D^0 - D^{0*}$ wave-function. The model predicts large decay widths into $J/\psi\pi^+\pi^-$ and $J/\psi\pi^+\pi^-\pi^0$ of similar magnitude. No $D\bar{D}$ molecules are expected, however a rich spectrum of $D^*\bar{D}^*$, $B\bar{B}^*$, and $B^*\bar{B}^*$ should exist.

Other works on the subject [29, 30, 31, 32] add further predictions to the molecular hypothesis. For once, even a bound state of lighter mass than the combined D^0-D^{0*} mass should be observable as a threshold enhancement in the $D^0\bar{D}^0\pi$ or $D^0\bar{D}^0\gamma$ spectrum[3]. Another expectation is that the branching fraction of the decay $B^0 \to X(3872)\ K^0$ should be suppressed compared to the decay $B^+ \to\ X(3872)\ K^+$ by an order of magnitude.

1.5.3 Multiquark Hypotheses

A different approach to the $X(3872)$ is used in the so-called multiquark hypotheses, which use four quarks to form a state. Multiquark states were already proposed in the 1970's [33]. Especially the $a_0(980)$ and $f_0(980)$ states were proposed as good candidates. However, contradictory predictions and missing experimental evidence resulted in insufficient support for the 4-quark hypothesis.

The unknown nature of the $X(3872)$ led to a resurgence of the 4-quark model. Various different implementations of the general 4-quark model have been suggested that can accommodate the $X(3872)$ as a multiquark state containing two light quarks and two charm quarks [34, 35, 36, 37, 38, 39, 40].

Most interesting from an experimental point of view is the model of Maiani *et al.* [34, 41], because it makes strong and verifiable predictions. This model is a 'diquark-antidiquark' model which divides the four constituent quarks into a $[cq][\bar{Q}\bar{q}']$ structure with light quarks $q, q' = u, d$ and a heavy quark $Q = c, s$, constraining itself on hidden and open charm states. The quarks are grouped into color triplet scalar or vector clusters. The interactions between the two clusters is dominated by spin-spin interactions. Binding is achieved by the color forces of gluon exchange – in contrast to the molecular picture, which is dominated by long-range colorless pion exchange.

The model predicts a number of states, most importantly four states related to the $X(3872)$, $X^+ = [cu][\bar{c}\bar{d}]$, $X^- = [cd][\bar{c}\bar{u}]$, $X_u^0 = [cu][\bar{c}\bar{u}]$, and $X_d^0 = [cd][\bar{c}\bar{d}]$. The two neutral states mix to form the physical states X_{low} and X_{high}, described by the mixing angle θ:

$$X_{low} = X_u^0 \cos\theta + X_d^0 \sin\theta,$$
$$X_{high} = -X_u^0 \sin\theta + X_d^0 \cos\theta.$$

Because of this, isospin is broken for the neutral mass eigenstates, and consequently in their strong decay as well. The mass difference between the two states is expected to be

$$m(X_{high}) - m(X_{low}) = \frac{7 \pm 2}{\cos(2\theta)}\ \mathrm{MeV}/c^2.$$

[3]The D^{0*} decays to $D^0\pi^0$ or $D^0\gamma$.

The fact that apparently only one narrow neutral state is observed at the B-factories is explained by stating that the two states X_{low} and X_{high} populate the decay channels $B^+ \to X(3872)K^+$ and $B^0 \to X(3872)K^0_S$ differently[4]. The ratio of these two decays is expected to be of the order of ≈ 1.

1.5.4 Alternate Hypotheses

Charmonium Hybrid

Hybrid mesons combine a regular meson state, in our case charmonium, with an excited gluonic degree of freedom. In fact, lattice gauge theory and hadron models predict a rich spectrum of charmonium hybrid mesons [42, 43]. Several predictions, either using the 'flux-tube model' [44, 45, 46] or lattice calculations [47], expect $c\bar{c}g$ hybrids in the mass range of $4.0 - 4.2\,\mathrm{GeV}/c^2$. Of special interest are the states with quantum numbers $J^{PC} = 0^{+-}$, 1^{-+}, and 2^{+-} since those cannot be obtained with a simple $c\bar{c}$ charmonium model and would, if observed, unambiguously proof an unconventional state.

Li [48] suggests the hybrid hypothesis for the $X(3872)$ and predicts a dominant decay $X(3872) \to J/\psi gg$. The $X(3872)$ should also have a sizable branching fraction to $J/\psi\sigma$.

The deviation of the measured mass of $3.87\,\mathrm{GeV}/c^2$ to the expected masses above $4.0\,\mathrm{GeV}/c^2$ is a serious argument against the hybrid hypothesis. However, since no experimental 'gauge' exists to guide systematic effects, predicted masses may shift significantly.

Cusp/Threshold Effect

In contrast to exotic models, Bugg [49, 50, 51] ascribes the resonance structure of the $X(3872)$ to a possible threshold cusp. These cusps can appear in any process, at the threshold where a coupled channel opens. In the case of the $X(3872)$, the resonance-like structure is explained in a way that randomly produced $D\bar{D}^*$ final states with low relative momentum de-excite into open channels like $J/\psi\pi\pi$ and produce a cusp in the $J/\psi\pi\pi$ mass spectrum.

Kalashnikova [52, 53] constructs a coupled channel model of the $c\bar{c}$ system with couplings to the $D\bar{D}$ continua ($D\bar{D}$, $D\bar{D}^*$, $D^*\bar{D}^*$, ...). In the calculations for the different charmonium states the χ'_{c1} stands out, because, in addition to the regular χ'_{c1} resonance at $\approx 4\,\mathrm{GeV}/c^2$, a virtual bound state just above the $D\bar{D}^*$ threshold is predicted, which produces a cusp in the $J/\psi\pi\pi$ final state.

[4]The need to investigate two separate decay modes is not an issue for the inclusive data samples studied in hadron colliders.

Glueball

Seth [54] proposes the assignment of a glueball to the $X(3872)$ — a bound state containing only gluons, no quarks. This model is based on the mass calculations by Morningstar and Peardon [55], who predict a state with quantum numbers 1^{--} at a mass of $m \approx 3850\,\mathrm{MeV}/c^2$.

This model assumes a small admixture of $c\bar{c}$ quark content stemming from the $\psi(2S)$ which is responsible for the decay to $J/\psi\pi^+\pi^-$. Then, as for the $\psi(2S)$, also the decays $X(3872) \to J/\psi\pi^0\pi^0$ and $X(3872) \to J/\psi\eta$ are expected. This, together with the quantum number prediction, can be used to test the hypothesis.

1.5.5 Summary of Hypotheses

In order to explain the $X(3872)$, three major hypotheses stand out: the charmonium, the molecule and the multiquark state. The charmonium hypothesis is strong, because it is after all a well-proven model for other states. It however requires adjustment to explain the $X(3872)$.

Next to the charmonium hypothesis, all other hypotheses are exotic in a sense, that they deviate from the known structures of matter in high energy physics. Be it a molecule or a multiquark state, an unambiguous identification would imply the existence of similar states and maybe even a completely new spectrum of particles. Although this is an intriguing, maybe even probable situation, care is required to draw this conclusion.

1.6 Recent Experimental Developments

The measurements up to the end of 2004 allowed no significant insight into the $X(3872)$ nature. They allowed no strong rejection of any hypothesis, either. The assignment as one of the charmonium states was doubtful, however far from excluded. The number of alternative hypothesis was growing, with no good handle for verification. This changed in 2005, when measurements started to shed light onto the nature of the $X(3872)$.

First evidence for other decay modes was finally seen in 2005. Belle found evidence ($4.0\,\sigma$) for the decay mode $X(3872) \to J/\psi\gamma$ [56], see figure 1.4. The branching fraction was determined as

$$\mathcal{B}(B^+ \to K^+X(3872), X(3872) \to J/\psi\gamma) = (1.8 \pm 0.6(\mathrm{stat}) \pm 0.1(\mathrm{syst})) \times 10^{-6}.$$

This allows to determine the partial width ratio:

$$\frac{\Gamma(X(3872) \to J/\psi\gamma)}{\Gamma(X(3872) \to J/\psi\pi^+\pi^-)} = 0.14 \pm 0.05.$$

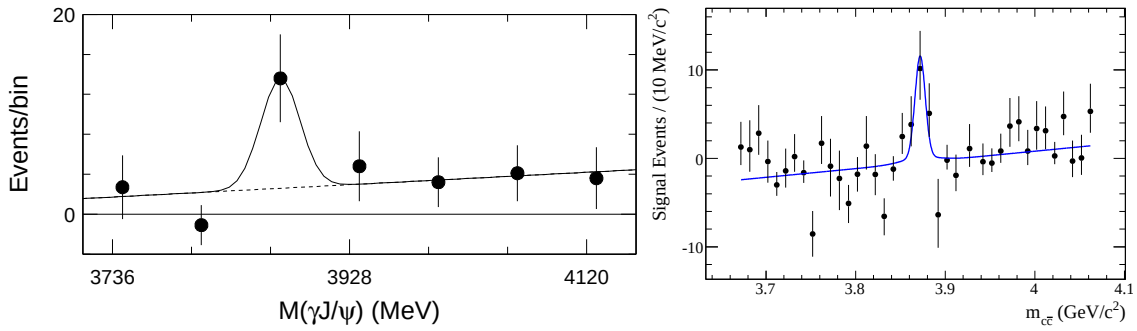

Figure 1.4: The independent pieces of evidence for the decay $X(3872) \to J/\psi\gamma$ by Belle (left) and *BABAR* (right).

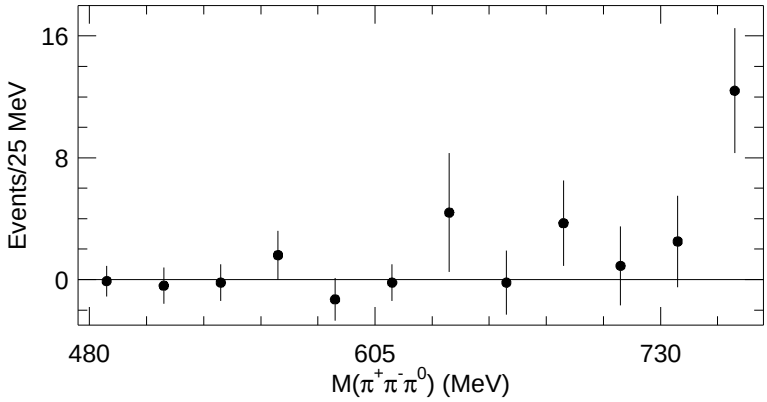

Figure 1.5: The indication for the decay mode $X(3872) \to J/\psi\pi^+\pi^-\pi^0$ by Belle. Both the signal itself and the interpretation as $X(3872) \to J/\psi\omega$ need independent confirmation.

Since the significance of the signal is not unambiguously convincing, it was very helpful that this decay mode was independently confirmed by *BABAR* [57], albeit with low significance as well (see figure 1.4). *BABAR* observed the $X(3872)$ in the decay to $J/\psi\gamma$ with a significance of $3.4\,\sigma$. Their determination of the branching fraction yields

$$\mathcal{B}(B^+ \to K^+X(3872), X(3872) \to J/\psi\gamma) = (3.3 \pm 1.0(\text{stat}) \pm 0.3(\text{syst})) \times 10^{-6}.$$

Belle also found evidence ($4.3\,\sigma$) [56] for the decay $X(3872) \to J/\psi\pi^+\pi^-\pi^0$ (see figure 1.5), which was interpreted as the decay $X(3872) \to J/\psi\,\omega$. This is a very important decay mode to understand the internal $X(3872)$ dynamics. Usually, this decay should be suppressed due to the fact that it is kinematically forbidden and can only proceed if the ω fluctuates to a lower mass. Because the ω is very narrow this should happen very rarely. In exotic models there are however different mechanisms that allow the decay to a virtual, off-shell ω that can enhance the ratio. An unexpectedly high branching ratio thus would indicate exotic content in the $X(3872)$.

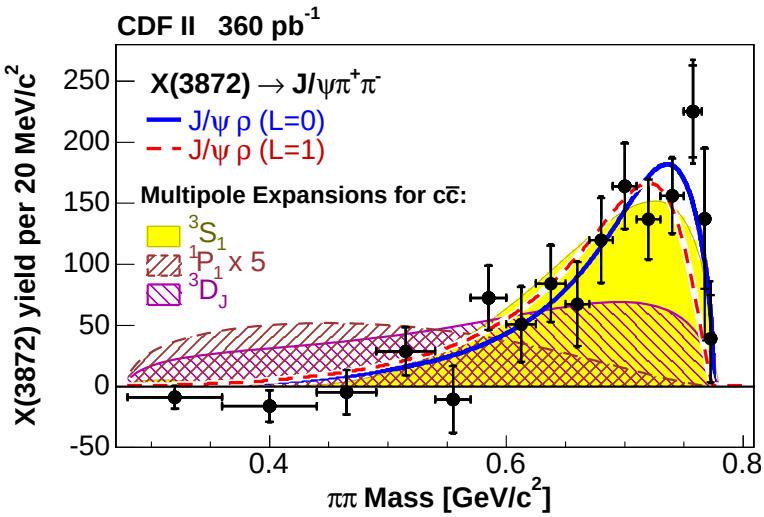

Figure 1.6: The measurement of the $\pi^+\pi^-$ mass spectrum in the decay $J/\psi\pi^+\pi^-$ by CDF. Shown as well are theory predictions for different $X(3872)$ assignments. An intermediate ρ^0 gives good fit probabilities, both in relative angular momentum $L = 0$ and $L = 1$ with the J/ψ.

The branching fraction to the decay mode $X(3872) \to J/\psi\pi^+\pi^-$ is measured to be

$$\frac{\mathcal{B}(X(3872) \to J/\psi\pi^+\pi^-\pi^0)}{\mathcal{B}(X(3872) \to J/\psi\pi^+\pi^-)} = 1.0 \pm 0.4(\text{stat}) \pm 0.3(\text{syst}).$$

Those results are of primary importance for the quantum numbers of the $X(3872)$. Both the ω and the photon are vector particles, which fixes the C-parity of the $X(3872)$ to $C_{X(3872)} = C(J/\psi) \cdot C(\gamma/\omega) = +1$. Further conclusions should however be drawn with care, especially if one wants to base arguments on the numerical values of the branching fractions, since the statistics is very low. The decay into $J/\psi\omega$ is not confirmed up to the present day.

Belle updated its investigation of the dipion mass behavior in the decay $X(3872) \to J/\psi\pi^+\pi^-$ [58]. It was concluded that the best fit is obtained by the interpretation of the $\pi\pi$-system as a ρ^0 meson, which is in relative angular momentum $L = 0$ with the J/ψ. This was investigated by CDF [59] as well. The dipion mass spectrum was measured with higher statistics and compared to various theoretical hypotheses (see figure 1.6). As a result it was shown that, although a decay via a ρ^0 indeed gives a very good fit result, the uncertainty on the choice of form factor parameters does not allow an unambiguous separation between the $L = 0$ or $L = 1$ case. The good agreement of the dipion mass shape with an intermediate ρ^0 agrees with the $C = +1$ assignment for the $X(3872)$. The question, whether the dipion system is in a relative S-wave or P-wave configuration with the J/ψ, is important for the quantum numbers as well. This issue will be covered in chapter 3.1 in more detail, for now it suffices to say that the quantum numbers $J^P = 0^+, 1^+, 2^+$ are allowed for a relative S–wave, while $J^P = 0^-, 1^-, 2^-, 3^-$ are allowed for a relative P-wave.

Belle expanded their early angular analysis by testing more quantum number com-

binations [58]. In combination with the observation of the $J/\psi\gamma$ mode and their conclusions about the behavior of the dipion-mass spectrum in the decay $X(3872) \to J/\psi\pi^+\pi^-$, Belle concludes that the assignment 1^{++} is favored, but 2^{++} not ruled out.

Furthermore, the angular correlations in the decay $X(3872) \to J/\psi\pi^+\pi^-$ were studied, which is the main result of this thesis and described in detail in chapter 3. It was published in reference [60]. Based on angular distributions alone, only the quantum number hypotheses 1^{++} and 2^{-+} can be accommodated with the observed data, thus drastically limiting the number of possible charmonium states, excluding the glueball hypothesis, and strengthening the molecular and multiquark models.

BABAR investigated a possible difference in the behavior between $X(3872)$ particles from B^+ and B^0 decays [7]. They observed a mass difference in the two decay modes of

$$\Delta m = 2.7 \pm 1.6(\text{stat}) \pm 0.4(\text{syst})\ \text{MeV}/c^2.$$

For the B^+ decay mode they also measured the $X(3872)$ width

$$\Gamma(X(3872)) = 1.1 \pm 1.5(\text{stat}) \pm 0.2(\text{syst})\ \text{MeV},$$

which corresponds to the limit

$$\Gamma(X(3872)) < 3.3\,\text{MeV}\ (90\%\ \text{C.L.}).$$

The two branching fractions were measured to be:

$$\mathcal{B}(B^0 \to K^0_S X(3872), X(3872) \to J/\psi\pi^+\pi^-) = (3.5 \pm 1.9(\text{stat}) \pm 0.4(\text{syst})) \times 10^{-6},$$
$$\mathcal{B}(B^+ \to K^+ X(3872), X(3872) \to J/\psi\pi^+\pi^-) = (8.4 \pm 1.5(\text{stat}) \pm 0.7(\text{syst})) \times 10^{-6},$$

forming the ratio

$$R = 0.41 \pm 0.24(\text{stat}) \pm 0.05(\text{syst}).$$

The same measurement was performed by Belle [61]. They determined the mass difference to be

$$\Delta m = 0.22 \pm 0.90(\text{stat}) \pm 0.27(\text{syst})\ \text{MeV}/c^2,$$

compatible with no mass difference. The relative branching fraction is

$$\frac{\mathcal{B}(B^0 \to K^0_S X(3872))}{\mathcal{B}(B^+ \to K^+ X(3872))} = 0.94 \pm 0.24(\text{stat}) \pm 0.10(\text{syst}).$$

These measurements are important for exotic interpretations, which predict more than one neural state and different branching fractions in neutral and charged B-decays. The experimental values from Belle and *BABAR* are compatible, but they are both based on low statistics. The central values do neither support the existence of two separate neutral states (predicted for multiquark hypotheses), nor do they indicate an order-of-magnitude difference in the B^0 and B^+ decay modes (predicted for molecular hypotheses).

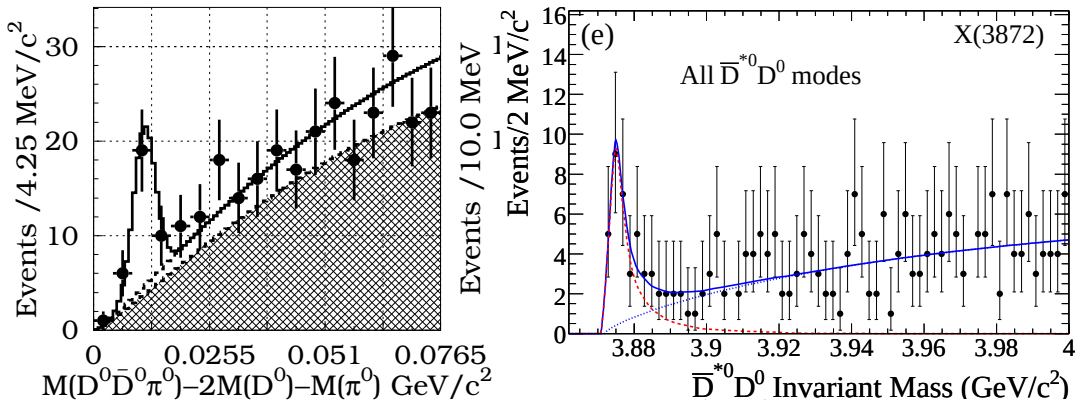

Figure 1.7: The invariant mass spectra of the $D^0\bar{D}^0\pi^0$ system observed by Belle (left) and *BABAR* (right). Both show an enhancement right above threshold.

In 2006 Belle reported a first observation of a threshold enhancement in the decay $B \to D^0\bar{D}^0\pi^0 K$ [62], interpreted to stem from a possible $X(3872) \to D^0\bar{D}^{0*}$ decay[5]. A peak above threshold is observed (see figure 1.7) with a measured mass of

$$m = 3875.4 \pm 0.7(\text{stat})^{+1.2}_{-2.0}(\text{syst})\ \text{MeV}/c^2.$$

The significance of the enhancement is $6.4\,\sigma$, where the two decay channels $B^+ \to D^0\bar{D}^0\pi^0 K^+$ $B^0 \to D^0\bar{D}^0\pi^0 K^-$ were combined.

The calculated branching fraction yielded a high value of

$$\mathcal{B}(B \to D^0\bar{D}^0\pi^0 K) = (1.27 \pm 0.31(\text{stat})^{+0.22}_{-0.39}(\text{syst})) \times 10^{-4},$$

which is by a factor of ≈ 10 higher than for the decay of the $X(3872)$ into $J/\psi\pi\pi$.

A similar structure was later observed by *BABAR* [63] (see figure 1.7). They investigate the invariant $m(\bar{D}^{*0}D^0)$ spectrum in decays of a $B^+(B^0)$ to the final states $\bar{D}^{*0}D^0K^+(K^0_S)$ or $\bar{D}^0D^{*0}K^+(K^0_S)$. A peak structure with a statistical significance of $4.9\,\sigma$ is observed at a mass of

$$m = 3875.1^{+0.7}_{-0.5}(\text{stat}) \pm 0.5(\text{syst})\ \text{MeV}/c^2$$

with a width of

$$\Gamma = 3.0^{+1.9}_{-1.4}(\text{stat}) \pm 0.9(\text{syst})\ \text{MeV}.$$

The big question in conjunction to this decay is whether this enhancement is related to the $X(3872)$. Since the central mass values are different by more than four standard deviations, this question is not easily answered. Most theoretical approaches tend to see it as the same state and attribute the higher mass to the difference in line shape between different decay channels [53, 64, 65, 66]. It could, however, fit as well into the multiquark approach as the observation of the expected second neutral particle.

[5]The possible observation of the decay $X(3872) \to D^0\bar{D}^{0*}$ does not contradict the fact of the unobserved $X(3872) \to D^0\bar{D}^0$ mode, because the spin of the $\bar{D}^{0*}$ is different compared to the $\bar{D}^0$.

1.7 Summary and Outline

The experimental results of the last sections are summarized in tables 1.4 and 1.5. A separate table is used for the recently observed $X(3875)$, for which it is not clear if it is the same particle as the $X(3872)$. Table 1.4 lists the measurements for the $X(3872)$, while table 1.5 gives an overview of the results for the $X(3875)$.

This chapter described that the discovery of the $X(3872)$ brought up questions about our understanding of matter in high energy physics that are still unanswered. While the number of experimental evidence is growing and also the theoretical understanding is making progress, there is still no 'silver bullet' which unambiguously would point to the nature of the $X(3872)$.

The most favorite options are at the moment the assignment as a molecular $D^0\bar{D}^{0*}$ state, the multiquark hypothesis which uses four quarks to form the $X(3872)$, and the conventional charmonium state — or a mixture of them.

After the experimental apparatus is introduced in chapter 2, this thesis investigates two different properties of the $X(3872)$. On the one hand the quantum numbers J^{PC} of the $X(3872)$ will be constrained, which will be described in chapter 3. On the other hand the invariant mass shape of the $X(3872)$ will be studied. This will clarify whether the $X(3872)$ mass shape is compatible with two neutral states, as predicted by multiquark hypotheses. If only one peak is found, its precise mass will be measured, which is of crucial importance for the theoretical understanding of the molecular hypothesis. This part of the analysis is described in chapter 4. The thesis will conclude in chapter 5 with a discussion of the implications of the results and an outlook.

property	measurement
mass m	$3872.0 \pm 0.6 \pm 0.5$ MeV/c^2 [1] $3871.3 \pm 0.7 \pm 0.4$ MeV/c^2 [2] $3871.8 \pm 3.1 \pm 3.0$ MeV/c^2 [3] $3871.3 \pm 0.6 \pm 0.1$ MeV/c^2 [7]
width Γ	1.4 ± 0.7 MeV, < 2.3 MeV (90% C.L.) [1] $1.1 \pm 1.5 \pm 0.2$ MeV, < 3.3 MeV (90% C.L.) [7]
J^{PC}	$1^{++}, 2^{++}$ [58] $1^{++}, 2^{-+}$ [60]
dipion system	prefers high masses, ρ-like [58, 59]
decay channels	$J/\psi\pi^+\pi^-$ [1, 2, 3, 67] $J/\psi\gamma$ [56, 57] $J/\psi\pi^+\pi^-\pi^0$ [56]
unsuccessful searches	$\gamma\chi_{c1}$ [1], $\gamma\chi_{c2}$ [8] $D^0\bar{D}^0$ [9], D^+D^- [9] $J/\psi\eta$ [10] $J/\psi\pi^-\pi^0$, $J/\psi\pi^+\pi^0$ [11] $J/\psi\pi^0\pi^0$ [12]
mass difference Δm in B^+/B^0 decays	$2.7 \pm 1.3(\text{stat}) \pm 0.2(\text{syst})$ MeV/c^2 [67] $0.22 \pm 0.90(\text{stat}) \pm 0.27(\text{syst})$ MeV/c^2 [61]
branching fractions	$\mathcal{B}(B^+ \to K^+(J/\psi\pi^+\pi^-)_{X(3872)}) = (13.0 \pm 2.9 \pm 0.7) \times 10^{-6}$ [1, 6] $\mathcal{B}(B^+ \to K^+(J/\psi\pi^+\pi^-)_{X(3872)}) = (8.4 \pm 1.5 \pm 0.7) \times 10^{-6}$ [7] $\mathcal{B}(B^0 \to K^0_S(J/\psi\pi^+\pi^-)_{X(3872)}) = (3.5 \pm 1.9 \pm 0.4) \times 10^{-6}$ [7] $\frac{\mathcal{B}(B^0 \to K^0 X(3872))}{\mathcal{B}(B^+ \to K^+ X(3872))} = 0.94 \pm 0.24 \pm 0.10$ [61] $\mathcal{B}(B^+ \to K^+(J/\psi\gamma)_{X(3872)}) = (1.8 \pm 0.6 \pm 0.1) \times 10^{-6}$ [56] $\mathcal{B}(B^+ \to K^+(J/\psi\gamma)_{X(3872)}) = (3.3 \pm 1.0 \pm 0.3) \times 10^{-6}$ [57] $\frac{\mathcal{B}(X(3872) \to J/\psi\pi^+\pi^-\pi^0)}{\mathcal{B}(X(3872) \to J/\psi\pi^+\pi^-)} = 1.0 \pm 0.4 \pm 0.3$ [56]

Table 1.4: A summary of the gathered experimental findings on the $X(3872)$.

property	measurement
mass m	$3875.4 \pm 0.7^{+1.2}_{-2.0}$ MeV/c^2 [62] $3875.1^{+0.7}_{-0.5} \pm 0.5$ MeV/c^2 [63]
width Γ	$3.0^{+1.9}_{-1.4} \pm 0.9$ MeV [63]
observed decay channel	$D^0\bar{D}^0\pi^0$ [62, 63]
branching fraction	$\mathcal{B}(B \to D^0\bar{D}^0\pi^0 K) = (1.27 \pm 0.31^{+0.22}_{-0.39}) \times 10^{-4}$ [62]

Table 1.5: A summary of the gathered experimental findings on the '$X(3875)$'.

Chapter 2

The CDF II Experiment

The CDF II experiment is hosted by the Fermi National Accelerator Laboratory, abbreviated as 'FNAL' and most commonly referred to as 'Fermilab'. Fermilab is a U.S. Department of Energy national laboratory, specializing in high-energy particle physics and hosting multiple particle physics experiments. It is located in the United States, in Batavia, Illinois — 50 km west of Chicago. Figure 2.1 shows an aerial view of the main part of the laboratory.

2.1 The Tevatron

The most striking structure of the Fermilab is the proton-antiproton collider 'Tevatron'. The Tevatron is a symmetric proton-antiproton collider ring, i.e. protons and antiprotons of the same energy are brought to collision. The Tevatron has been the accelerator with the highest available center-of-mass energy in the world since its start in 1995.

During the first phase of operations from 1992 to 1996 — often referred to as 'Run I' — the energy of the collisions was $\sqrt{s} = 1.8\,\text{TeV}$. This is also responsible for the name of the accelerator ('TeV-atron'). The most important measurement during Run I was the discovery of the top-quark. The second phase ('Run II') started in 2001 and is still ongoing. Current plans are to run until 2009, running into 2010 may however still be possible. For Run II the Tevatron was upgraded to achieve a higher luminosity, as well as a center-of-mass energy of $\sqrt{s} = 1.96\,\text{TeV}$.

2.1.1 The Accelerator Chain

In order to accelerate and finally collide the protons and antiprotons, a sophisticated system of accelerator steps is in place. A schematic overview of the accelerator chain is shown in figure 2.2.

The first step in the acceleration chain is the production and pre-acceleration of negatively ionized hydrogen atoms in a Cockroft-Walton-type accelerator. The ions

Figure 2.1: Aerial view of the main part of the Fermilab facility. Although the Tevatron itself is of course underground, the maintenance road, located directly inside the ring, nicely indicates its course in the center of the picture.

reach an energy of 750 keV. The Linear Accelerator ('Linac') is the next level of acceleration for the hydrogen ions. They get accelerated to an energy of 400 MeV and are then transferred into the 'Booster'.

The Booster is a synchrotron of 75 m radius and serves two purposes. First, it strips the electrons of the negatively charged hydrogen atoms at injection, so that only the bare proton remains. Second, the protons are accelerated further up to an energy of 8 GeV, before they get transferred to the 'Main Injector'.

The Main Injector is a circular synchrotron as well, however seven times larger than the Booster. The incoming protons are used for separate purposes. In Tevatron operations they are needed for:

1. Antiproton production — The process of antiproton production, often referred to as 'stacking', uses accelerated protons from the main injector and transfers them to the antiproton source. There, the protons hit a nickel target, producing a spray of random secondary particles. From this spray, antiprotons with an energy of 8 GeV are selected and subsequently cooled in the 'Debuncher' and the 'Accumulator'. From there, they are transferred further to the 'Recycler'. The name 'Recycler' does not reflect the actual role of this antiproton storage ring. While its original purpose was to gather and 'recycle' antiprotons from $p\bar{p}$-collisions, it is now used to accumulate a large number of antiprotons before they are used for collisions.

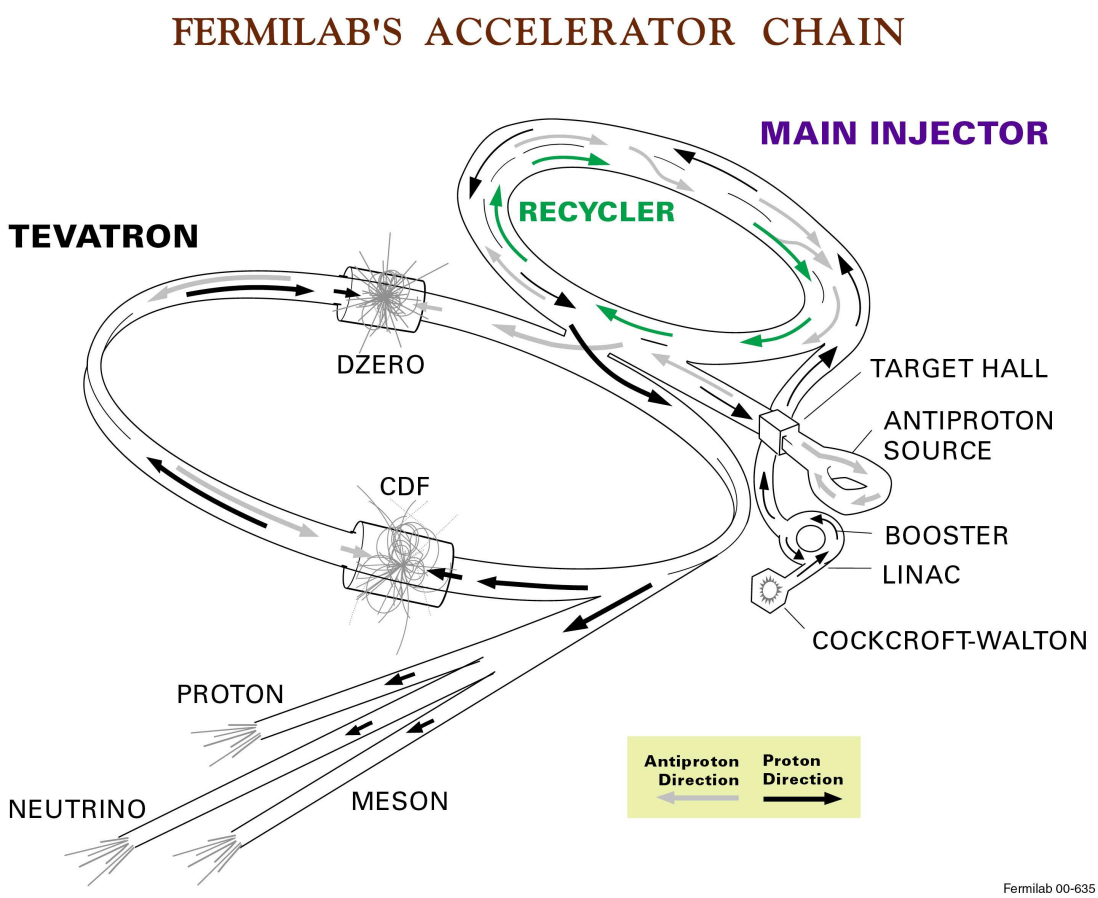

Figure 2.2: Schematic overview of the Tevatron accelerator chain.

2. Acceleration — As a final step before acceleration in the Tevatron, the protons from the Booster are accelerated to an energy of 150 GeV, before they get injected as a single bunch into the Tevatron. This procedure is repeated 36 times, leading to 36 proton bunches in the Tevatron. The same procedure is applied for the antiprotons from the Recycler, resulting in a 36×36 bunch structure in the Tevatron.

The final acceleration takes place in the Tevatron. The Tevatron, although responsible for the final acceleration of the particles to $E = 980\,\text{GeV}$, is primarily a storage ring. This allows to remain in collision mode for a long time. It is also the reason why the time from filling the Tevatron until dumping the beam is referred to as a 'store'.

The proton and antiproton beams are brought to collision at two interaction points: B0, where the CDF II experiment is located, and D0, which also was used to name the detector and the collaboration.

The time limiting process in the procedure is the accumulation of enough antiprotons. Once this is achieved, collisions are initialized in the following order.

1. Loading protons from the Main Injector into the Tevatron ($\approx$ 10 minutes).
2. Loading antiprotons from the Main Injector into the Tevatron ($\approx$ 45 minutes).
3. Increase the beam energy to 980 GeV ('Ramping', $\approx$ 1 minute).
4. Start collisions by activating magnets, bringing the two separate beams to collision.
5. Clean the beam environment ('Scraping', $\approx$ 10 minutes). This process cleans the 'halo' of the beam, which is necessary because the particles from this halo usually do not take part in the collisions, but have a high probability to interact with the beam confinement material — potentially causing irreparable damage to sensitive detector parts.
6. Power on detectors, record collisions.
7. Continuously produce collisions for $\approx$ 24 hours.
8. Dump the beam into absorber material and start over.

2.1.2 Luminosity

The luminosity is a quantity which describes the number of potential interactions. It is the main criterion for the collider performance. The instantaneous luminosity $\mathcal{L}$ is given by

$$\mathcal{L} = n \cdot f \cdot \frac{N_p N_{\bar{p}}}{2\pi(\sigma_p^2 + \sigma_{\bar{p}}^2)} \cdot F,$$

where n is the number of bunches, f is the revolution frequency, and N_p ($N_{\bar{p}}$) is the number of protons (antiprotons) per bunch. σ_p ($\sigma_{\bar{p}}$) is the average transverse width of the proton (antiproton) bunch structure. F is a form factor efficiency because of the non-optimal bunch-structure, which is of the order of 70%.

The goal of the Tevatron is to obtain a luminosity as high as possible. This translates into more observable interactions at the experiments. The two important quantities connected to this are the time-integrated luminosity, $\mathcal{L}_{int} = \int \mathcal{L}\, dt$, and the cross section of a certain physics process σ, which corresponds to the probability to obtain this physics process. They directly give the expected number of occurrences for a given process by

$$N = \sigma \cdot \mathcal{L}_{int}.$$

The convenient unit for the cross section is the 'picobarn' (pb), with $1\text{pb} = 10^{-36}\text{cm}^2$. The time integrated luminosity uses inverse picobarn (pb^{-1}). For the instantaneous luminosity SI units are usually used. While the cross section for a certain process is constant within a fixed environment, the expected number of occurrences scales directly with the integrated luminosity. Since most of the processes one is interested in have a very small cross section, one needs a high integrated luminosity to observe a sufficient amount of events.

The instantaneous luminosity changes during a store. The initial luminosity is the luminosity at the beginning of the store. During the store the luminosity drops roughly exponentially, since the amount of protons and antiprotons decreases (because of collisions or losses) at a rate proportional to their number. After a certain amount of time it is more efficient to abort the store and start a new one, which is usually after ≈ 24 hours — this is however highly influenced by other operational conditions.

Figure 2.3 shows the evolution of the initial luminosity at the CDF interaction point over time. It shows that over the course of time the accelerator complex has become more and more understood which is the reason for the steady rise in luminosity. The design luminosity of $270 \times 10^{30}\,\text{cm}^{-2}\,\text{s}^{-1}$ was reached in the end of 2006. Figure 2.4 shows the integrated luminosity for the CDF experiment. One has to distinguish between the delivered luminosity of the Tevatron and the recorded luminosity of the experiment. The recorded luminosity is always lower, since for technical reasons the CDF II detector is not recording data at 100% efficiency. The data taking efficiency is at a value of 80–90 %. Currently (May 2008) $4.0\,\text{fb}^{-1}$ have been delivered, out of which $3.3\,\text{fb}^{-1}$ have been recorded. The current aim is to deliver 6–7 fb^{-1} until the end of 2009.

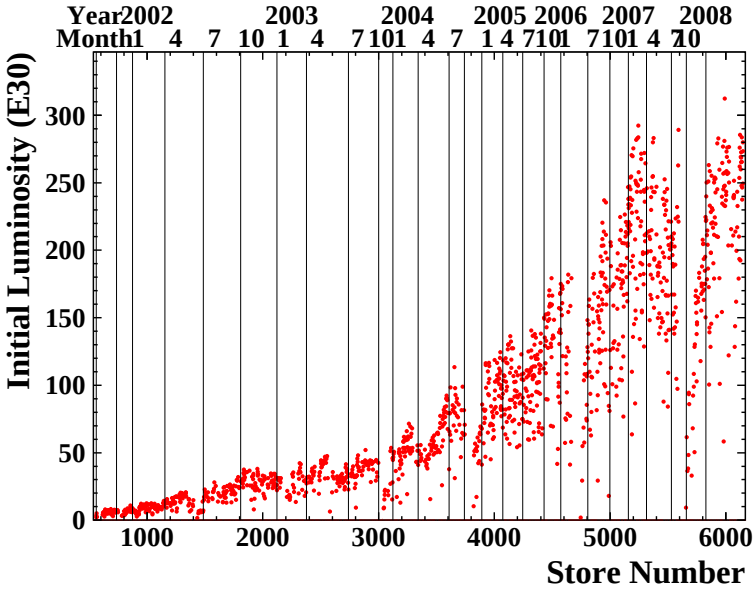

Figure 2.3: Initial luminosities over time for all stores in CDF Run II. The spread in luminosity mainly occurs because of different levels of quality for the antiproton beam, which is the limiting factor for the luminosity.

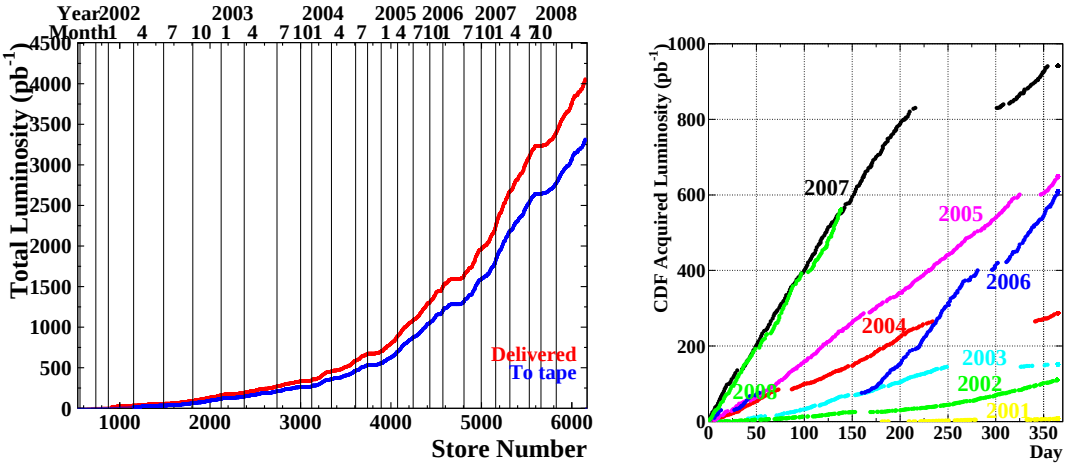

Figure 2.4: Evolution of the integrated luminosity. The left plot shows both the delivered (red) and the recorded luminosity (blue). The right plot shows the integrated luminosity separated for each year.

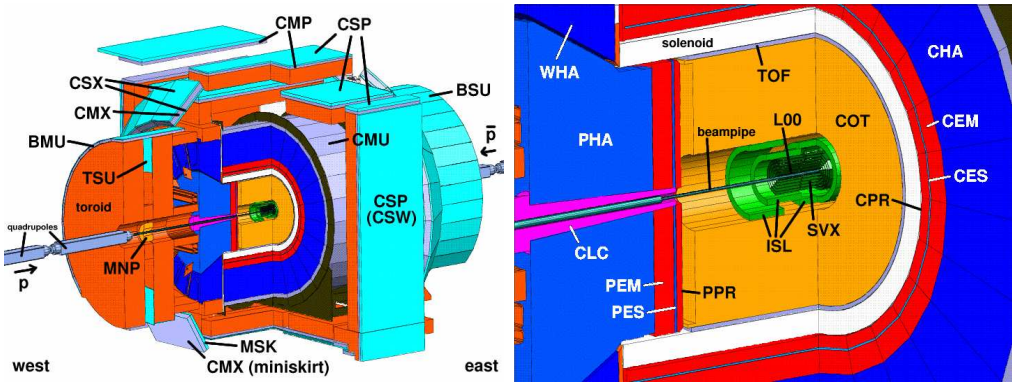

Figure 2.5: Cutaway view of the detector (left). The left figure shows the whole detector. Labelled are only the muon systems which make up the outermost layers of the detector. The right figure plot shows a zoomed version and labels the calorimeter and tracking systems.

2.2 The CDF II Detector

2.2.1 General Overview

The 'Collider Detector at Fermilab' (CDF) is an azimuthally and forward-backward symmetric general-purpose detector [68, 69, 70, 71]. It features a vertexing and tracking system, particle identification, a superconducting solenoid, calorimetry and muon chambers. Figures 2.5 and 2.6 show the layout of the detector in a cutaway view and an elevation view.

In the detector coordinate system cylindrical coordinates are used. The z-axis points along the proton beam direction (i.e. at CDF in eastward direction). The y-axis points upwards and the x-axis northwards, radially out of the ring. The azimuthal angle ϕ is measured from $\phi = 0$ in the Tevatron plane, the polar angle θ is measured from the positive z-direction. Instead of the polar angle θ, one often uses the pseudorapidity $\eta = -\ln(\tan(\theta/2))$, because the production of relativistic particles is uniform over η. The radius r is used to denote the distance from the beam line.

2.2.2 Tracking System

The tracking system is contained in the superconducting solenoid which generates a 1.4 T magnetic field parallel to the beam axis. Precise and efficient reconstruction of charged particles is an essential part of most analyses studying b- or c-hadrons, e.g. for good momentum resolution or good signal separation from background. The tracking system consists of two major systems — the silicon system for precise spatial information near the interaction point and the drift chamber for good momentum resolution.

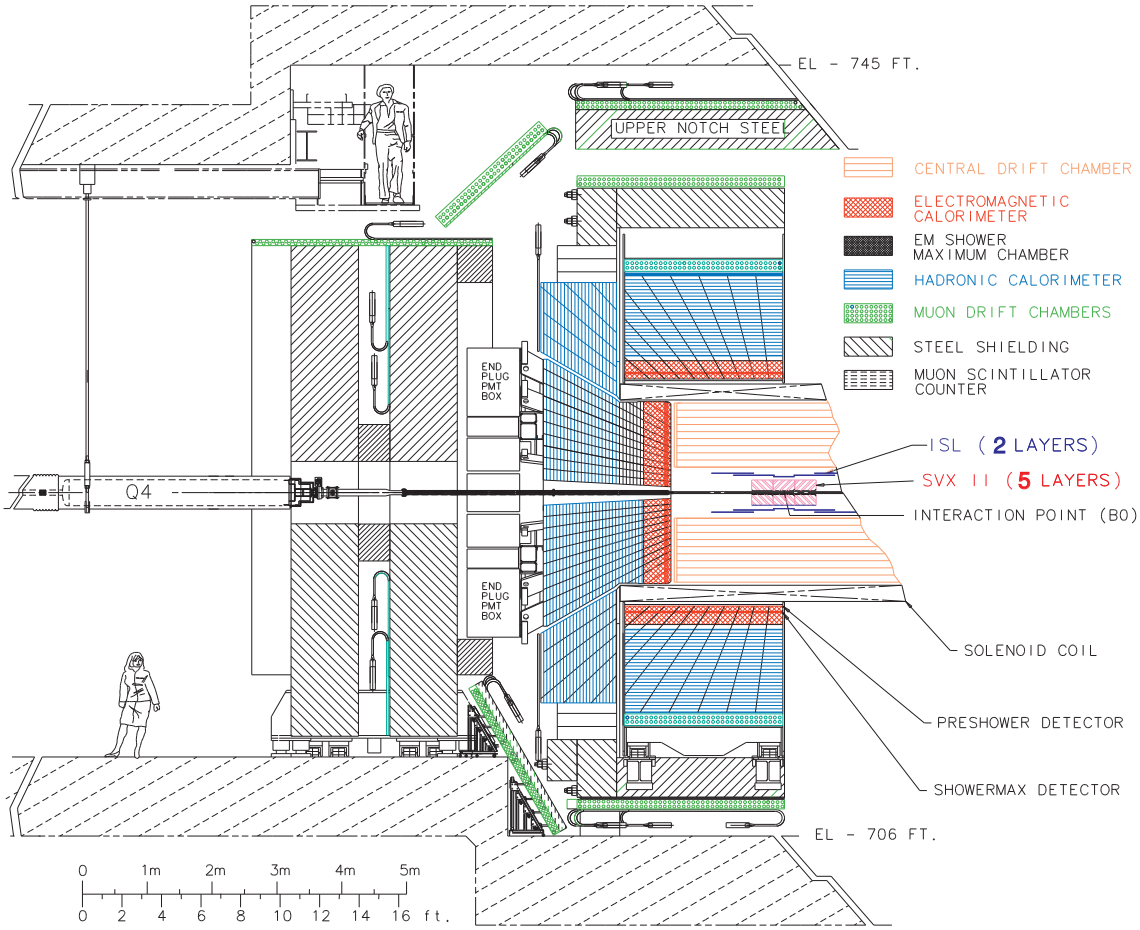

Figure 2.6: Elevation view of the CDF II detector.

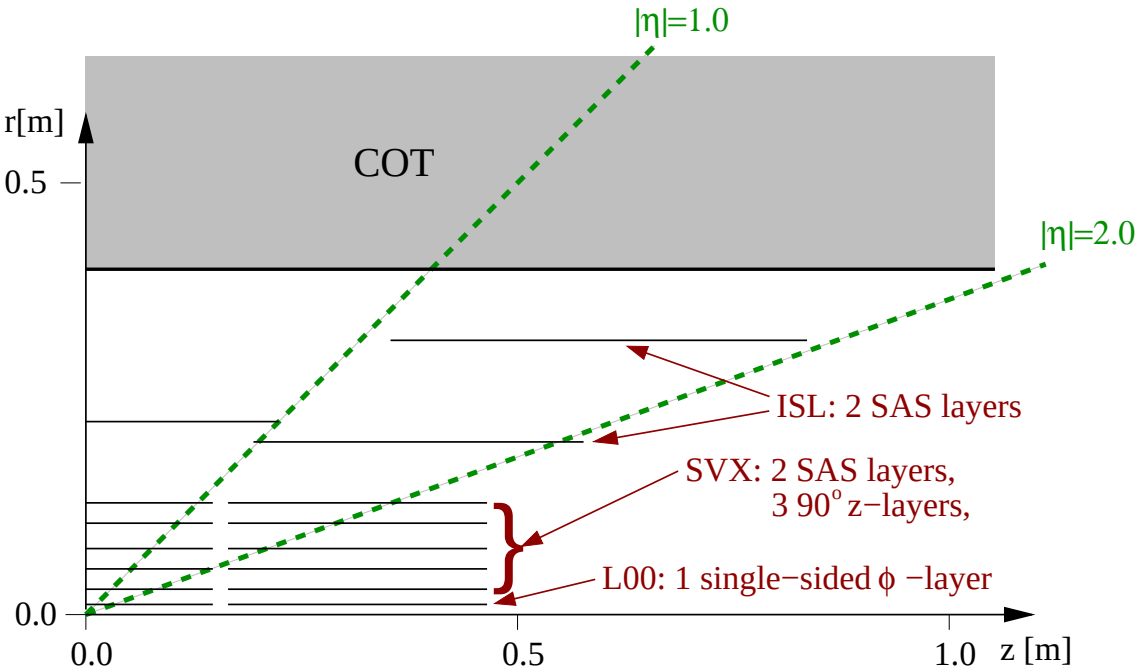

Figure 2.7: Schematic layer view of the silicon tracking system.

Silicon Detector

The most important part of the silicon detector is the 'Silicon Vertex Detector' (SVX II) [72], which delivers most of the silicon tracking information. Its main purpose is high-precision tracking which allows precise reconstruction of secondary vertices. The SVX II has five radially separated readout layers (numbered from 0 to 4), with Layer 0 at $r = 2.5$ cm and Layer 4 at $r = 10.7$ cm. The SVX covers the z-range from $z = -43.5$ cm to $z = +43.5$ cm, which corresponds to an η-coverage of $|\eta| < 2.0$. All layers are double-sided, one side performing a measurement in the $r - \phi$ plane, while the other side gives information about the z-position. For the z-position measurement two different models are used. Layers 0, 1 and 3 use a 90° angle (Z90) with respect to the beam axis ('stereo angle') to obtain a precise measurement. In contrast, Layers 2 and 4 use a small 1.2° stereo angle (SAS) for the measurement to reduce hit combination ambiguities.

The innermost layer of the silicon system is called 'Layer 00' (L00) [73]. L00 adds one layer of single-sided $r - \phi$ measurements close to the beam pipe. The main purpose is the improvement of track measurements, but it also additionally serves as 'radiation shield' for the innermost SVX layer, since the silicon used for L00 is more radiation hard than that for the SVX. In order to avoid gaps in ϕ, the single silicon detector parts are arranged in two alternating layers, at radii $r = 1.35$ cm and $r = 1.62$ cm.

The outermost part of the silicon detector are the 'Intermediate Silicon Layers' (ISL) [74]. Their main purpose is to enhance linking of tracks between the SVX

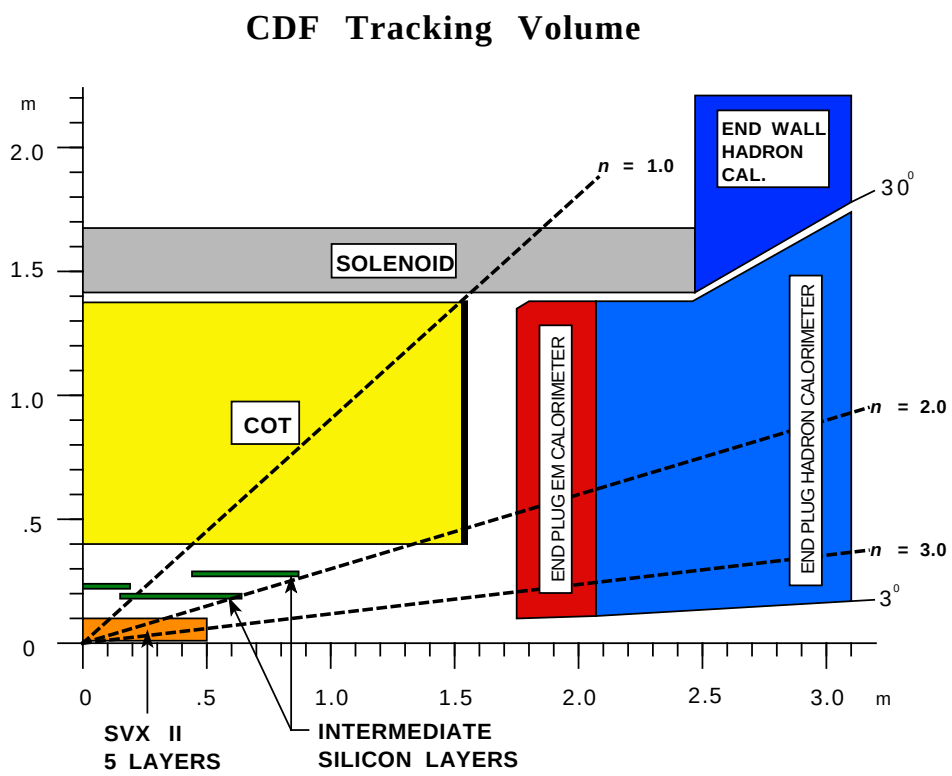

Figure 2.8: The CDF tracking system.

and the drift chamber. They also allow to perform tracking based only on silicon information, when no drift chamber information is available. The ISL adds one extra double-sided layer at $r \approx 25\,\text{cm}$, which is divided into five overlapping 'barrels'. The central layer at radius 22 cm covers the η range from -1 to +1, while the two forward and the two backward layers with $|\eta| > 1$ are located at radii of $r = 20$ cm and $r = 28\,\text{cm}$. A schematic representation of the silicon layers can be seen in figure 2.7.

Drift Chamber

The drift chamber, called the 'Central Outer Tracker' (COT) [75], is one of the most important detector parts for this thesis. It provides a general-purpose tracking for charged particles in the central region of the detector and, because of its large tracking volume, provides precise momentum measurement. The COT is a cylindrical drift chamber with an active volume from $r = 43.4\,\text{cm}$ to $r = 132.3\,\text{cm}$ with a length of $l = 3.1\,\text{m}$, covering the central part of $|\eta| < 1$. The location of the COT is shown in figure 2.8.

The drift chamber is filled with a 50:50 mixture of argon and ethane. 2530 cells are used in the COT, where each cell is a set of sense wires, collecting the information, and potential wires, shaping the electrical field. The anode cells are separated by field panels, serving as the cathode. Because of the magnetic field the negatively charged electrons do not drift along the electrical field direction. To account for

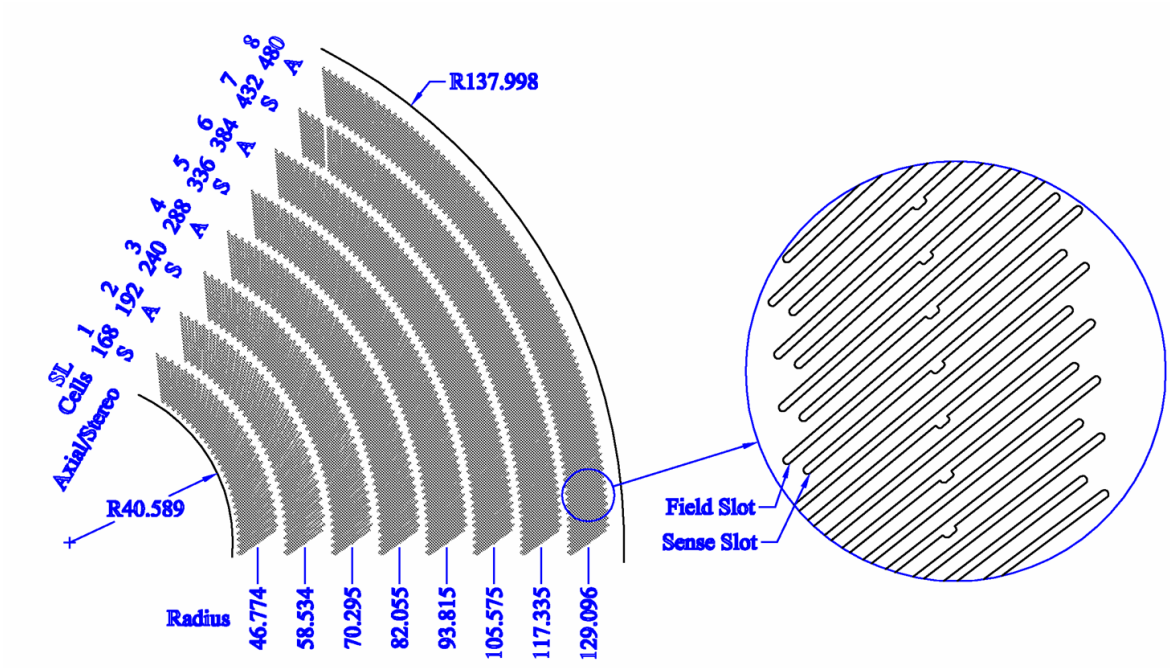

Figure 2.9: The COT cell layout. One can see the eight superlayers, each with alternating order of field slots and sense slots, which are rotated by the Lorentz angle.

this, the cells are rotated by an angle ('Lorentz angle'), which for the COT at CDF is 35°. The cells are divided into eight layers ('Superlayers'), out of which four are oriented parallel to the beam, responsible for measurements in the $r-\phi$ plane ('axial layers'). The other four layers have a small stereo angle of 2°, giving information about the z-coordinate ('stereo layers'). Figure 2.9 shows the cell layout of a part of the COT.

The spatial resolution of the COT is of course much worse than that of the silicon detector. Because of the large volume, the large number of hits, and a low track density, it provides a very good momentum resolution of

$$\frac{\sigma(p_T)}{p_T} = 0.15\% \times p_T \frac{1}{\mathrm{GeV}/c}.$$

2.2.3 Muon Detection System

Muon identification heavily relies on the fact, that muons are minimal ionizing particles and have the highest probability of all long-lived particles to traverse the detector without being absorbed. The muon detector itself is a system of scintillators and proportional chambers, which measure charged particles in general. In order to detect nearly only muons, there needs to be sufficient shielding in place, so that other long-lived particles like pions, kaons, and electrons get absorbed before they reach the muon detectors. This is achieved by placing the muon detectors at the

outermost radius of the detector, so that the other detector parts, especially the massive hadronic calorimeter, act as shielding. Hadrons still are responsible for the major part of misidentifications, either because they 'survive' until detection or because they decay into real muons which are not of interest for the studied process.

Muons are not fully reconstructed in the muon chambers. They only leave small track segments ('muon stubs') in the muon system, which need to be matched to tracks from the COT.

The muon system is comprised out of several subdetectors (also see figure 2.5). The 'Central Muon Detector' (CMU) [76] is a wire chamber and covers the central part of the detector with $|\eta| < 0.6$. The CMU does not possess full coverage in the $\eta - \phi$ plane. It has gaps in ϕ, since the sensitive part of the wedges only cover 12.6° out of 15°. More notably is the gap of $d = 18\,\text{cm}$ between the west and east half, which leads to a characteristic drop in acceptance for $\eta = 0$.

The 'Central Muon Upgrade' (CMP) has the same $\eta - \phi$ coverage as the CMU. The CMP consists of four layers of single-wire drift chambers. Since the drift time can be much larger than the time between two interactions, the CMP in addition utilizes a set of scintillators ('Central Scintillator Upgrade', CSP/CSW) to provide timing information. Because of the different geometry — a shape like a rectangular box, compared to the cylindrical design of the CMU — the CMP can partly cover for the gaps of the CMU in ϕ and z. The main purpose of the CMP however is the confirmation of muons in the CMU. Because the CMP is even further away from the interaction point and has an additional steel absorber shielding, the rate of charged hadrons which are mistaken as muons is much smaller than for the CMU. Together, the central muon system thus provides very clean muon selection.

The main purpose of the 'Central Muon Extension' (CMX) is to extend the coverage in $|\eta|$ from $|\eta| < 0.6$ to $|\eta| < 1.0$. It is composed of several structures. For Run I, only the easily accessible part in ϕ between collision hall floor and ceiling was covered. The bottom part had a gap of 90°, while the top part was missing 30°. Run II added structures for the remaining gaps, the so-called 'Keystone' for the western upper part[1] and the 'Miniskirt' for the bottom part, leading to almost full coverage in ϕ (see figure 2.10). The CMX uses the same drift chambers as the CMP, thus also requiring scintillators ('Central Scintillator Extension/CMX Miniskirt Scintillators' CSX/MSX) for timing information.

The 'Barrel Muon Chambers' (BMU) extend the coverage up to $|\eta| < 1.5$. The BMU drift chambers (of the same type as the CMP and CMX) are installed on top of the steel toroids at both ends of the CDF detector. Together with the scintillator systems named 'Barrel Scintillator Upgrade/Toroid Scintillator Upgrade' (BSU/TSU), the muon systems of BMU, BSU, and TSU make up the 'Intermediate Muon System' (IMU).

Table 2.1 summarizes the most important aspects of the different muon systems.

[1] The corresponding section on the east side remains uninstrumented because this region is occupied by solenoid cryogenics.

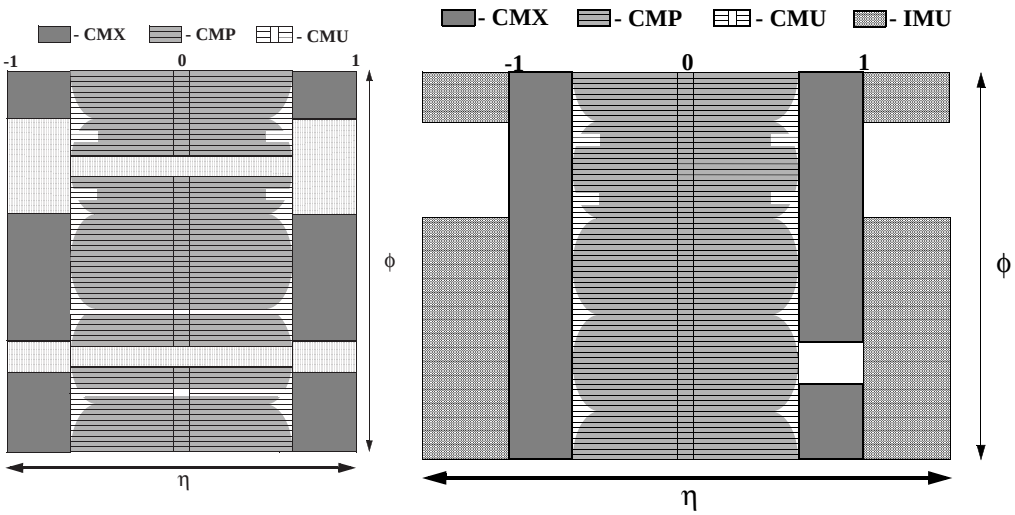

Figure 2.10: The $\eta - \phi$-coverage of the CDF muon systems for Run I (left) and Run II (right). In Run II the central part of $|\eta| < 1.0$ is completely covered, with a small exception on the eastern upper part.

	CMU	CMP	CMX	BMU
pseudorapidity coverage	$\|\eta\| < 0.6$	$\|\eta\| < 0.6$	$0.6 < \|\eta\| < 1.0$	$1.0 < \|\eta\| < 1.5$
minimum p_T [GeV/c]	1.4	2.0 – 2.2	1.4 – 1.8	2.1
maximum drift time [ns]	800	1400	1400	800

Table 2.1: Technical specifications of the CDF muon systems.

2.2.4 Other Detector Systems

The previous section described the detector components most central to this thesis. Since the CDF detector is a general purpose detector, there are further detector components, not used in this thesis, that are concisely described here.

Time of Flight System

The 'Time of Flight' system (TOF) [77] is located between the drift chamber and the solenoid. It consists of 216 scintillator bars, covering $|\eta| < 1$. It measures the time between the collision and an obtained signal, which can be combined with the momentum from the COT and the path length to obtain the particle mass, thus identifying the particle. The time resolution of the TOF is ≈ 100 ps, allowing most importantly separation of kaons from pions at low momenta (smaller ≈ 2 GeV/c).

detector	η range	resolution	thickness
CEM	$\lvert\eta\rvert < 1.1$	$1.5\% \oplus 13.5\% \times f(E,\theta)$	$18\ X_0$
PEM	$1.1 < \lvert\eta\rvert < 3.64$	$1\% \oplus 16\% \times f(E,\theta)$	$23.2\ X_0$
CHA	$\lvert\eta\rvert < 0.9$	$3\% \oplus 50\% \times f(E,\theta)$	$4.7\ \lambda_0$
WHA	$0.9 < \lvert\eta\rvert < 1.3$	$4\% \oplus 75\% \times f(E,\theta)$	$4.7\ \lambda_0$
PHA	$1.3 < \lvert\eta\rvert < 3.64$	$5\% \oplus 80\% \times f(E,\theta)$	$7\ \lambda_0$

Table 2.2: Technical specifications of the CDF calorimeter systems. $f(E,\theta)$ is the function $f(E,\theta) = 1/\sqrt{E[\mathrm{GeV}]\ \sin\theta}$, which results in good resolutions for central and high-energetic particles. The more forward/backward or low energetic the particles are, the worse is the resolution. The depth is given in radiation lengths X_0 and hadronic interaction lengths λ_0 [81].

Calorimetry

The calorimetry system of CDF [78, 79, 80] is divided into two major systems: the electromagnetic and the hadronic calorimeter systems, designed to absorb electrons/photons and hadrons, respectively.

Both calorimeter systems are located outside the solenoid. The electromagnetic calorimeter is composed of the 'Central Electromagnetic Calorimeter' (CEM) and the 'Plug Electromagnetic Calorimeter' (PEM). Both are supplemented with shower detectors ('Central/Plug Electromagnetic ShowerMax' chamber, CES/PES) to measure the location of the shower. In conjunction with the tracking information of the COT, this can be used to separate neutral pions from photons. The hadronic calorimeter consists of the 'Central Hadron Calorimeter' (CHA), the 'Wall Hadron Calorimeter' (WHA), and the 'Plug Hadron Calorimeter' (PHA),

All calorimeter systems are sampling calorimeters, meaning that they have alternating layers of active scintillator and absorber material. Table 2.2 lists the basic properties of the different calorimeter systems.

Luminosity Counters

The determination of the instantaneous luminosity is provided by a system of Cherenkov counters, the 'Cherenkov Luminosity Counters' (CLC) [82]. The CLC is located near the beam line next to the plug calorimeter. It uses inclusive elastic $p\bar{p}$ events for measurement. There are two ways to determine the luminosity.

One measurement uses the information, at which ratio the detector did *not* measure enough Cherenkov light signal, i.e. at which ratio a so-called 'empty bunch-crossing', a bunch-crossing without interaction took place. From the Poisson probability to get 0 interactions, $p = \exp(-\mu)$, this rate can be used to calculate the average rate of interactions per bunch crossing μ. The luminosity then readily computes as

$$\mathcal{L} = \frac{\mu\, f}{\sigma_{p\bar{p}}},$$

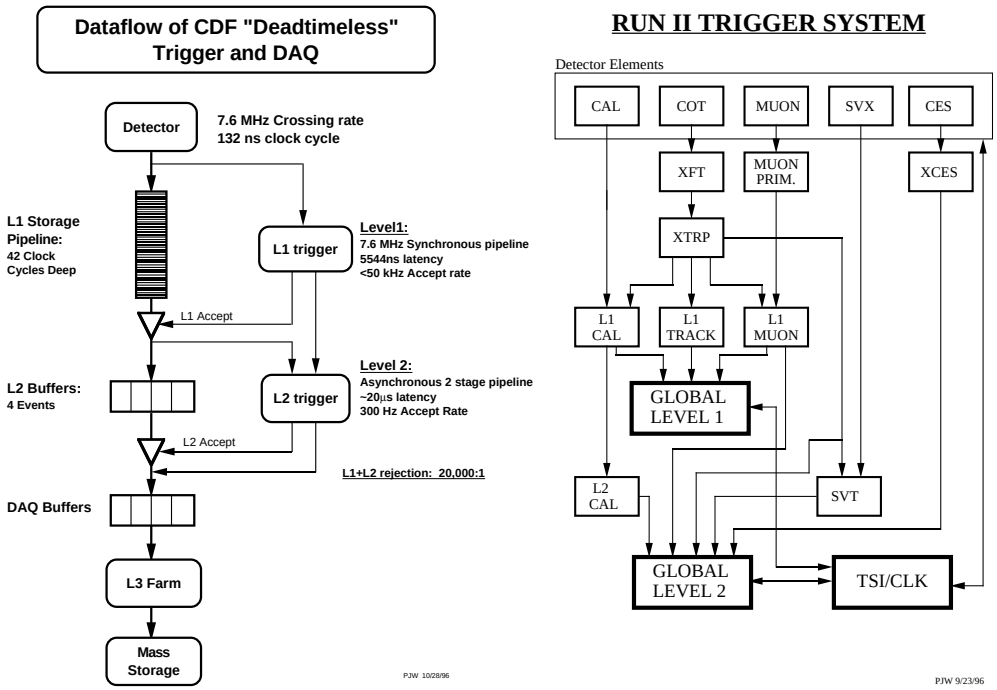

Figure 2.11: Schematics for the CDF II trigger system. The left figure shows the overall layout, while the right figure shows the information flow between the different trigger decision components.

where f is the Tevatron bunch crossing rate and $\sigma_{p\bar{p}}$ is the $p\bar{p}$ cross-section. Another method simply relates the measured number N_{meas} of actual hits in the CLC to the number that are expected for one interaction N_{exp}. The expected number is known from low luminosity measurements. μ then simply is N_{meas}/N_{exp}. The accuracy of the luminosity measurement is about 5%.

2.2.5 Trigger System

The trigger system at CDF plays a crucial role. Because of the large interaction rate the CDF detector measures more information than can be processed and stored. With approximately one interaction per bunch crossing and a rate of one crossing per 396ns, roughly 2.5 million events take place every second. With a rough estimate of $\approx$ 100 kByte per detector event, this would equal a data rate of 250 GByte per second. Although one might be able to store and process this amount of data with a huge effort, it is in no way desirable to read out every event — for the simple fact that most events do not contain any processes one is interested in. As a consequence a system is required that intelligently selects the few interesting events from the vast number of events produced in every second. This is achieved by a three-level trigger system, that decides during operations which events are recorded for further analysis. Figure 2.11 shows an schematic view of the CDF II trigger data flow.

The first step is the Level-1 trigger. It processes each detector event and has to

perform decisions at a very fast rate. On average one out of 100 events is accepted, resulting in a Level-1 acceptance rate of $\approx 25\,\mathrm{kHz}$. The accepted events are passed to Level-2, which has a buffer that can store 4 events. If the Level-2 trigger accepts the event, which is about one out of 50, the whole detector information is read out and passed to the Level-3 trigger. The input rate for the Level-3 trigger is now of the order of 500 Hz. Level-3 collects all data fragments from the different detector parts and forms one single event with the so-called 'event builder'. If Level-3 accepts the event, which happens for about one out of five, it gets written on a mass storage device. The final rate is of the order of 100 Hz.

Since the trigger has to make its decisions very fast on Level-1 and Level-2, no full reconstruction of the whole detector event is possible, and the trigger has to rely on certain, quickly available quantities. For Level-1, three main classes are considered: muon information, calorimeter information and tracking information from the 'extremely fast tracker' (XFT) [83], which uses COT information to get a rough information about the track parameters. The 'extrapolator unit' (XTRP) might give additional information by matching XFT tracks to muon or calorimeter information. At Level-2, more time is available to process the event. Because of this more information can be processed, most importantly information from the silicon detector to identify events with a displaced secondary vertex. There is also enough time available to calculate more complex quantities, which can be used to classify the event. Level-3 finally is implemented as software on dedicated computers. The event is fully reconstructed, allowing for precise information that can be used for classification. Because of the implementation in software, even complex decision processes can be realized.

Chapter 3

Determination of the Quantum Numbers J^{PC}

The determination of the quantum numbers J^{PC} is of crucial importance for the understanding of the $X(3872)$. For a conventional charmonium hypothesis, the quantum numbers would almost unambiguously determine which spectroscopic state needs to be assigned to the $X(3872)$. In case of the determination of 'unnatural' quantum numbers, i.e. quantum numbers that cannot be obtained within a quark model spectrum, the charmonium hypothesis could even be immediately rejected. Exotic hypotheses also give predictions for the quantum numbers. $J^{PC} = 1^{++}$ is the ground state prediction for a $D\bar{D}^{0*}$ bound state and the glueball hypothesis implies $J^{PC} = 1^{--}$.

In order to determine the quantum numbers of the $X(3872)$, angular correlations between the decay products in the decay $X(3872) \to J/\psi\pi^+\pi^-$ are studied and compared to expectations for different J^{PC} hypotheses. These hypotheses are obtained by reweighting a generic three-body phase-space simulation with J^{PC}-specific decay weights. The $\psi(2S)$ with known quantum numbers, decaying into the same final state as the $X(3872)$ with high available statistics, serves as a reference for the validation of the analysis.

This chapter is organized as follows: section 3.1 describes the decay topology and the construction of the decay weights. Section 3.2 details the selection procedure of the measured $X(3872)$ candidate sample, while section 3.3 describes the generation of the simulated samples. The actual measurement and the comparison to expectations is described in section 3.4. Systematic uncertainties are discussed in section 3.5.

3.1 Decay Topology and Amplitude Construction

At CDF the $X(3872)$ is observed in the three-body decay channel

$$X(3872) \to J/\psi\pi^+\pi^-,$$

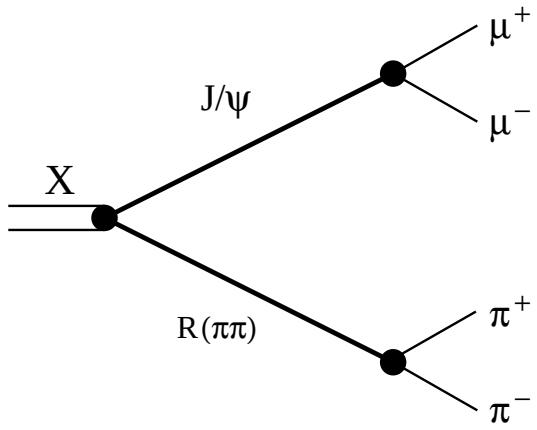

Figure 3.1: Decay Topology of the $X(3872)$. The decay proceeds in three sequential two-body decays.

where the J/ψ is reconstructed in its decay to two muons. The decay is modelled as a sequence of two-body decays, where the two charged pions in the final state decay via an intermediate dipion resonance $R(\pi\pi)$:

$$\begin{aligned} X(3872) &\to J/\psi R(\pi\pi), \\ J/\psi &\to \mu^+\mu^-, \\ R(\pi\pi) &\to \pi^+\pi^-. \end{aligned}$$

This is schematically shown in figure 3.1.

Decay amplitudes in the $X(3872)$ decay are constructed using the helicity formalism, which allows a straightforward treatment of sequential two-body decays. This thesis uses conventions employed by Richman [84]. Figure 3.1 illustrates the necessary components of the complete decay matrix element. It consists of

- a vertex decay matrix element describing the decay $X(3872) \to J/\psi R(\pi\pi)$,
- a vertex decay matrix element describing the decay $J/\psi \to \mu^+\mu^-$,
- a vertex decay matrix element describing the decay $R(\pi\pi) \to \pi^+\pi^-$,
- a propagator term describing the time evolution of the intermediate J/ψ,
- a propagator term describing the time evolution of the intermediate $R(\pi\pi)$-system.

In the helicity formalism the angles describing the decay direction are defined in the helicity frame, i.e. in the rest frame of a decaying particle (center-of-momentum system 'cms'). The definition of the decay angles in the sequential two-body decay chain of the $X(3872)$ is illustrated in figure 3.2. The polar angles θ are defined as the angle between the mother particle direction and the momentum of one of the

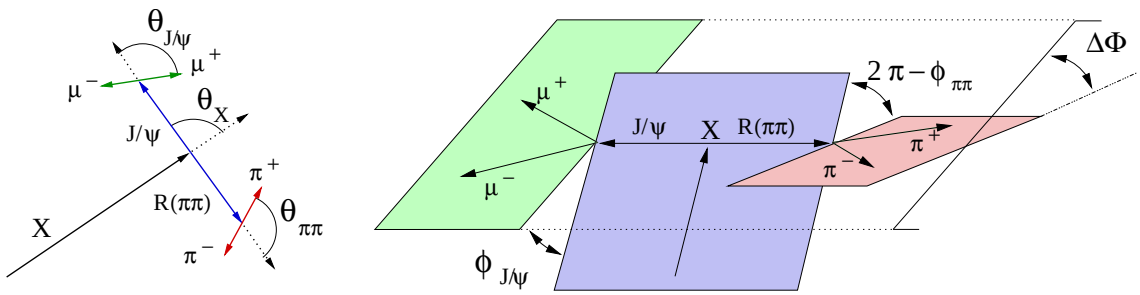

Figure 3.2: Definition of the angles, used to describe the particle momenta in the decay chain. $\Delta\Phi$ is the angle between the $\pi^+\pi^-$ and $\mu^+\mu^-$ decay planes.

decay	$X \to J/\psi R(\pi\pi)$	$J/\psi \to \mu^+\mu^-$	$R(\pi\pi) \to \pi^+\pi^-$
angles	θ_X, ϕ_X	$\theta_{J/\psi}$, $\phi_{J/\psi}$	$\theta_{\pi\pi}$, $\phi_{\pi\pi}$
mother momentum	$\vec{p}_X$	$\vec{p}_{J/\psi}$ in $X(3872)$ cms	$\vec{p}_{\pi\pi}$ in $X(3872)$ cms
daughter momentum	$\vec{p}_{J/\psi}$ in $X(3872)$ cms	$\vec{p}_{\mu^+}$ in J/ψ cms in $X(3872)$ cms	$\vec{p}_{\pi^+}$ in $R(\pi\pi)$ cms in $X(3872)$ cms
reference vector	beam axis	$\vec{p}_X$	$\vec{p}_X$

Table 3.1: Momenta and vectors, used for angle calculation. θ is the angle between mother momentum and daughter momentum. ϕ is the angle between two planes, one spanned by the daughter momentum and the mother momentum and the other spanned by the mother momentum and the reference vector.

daughter particles in the mother rest frame. Since in the mother rest frame both daughter particles are 'back-to-back', it does not matter which particle is chosen, but this arbitrary selection needs to be applied consistently. The definition of an azimuthal angle ϕ needs an additional independent reference vector in order to define a proper $\phi = 0$ reference. Used is either the proton beam axis or the $X(3872)$ momentum, depending on the decay. The momenta used for the angle calculations are listed in table 3.1.

It is of primary importance for the analysis to know about the variables which are sensitive to the quantum numbers J^{PC} of the $X(3872)$. The differential $X(3872)$ cross section is given by

$$
\begin{aligned}
d^{11}\sigma/(d\omega^{11}) = \quad & d\sigma/(dm_X^2 && J/\psi\pi^+\pi^- \text{ invariant mass} \\
& dp_T^2\, d\eta\, d\phi && \text{X(3872) production in laboratory frame} \\
& dm_{\pi\pi}^2\, d\cos\theta_X\, d\phi_X && \text{X(3872) decay into } J/\psi R(\pi\pi) \\
& d\cos\theta_{J/\psi}\, d\phi_{J/\psi} && J/\psi \text{ decay into } \mu^+\mu^- \\
& d\cos\theta_{\pi\pi}\, d\phi_{\pi\pi}) && R(\pi\pi) \text{ decay into } \pi^+\pi^-
\end{aligned}
$$

where p_T^2, η and ϕ describe the $X(3872)$ in the lab frame. The $X(3872)$ decay into J/ψ and $R(\pi\pi)$ is described by the decay angles $\cos(\theta_X)$ and ϕ_X. The subsequent

decay of the J/ψ is determined by the angles $\cos\theta_{J/\psi}$ and $\phi_{J/\psi}$, and that of the $R(\pi\pi)$-system by $\cos\theta_{\pi\pi}$ and $\phi_{\pi\pi}$.

At the Tevatron, the momentum distribution of the $X(3872)$ is independent of its quantum numbers, since the state is produced in the fragmentation of the collision products. Information about the quantum numbers J^{PC} is however contained in the mass distribution $m_{\pi\pi}$ of the dipion resonance, since the $X(3872)$ quantum numbers affect both the resonance nature of the intermediate dipion resonance and the mass dependence of the decay.

From the rotational symmetry of the system it can be deduced that for unpolarized $X(3872)$ production only the following angles depend on the quantum numbers J^{PC} of the $X(3872)$:

- $\cos\theta_{J/\psi}$,
- $\cos\theta_{\pi\pi}$,
- $\Delta\phi = 2\pi - \phi_{J/\psi} - \phi_{\pi\pi}$.

All ϕ angles on their own merely add an insignificant phase. The decay planes of the dipion and dimuon system can however depend on each other, so that the combination of $\phi_{J/\psi}$ and $\phi_{\pi\pi}$ is important. The angle $\cos\theta_X$ only contains information if the $X(3872)$ is polarized.

3.1.1 Conservation Rules in the $X(3872)$ Decay

Any single two-body decay of a mother particle I into its daughter particles F_1 and F_2 can be schematically written as:

$$\begin{aligned} I &\to F_1 F_2 \\ J_I^{P_I C_I} &\to J_1^{P_1 C_1} J_2^{P_2 C_2}. \end{aligned}$$

The first conserved quantity is the total angular momentum J. The total final-state angular momentum J_F is determined by combining the spins J_1 and J_2 of the final-state particles to a common spin S_F, which in turn is combined with the relative angular momentum L_F between the two final state particles to the total final-state angular momentum J_F:

$$\begin{aligned} S_F &= J_1 \oplus J_2, \\ J_F &= L_F \oplus S_F. \end{aligned}$$

The $X(3872)$ decay and each of its sub-decays are electromagnetic or strong decays. Because of this, C-parity and parity are conserved quantities as well. The

conservation rules are:

$$\begin{aligned} J_I &= J_F, \\ P_I &= P_F = P_1\, P_2 \times (-1)^{L_F}, \\ C_I &= C_F. \end{aligned}$$

In order to determine the final state C-parity C_F the nature of the daughter particles needs to be considered. C_F is given by:

- $C_F = C_1\, C_2$ for a system of neutral daughter particles,
- $C_F = (-1)^{L_F+S_F}$ for a neutral system of two charged fermions,
- $C_F = (-1)^{L_F+S_F}$ for a neutral system of two charged bosons.

A note on nomenclature: In this chapter, the particle names of the $X(3872)$, the J/ψ, and the $R(\pi\pi)$-system will often be used as an index (X, J/ψ, $\pi\pi$). They can occur in two ways. On the one hand the index is used to indicate a property, like in $J_{\pi\pi}$ as the angular momentum of the $R(\pi\pi)$-system. On the other hand it is used to indicate the connection of a property to a certain decay and the index denotes the mother particle in this decay. $L_{\pi\pi}$ thus does not refer to the relative angular momentum of the $R(\pi\pi)$-system (which also would not make any sense), but to the relative angular momentum of the decay products *in the decay* of the $R(\pi\pi)$-system. As a guideline, all quantities necessarily involving more than one particle to give a proper meaning denote the decay.

The quantum numbers of most of the involved particles are known. For the J/ψ they are $J^{PC} = 1^{--}$, the charged pions have $J^P = 0^-$, and the muons have $J = 1/2$. Since pions are charged they are not eigenstates of the charge parity operation C. Muons are point-like particles and are defined with positive intrinsic parity for particles and negative intrinsic parity for antiparticles. The quantum numbers J^{PC} of the dipion system can be constrained. Since the allowed dipion mass range is limited to the low mass range of

$$\begin{aligned} 2m_\pi < m_{\pi\pi} &< m_{X(3872)} - m_{J/\psi}, \\ 280\,\mathrm{MeV}/c^2 < m_{\pi\pi} &< 775\,\mathrm{MeV}/c^2, \end{aligned}$$

only low spin systems for the dipion system are assumed to be dominant. A relative angular momentum between the two pions $L_{\pi\pi} = 0$ results in a 0^{++}-dipion system, while $L_{\pi\pi} = 1$ equals to $J^{PC} = 1^{--}$, as will be explained in the next section. Higher angular momenta are improbable, since the lowest dipion resonance with $L_{\pi\pi} = 2$ is the $f_2(1270)$, whose mass is greater than the allowed dipion mass in the $X(3872)$ decay by $500\,\mathrm{MeV}/c^2$.

The selection rules become important at several places. In the decay $R(\pi\pi) \to \pi^+\pi^-$ the value of $S_{\pi\pi}$ always is 0, because the two pions have spin 0. This in turn leads

J_X^{PC}	$J_{J/\psi}^{PC}$	$J_{\pi\pi}^{PC}$	S	parity-allowed LS
0^{++}	1^{--}	1^{--}	0,1,2	00, 22
0^{+-}	1^{--}	0^{++}	1	11
0^{-+}	1^{--}	1^{--}	0,1,2	11
0^{--}	1^{--}	0^{++}	1	none $\rightarrow$ forbidden
1^{++}	1^{--}	1^{--}	0,1,2	01, 21, 22
1^{+-}	1^{--}	0^{++}	1	11
1^{-+}	1^{--}	1^{--}	0,1,2	10, 11, 12, 32
1^{--}	1^{--}	0^{++}	1	01, 21
2^{++}	1^{--}	1^{--}	0,1,2	02, 21, 22, 23, 42
2^{+-}	1^{--}	0^{++}	1	11, 31
2^{-+}	1^{--}	1^{--}	0,1,2	11, 12, 31, 32
2^{--}	1^{--}	0^{++}	1	21
3^{+-}	1^{--}	0^{++}	1	31
3^{--}	1^{--}	0^{++}	1	21, 41

Table 3.2: Parity-allowed LS combinations in the $X(3872) \rightarrow J/\psi R(\pi\pi)$ decay. Listed are all tested J^{PC} hypotheses, the daughter quantum numbers, and their allowed combinations of combined spin S_X and relative angular momentum L_X.

to $J_{\pi\pi} = L_{\pi\pi}$. The quantum numbers of a state, decaying into two charged pions, are thus completely determined by their relative angular momentum:

$$\begin{aligned} J_{\pi\pi} &= L_{\pi\pi}, \\ P_{\pi\pi} &= (-1)^{L_{\pi\pi}}, \\ C_{\pi\pi} &= (+1) \times (-1)^{L_{\pi\pi}}. \end{aligned}$$

Several constraints are obtained for the decay $X(3872) \rightarrow J/\psi R(\pi\pi)$. Because of conservation of C-parity and the negative C-parity of the J/ψ, a C-odd $X(3872)$ always decays into a C-even dipion state and vice versa. Since only dipion states with spin $J_{\pi\pi} = 0$ and $J_{\pi\pi} = 1$ are considered, the C-parity of the $X(3872)$ effectively determines the spin of the dipion system. This selective effect is the only, but very important, consequence of the C-parity of the $X(3872)$ for the studied decay $X(3872) \rightarrow J/\psi\pi^+\pi^-$.

It is important to determine the allowed combinations of combined spin S_X and relative angular momentum L_X in the $X(3872)$ decay. While the possible combinations are given by angular momentum conservation, the additional conservation of parity reduces the allowed combinations to combinations with either odd or even relative angular momentum L_X. Table 3.2 lists the allowed possibilities in the decay $X(3872) \rightarrow J/\psi R(\pi\pi)$ for each considered quantum number hypothesis.

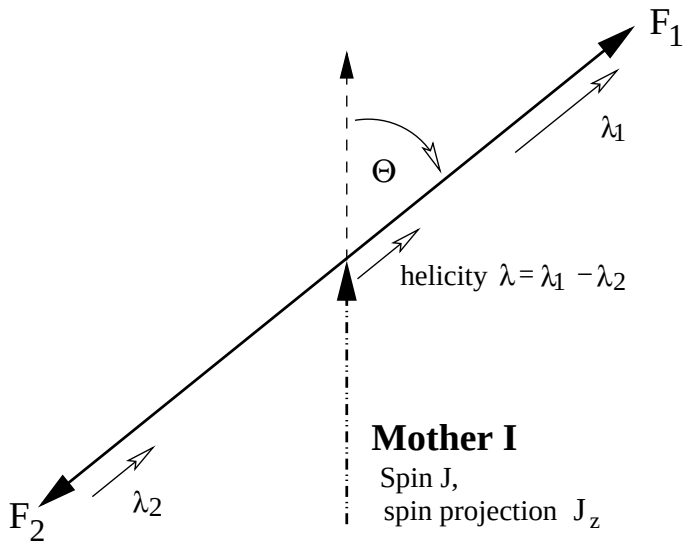

Figure 3.3: Illustration of the decay topology, with the mother particle decaying into final state particles F_1 and F_2 with helicities λ_1 and λ_2.

3.1.2 Construction of a Vertex Decay Matrix Element

The decay matrix element of a single vertex is determined both by the momenta of the incoming and outgoing particles and by the involved spins. Since the matrix element is constructed in the helicity formalism, the decay is examined in the mother particle rest frame.

In the mother particle rest frame the following transition takes place:

$$I(\vec{p} = 0, J, J_z) \rightarrow F_1(\vec{p_1} = \vec{p_F}, \lambda_1)\ F_2(\vec{p_2} = -\vec{p_F}, \lambda_2).$$

This is illustrated in figure 3.3. The mother particle, characterized by its spin J and spin projection J_z along an arbitrarily selected quantization axis, decays into two particles F_1 and F_2 with helicities λ_1 and λ_2. The helicity is defined as the projection of the spin eigenstate vector on the momentum axis, i.e. $\lambda = \vec{s} \cdot \frac{\vec{p}}{|\vec{p}|}$.

In the center-of-momentum system the two daughter particles decay 'back-to-back', so that $\vec{p_1} = -\vec{p_2}$. They move along an axis, rotated by a polar angle θ and an azimuthal angle ϕ with respect to the original momentum direction of the mother particle. The direction of the axis is defined to be given by the momentum of particle 1. Taking this axis as new spin quantization axis, the total combined angular momentum projection is simply $\lambda = \lambda_1 + (-\lambda_2)$. λ_2 is subtracted because it is defined with the momentum $\vec{p_2}$, which is anti-parallel to the quantization axis. There is no orbital angular momentum contribution because, due to $\vec{L} = \vec{r} \times \vec{p}$, any orbital angular momentum is perpendicular to the quantization axis (given by $\vec{p}$), so that the projection on the axis is zero.

The angular dependence of such a single decay vertex is given by the Wigner rotation functions $D^J_{J_z,\lambda}(\alpha, \beta, \gamma)$. They are listed for low spins J in reference [5], higher

spins can be found in reference [85]. Within the helicity formalism, the angles α, β, and γ are identified with ϕ, θ, and $-\phi$. Because of this the Wigner functions will be denoted throughout the thesis by $D^J_{J_z,\lambda}(\theta,\phi)$. The Wigner functions give a quantitative answer to the question 'Given a state with spin J and spin projection J_z along a quantization axis, what is the amplitude to find the spin projection λ with a new quantization axis, turned by (θ,ϕ)?' The angular dependence of the Wigner functions can be separated into two terms

$$D^J_{J_z,\lambda}(\theta,\phi) = d^J_{J_z,\lambda}(\theta)e^{i\phi(J_z-\lambda)},$$

where the $d^J_{J_z,\lambda}(\theta)$ functions are the so-called reduced Wigner functions. In the following the quantization axis of the mother state will be defined by its momentum as well, so that J_z becomes λ_I.

The relation above gives the angular dependence of a transition with defined spin projections. In general, a decay can proceed through different possible spin projections settings, which are not measured. As a consequence, a sum over all the possibilities needs to be formed — in a coherent or incoherent way, depending on the measurability of the spin projection. Each summand gets in addition multiplied by a rotationally invariant coupling term $A(\lambda_1,\lambda_2)$ which contains the remaining kinematical dependences. While A does not contain angular dependences, it still depends on the values of the daughter helicities.

The main task is now to determine the helicity couplings $A(\lambda_1,\lambda_2)$. In general they cannot be determined without introducing model dependence. In the present case, however, the helicity couplings mostly can be successfully estimated from general assumptions. The crucial point is the transformation from the helicity framework into the LS-framework.

The LS-framework uses the different combinations LS of combined spin S and relative angular momentum L of the daughter particles to characterize all independent decay amplitudes. It uses a fixed frame for the quantization axis as compared to the helicity formalism, where the quantization axis changes between mother system and daughter system. The number of independent LS-couplings is the same as in the helicity formalism. The couplings can be related by a coefficient matrix $\widehat{C}$:

$$A_{hel} = \widehat{C}\, B_{LS},$$

where A_{hel} is a vector of the n helicity couplings, B_{LS} is a vector of the n LS-couplings and $\widehat{C}$ is an $n \times n$ matrix relating the two coupling sets. Each helicity coupling thus can be written as a linear combination of different LS-couplings:

$$A_{hel}(\lambda_1,\lambda_2) = \sum_i c_{LS_i}(\lambda_1,\lambda_2)\; B(LS_i)$$

The main purpose of this transformation is that in the LS formalism the determination of dominant and suppressed couplings is dynamically possible. The rule is simple — low relative angular momenta L require lower energies and are thus

favored over high L. Since the allowed L-values for a given J^{PC} assignment to the $X(3872)$ go in steps of 2 because of parity-conservation, amplitudes other than the lowest ones in L are suppressed by two units of angular momentum. This assumption becomes weaker with increasing available energy. It will be seen later that only in the $X(3872)$ decay (not in the J/ψ or $R(\pi\pi)$ decay) this assumption is necessary — there however only a kinetic energy of up to 500 MeV is available[1]. Selecting the dominant LS-coupling with lowest L, $B(LS_{min})$, reduces the relation for given λ_1 and λ_2 simply to:

$$A(\lambda_1, \lambda_2) = c_{LS_{min}}(\lambda_1, \lambda_2) B(LS_{min}).$$

In the following the index min will be omitted. It is implicitly assumed that L refers to the lowest allowed value. The kinematic dependence of $B(LS)$ is given [86] near threshold by

$$B(LS) \propto k^{*L},$$

where k^* is the three-momentum magnitude of one of the two daughter particles in the decay. In the mother rest frame both daughter particles have the same momentum magnitude, only their directions are opposite. The momentum magnitude is labelled $k^* = |\vec{p_1}| = |\vec{p_2}|$. To avoid divergence of the matrix element for higher momenta, this term gets multiplied by a form factor $f_L(k^*)$. The form factor is constructed to have negligible effect for low momenta and to cancel the L power-dependence for high momenta. This thesis uses a widely used model by Blatt and Weisskopf [87]. The form factors for $L \leq 3$ are:

$$\begin{aligned}
f_{L=0}(k^*) &\propto 1 \quad , \\
f_{L=1}(k^*) &\propto \sqrt{\frac{r^2}{1 + (k^* r)^2}} \quad , \\
f_{L=2}(k^*) &\propto \sqrt{\frac{r^4}{9 + 3(k^* r)^2 + (k^* r)^4}} \quad , \\
f_{L=3}(k^*) &\propto \sqrt{\frac{r^6}{225 + 45(k^* r)^2 + 6(k^* r)^4 + (k^* r)^6}} \quad .
\end{aligned}$$

The form factor has one free parameter, the interaction radius r of the mother particle. For large values of r the power-dependence quickly gets dampened, while a very small value only affects very large momenta. We use a common value of $r = 1$ fm. The effect of different assignments for the quantum number analysis is tested in the systematic studies. The momentum dependence thus is given by $k^{*L} f_L(k^*)$.

In addition, the coefficients $c_{LS}(\lambda_1, \lambda_2)$ need to be determined. They can most conveniently be determined for the case when $\phi = \theta = 0$. The LS-frame then coincides with the helicity frame and the quantization axes are the same. The

[1] In the experimental candidate selection procedure this value is even required to be smaller than 100 MeV.

values $c_{LS}(\lambda_1, \lambda_2)$ are obtained [88, 89] by

$$c_{LS}(\lambda_1, \lambda_2) = \left(\begin{array}{cc|c} J_1 & J_2 & S \\ \lambda_1 & -\lambda_2 & \lambda_1 - \lambda_2 \end{array}\right) \times \left(\begin{array}{cc|c} L & S & J \\ 0 & \lambda_1 - \lambda_2 & \lambda_1 - \lambda_2 \end{array}\right)$$

as a product of two Clebsch-Gordan coefficients. The first coefficient describes the coupling of the two daughter particles to the combined spin S, and the second the combination of L and S to the total angular momentum J. The orbital angular momentum does not contribute, since in the chosen frame any orbital momentum is perpendicular to the quantization axis.

In conclusion, a single decay matrix element was constructed. It describes the two-body decay of a particle with spin J and helicity λ_I into two daughter particles with helicities λ_1 and λ_2 and momentum magnitude k^* each. Under angular change (θ, ϕ) of the quantization axis the matrix element is given by:

$$\mathcal{M}(|J, \lambda_I\rangle \to |L, S, \lambda_1, \lambda_2, k^*, \theta, \phi\rangle) \quad \propto \quad c_{LS}(\lambda_1, \lambda_2)\, D^J_{\lambda_I, \lambda_1 - \lambda_2}(\theta, \phi)\, k^{*L} f_L(k^*). \tag{3.1}$$

3.1.3 Construction of the Full Decay Matrix Element

The full decay matrix element consists of the combination of the three two-body decay vertex elements and the connecting propagators. This is schematically written as

$$\begin{aligned} \mathcal{M}_{total} = & \mathcal{M}(X(3872) \to J/\psi R(\pi\pi)) \\ & \times J/\psi\text{-Propagator} \times \mathcal{M}(J/\psi \to \mu^+\mu^-) \\ & \times R(\pi\pi)\text{-Propagator} \times \mathcal{M}(R(\pi\pi) \to \pi^+\pi^-). \end{aligned}$$

To simulate the transition rate T, the matrix element will be used to reweight pure phase space simulation events according to the golden rule

$$T(X(3872) \to \mu^+\mu^-\pi^+\pi^-) = \frac{2\pi}{\hbar} |M_{total}|^2 \text{PS}.$$

The description of the phase-space PS will be handled by the simulation. In order to form a weight w from the matrix element, the matrix element needs to be squared and summed over all possible helicities, since those are not measured. This leads to

$$w \propto \frac{1}{2J+1} \sum_{\lambda_X} \sum_{\lambda_{\mu^+}} \sum_{\lambda_{\mu^-}} \sum_{\lambda_{\pi^+}} \sum_{\lambda_{\pi^-}} \left| \sum_{\lambda_{J/\psi}} \sum_{\lambda_{\pi\pi}} \mathcal{M}_{total} \right|^2,$$

averaging over all initial state helicities λ_X, incoherently summing over all final state helicities and coherently summing over all intermediate state helicities. This looks like a very tedious calculation, however, this general equation is simplified significantly by exploiting specific properties of the analyzed decay.

It should be noted that the decay weight will be exclusively used to compare shapes. Any overall normalization from global factorizing constants or coefficients is neglected.

The Decay $X(3872) \to J/\psi R(\pi\pi)$

This decay is the most important decay in the decay chain. No major simplifications are possible because only the quantum numbers of the J/ψ are known. The matrix element is

$$\mathcal{M}(X(3872) \to J/\psi R(\pi\pi)) \propto \quad c_{LS}(\lambda_{J/\psi}, \lambda_{\pi\pi})\, D^{J_X}_{\lambda_X, \lambda_{J/\psi} - \lambda_{\pi\pi}}(\theta_X, \phi_X)\, {k^*_X}^{L_X} f_{L_X}(k^*_X),$$

considering the appropriate LS choice from table 3.2 and with k_X as the momentum magnitude of the daughter particles in the $X(3872)$ decay.

It should be noted that in this decay it is not always possible to reduce the number of independent amplitudes to one. For the assignments $J^{PC} = 1^{-+}$ and $J^{PC} = 2^{-+}$ three, respectively two, couplings remain, so that no firm prediction is possible. In this analysis these states will be treated separately.

It is also of importance that the value of k^*_X is completely determined by the masses involved:

$$k^*_X = \frac{c}{2m_X}\sqrt{m_X^4 + m_{J/\psi}^4 + m_{\pi\pi}^4 - 2\left(m_X^2 m_{J/\psi}^2 + m_X^2 m_{\pi\pi}^2 + m_{J/\psi}^2 m_{\pi\pi}^2\right)}.$$

In the $X(3872)$ decay both the mass of the J/ψ and the mass of the $X(3872)$ are nearly constant. k^*_X then only depends on $m_{\pi\pi}$. Any change of the treatment of k^*_X thus directly translates into a change of the $m_{\pi\pi}$ distribution.

The Decay $R(\pi\pi) \to \pi^+\pi^-$

This decay leads to considerable simplifications, since the final state pions have spin 0. This completely removes the sum over the final state helicities of the pions. Since also the combined pion spin is 0, $L_{\pi\pi}$ must be identical to $J_{\pi\pi}$. The only helicity coupling $A(\lambda_{\pi^+} = 0, \lambda_{\pi^-} = 0)$ has the momentum dependence ${k^*_{\pi\pi}}^{L_{\pi\pi}} f_{L_{\pi\pi}}(k^*_{\pi\pi})$. The vertex matrix element is then given by

$$\mathcal{M}(R(\pi\pi) \to \pi^+\pi^-) \propto \; D^{J_{\pi\pi}}_{\lambda_{\pi\pi},0}(\theta_{\pi\pi}, \phi_{\pi\pi})\, {k^*_{\pi\pi}}^{J_{\pi\pi}} f_{J_{\pi\pi}}(k^*_{\pi\pi}).$$

Also here the dependence on $k^*_{\pi\pi}$ is really a dependence on $m_{\pi\pi}$. Since the pion masses are identical and constant, one simply obtains

$$k^*_{\pi\pi} = \frac{c}{2}\sqrt{m_{\pi\pi}^2 - 4m_\pi^2}.$$

The Decay $J/\psi \to \mu^+\mu^-$

Some simplifications are possible in this decay, because all quantum numbers of the involved particles are fixed. In addition all involved masses are fixed because

the muons have fixed masses and the J/ψ is an extremely narrow resonance. As a consequence

$$k^*_{J/\psi} = \frac{c}{2}\sqrt{m^2_{J/\psi} - 4m^2_\mu} \approx 1.54\,\mathrm{GeV}/c$$

is constant, so that any momentum dependence can be ignored.

The decay exhibits one specialty: it is dominated by the annihilation of the two charm quarks of the J/ψ into a virtual photon which splits into two muons. A photon is however massless and because of that it cannot have helicity 0, i.e. it is transversely polarized. This is not completely true here, because the photon is virtual and off-shell and thus also can have a mass, but in the limit where the decaying particle is much heavier than the muon, the transversality is still a very good approximation. So from the $2\times 2 = 4$ possible helicity combinations only those with $\lambda_{\mu^+} - \lambda_{\mu^-} = \pm 1$ need to be considered.

For those two terms, the helicity couplings $A(+\frac{1}{2}, -\frac{1}{2})$ and $A(-\frac{1}{2}, +\frac{1}{2})$ occur. It can be shown [84] that parity relates two couplings $A(\lambda_1, \lambda_2)$ and $A(-\lambda_1, -\lambda_2)$ by the relation

$$A(\lambda_1, \lambda_2) = \eta \ \times \ A(-\lambda_1, -\lambda_2).$$

η is the so-called 'naturality', defined as

$$\eta = P\, P_1\, P_2 \times (-1)^{J-J_1-J_2}.$$

P, P_1, and P_2 are the intrinsic parities of the involved particles.

Since the quantum numbers of the J/ψ are 1^-, the combined parity of two muons is (-1), and the muon spin is $1/2$, it follows that the naturality is $\eta = (-1) \times (-1)\times(-1)^{1-1/2-1/2} = +1$. As a consequence only one independent helicity coupling $c(\lambda_{\mu^+}, \lambda_{\mu^-})$ remains. It can be treated as an overall constant and can be ignored.

The simplified matrix element thus reads:

$$\mathcal{M}(J/\psi \to \mu^+\mu^-) \propto \ D^1_{\lambda_{J/\psi}, \underbrace{\lambda_{\mu^+} - \lambda_{\mu^-}}_{=\pm 1}}(\theta_{J/\psi}, \phi_{J/\psi}).$$

Dipion Mass Ambiguity and Treatment

So far the propagator terms in the complete matrix element were not specified. They effectively introduce an additional dependence on the J/ψ and the dipion masses. The J/ψ-propagator was already implicitly used, since the intermediate dimuon system was always treated as a J/ψ with fixed world average J/ψ mass [5], not allowing for any mass deviations. This is motivated by the fact, that the decay time of the J/ψ is so large that the uncertainty in energy spread ($\Gamma = 93.4 \pm 2.1\,\mathrm{keV}$ [6]) is very small and can be neglected.

The behavior is different for the dipion system. It can be a ρ meson with quantum numbers 1^{--}. The mass behavior of the dipion system is then given by a relativistic

Breit-Wigner function,

$$\text{Propagator}_\rho(m_{\pi\pi}) = BW_\rho(m_{\pi\pi}) = \frac{1}{m_{\pi\pi}^2 - m_\rho^2 + i m_\rho \Gamma_\rho}.$$

m_ρ is the world average ρ mass $m_\rho = 775.8\,\text{MeV}/c^2$ [5]. Since the ρ is a broad resonance, kinematical factors will change over its mass range. This is reflected in an energy-dependent width [90], modifying the nominal width $\Gamma_{\rho,0} = 150.3\,\text{MeV}$ [5] as a function of $m_{\pi\pi}$:

$$\Gamma_\rho(m_{\pi\pi}) = \Gamma_{\rho,0} \times \left(\frac{k^*_{\pi^+}(m_{\pi\pi})}{k^*_{\pi^+}(m_{\pi\pi} = m_\rho)} \right)^{(2L_{\pi\pi}+1=3)} \frac{m_\rho}{m_{\pi\pi}} \frac{f^2_{L_{\pi\pi}=1}(k^*_{\pi^+}(m_{\pi\pi}))}{f^2_{L_{\pi\pi}=1}(k^*_{\pi^+}(m_{\pi\pi} = m_\rho))}.$$

The Blatt-Weisskopf form factors enter with the same interaction radius choice as in section 3.1.2.

No unambiguous treatment is however possible for the case when the dipion system has the quantum numbers 0^{++}. There is no single narrow resonance dominating the dipion system in S-wave — at this point any description leads to a strong model-dependence in the resulting dipion mass spectrum.

This ambiguity leads to a freedom in the total matrix element and has two consequences. First, $m_{\pi\pi}$ cannot be used as a discriminating variable between different J^{PC} states, since the outcome may strongly depend on the chosen model. Only angular distributions will thus be used to discriminate between different J^{PC} hypotheses. Second, it still needs to be decided which dipion mass model should be used. Although there is no direct correlation between the angular distributions and the dipion mass distribution, correlations can be induced by detector acceptance effects. Assuming a wrong model for the dipion mass shape then could lead to systematically wrong predictions.

To minimize the danger of systematically changing the predicted angular distributions, information about known facts of the dipion mass shape is used. A dedicated analysis of the dipion mass [59] finds good agreement between the measured dipion mass distribution and the following model:

- propagator for the dipion system: ρ^0 with world average width and mass,
- relative angular momentum between $R(\pi\pi) \equiv \rho^0$ and J/ψ: $L_X = 0$,
- relative angular momentum between π^+ and π^-: $L_{\pi\pi} = J_{\pi\pi} = 1$.

Those parameters are fixed in the $m_{\pi\pi}$-dependent part of the description of the total decay matrix element, no matter whether those parameters would be correct for the J^{PC} hypothesis or not. For example, the hypothesis 1^{+-} which would usually use an S-wave propagator description, $L_X = 1$, and $L_{\pi\pi} = 0$, still uses the aforementioned model in the calculation. The effect of this particular choice of the dipion mass spectrum will be investigated in the systematic section 3.5 of the analysis.

The Complete Decay Weight

Considering the simplifications from the separate decay vertices, the final decay weight is

$$w(J^{PC}) \propto \frac{1}{2J_X+1} \sum_{\lambda_X} \underbrace{\sum_{\lambda_{\mu^+}} \sum_{\lambda_{\mu^-}}}_{\lambda_{\mu^+}-\lambda_{\mu^-}=\pm 1} \left| \sum_{\lambda_{J/\psi}} \sum_{\lambda_{\pi\pi}} M_{total} \right|^2$$

with

$$\begin{aligned} M_{total} \propto\ & c_{LS}(\lambda_{J/\psi}, \lambda_{\pi\pi})\ D^{J_X}_{\lambda_X, \lambda_{J/\psi}-\lambda_{\pi\pi}}(\theta_X, \phi_X)\ f_{L_X}(k^*_X) {k^*_X}^{L_X} \\ & \times \text{Propagator}(m_{\pi\pi}) \\ & \times D^{J_{\pi\pi}}_{\lambda_{\pi\pi},0}(\theta_{\pi\pi}, \phi_{\pi\pi})\ f_{J_{\pi\pi}}(k^*_{\pi\pi}) {k^*_{\pi\pi}}^{J_{\pi\pi}} \\ & \times D^1_{\lambda_{J/\psi}, \lambda_{\mu^+}-\lambda_{\mu^-}}(\theta_{J/\psi}, \phi_{J/\psi}). \end{aligned}$$

Considering the particular choice for all dipion mass dependences, this further simplifies to

$$\begin{aligned} M_{total} \propto\ & c_{LS}(\lambda_{J/\psi}, \lambda_{\pi\pi})\ D^{J_X}_{\lambda_X, \lambda_{J/\psi}-\lambda_{\pi\pi}}(\theta_X, \phi_X) \\ & \times (m^2_{\pi\pi} - m^2_\rho + i m_\rho \Gamma_\rho)^{-1} \\ & \times D^{J_{\pi\pi}}_{\lambda_{\pi\pi},0}(\theta_{\pi\pi}, \phi_{\pi\pi})\ f_1(k^*_{\pi\pi}) {k^*_{\pi\pi}}^1 \\ & \times D^1_{\lambda_{J/\psi}, \lambda_{\mu^+}-\lambda_{\mu^-}}(\theta_{J/\psi}, \phi_{J/\psi}). \end{aligned}$$

The obtained angular distributions for each J^{PC} hypothesis are shown in Appendix A.1.

3.1.4 Matrix Element for the $\psi(2S)$ Decay

The $\psi(2S)$ in its decay mode to $J/\psi\pi^+\pi^-$ will be used throughout the analysis for testing purposes and to derive information for the generation of the simulation. The treatment for the $\psi(2S)$ is identical to the $X(3872)$ treatment. A matrix element for the $\psi(2S)$ decay will be constructed, which will be used to reweight a simulated phase-space sample in order to simulate $\psi(2S)$ events.

The $\psi(2S)$ serves two purposes. First it serves as a high-statistics sample to adjust the event simulation, so that the simulated $\psi(2S)$ sample reasonably agrees with the measured $\psi(2S)$ momentum distributions. For this case a matrix element, known to describe the $\psi(2S)$ is needed. In this thesis, a matrix element from Novikov and

Shifman [91] is used, that yielded good agreement with high-statistics measurements from BES [92]. It is given by:

$$M_{\psi(2S)} \propto {m_{\pi\pi}}^2 - \kappa(\Delta M)^2 \left(1 + \frac{2m_\pi^2}{{m_{\pi\pi}}^2}\right) + \frac{3}{2}\kappa \left[(\Delta M)^2 - {m_{\pi\pi}}^2\right] \left(1 - \frac{4m_\pi^2}{m_{\pi\pi}^2}\right) \left(\cos^2\theta_{\pi\pi} - \frac{1}{3}\right).$$

ΔM is the mass difference between the $\psi(2S)$ and the J/ψ. κ is a free parameter, determined by BES to be

$$\kappa = 0.183 \pm 0.002(\text{stat}) \pm 0.003(\text{syst}).$$

The second purpose is to test the quantum number analysis method with the $\psi(2S)$, where the hypothesis $J^{PC} = 1^{--}$ must not be excluded. The matrix elements are constructed in a nearly identical way as for the $X(3872)$, since the decay topology is the same.

The only change originates from a different choice of the dipion mass modelling. In the $X(3872)$ case a model was chosen which is known to describe the $m_{\pi\pi}$ distribution for the $X(3872)$. Similarly, for the $\psi(2S)$ a model is chosen that is known to describe the $\psi(2S)$. A model, which is known to describe the dipion system in the decay $\psi(2S) \to J/\psi\pi^+\pi^-$ is an 'Adler-zero' by Voloshin and Zhakarov [93]. Their dipion mass prediction is of the form

$$\frac{d\sigma}{dm_{\pi\pi}} \propto \text{phase-space} \times (m_{\pi\pi}^2 - \lambda m_\pi^2)^2,$$

λ is a free parameter which was precisely measured by BES [92]:

$$\lambda = 4.35 \pm 0.06 \pm 0.17.$$

In addition, the k^* dependences are fixed to the correct description for the $J^{PC} = 1^{--}$ case. This leads to $L_{\psi(2S)} = 0$ and $L_{\pi\pi} = 0$.

With the fixed mass dependence, the generic angular matrix element for the $\psi(2S)$ is then given by:

$$\begin{aligned} M_{total,\psi(2S)} \propto\ & c_{LS}(\lambda_{J/\psi}, \lambda_{\pi\pi})\ D^{J_{\psi(2S)}}_{\lambda_{\psi(2S)},\lambda_{J/\psi}-\lambda_{\pi\pi}}(\theta_{\psi(2S)}, \phi_{\psi(2S)}) \\ & \times (m_{\pi\pi}^2 - 4.35 m_\pi^2) \\ & \times D^{J_{\pi\pi}}_{\lambda_{\pi\pi},0}(\theta_{\pi\pi}, \phi_{\pi\pi}) \\ & \times D^{1}_{\lambda_{J/\psi},\lambda_{\mu^+}-\lambda_{\mu^-}}(\theta_{J/\psi}, \phi_{J/\psi}) \ . \end{aligned}$$

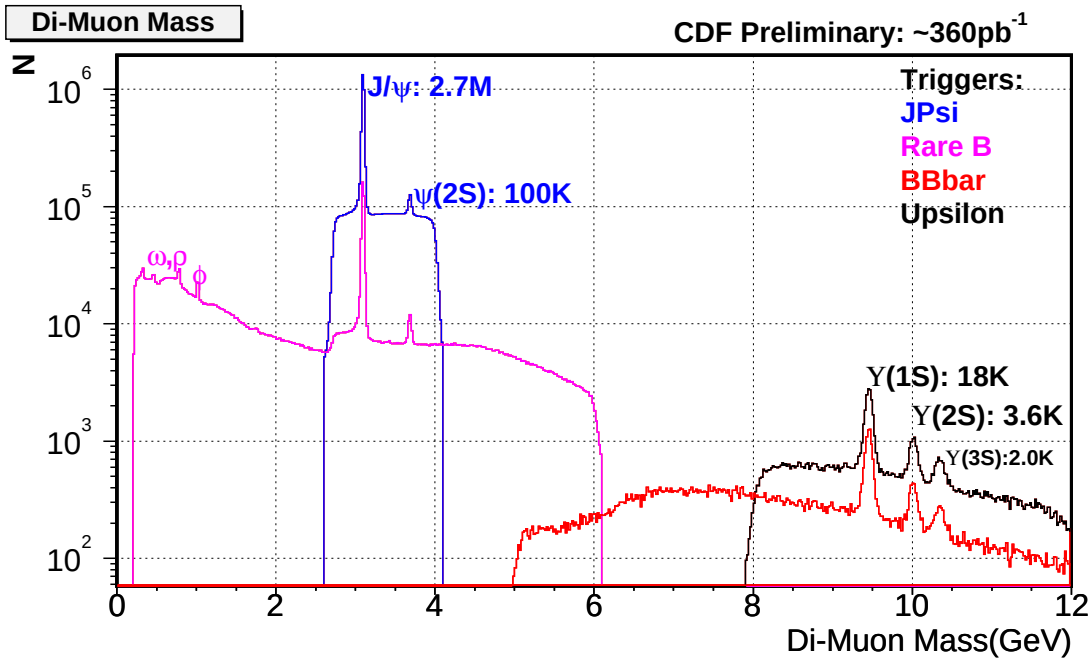

Figure 3.4: Different dimuon triggers implemented in the CDF trigger system. This analysis uses the J/ψ trigger (blue), selecting dimuon pairs in the mass range from $2.5\,\mathrm{GeV}/c^2$ to $4.0\,\mathrm{GeV}/c^2$. Although there is still a considerable amount of background, the J/ψ signal is more prominent by an order of magnitude already at trigger level.

3.2 Data Reconstruction

The quantum number analysis is being performed using all data taken until September 2005. The corresponding CDF dataset names are `jpmm0d` and `jpmm0h`, spanning the run numbers 138425–203799. The amount of measured data corresponds to an integrated luminosity of $\mathcal{L} \approx 780$ pb^{-1}. The data was selected by the $J/\psi \to \mu^+\mu^-$ trigger, leading to a clean sample of J/ψ candidates that can be combined with pions to form the $X(3872)$ candidates. Figure 3.4 shows the dimuon candidate mass distribution from various dimuon triggers.

The $X(3872)$ can also be reconstructed in the exclusive decay channel $X(3872) \to e^+e^-\pi^+\pi^-$, with the J/ψ decaying into an electron-positron pair [94]. This decay occurs with the same rate as the decay into two muons. However, the reconstruction of the electron-positron mode is much more difficult than the reconstruction in the muon mode, because in the muon mode one strongly benefits from the dedicated muon trigger system, cleaner muon selection and less bremsstrahlung effects. Because of this, only muons are used in the J/ψ reconstruction.

The events are reconstructed using CDF software release 6.1.1. In the reconstruction, $X(3872)$ candidates are obtained in two steps. First two muons are combined to a J/ψ candidate, which in turn is combined with two pions to an $X(3872)$ candidate. For most parts the selection process closely resembles that of the CDF

$X(3872)$ confirmation analysis [2, 95].

3.2.1 Preselection Cuts

Each track is required to pass the following selection criteria, designed to apply basic quality requirements and to remove obvious background.

- The tracks were required to have a minimal number of hits in the SVX ($r - \phi$ layer) and the COT. Depending on the tracking algorithm by which the track was reconstructed, at least 2 SVX hits (for Inside-out, Outside-in and SVX-stand-alone algorithms) and 10 hits in both the axial and stereo layers of the COT (for Inside-out, Outside-in and COT-stand-alone algorithms) are required. As indicated by the names, the different algorithms use different methods to build the tracks from the detector hits. They either start at the outer radius of the COT and continue to pick up hits into the SVX (Outside-in), the other way round (Inside-out), or they rely exclusively on hits from either COT or SVX.
- Tracks are taken from the central region of the detector, i.e. $|\eta| < 1$.
- Tracks interpreted as pion candidates are required to have $p_T > 0.4\,\mathrm{GeV}/c$, whereas no p_T cut was imposed on muon candidates.
- The reconstructed J/ψ-mass needs to be in the mass range $3.02\,\mathrm{GeV}/c^2 < m_{\mu\mu} < 3.16\,\mathrm{GeV}/c^2$.

J/ψ candidates are obtained by fitting opposite-charge muon candidate tracks to a common vertex using the `CTVMFT` fitter [96]. Figure 3.5 shows the J/ψ mass distribution after basic selection cuts. A very large and clean signal is obtained.

3.2.2 $X(3872)$ Candidate Reconstruction

The J/ψ candidates obtained according to section 3.2.1 are combined with two pion candidate tracks to form an $X(3872)$ candidate. Because the lifetime of an intermediate dipion system is very short, its decay length would be very small, much smaller than the spatial detector resolution. For this reason, no vertex fit is performed to form a dipion system of the two pions. Instead, the two pions are directly fitted to a common vertex with the J/ψ candidate in order to form the $X(3872)$ candidate. To improve the mass and momentum resolution of the measurement, the J/ψ mass is constrained to the nominal world average J/ψ mass value in this fit. This is a common procedure for narrow resonances where any mass deviation stems from detector resolution effects. Using the extra information of the true J/ψ mass, instead of the measured mass with its inaccuracies, improves the resolution.

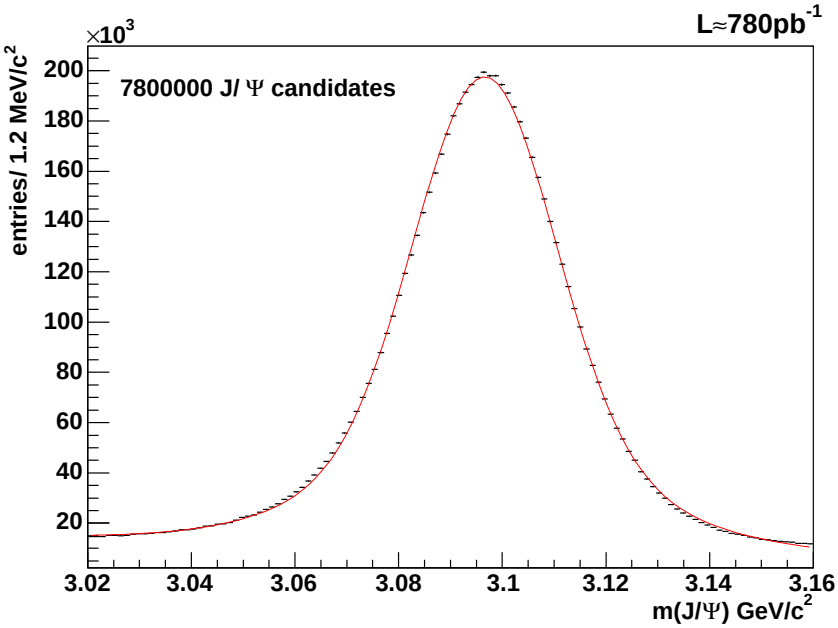

Figure 3.5: Distribution of the reconstructed dimuon mass. In addition to the preselection requirements, a transverse momentum of $p_T(J/\psi) > 4.0$ GeV/c and a dimuon vertex fit quality of $\chi^2 < 15$ is required. 7.8 million J/ψ candidates can be seen on a very low background.

The following selection cuts (in addition to the preselection cuts) are applied in the sample selection:

- the pion charges must be opposite,
- the transverse momentum p_T of each pion must be greater than 0.4 GeV/c,
- the transverse momentum p_T of each muon must be greater than 1.5 GeV/c,
- the χ^2 of the dimuon vertex is required to be less than 15,
- the χ^2 of the $J/\psi\pi\pi$ vertex fit is required to be less than 25,
- the reconstructed dimuon mass needs to be within a $\pm 60\,\mathrm{MeV}/c^2$ mass window with respect to the world average J/ψ mass,
- all $X(3872)$ candidates are required to have masses within $3.65\ \mathrm{GeV}/c^2 \leq m(J/\psi\pi^+\pi^-) \leq 4.00\ \mathrm{GeV}/c^2$,
- both pions are required to lie in a cone around the $X(3872)$ momentum vector with $\Delta R < 0.7$,

where $\Delta R = \sqrt{(\Delta\Phi)^2 + (\Delta\eta)^2}$. Here $\Delta\Phi$ is the azimuthal angle and $\Delta\eta$ the pseudo-rapidity of the pion with respect to the $X(3872)$ candidate momentum vector.

The p_T-requirements are in place to remove badly measured tracks, because due to detector geometry and magnetic field strength only very few well-measured pions can reach the COT with $p_T < 0.4\,\mathrm{GeV}/c$. In the same way only very few well-measured muons can reach the muon chambers with $p_T < 1.5\,\mathrm{GeV}/c$. The cuts on the vertex fit χ^2 removes events for which the tracks do not agree to come from a common point of origin. Since the pions decay in a frame boosted relative to the detector frame they are distributed in a cone around the flight direction of the $X(3872)$. Cutting on the cone size ΔR is motivated by the fact that the pions are mostly distributed very close to the $X(3872)$ in the $\eta - \phi$ plane. The pions are close because they do not obtain much kinetic energy compared to the momentum of the $X(3872)$ in the lab frame — the kinetic energy available for the two pions only is $\approx 500\,\mathrm{MeV}/c^2$. The mass cut finally is designed to remove mass regions one is not interested in, for the simple reason of reducing the sample size.

3.2.3 Final Cut Optimization

The final cut optimization is performed data-driven and in a different way than in the CDF $X(3872)$ confirmation analysis. In the optimization the $X(3872)$ signal significance is used as the figure of merit. It is defined as $S/\sqrt{S+B}$, with the signal and background yield S and B determined in a $\pm 1.5\sigma$ mass window around the $X(3872)$ mass. S and B are determined from a fit to the mass spectrum, where the fit model uses a second order polynomial to describe the background and a simple Gaussian function to describe the $X(3872)$ signal.

The following quantities are used for the final selection cuts:

- the maximum Q-value of the candidate,
- the minimum transverse momentum p_T of the $X(3872)$ candidate $p_{T,X}$,
- the minimum transverse momentum p_T of the J/ψ candidate $p_{T,J/\psi}$,
- the maximum number of candidates per detector event passing the preselection cuts $nCand$.

The quantity $Q = m_{J/\psi\pi\pi} - m_{PDG,J/\psi} - m_{\pi\pi}$ corresponds to the available kinetic energy in the decay. A cut on this variable replaces the cut on the dipion system mass, which was previously used in the the CDF $X(3872)$ confirmation analysis. For fixed $X(3872)$ and J/ψ masses the quantities Q and $m_{\pi\pi}$ are 100% correlated. Because of this, the replacement does not affect the signal shape. However, there is one important difference: a Q-value cut has less serious effects on the shape of the $J/\psi\pi^+\pi^-$ background spectrum, resulting in an easier treatment to describe the shape. For soft $m_{\pi\pi}$ cuts this effect is small, but cutting hard on $m_{\pi\pi}$ translates into a quite sharp falloff in the $J/\psi\pi^+\pi^-$ mass spectrum, which is avoided by cutting on Q.

The cuts on p_T remove low-p_T background events that originate from random fragmentation products. Cutting on the number of candidates increases the *a priori* signal probability of a candidate. In each detector event, there is either none or, much more rarely, one $X(3872)$ candidate event. Cutting on the number of candidates simply removes events where many of the candidates (namely at least $nCand-1$) are known to be background. The most important cut variable is however the Q-value. This variable separates well between signal and background. In the $X(3872)$ decay low Q-values are preferred, while the background is distributed quite uniformly.

As a first step in the cut optimization, a large amount of random sets of cuts on the selected quantities is tested to obtain the behavior of the significance as a function of the cuts. A range with high significance in each variable is determined.

The determined range is scanned in the following 4-dimensional grid:

- $5.5\,\mathrm{GeV}/c \leq p_{T,X} \leq 9.0\,\mathrm{GeV}/c$ in $0.25\,\mathrm{GeV}/c$ steps,
- $3.0\,\mathrm{GeV}/c \leq p_{T,J/\psi} \leq 6.0\,\mathrm{GeV}/c$ in $0.25\,\mathrm{GeV}/c$ steps,
- $0.05\,\mathrm{GeV}/c^2 \leq Q \leq 0.13\,\mathrm{GeV}/c^2$ in $0.01\,\mathrm{GeV}/c^2$ steps,
- $2 \leq$ number of Candidates ≤ 15 in steps of 1.

Among the cut sets with highest significance, one point is selected. The following set of cuts yields a significance of $S/\sqrt{S+B} = 24.1$:

- $Q < 0.10\,\mathrm{GeV}/c^2$,
- $p_{T,X} > 6.0\,\mathrm{GeV}/c$,
- $p_{T,J/\psi} > 4.0\,\mathrm{GeV}/c$,
- $nCand < 5$.

In order to show that this cut choice does not select an uncharacteristically large fluctuation, figure 3.6 illustrates the smooth behavior of the significance as a function of the cut values in each quantity.

Figure 3.7 shows the distribution of the invariant $J/\psi\pi^+\pi^-$ mass spectrum after the final cut selection, both in the complete mass region as well as in a narrower mass window, focussing on the $X(3872)$. Roughly 2300 $X(3872)$ candidates are observed.

From a fit to the invariant mass spectrum, the values

$$m(X(3872)) = 3871.7 \pm 0.3\,\mathrm{MeV}/c^2,$$
$$\sigma(X(3872)) = 5.0 \pm 0.3\,\mathrm{MeV}/c^2$$

are obtained. The fit function uses a second order polynomial for the background description and a Gaussian function for the signal.

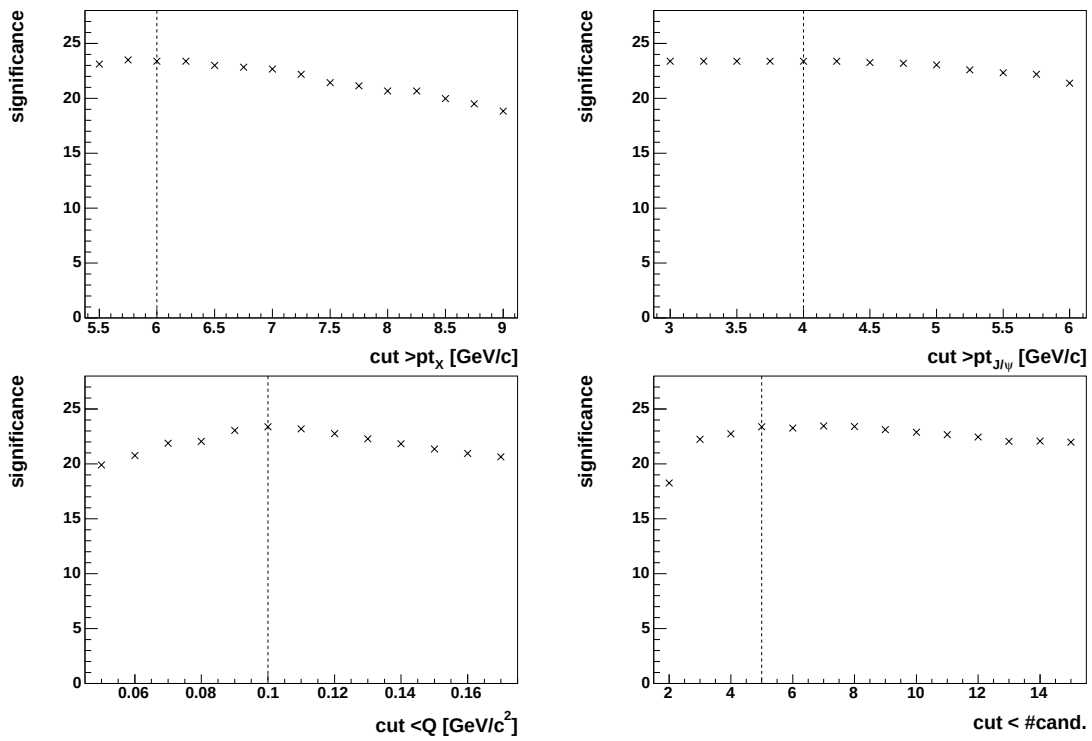

Figure 3.6: The signal significance $S/\sqrt{S+B}$ of the final selection cut set, while varying one of the four cuts. Shown are the significances as a function of the cut value, while keeping the other cut values fixed. The horizontal line illustrates the cut choice.

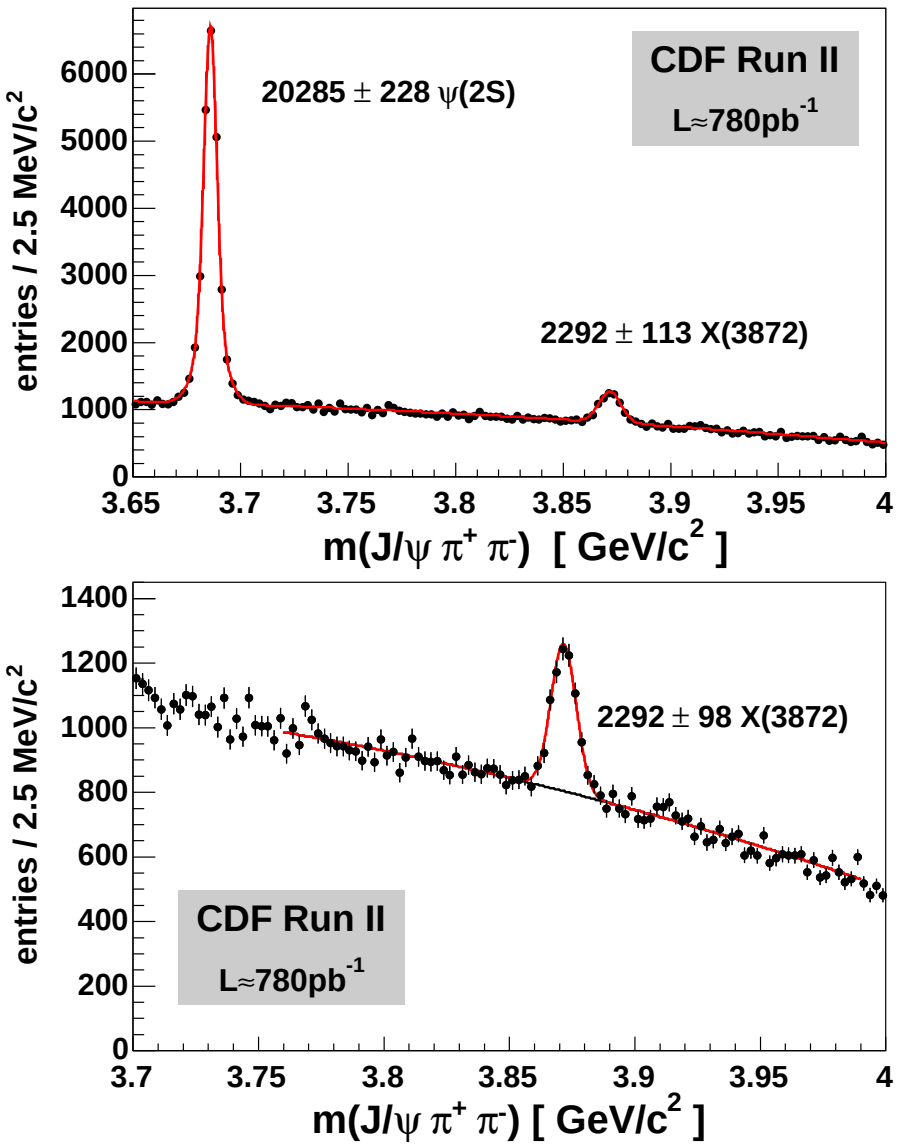

Figure 3.7: The $J/\psi\pi^+\pi^-$ mass spectrum with fit to the total spectrum after applying all selection cuts. While in the upper plot the $\psi(2S)$ at $\approx 3.68\,\mathrm{GeV}/c^2$ dominates the spectrum, the $X(3872)$ also yields a clear peak at $\approx 3.87\,\mathrm{GeV}/c^2$. In the bottom plot the $J/\psi\pi^+\pi^-$ mass spectrum with fit is shown in a mass range without the $\psi(2S)$.

3.2.4 Measurement of Data Distributions

In this thesis it is of particular interest to measure signal distributions without background contribution. The measured sample is however dominated by background events which have distributions different than the signal. A method that can determine the distributions of signal events only is thus required.

The method chosen in this thesis is often referred to as 'slicing' method. This method requires at least one quantity which allows to draw conclusions on the number of signal events S_i contained in a given sample i. In case of the $X(3872)$, the chosen quantity is the invariant $J/\psi\pi^+\pi^-$ mass. The signal is clearly separated from the background events in the form of a narrow peak, which allows to determine the number of signal events from a fit to the mass spectrum. Figure 3.7 shows an example of such a fit, yielding 2292 signal events. Any distribution $f(x)$ is obtained by dividing the quantity of interest x (like p_T, η, ...) into intervals i. The full data sample then is divided into subsamples corresponding to the chosen intervals. Fitting each interval results into a set of signal yields f_i, which constitute the distribution.

The method is limited by the available statistics. While it is desirable to have as many intervals as possible to characterize the properties of the distribution, too many intervals result in low statistics in each interval and a large uncertainty of the single fit yields. For this reason it is required to balance the number of intervals against the yield uncertainties of the single intervals. The method should also be used with extreme care, if the quantity of interest is correlated to the variable, which is used to estimate the signal yield. The dipion mass is an example — different dipion mass intervals also potentially select different intervals of the $J/\psi\pi^+\pi^-$ mass. As a result the shape of the $J/\psi\pi^+\pi^-$ mass looks potentially different in each interval and extra care is required to ensure that the fit to extract the signal yield describes the spectrum well in each interval.

For the determination of the $X(3872)$ yields and their uncertainties, the fit model uses a second order polynomial to describe the smooth background. A Gaussian function describes the $X(3872)$ signal peak. Both the central value and the width of the Gaussian function are fixed to the values of $m = 3871.7\,\mathrm{MeV}/c^2$ and $\sigma = 5.0\,\mathrm{MeV}/c^2$ as determined by a binned maximum likelihood fit to the full sample (see section 3.2). The mass spectrum is fitted in a window of $\pm 110\,\mathrm{MeV}/c^2$ around the fixed signal mass. The histogram bin width is chosen to be $2.5\,\mathrm{MeV}/c^2$, of the order of half the expected detector resolution. The $\psi(2S)$ is studied similarly. Only the parameters for the fit are different. The signal description uses two Gaussian functions with same central value of $m = 3686.04\,\mathrm{MeV}/c^2$, but different relative contributions and widths. The narrow part uses a width of $\sigma = 2.752\,\mathrm{MeV}/c^2$. The broad part is broader by a factor of $f_\sigma = 2.452$ and contributes 35.4% of the signal. These values have been determined from a fit to the complete sample.

3.3 Monte Carlo Simulation Sample

The simulation sample is used to predict the distributions for different J^{PC} hypotheses. While the angular distributions and the available phase-space could in principle be determined analytically, this approach is not practical to model the detector effects. Because of this, a Monte Carlo approach is chosen. The simulation is custom implemented for the $X(3872)$ and $\psi(2S)$ decays — no standard simulation package is used.

The generation can be separated into three phases:

1. Generation of the four-momentum distribution of the decaying $X(3872)$ and simulation of the decay into the final state according to phase space.
2. Simulation of detector effects. Which events would be detected and which not?
3. Reweighting of the sample according to J^{PC} hypothesis.

Two samples are created. One describes the $X(3872)$ while the other one describes the $\psi(2S)$. They only differ in the properties of the decaying particle. The only specific information about the $X(3872)$ entering in the simulation before the reweighting is its mass. The simulation itself is largely based on general assumptions. Data-driven 'tuning' is only performed to achieve reasonable agreement in the $\psi(2S)$ transverse momentum and pseudorapidity distributions.

3.3.1 Event Generation

The first step in the event generation is the generation of the four-momentum of the decaying particle. The four-momentum can be determined from the quantities mass m, transverse momentum p_T, pseudorapidity η, and azimuthal angle ϕ. p_T, η, and ϕ form the three-momentum $\vec{p}$, which can be combined with m to the energy E. They are generated as follows:

- Mass m: The $\psi(2S)$ sample uses a central mass value of $3686\,\mathrm{MeV}/c^2$. This value is smeared by a Gaussian distribution with width $\sigma(\psi(2S)) = 2.75\mathrm{MeV}/c^2$ to model effective detector resolution effects. For the $X(3872)$ sample a central mass of $3871.7\,\mathrm{MeV}/c^2$ is used with a width of $\sigma(X(3872)) = 5.0\,\mathrm{MeV}/c^2$.
- Transverse momentum p_T: For both $\psi(2S)$ and $X(3872)$ samples an acceptance-corrected measurement of the $\psi(2S)$ p_T distribution is used. The non-trivial shape is modelled by $d\sigma/dp_T = p_T^{203.9}/(0.85^2\,\mathrm{GeV}^2/c^2 + {p_T}^2)^{105.0}$ and created in the p_T range from $5.5\,\mathrm{GeV}/c$ to $30.0\,\mathrm{GeV}/c$.
- Pseudorapidity η: Detector events are uniformly distributed in η. Together with the restriction to the central part of the detector this leads to the choice for the uniform distribution of η between -1.2 and 1.2.

- Azimuthal angle ϕ: Because of the symmetry in ϕ, it is generated uniformly between 0 and 2π.

The most important assumption in the generation is to assume the same behavior in p_T for the $X(3872)$ and the $\psi(2S)$. This is motivated by the fact that, while no precise knowledge about the $X(3872)$ exists, it is however known from measurement [3] that production and decay properties of the two particles are similar, so that assuming the same behavior is the most efficient approach.

For the created four-momentum a three-body phase-space decay is simulated into $J/\psi\pi^+\pi^-$. This analysis uses the `ROOT` class `TGenPhaseSpace` [97], which randomly creates final state momenta and calculates a weight which corresponds to the probability of obtaining this final state event. In order to keep the treatment as simple as possible, this weight is not kept in the further sample but is rather used to perform a simple acceptance-rejection step[2] .

As a final step the J/ψ decay to $\mu^+\mu^-$ is simulated. This two-body decay has a fixed phase-space weight since all involved masses are completely fixed. Only the direction of the decay products in the J/ψ rest frame is isotropically generated.

3.3.2 Detector Acceptance

The next step is to model detector effects. Since the final state particles have low transverse momentum, $\lesssim 2\,\mathrm{GeV}/c$ for pions and $\lesssim 10\,\mathrm{GeV}/c$ for muons, acceptance will play a major part in the event distributions.

The largest effect on the angular distributions is expected from the p_T-cuts on the final state muons and pions. In order to be reconstructed, *every* final state particle needs to pass the corresponding p_T requirement. The most important effects, visualized in figure 3.8, are:

- The distribution of the decay angle $\cos(\theta_X)$ becomes asymmetric. If the dipion system decays backward compared to the original $X(3872)$ direction, the pions are likely to have low momentum in the lab frame. Because they gain very little extra kinetic energy in the dipion decay, it is very likely that one of the pions fails the acceptance threshold. The same situation is true for the muons. They, however, gain $\approx 1.5\,\mathrm{GeV}$ in kinetic energy in the J/ψ decay, so that muons are more likely to be detected. Since θ_X is defined with the J/ψ direction, the decay shows a backward preference.

- The decay angles $\cos(\theta_X)$ and $\cos(\theta_{J/\psi})$ become strongly correlated. The acceptance favored direction of the subsequent J/ψ decay into two muons changes, depending on the direction of the initial J/ψ direction in the $X(3872)$ decay.

[2] An acceptance-rejection step accepts or rejects events based on their weights. A random number is created uniformly between 0 and the largest possible weight. If the random number is smaller than the weight the event is kept, otherwise it is rejected.

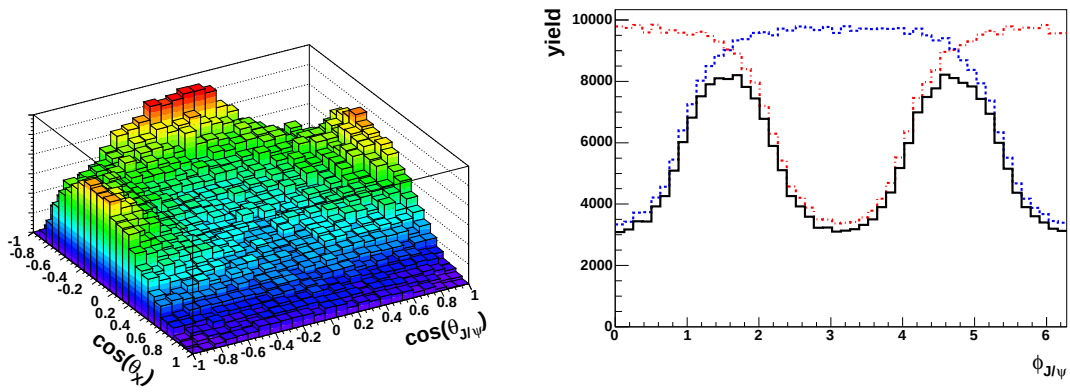

Figure 3.8: Acceptance effects on the angular distributions. The left plot shows the induced correlation between $\cos(\theta_X)$ and $\cos(\theta_{J/\psi})$. In addition, the forward decay suppression of $\cos(\theta_X)$ can be observed. The right plot illustrates the acceptance effect on $\phi_{J/\psi}$. Shown are the two distributions where only one muon needs to pass the p_T requirement and the one where both need to. While a p_T-cut on only one of the muons results in 'backward' dips at either $\phi_{J/\psi} = 0$ or $\phi_{J/\psi} = \pi$, both cuts together lead to a preference of 'orthogonal' angles $\phi_{J/\psi} = \pi/2$ or $\phi_{J/\psi} = 3\pi/2$.

This is also true for $\cos(\theta_X)$ and $\cos(\theta_{\pi\pi})$, which become correlated as well. The correlation is however less strong, since in this case the acceptance is dominated by the initial direction of $X(3872)$ decay.

- The azimuthal angle $\phi_{J/\psi}$ becomes strongly sculpted. For each muon, angles are favored that minimize the probability to pick up too much momentum in backward direction. Since the momentum vector $\vec{p_X}$ is used to determine $\phi = 0$, a value of $\phi = 0$ results in the highest possible transverse momentum for the positively charged muons, while the negatively charged muon has the lowest possible transverse momentum. The opposite situation is true for $\phi = 180°$ (compare figure 3.2). Since both muons have to pass the acceptance requirements, the combination leads to the favored decay angles of $\phi = 90°$ and $\phi = 270°$. Exactly the same effect also applies to the angle $\phi_{\pi\pi}$.

The effects are modelled by a simple detector and trigger model, which takes into account the different p_T thresholds and geometric acceptances. Although it is certainly not a 'realistic' description of the detector because of its simplicity, it turns out to describe both the $\psi(2S)$ and $X(3872)$ distributions sufficiently well to predict angular distributions.

The model consists of:

- For each event a position of the primary vertex position along the beamline is generated from a Gaussian distribution of width $\sigma = 29$ cm around the center of the detector at $z = 0$ cm. An effective pseudorapidity η_{eff} is calculated at the detector positions of the COT (for pions) and the muon chambers (for muons) to account for this z-shift. η_{eff} is exclusively used for the fiducial

acceptance cuts in order to simulate the geometric acceptance in η, and for the assignment whether a muon would have been detected in the CMU or the CMX.

- Muons are identified above a p_T of $1.5\,\mathrm{GeV}/c$ in the CMU and above $2.0\,\mathrm{GeV}/c$ in the CMX. The CMU effective region is defined by $0.028 \leq |\eta_{\mathrm{eff}}| \leq 0.6$ (taking into account the muon chamber gap at $z = 0\,\mathrm{cm}$), the CMX by $0.6 \leq |\eta_{\mathrm{eff}}| \leq 1.0$. Due to the limited ϕ-coverage of the CMX in the beginning of Run II, it is simulated to have an efficiency of 75%.

- The muon trigger simulation demands 2 CMU muons or one CMU and one CMX muon.

- The decreasing pion reconstruction efficiency towards the reconstruction threshold of $p_T = 400\,\mathrm{MeV}/c$ is derived from a 'realistic' CDF detector simulation. The dependence is modeled by $\epsilon(p_{T,\pi}) = 0.8{+}0.2(p_{T,\pi} - c_1)^2/(c_2 + (p_{T,\pi} - c_1)^2)$, with $c_1 = 0.4\,\mathrm{GeV}/c$ and $c_2 = 0.005\,\mathrm{GeV}^2/c^2$.

- The non-uniformity of the COT-efficiency in ϕ is modelled after measured data and applied for each muon or pion track.

3.3.3 Event Reweighting

After applying the selection cuts from section 3.2, a comparison of simulated events to $\psi(2S)$ data shows slight discrepancies in η and p_T that are corrected for by a final reweighting procedure. The corrections are determined by fitting the ratios of measured $\psi(2S)$ distribution and predicted distributions. The correction functions are obtained to be

$$f(p_{T,X}) = 0.94 + \exp^{0.23-0.34\,p_{T,X}[\mathrm{GeV}/c]},$$
$$f(\eta_X) = 0.91 + \frac{0.44}{1 + \exp(-11.3|\eta_X| - 0.52)}.$$

They are shown in figure 3.9. The correction functions are implemented by an acceptance/rejection method.

Distributions for specific J^{PC} are easily available with the decay weights from section 3.1. For each simulated event i, a weight for each J^{PC} hypothesis $w_i(J^{PC})$ is obtained. Any distribution is now simply obtained by filling a corresponding histogram with the simulated events, not using the weight 1 for each event, but using the weight $w_i(J^{PC})$. This reweighting only affects quantities which directly or indirectly depend on the quantum numbers of the $X(3872)$. For other quantities the effect over the integrated sample should vanish.

The obtained angular distributions, used to distinguish between the different J^{PC} hypotheses, are shown in Appendix A.1 for each J^{PC} hypothesis. Both the effect of the pure J^{PC}-reweighting, as well as the additional acceptance effects are displayed.

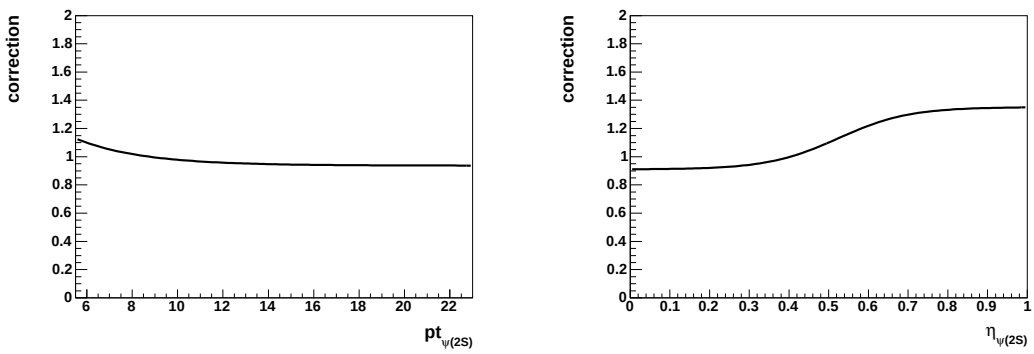

Figure 3.9: Correction functions used to account for discrepancies between $\psi(2S)$ data and simulation.

3.3.4 Simulation Verification with $\psi(2S)$ Measurements

To verify the simulation procedure, the generated events are compared to the distributions of the transverse momentum and the pseudorapidity of the involved particles, as well as to the angular distributions. These checks are made using the $\psi(2S)$ signal, where statistics is high enough to perform an adequate measurement. For reweighting the $\psi(2S)$ simulation, the amplitude model of Novikov and Shifman (described in section 3.1) is used. Figures 3.10 and 3.11 illustrate the good agreement between simulation and measurement. Figure 3.12 shows the agreement for the distributions of the decay angles. It can be seen that the simulated angular distributions describe the data very well.

Shown as well is the agreement of the transverse momentum and pseudorapidity distributions for the $X(3872)$ (see figures 3.13 and 3.14). The distributions from the simulation — not using any weight since the correct weight is not known — agree reasonably well with the corresponding measured data distributions.

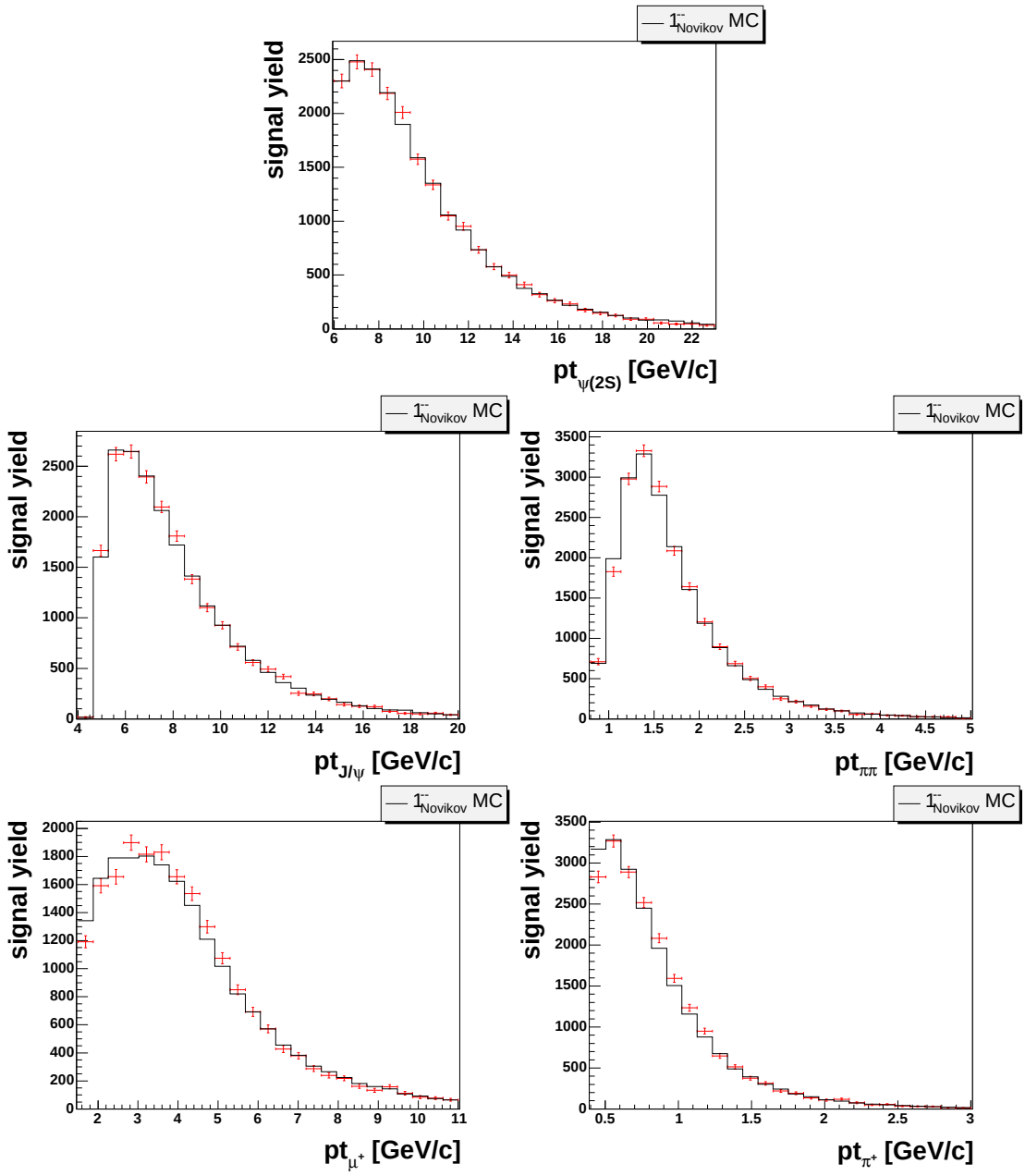

Figure 3.10: Comparison between the transverse momentum (p_T) distributions from the simulation (histogram) and from the $\psi(2S)$ measurement (points).

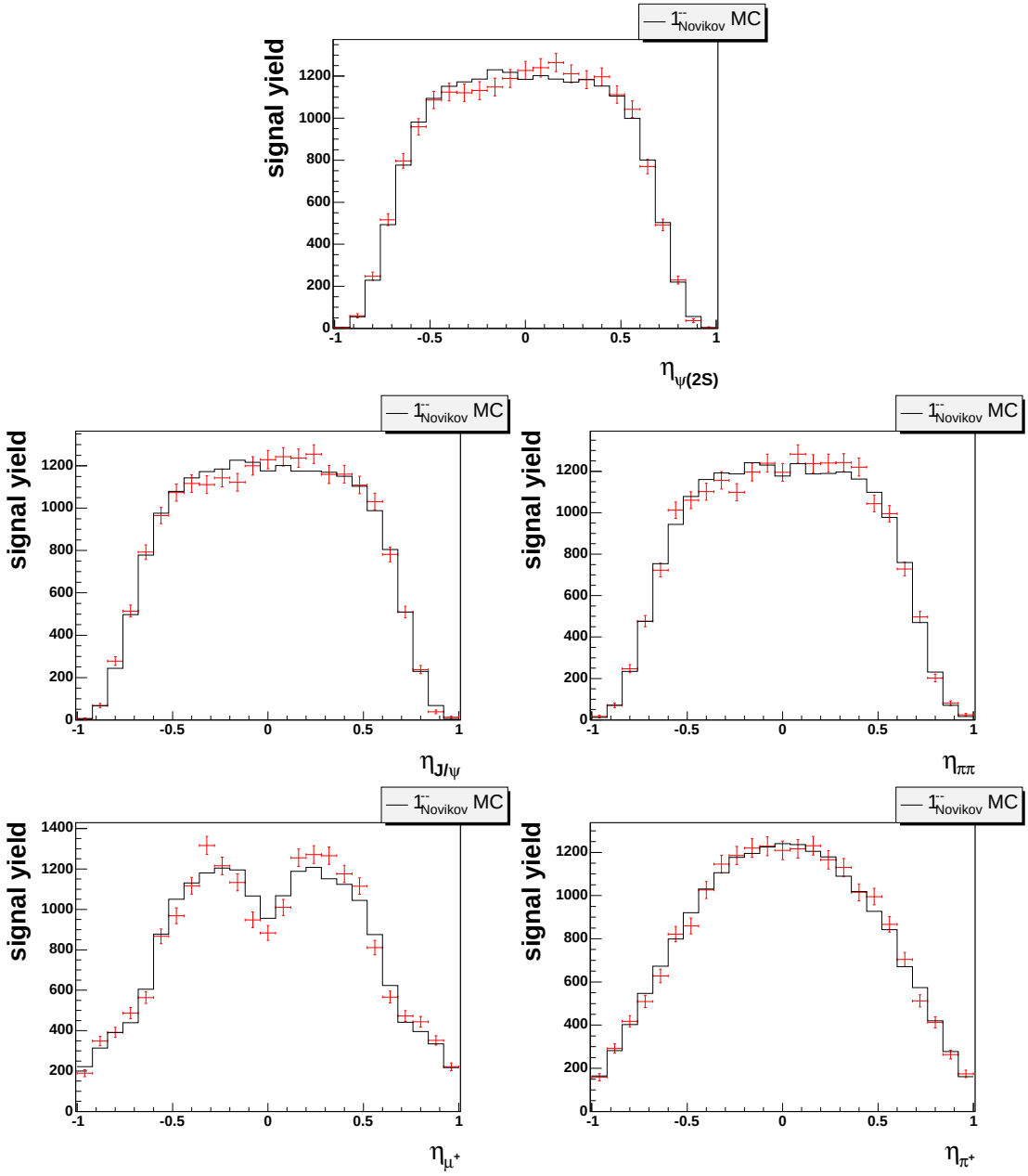

Figure 3.11: Comparison between the pseudorapidity (η) distributions from the simulation (histogram) and from the $\psi(2S)$ measurement (points).

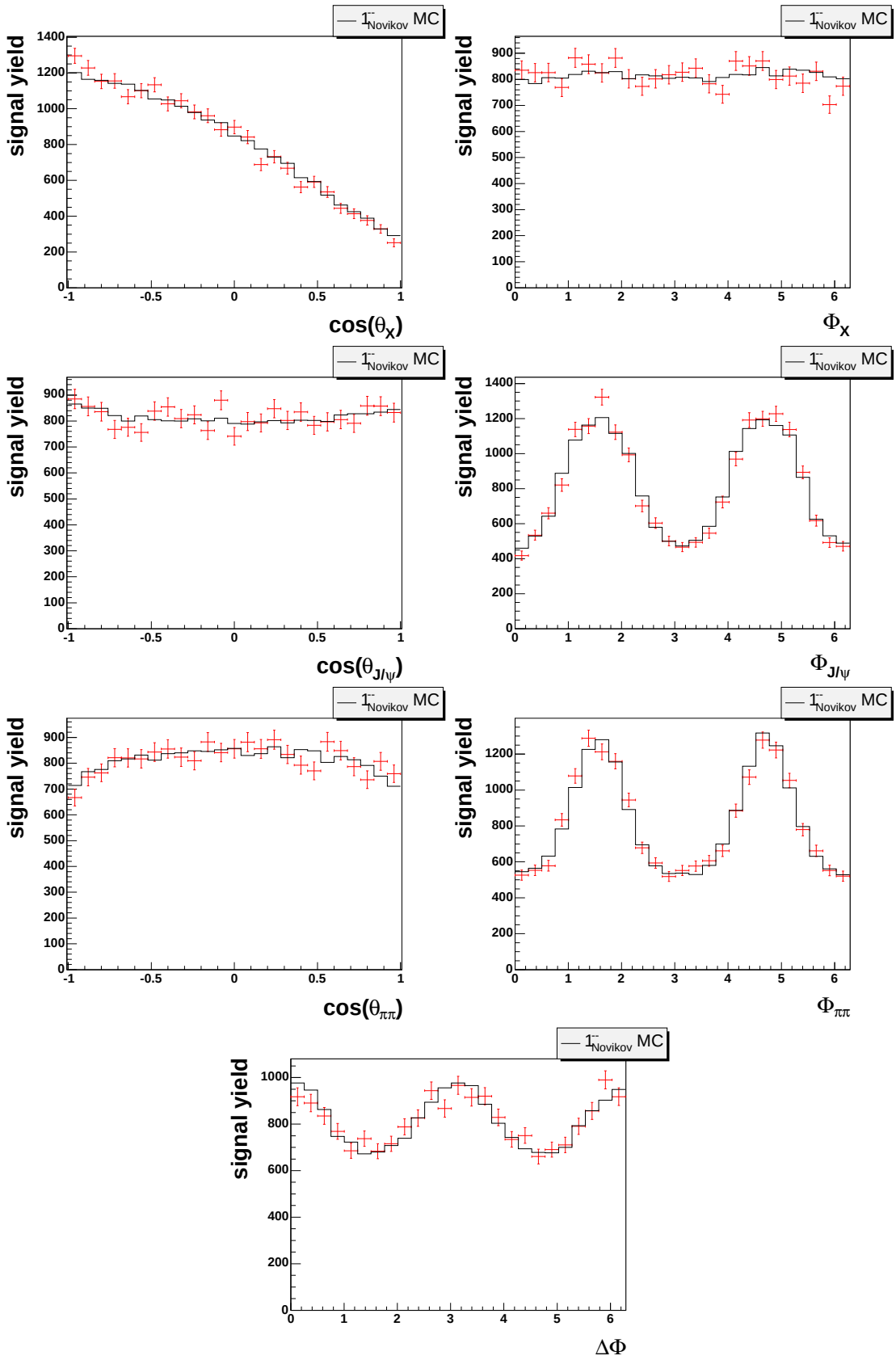

Figure 3.12: Comparison between the angular distributions from the simulation (histogram) and from the $\psi(2S)$ measurement (points).

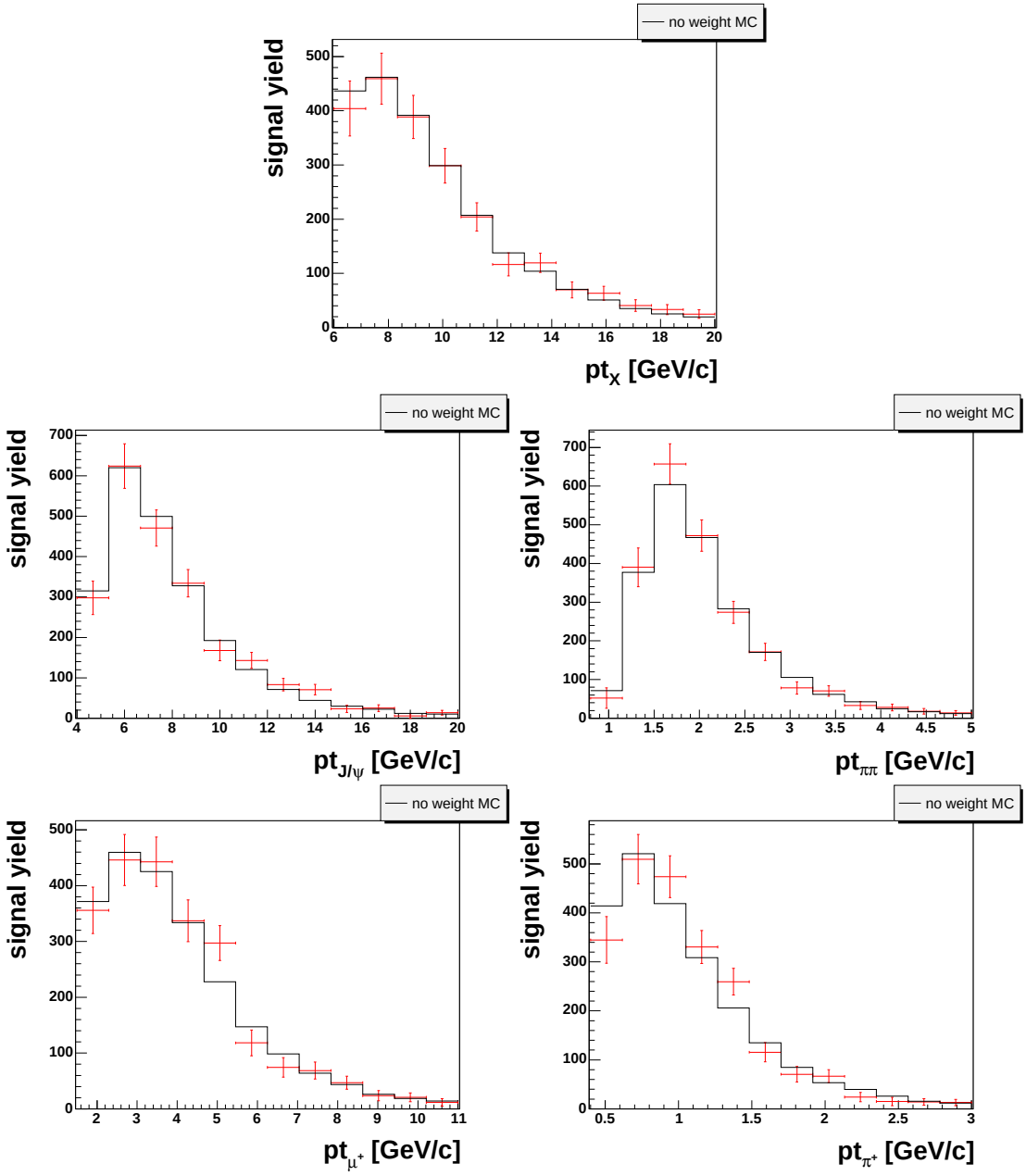

Figure 3.13: Comparison between the transverse momentum (p_T) distributions from the simulation (histogram) and from the $X(3872)$ measurement (points).

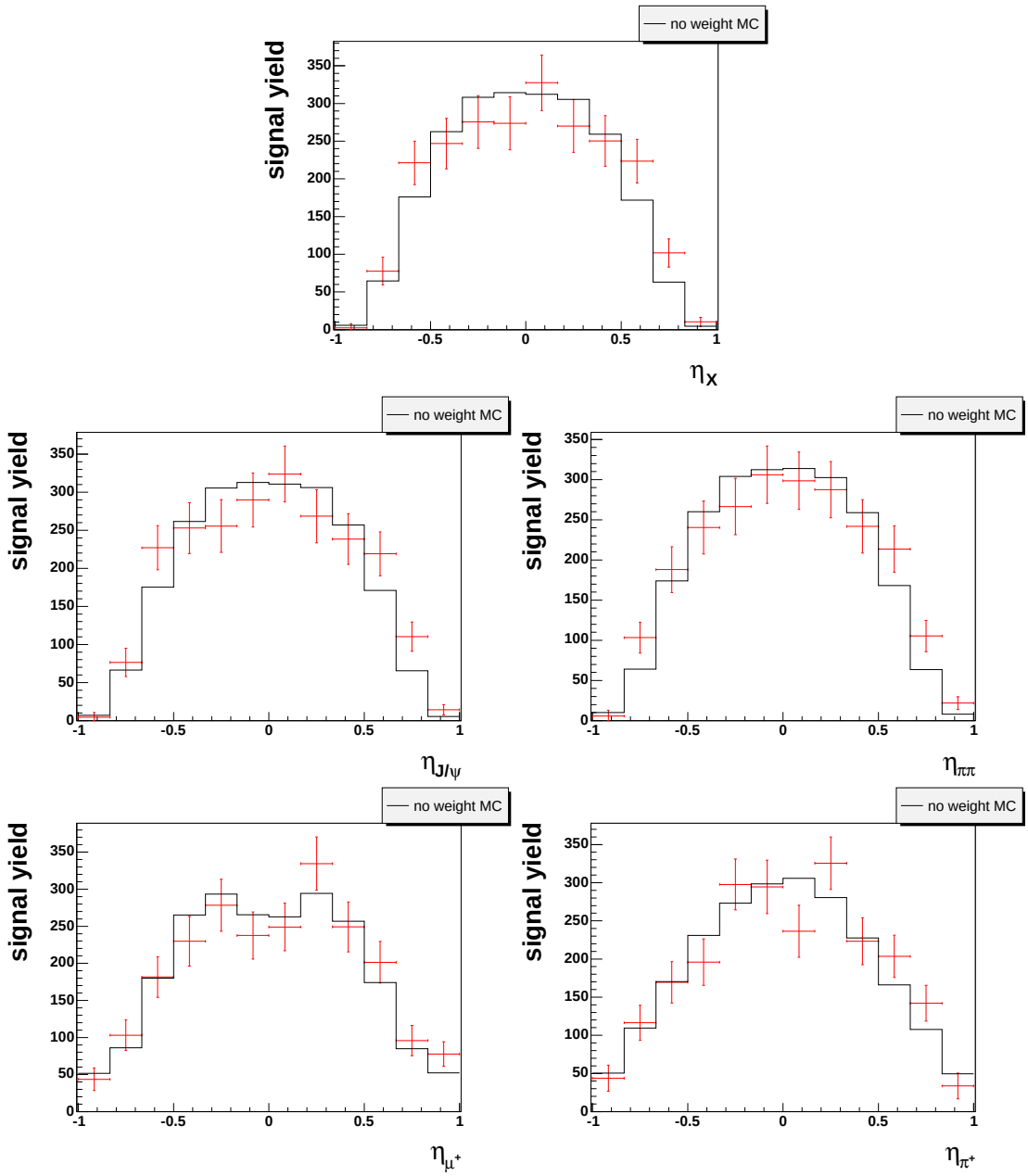

Figure 3.14: Comparison between the pseudorapidity (η) distributions from the simulation (histogram) and from the $X(3872)$ measurement (points).

3.4 Measurement and Comparison of Angular Distributions

This section presents the actual determination of the quantum numbers J^{PC} of the $X(3872)$. Its angular distributions will be measured and compared to predictions for different J^{PC}. Depending on the quality of the agreement, each considered J^{PC} state will be either accepted or rejected.

The comparison uses a χ^2-approach to quantify the agreement between predictions and the measurement. Both the distribution of the predictions and the distribution of the measurement are given by a set of yield values y_i corresponding to a set of angular intervals x_i. The χ^2 is defined as

$$\chi^2 = \sum_i \frac{\left(y_{data,i} - y_{MC,i}\right)^2}{\sigma_i^2}, \tag{3.2}$$

where $y_{data,i}$ is the measured data yield for the interval i. σ_i is the corresponding statistical yield uncertainty. No other uncertainties enter at this point. The statistical uncertainty of the simulation is negligible since the simulation event count is much higher than in measured data. The inclusion of systematic uncertainties at this point is impractical, because it would result into a complicated treatment of correlated uncertainties between the different angular intervals. Instead it will be checked that systematic effects do not change the conclusion of the analysis (see section 3.5).

$y_{MC,i}$ is the predicted yield in interval i. To fix the *a priori* undefined normalization of the prediction, the χ^2 is minimized with respect to the normalization. This conservative approach prevents the exclusion of any hypothesis because of a wrongly chosen normalization. The normalized prediction yield is obtained as

$$\begin{aligned} y_{MC,i} &= n\, y_{MC_{arb},i} \\ n &= \sum_i \frac{y_{data,i}\, y_{MC_{arb},i}}{\sigma_i^2} \Big/ \sum_i \frac{y_{MC_{arb},i}^2}{\sigma_i^2}, \end{aligned}$$

where $y_{MC_{arb},i}$ is the arbitrarily normalized simulation yield and n is the normalization constant, determined from analytically minimizing equation 3.2.

The number of degrees of freedom is given by the number of intervals. One degree of freedom is lost because of the normalization minimization, so that for a comparison of N intervals $N-1$ degrees of freedom remain. The obtained χ^2, together with the number of degrees of freedom, determine the quality of the agreement between the model and the measurement. For a correct model, the expectation value of the χ^2 equals the number of degrees of freedom. From the χ^2 and the number of degrees of freedom (d.o.f.), one can additionally calculate the χ^2-probability $P(\chi^2, \text{d.o.f.})$. For a given number of degrees of freedom, it corresponds to the probability that for a true hypothesis a value of χ^2 or larger is found.

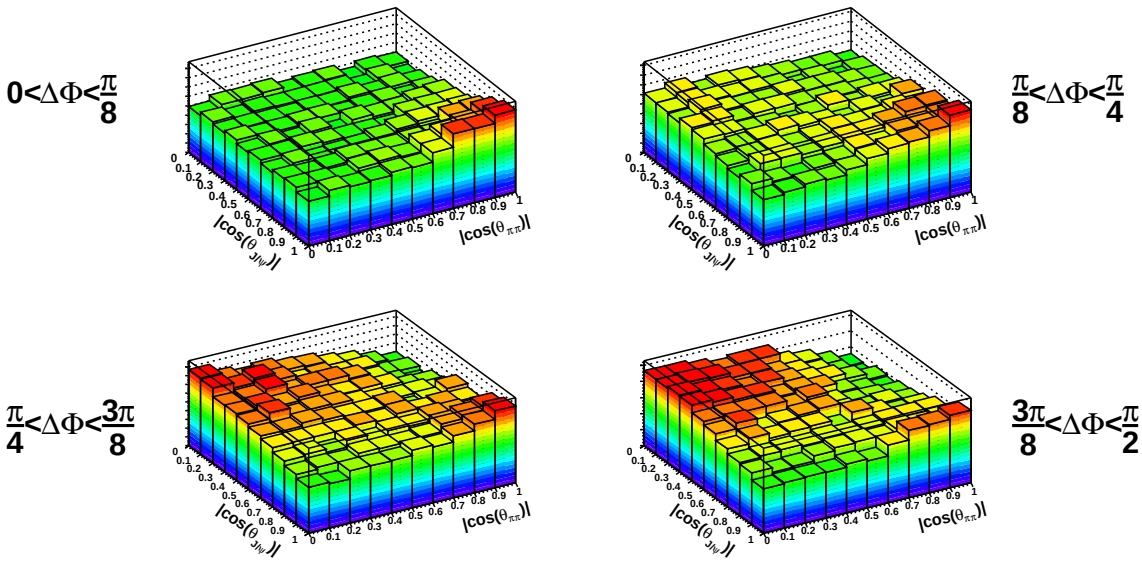

Figure 3.15: Illustration of possible angular correlations. Shown is the distribution of $|\cos(\theta_{\pi\pi})|$ against $|\cos(\theta_{J/\psi})|$ in different intervals of $\Delta\Phi$ for the hypothesis $J^{PC} = 1^{++}$. The correlation between $|\cos(\theta_{\pi\pi})|$ and $|\cos(\theta_{J/\psi})|$ changes, illustrating a correlation between all three angles.

3.4.1 Measurement of Angular Distributions

The discriminating information to distinguish between different J^{PC}-hypotheses is given by the angular distributions $\cos(\theta_{J/\psi})$, $\cos(\theta_{\pi\pi})$, and $\Delta\Phi$. Since the distributions are assumed to be symmetric concerning the exchange of particle and antiparticle ($\pi^+ \leftrightarrow \pi^-$, $\mu^+ \leftrightarrow \mu^-$), the statistical power can be increased by investigating the absolute values of $\cos(\theta_{J/\psi})$ and $\cos(\theta_{\pi\pi})$. $\Delta\Phi$, as the difference between the dipion and dimuon decay planes, even shows a two-fold symmetry, so that $||\Delta\Phi - \pi| - \frac{\pi}{2}|$ is used. Information is not only contained in the single projections of the angular distributions, but also in their correlations as illustrated in figure 3.15.

In order to be sensitive to the shape of the angular distributions, as many intervals as possible are desirable. However, since the available statistics is limited for the $X(3872)$, a high number of intervals results in a large yield uncertainty. So the number of intervals needs to be balanced against the available statistics. This issue also impacts the principal choice of the binning dimension: Investigating the three angular variables separately increases the number of intervals with the same statistical power by a factor of 3, at the cost of the loss of all possible correlation information between the angular variables.

The optimal strategy was determined by simulation. The figure of merit in the optimization is the discrimination power between the two hypotheses $J^{PC} = 1^{++}$ and $J^{PC} = 2^{++}$. This choice is motivated by the fact, that a determination of the $X(3872)$ quantum numbers by Belle remained with the favored hypotheses $J^{PC} = 1^{++}$ and $J^{PC} = 2^{++}$ [58], so that a further separation between those two hypotheses

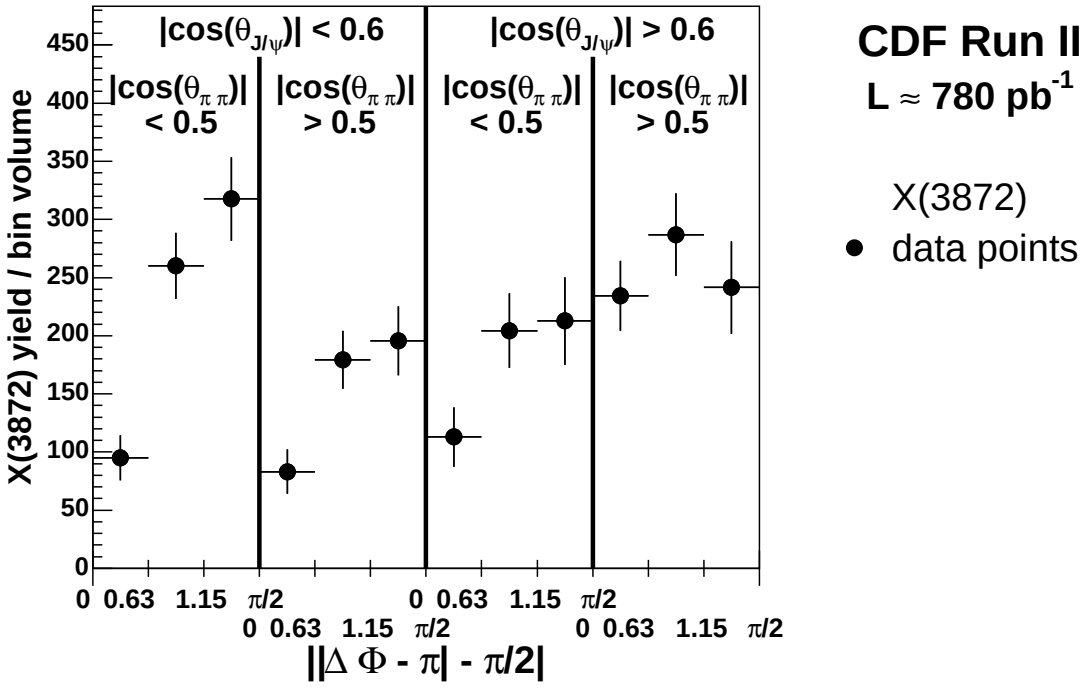

Figure 3.16: Measurement of the three-dimensional angular distribution.

if of primary experimental interest. The following binning is obtained:

- 3 bins with bin borders (0, 0.63, 1.15, $\frac{\pi}{2}$) for $||\Delta\Phi - \pi| - \frac{\pi}{2}|$,
- 2 bins with bin borders (0, 0.6, 1.0) for $|\cos(\theta_{J/\psi})|$,
- 2 bins with bin borders (0, 0.5, 1.0) for $|\cos(\theta_{\pi\pi})|$.

This choice results in a total number of 12 intervals, which corresponds to 11 degrees of freedom for the χ^2-comparison. A non-equidistant binning yielded slightly better results than an equidistant binning.

The numerical values of the measured distribution can be found in table 3.3. All single mass spectrum fits are shown in Appendix A.2. A graphical representation is given in figure 3.16. To avoid that the different interval volumes affect the graphical representation of the distribution, the interval yields are rescaled to unit interval volume.

3.4.2 Comparison of Measured Distributions to Predictions

The measured distribution is compared to the J^{PC}-hypotheses. In this section the comparison is only performed for hypotheses with known angular distributions. The hypotheses $J^{PC} = 1^{-+}$ and $J^{PC} = 2^{-+}$ which have some remaining ambiguity in their matrix elements are considered in the next section. The results are shown in

angular interval	relative volume	measured yield	normalized yield
$\lvert\cos(\theta_{J/\psi})\rvert < 0.6$ $\lvert\cos(\theta_{\pi\pi})\rvert < 0.5$ $0 < \lvert\lvert\Delta\Phi - \pi\rvert - \frac{\pi}{2}\rvert < 0.63$	1.44	137.1 ± 27.9	94.9 ± 19.3
$\lvert\cos(\theta_{J/\psi})\rvert < 0.6$ $\lvert\cos(\theta_{\pi\pi})\rvert < 0.5$ $0.63 < \lvert\lvert\Delta\Phi - \pi\rvert - \frac{\pi}{2}\rvert < 1.15$	1.19	309.9 ± 33.8	260.1 ± 28.4
$\lvert\cos(\theta_{J/\psi})\rvert < 0.6$ $\lvert\cos(\theta_{\pi\pi})\rvert < 0.5$ $1.15 < \lvert\lvert\Delta\Phi - \pi\rvert - \frac{\pi}{2}\rvert < \pi/2$	0.96	306.3 ± 34.8	317.6 ± 36.0
$\lvert\cos(\theta_{J/\psi})\rvert < 0.6$ $\lvert\cos(\theta_{\pi\pi})\rvert > 0.5$ $0 < \lvert\lvert\Delta\Phi - \pi\rvert - \frac{\pi}{2}\rvert < 0.63$	1.44	119.8 ± 27.6	83.0 ± 19.1
$\lvert\cos(\theta_{J/\psi})\rvert < 0.6$ $\lvert\cos(\theta_{\pi\pi})\rvert > 0.5$ $0.63 < \lvert\lvert\Delta\Phi - \pi\rvert - \frac{\pi}{2}\rvert < 1.15$	1.19	213.5 ± 29.8	179.2 ± 25.0
$\lvert\cos(\theta_{J/\psi})\rvert < 0.6$ $\lvert\cos(\theta_{\pi\pi})\rvert > 0.5$ $1.15 < \lvert\lvert\Delta\Phi - \pi\rvert - \frac{\pi}{2}\rvert < \pi/2$	0.96	188.7 ± 28.8	195.6 ± 29.8
$\lvert\cos(\theta_{J/\psi})\rvert > 0.6$ $\lvert\cos(\theta_{\pi\pi})\rvert < 0.5$ $0 < \lvert\lvert\Delta\Phi - \pi\rvert - \frac{\pi}{2}\rvert < 0.63$	0.96	108.8 ± 24.7	113.0 ± 25.6
$\lvert\cos(\theta_{J/\psi})\rvert > 0.6$ $\lvert\cos(\theta_{\pi\pi})\rvert < 0.5$ $0.63 < \lvert\lvert\Delta\Phi - \pi\rvert - \frac{\pi}{2}\rvert < 1.15$	0.79	162.4 ± 25.5	204.4 ± 32.1
$\lvert\cos(\theta_{J/\psi})\rvert > 0.6$ $\lvert\cos(\theta_{\pi\pi})\rvert < 0.5$ $1.15 < \lvert\lvert\Delta\Phi - \pi\rvert - \frac{\pi}{2}\rvert < \pi/2$	0.64	136.7 ± 24.2	212.6 ± 37.6
$\lvert\cos(\theta_{J/\psi})\rvert > 0.6$ $\lvert\cos(\theta_{\pi\pi})\rvert > 0.5$ $0 < \lvert\lvert\Delta\Phi - \pi\rvert - \frac{\pi}{2}\rvert < 0.63$	0.96	225.6 ± 29.0	234.4 ± 30.1
$\lvert\cos(\theta_{J/\psi})\rvert > 0.6$ $\lvert\cos(\theta_{\pi\pi})\rvert > 0.5$ $0.63 < \lvert\lvert\Delta\Phi - \pi\rvert - \frac{\pi}{2}\rvert < 1.15$	0.79	227.9 ± 28.2	286.9 ± 35.5
$\lvert\cos(\theta_{J/\psi})\rvert > 0.6$ $\lvert\cos(\theta_{\pi\pi})\rvert > 0.5$ $1.15 < \lvert\lvert\Delta\Phi - \pi\rvert - \frac{\pi}{2}\rvert < \pi/2$	0.64	155.2 ± 25.7	241.5 ± 39.9

Table 3.3: Measured $X(3872)$ yield in each angular interval. The first two columns list the interval boundaries and the relative ratio of the interval volume to a unit interval volume. The measured yield with corresponding error is listed in the third row. The rescaled yield, which is simply determined by dividing by the relative volume, is listed in the last column.

hypothesis	χ^2 (11 d.o.f.)	χ^2 probability
1^{++}	13.23	0.28
1^{--}	35.13	2.4×10^{-4}
2^{+-}	38.91	5.5×10^{-5}
2^{--}	39.82	3.8×10^{-5}
1^{+-}	39.82	3.8×10^{-5}
3^{+-}	39.82	3.8×10^{-5}
3^{--}	41.00	2.4×10^{-5}
2^{++}	43.02	1.1×10^{-5}
0^{-+}	103.59	3.5×10^{-17}
0^{+-}	129.21	$\leq1\times10^{-20}$
0^{++}	163.07	$\leq1\times10^{-20}$

Table 3.4: Results of the three-dimensional angular analysis for the states with known angular distributions. Listed are the state, the obtained χ^2 and the corresponding χ^2 probability for 11 degrees of freedom.

table 3.4. Only the hypothesis with $J^{PC} = 1^{++}$ is able to describe the measured data. It has an acceptable χ^2 of 13.23, which corresponds to a χ^2-probability of $P = 27.8\%$. The hypothesis $J^{PC} = 1^{--}$ already has a probability of less than 1 in 1000 to observe its χ^2 of 35.13. In terms of Gaussian confidence regions, a hypothesis is excluded at $3\,\sigma$ confidence level if the χ^2 value for 11 degrees of freedom is larger than 28.5, and excluded at $5\,\sigma$ confidence level if the χ^2 value is larger than 50.2. All hypotheses except $J^{PC} = 1^{++}$ are thus excluded at the $3\,\sigma$ confidence level, all spin 0 states are excluded by more than $5\,\sigma$. It can also be observed that the hypotheses $J^{PC} = 1^{+-}$, $J^{PC} = 2^{--}$, and $J^{PC} = 3^{+-}$ have the same χ^2 values. This is not accidental, since their angular distributions are identical.

Treatment of the Hypotheses $J^{PC} = 1^{-+}$ and $J^{PC} = 2^{-+}$

For the hypotheses $J^{PC} = 1^{-+}$ and $J^{PC} = 2^{-+}$ it is not possible to predict the angular distributions, since at least two coupling terms contribute with unknown relative strength. In case of the $J^{PC} = 1^{-+}$ three different couplings remain, while in case of the $J^{PC} = 2^{-+}$ there are two (see table 3.2 in section 3.1). In this section they will be referred to as S-amplitudes.

In order to evaluate the hypotheses $J^{PC} = 1^{-+}$ and $J^{PC} = 2^{-+}$ as possible assignments for the $X(3872)$, it is no longer possible to perform a comparison to one single predicted distribution. A hypothesis can only be rejected if from the multitude of possible distributions none is able to describe the data.

The matrix element of the two states is formed as the coherent sum of the contribut-

ing S-amplitudes. Their mixing is described by a set of complex coefficients:

$$\begin{aligned}\mathcal{M}(1^{-+}) &= r_0 e^{i\phi_0}\mathcal{M}(1^{-+}_{S=0})\\ &+ r_1 e^{i\phi_1}\mathcal{M}(1^{-+}_{S=1})\\ &+ r_2 e^{i\phi_2}\mathcal{M}(1^{-+}_{S=2}),\\ \mathcal{M}(2^{-+}) &= s_1 e^{i\gamma_1}\mathcal{M}(2^{-+}_{S=1})\\ &+ s_2 e^{i\gamma_2}\mathcal{M}(2^{-+}_{S=2})\end{aligned}$$

The indices denote the combined spin of the J/ψ and the $(\pi^+\pi^-)$ system. Since the overall strength and phase of the coupling are irrelevant, only two relative complex coefficients remain for the $J^{PC} = 1^{-+}$ hypothesis. One complex coefficient remains for the $J^{PC} = 2^{-+}$ hypothesis.

As a first step the analysis is performed for the single S-amplitudes of the $J^{PC} = 1^{-+}$ and $J^{PC} = 2^{-+}$ hypotheses. Measurement compatibility with a single configuration will already prevent the firm exclusion of the corresponding J^{PC} state, since in this case already one possibility would have been identified that successfully describes the measured data. The following results are obtained:

hypothesis	χ^2 (11 d.o.f.)	χ^2 probability
$1^{-+}_{S=0}$	163.07	$\leq 1\times10^{-20}$
$1^{-+}_{S=1}$	49.34	8.22×10^{-7}
$1^{-+}_{S=2}$	87.51	5.11×10^{-14}
$2^{-+}_{S=1}$	13.56	0.26
$2^{-+}_{S=2}$	74.39	1.77×10^{-11}

The $S = 1$ configuration of the $J^{PC} = 2^{-+}$ hypothesis already shows good agreement with measured data, whereas no single S-amplitude of the $J^{PC} = 1^{-+}$ hypothesis results in an adequate description. As a consequence, $J^{PC} = 2^{-+}$ already needs to be included in the list of possible assignments for the $X(3872)$, whereas the situation is not yet determined for the $J^{PC} = 1^{-+}$ hypothesis.

The next step in the analysis of the $J^{PC} = 1^{-+}$ state is a scan of various possibilities of mixing parameters. As a first set, the scenario is investigated where only two of the three S-amplitudes contribute. The following values are used in the scan:

1. neglect $1^{-+}_{S=2}$: $r_2 = 0$
   $r_0 = 1$, $\phi_0 = 0$
   $r_1 = \sqrt{\frac{1}{100}}, \sqrt{\frac{1}{50}}, \sqrt{\frac{1}{30}}, \sqrt{\frac{1}{10}}, \sqrt{\frac{1}{9}}, \sqrt{\frac{1}{8}}, \sqrt{\frac{1}{7}}, \sqrt{\frac{1}{6}}, \sqrt{\frac{1}{5}}, \sqrt{\frac{1}{4}}, \sqrt{\frac{1}{3}}, \sqrt{\frac{1}{2}},$
   $1, \sqrt{2}, \sqrt{3}, \sqrt{4}, \sqrt{5}, \sqrt{6}, \sqrt{7}, \sqrt{8}, \sqrt{9}, \sqrt{10}, \sqrt{30}, \sqrt{50}, \sqrt{100}$
   $\phi_1 = 0, \frac{\pi}{8}, \frac{2\pi}{8}, \frac{3\pi}{8}, \frac{4\pi}{8}, \frac{5\pi}{8}, \frac{6\pi}{8}, \frac{7\pi}{8}, \pi$

2. neglect $1^{-+}_{S=1}$: $r_1 = 0$
   $r_0 = 1$, $\phi_0 = 0$
   r_2 and ϕ_2 analogous to first case

3. neglect $1^{-+}_{S=0}$: $r_0 = 0$
   $r_1 = 1$, $\phi_1 = 0$
   r_2 and ϕ_2 analogous to first case

The second set of scans investigates a 4-dimensional grid, allowing mixing between all contributing S-amplitudes. The following mixing values are investigated:

- $r_0 = 1$, $\phi_0 = 0$:
  $r_1 = \sqrt{\frac{1}{4}}, \sqrt{\frac{1}{2}}, 1, \sqrt{2}, \sqrt{4}$
  $r_2 = \sqrt{\frac{1}{4}}, \sqrt{\frac{1}{2}}, 1, \sqrt{2}, \sqrt{4}$
  $\phi_1 = 0, \pi/2, \pi, 3\pi/2$
  $\phi_2 = 0, \pi/2, \pi, 3\pi/2$

The final set uses the best single amplitude with $S = 1$ as base configuration, and it is investigated whether small contributions from the two remaining S-amplitudes lead to improvements. This set employs the values:

- $r_1 = 1$, $\phi_1 = 0$:
  $r_0 = \sqrt{\frac{1}{200}}, \sqrt{\frac{1}{100}}, \sqrt{\frac{1}{50}}$
  $r_1 = \sqrt{\frac{1}{200}}, \sqrt{\frac{1}{100}}, \sqrt{\frac{1}{50}}$
  $\phi_0 = \pi/4, 2\pi/4, 3\pi/4, 4\pi/4, 5\pi/4, 6\pi/4, 7\pi/4$
  $\phi_2 = \pi/4, 2\pi/4, 3\pi/4, 4\pi/4, 5\pi/4, 6\pi/4, 7\pi/4$

As a result of all scans it is found that the best combinations have a χ^2 of ≈ 47, which is slightly better than the best single amplitude. Their χ^2 probabilities are however still of the order of 10^{-5}, excluded at almost $5\,\sigma$ confidence level. The best value is obtained for the case where small admixtures of the $S = 0$ and $S = 2$ amplitudes are added to a dominant $S = 1$ amplitude.

In addition to selecting the coefficients from a fixed grid, a further determination approach was performed with a direct fit. This means that the mixing coefficients were used as free parameters in a fit, which minimizes the χ^2 of the resulting $J^{PC} = 1^{-+}$ state. Since the four-dimensional parameter-space has many local minima due to the periodic structure of the phases, it is not expected to find a global minimum with an arbitrary set of starting values. As a consequence, the fit is performed with multiple different sets of starting values which yielded the best values in the previously performed scan. As a result of the procedure, the best χ^2 value is found to be $\chi^2 = 45.4$, with the following set of parameters: $r_0 = -0.196, \phi_0 = 1.92$; $r_1 = 1.0, \phi_1 = 0.0$, $r_2 = 0.20, \phi_2 = 1.9$. While it cannot be completely ruled out that the global minimum is different, it is very improbable that this minimum is both small enough to be a good candidate *and* that a true $X(3872)$ with $J^{PC} = 1^{-+}$ would be realized in such configuration.

From this point on, the $J^{PC} = 1^{-+}$ configuration with the best obtained χ^2 value will be simply referenced as $J^{PC} = 1^{-+}$. From the χ^2 of 45.4 it is concluded that the $J^{PC} = 1^{-+}$ hypothesis is not compatible with data.

hypothesis	χ^2 (11 d.o.f.)	χ^2 probability
1^{++}	13.23	0.28
2^{-+}	13.56	0.26
1^{--}	35.13	2.4×10^{-4}
2^{+-}	38.91	5.49×10^{-5}
2^{--}	39.82	3.84×10^{-5}
1^{+-}	39.82	3.84×10^{-5}
3^{+-}	39.82	3.84×10^{-5}
3^{--}	41.00	2.41×10^{-5}
2^{++}	43.02	1.08×10^{-5}
1^{-+}	45.40	4.13×10^{-6}
0^{-+}	103.59	3.46×10^{-17}
0^{+-}	129.21	$\leq1\times10^{-20}$
0^{++}	163.07	$\leq1\times10^{-20}$

Table 3.5: Results of the three-dimensional angular analysis including all tested hypotheses. Listed are the J^{PC} hypothesis, the obtained χ^2 and the corresponding χ^2 probability for 11 degrees of freedom.

Furthermore, a similar scan has been performed for the already accepted $J^{PC} = 2^{-+}$ state to study the effect of a an admixture of the 'bad' $S = 2$ amplitude to the $S = 1$ amplitude. The aim is to investigate whether only the very particular choice of the $S = 1$ amplitude is able to describe the data. This would make the $J^{PC} = 2^{-+}$ hypothesis weaker, since there is *a priori* no good reason why the $J^{PC} = 2^{-+}$ state should in nature be realized as a single amplitude. Performing a similar fit/scan procedure as for the $J^{PC} = 1^{-+}$ hypothesis, it is found that even a $1 : 1$ mixing of both amplitudes is able to describe the data on a 1% to 5% level. Hence it can be concluded that besides a pure $S = 1$ $J^{PC} = 2^{-+}$ state also a mixture of both amplitudes is a valid $X(3872)$ candidate. However, no admixture is found which would sizably improve the $J^{PC} = 2^{-+}$ χ^2 probability compared to the pure $S = 1$ amplitude. For this reason $J^{PC} = 2^{-+}$ will from this point on only be used to reference to the pure $S = 1$ amplitude.

As a final result, all considered states are listed together in table 3.5. A graphical representation of the measured data distribution and the predicted distributions is shown in figure 3.17. Shown are the measured data points, rescaled to unit interval volume, and the predicted distributions for various hypotheses: the two best hypotheses $J^{PC} = 1^{++}$ and $J^{PC} = 2^{-+}$, as well as the third best ($J^{PC} = 1^{--}$) and the worst hypothesis ($J^{PC} = 0^{++}$). A graphical representation for each hypothesis can be found in Appendix A.3.

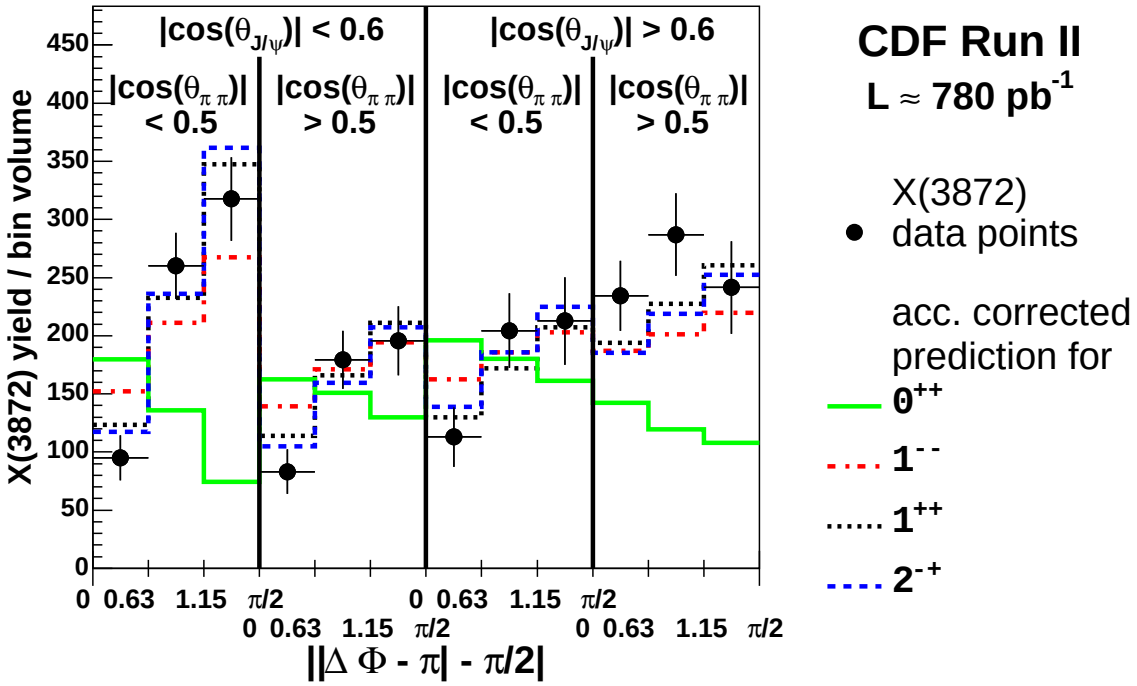

Figure 3.17: Result of the three-dimensional angular correlation analysis. The measured data points are shown together with the predictions computed for four different hypotheses.

3.5 Systematic Uncertainties

In this section possible sources of uncertainty in the determination of the quantum number results are investigated. Multiple cross-checks have been performed to check the stability of the result. Most importantly, each check must not endanger the main conclusion of the analysis — that only $J^{PC} = 1^{++}$ and $J^{PC} = 2^{-+}$ can describe the measured data.

3.5.1 Determination of the Quantum Numbers J^{PC} of the $\psi(2S)$

The most important cross-check is the verification of the method on a known state. In this case, can the procedure designed to determine the unknown quantum numbers of the $X(3872)$ correctly determine the known quantum numbers of the $\psi(2S)$? This state is well suited to cross-check the analysis method, since it decays into the same final state $J/\psi\pi^+\pi^-$. The analysis is performed similarly. A slight change is introduced by adjusting the $\psi(2S)$ fit model for each single fit. This will be detailed in section 3.5.5. All settings that were optimized for the $X(3872)$ analysis like the binning or the cut selection remain unchanged, in order to keep the measurement method as close as possible to the method in the $X(3872)$ measurement.

It is not the aim of this cross-check to 'tune' the procedure to obtain perfectly

hypothesis	χ^2 (11 d.o.f.)	χ^2 probability
$1^{--}_{Novikov}$	15.07	0.18
1^{--}	23.50	0.02
2^{++}	26.33	0.01
2^{+-}	47.35	1.87×10^{-6}
3^{--}	70.15	1.15×10^{-10}
1^{++}	399.54	$\leq1\times10^{-20}$
3^{+-}	504.81	$\leq1\times10^{-20}$
2^{--}	504.81	$\leq1\times10^{-20}$
1^{+-}	504.81	$\leq1\times10^{-20}$
2^{-+}	505.12	$\leq1\times10^{-20}$
1^{-+}	516.49	$\leq1\times10^{-20}$
0^{++}	1500.33	$\leq1\times10^{-20}$
0^{+-}	1847.01	$\leq1\times10^{-20}$
0^{-+}	3169.17	$\leq1\times10^{-20}$

Table 3.6: Results of the three-dimensional angular analysis for the $\psi(2S)$. Listed are the J^{PC} hypothesis, the obtained χ^2 and the corresponding χ^2 probability for 11 degrees of freedom.

acceptable values, since this would endanger the generalized applicability of the method to an unknown state. The point of interest is rather, whether the correct quantum numbers are favored over wrong ones. In addition, the correct quantum numbers also need to be compatible with the data measurement.

Table 3.6 lists the results of the comparison for the $\psi(2S)$. The true quantum numbers, $J^{PC} = 1^{--}$, are the favored quantum numbers of the 'generic' hypotheses. Only the dedicated $\psi(2S)$ model by Novikov and Shifman, introduced in section 3.1, naturally obtains a better result. From the remaining J^{PC} hypotheses only $J^{PC} = 2^{++}$ shows a similar agreement to data, all others have probabilities smaller than 10^{-5}.

The χ^2 probability of the generic $J^{PC} = 1^{--}$ hypothesis is of the order of 1% — in view of the generality of the underlying model and possible mismodelling effects in the simulation, this is a very good result. It is illustrated in figure 3.18. One can nicely see both the good agreement of the $\psi(2S)$ measurement with the prediction, as well as the closeness of the generic $J^{PC} = 1^{--}$ hypothesis to the dedicated model. The figure also impressively demonstrates the sensitivity of the χ^2 to small changes in the predictions at high statistics. With the uncertainties from the $X(3872)$ measurement there would have barely been a difference in the χ^2 values for the best hypotheses. As well shown in the comparison is the $J^{PC} = 1^{++}$ hypothesis that yielded the best result in the $X(3872)$ comparison. It clearly is not able to describe the measured data in case of the $\psi(2S)$.

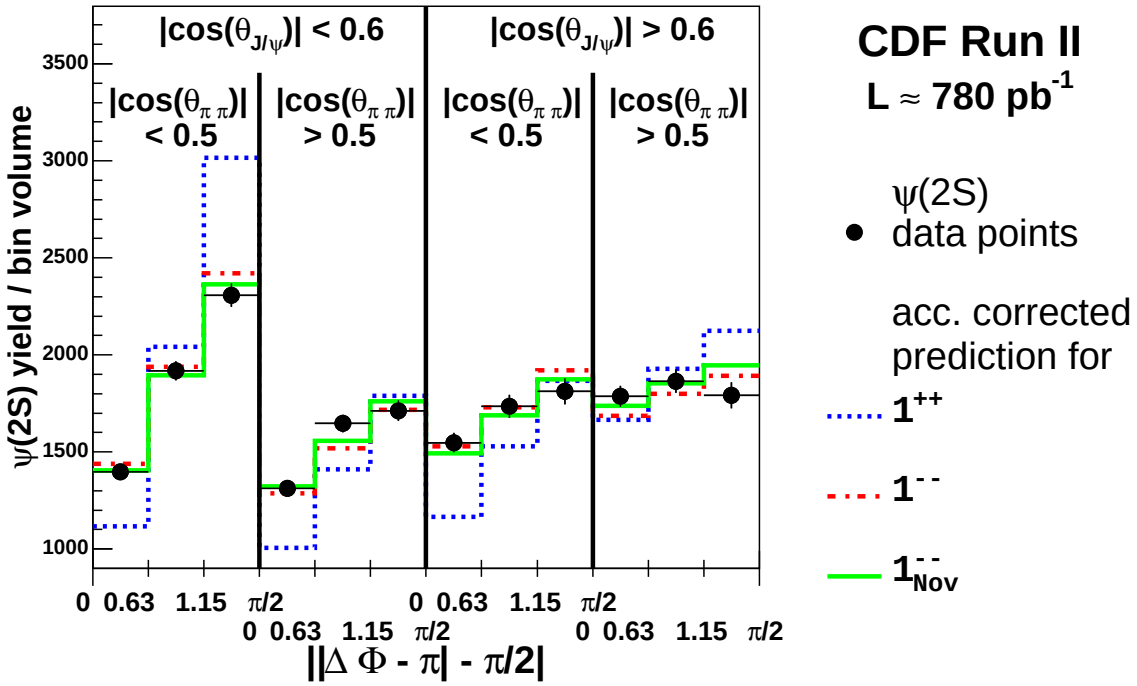

Figure 3.18: Result of the three-dimensional angular analysis for the $\psi(2S)$. The measured data points are shown together with the predictions computed for three different hypotheses.

3.5.2 Selection Effects

The obtained result must not depend on the particular selection of the data sample. This section checks the stability of the result at different signal selection working points.

As a first check, four different working points are selected in addition to the 'default' analysis working point. These four working points need to have high statistical significance as well, since otherwise any comparison would be dominated by the difference in effective statistics. For the resulting five working points, the mean χ^2 values and the variation in χ^2 is determined.

The following five working points are used:

- $Q < 0.10\,\mathrm{GeV}/c^2$, $p_{T,X} > 6.00\,\mathrm{GeV}/c$, $p_{T,J/\psi} > 4.00\,\mathrm{GeV}/c$, $nCand < 5$ with significance 23.4,
- $Q < 0.09\,\mathrm{GeV}/c^2$, $p_{T,X} > 6.00\,\mathrm{GeV}/c$, $p_{T,J/\psi} > 4.25\,\mathrm{GeV}/c$, $nCand < 6$ with significance 23.3,
- $Q < 0.11\,\mathrm{GeV}/c^2$, $p_{T,X} > 7.00\,\mathrm{GeV}/c$, $p_{T,J/\psi} > 4.50\,\mathrm{GeV}/c$, $nCand < 5$ with significance 23.0,
- $Q < 0.10\,\mathrm{GeV}/c^2$, $p_{T,X} > 6.25\,\mathrm{GeV}/c$, $p_{T,J/\psi} > 4.75\,\mathrm{GeV}/c$, $nCand < 8$ with significance 23.1,

hypothesis	average χ^2 (11 d.o.f.)	χ^2 probability
1^{++}	14.94 ± 1.92	0.19
2^{-+}	15.58 ± 1.85	0.16
1^{--}	35.20 ± 4.04	2.3×10^{-4}
2^{--}	35.35 ± 5.69	2.2×10^{-4}
1^{+-}	35.35 ± 5.69	2.2×10^{-4}
3^{+-}	35.35 ± 5.69	2.2×10^{-4}
2^{+-}	39.74 ± 3.98	4.0×10^{-5}
3^{--}	42.14 ± 3.98	1.5×10^{-5}
2^{++}	42.59 ± 4.62	1.3×10^{-5}
1^{-+}	45.18 ± 3.39	4.5×10^{-6}
0^{-+}	104.86 ± 2.50	1.9×10^{-17}
0^{+-}	133.63 ± 5.61	$\leq1\times10^{-20}$
0^{++}	155.59 ± 11.26	$\leq1\times10^{-20}$

Table 3.7: Cross-check of the three-dimensional angular analysis for different working points. Listed are the single J^{PC} hypothesis, the average χ^2 with standard deviation, and the corresponding χ^2 probability for 11 degrees of freedom.

- $Q < 0.12\,\mathrm{GeV}/c^2$, $p_{T,X} > 6.25\,\mathrm{GeV}/c$, $p_{T,J/\psi} > 4.50\,\mathrm{GeV}/c$, $nCand < 6$ with significance 22.9.

The χ^2 results of the different working points are shown in table 3.7. Besides a statistical spread no effect is observed.

As a second check, the impact of a different cut selection is studied by individually varying the cuts on the single cut variables, while the rest of the selection cuts remains fixed. The final selection variables Q, $p_{T,X}$, $p_{T,J/\psi}$ and $nCand$ are varied, as shown in figure 3.19. While the variation of the Q-value shows some structure, the interpretation concerning the question, which hypotheses are acceptable or not, stays consistent. The hypotheses $J^{PC} = 1^{++}$ and $J^{PC} = 2^{-+}$ always stay below the value of $\chi^2 = 28.5$ (corresponding to $3\,\sigma$), while all other hypotheses always stay above.

3.5.3 $X(3872)$ Polarization Effects

In the construction of the matrix elements the $X(3872)$ was assumed to be unpolarized. This is a reasonable assumption for prompt production, where the $X(3872)$ is produced as a fragmentation product. This is different from the $X(3872)$ production in B-decays at Belle and *BABAR*: In the observed decay mode $B^+ \to K^+X(3872)$, both the K^+ and the B^+ have spin 0, only allowing the $X(3872)$ to have spin projection $\lambda_X = 0$.

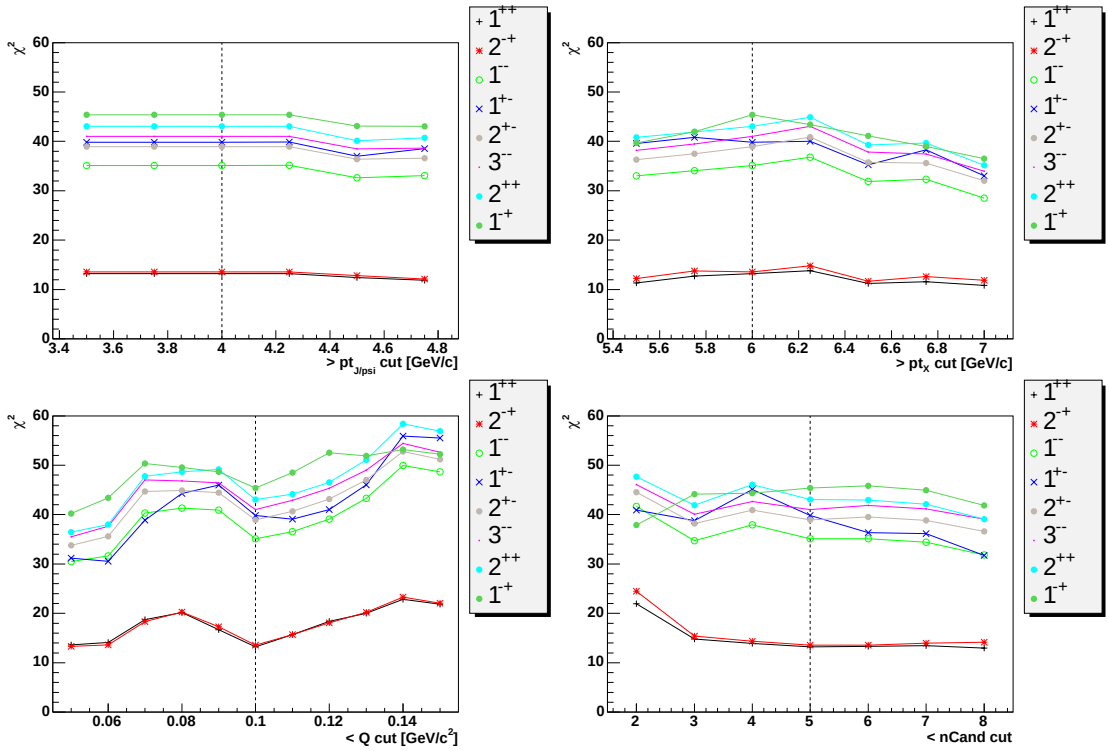

Figure 3.19: χ^2 for cut variations of single variables. Shown are the resulting χ^2-values for the J^{PC} hypotheses with χ^2 values below 60.

Polarized states are experimentally nice for angular distribution studies, if the polarization is known. The reason is that polarized states have a unique spin configuration in the initial state, compared to the unpolarized scenario where all spin configurations are possible and have to be averaged over. Polarization thus leads to an additional discriminating variable, in the case of the $X(3872)$ decay this is the helicity angle θ_X. In the 'default' unpolarized case, the sum over all polarizations leads to a uniform distribution of this angle, since the sum over a set of squared Wigner functions equals one:

$$\sum_{\lambda_X} |d^J_{\lambda_X,\lambda}(\theta_X)|^2 = 1,$$

for any value of λ. In the polarized case, where the sum is either weighted or incomplete, this is no longer the case, so that a net dependence on θ_X may result.

Polarization of the $X(3872)$ does mathematically not change the integrated angular dependence of any angles other than θ_X. However, as explained in section 3.3, acceptance effects induces correlations between the remaining helicity angles and θ_X. This leads to the fact, that, because of the change of behavior of θ_X, also other decay angles might change shape.

Those two facts allow to determine the possibility of changes in the result due to polarization effects. Any significant change of the analyzed angular distributions

J^{PC}	unpolarized	P 01	P 10
1^{++}	13.23 ✓	16.79 ✓	11.82 ✓
1^{-+}	45.40 ✓	47.36 ×	45.26 ✓
1^{+-}	39.82 ✓	37.31 ×	65.80 ×
1^{--}	35.13 ✓	37.36 ✓	32.03 ✓

J^{PC}	unpolarized	P 001	P 010	P 100	P 011	P 110	P 101
2^{++}	43.02 ✓	39.06 ✓	44.18 ✓	52.27 ✓	41.04 ✓	46.66 ✓	42.30 ✓
2^{-+}	13.56 ✓	11.75 ✓	14.98 ✓	15.79 ✓	12.48 ✓	16.72 ×	12.71 ✓
2^{+-}	38.91 ✓	32.36 ×	49.78 ×	73.73 ×	34.29 ✓	56.93 ×	34.07 ✓
2^{--}	39.82 ✓	44.71 ×	37.35 ×	54.18 ×	37.89 ×	41.97 ×	43.87 ×

J^{PC}	unpolarized	P 0001	P 0010	P 0100	P 1000	P 0011	P 0101	P 1001
3^{+-}	39.82 ✓	55.23 ×	40.25 ✓	43.82 ×	50.71 ×	43.88 ×	39.42 ×	45.34 ×
3^{--}	41.00 ✓	34.61 ×	42.63 ×	67.58 ×	82.19 ×	32.48 ×	34.90 ×	30.79 ×
J^{PC}	unpolarized	P 0110	P 1010	P 1100	P 0111	P 1011	P 1101	P 1110
3^{+-}	39.82 ✓	40.52 ×	42.20 ×	45.93 ×	39.42 ✓	42.10 ×	39.62 ✓	42.14 ×
3^{--}	41.00 ✓	52.80 ×	51.80 ×	72.16 ×	37.30 ✓	34.81 ✓	40.29 ×	57.58 ×

Table 3.8: Effect of polarized X decay on the χ^2. The listed polarization cases 'P' represent the spin 0,1,2,3 component set to 0 or to 1. In addition a ✓ indicates, whether the considered state has an acceptable χ^2 in $\cos(\theta_X)$ smaller than 20 for 11 degrees of freedom.

for a given state can only enter by acceptance effects via θ_X. In this case however, also the shape of $\cos(\theta_X)$ would have to be significantly different from the 'default' analysis. So by checking the agreement of both $\cos(\theta_X)$ and the usual decay angular distributions, a possible polarization effect can be evaluated.

To quantitatively give results for polarized assumptions, each polarizable state is assumed in all possible completely polarized conditions. Spin 2 and spin 3 states are assumed in all 'binary' possibilities of their contributing spin projection components. This notation e.g. denotes (1000) when only amplitudes with $\lambda_X = 0$ contribute, (0010) for contributions from only $\lambda_X = \pm 2$, or (0101) for contributions from only $\lambda_X = \pm 1$ and $\lambda_X = \pm 3$. For each polarization assumption a χ^2 is calculated for the three-dimensional angular distributions. In addition, the distribution of $\cos(\theta_X)$ is compared to the measured distribution in 12 equidistant intervals from -1 to 1. In contrast to the so far analyzed decay angles, no symmetry can be exploited. The angular distribution becomes heavily asymmetric due to acceptance effects, as explained in section 3.3.

Table 3.8 shows the results of the polarization study. Listed are the obtained χ^2 values for different polarizations. In addition a tick mark ✓ indicates, whether the $\cos(\theta_X)$ distribution agrees with data. Good agreement in $\cos(\theta_X)$ is defined as

having a χ^2 lower than 20, corresponding to 2σ at 11 degrees of freedom. It can be deduced from the table that even without the additional requirement of $\cos(\theta_X)$ the result does not change. $J^{PC} = 1^{++}$ and $J^{PC} = 2^{-+}$ always remain good candidates, while all other hypotheses always stay excluded at the $3\,\sigma$ level. In addition, big changes in the three-dimensional χ^2 to the value from the unpolarized χ^2 prediction are accompanied by a disagreement in $\cos(\theta_X)$.

It can be concluded that even strong polarization would not change the result. Furthermore, any polarization leading to a potential big change in the three-dimensional χ^2 is disfavored by the resulting disagreement with the measured $\cos(\theta_X)$ distribution.

3.5.4 Further Cross-Checks

This section contains a variety of further cross-checks. A description and numbering of the different tests is followed by an overview table of the results.

In order to check for the correctness of the simple simulation of the J/ψ trigger, two checks are performed. If not successful, it would indicate that a more detailed simulation of the muon chambers and the triggers is needed. In the first check ('Check 1') only those J/ψ are used, where both muons were detected in the central muon chambers CMU and CMP. This excludes the candidates, where one of the muons was detected by the CMX muon system. The CMX is excluded by requiring a pseudorapidity of $|\eta|$ smaller than 0.6. The J/ψ trigger incorporates various possibilities to trigger a J/ψ, so-called 'trigger paths', which have different requirements for the properties of a dimuon system. Those paths have different p_T-thresholds for the muons, with the most important 'step' at 2.0 GeV/c. In order to test a possible mismodelling of the simulation, all events with muon transverse momentum $p_T < 2.0\,\mathrm{GeV}/c$ are rejected ('Check 2').

In 'Check 3' and 'Check 4' the consistency between the data taken before and after the Tevatron shutdown in August 2004 (datasets `jpmm0d` and `jpmm0h`) is investigated. The experimental apparatus does not perform identically over time, but changes its performance with e.g. trigger changes, luminosity improvements, or detector aging. It may therefore be possible, that some aspects of the simulation, which were valid for a certain point in time, are not valid anymore later. Since the two datasets are approximately the same in size, each check only has half the statistical power.

At the Tevatron the $X(3872)$ is predominantly produced as a fragmentation product. A small fraction however also originates from B decays. An effect on the analysis is investigated by further suppressing the amount of candidates from B decays. This is achieved by cutting on low values of the variable ct, since B mesons have a long average lifetime. Checks number 5 and 6 require ct to be less than $250\,\mu m$ and less than $100\,\mu m$, respectively.

Finally, 'Check 7' represents an alternative to the non-equidistant three-dimensional binning by simply using equidistant intervals in the three-dimensional angular space.

The results of the checks 1–7 are listed in table 3.9. It can be seen that in nearly all cases the excluded assignments become better, simply because most checks significantly reduce the statistical power of the test. The general behavior is however identical in each check — $J^{PC} = 1^{++}$ and $J^{PC} = 2^{-+}$ always are the best hypotheses, better by at least an order of magnitude in probability. All cross-checks thus are successful.

3.5.5 Measurement and Simulation Effects

This section investigates influences from the data measurement method and effects of the simulation.

The data points are extracted from the sample by the 'slicing method'. For each data point a corresponding histogram of the $J/\psi\pi^+\pi^-$ mass spectrum is fitted using a binned likelihood fit. The fit uses a fixed signal shape for the determination of the yield in each angular interval. It may however be, that because of detector effects, the mass or the width shows a dependence on the angular distribution, and with that on the angular bins. This effect is investigated by studying the mass and the width of the $X(3872)$ in each angular variable separately. They are determined in each angular bin by a fit to the invariant $J/\psi\pi^+\pi^-$ mass, where either the mass or the width is not fixed, but left as a free parameter to be determined. Figures 3.20 and 3.21 show the fitted values for width and position in the $X(3872)$ case. All distributions are well compatible with a constant behavior.

The check is also performed on the $\psi(2S)$. Figures 3.22 and 3.23 illustrate the behavior of the position and the width of the narrow part of the signal (The signal is parameterized by two Gaussian functions with common mean, unlike the $X(3872)$ which only uses one Gaussian function). Here a dependence is observed in the helicity angle of the dimuon system, which is parameterized as

$$\sigma(|\cos(\theta_{J/\psi})|) = 2.65\,\mathrm{MeV}/c^2 + 0.34\,\mathrm{MeV}/c^2\,|\cos(\theta_{J/\psi})|^2.$$

Because of this effect, all $\psi(2S)$ fits which determine angular distributions based on intervals in $|\cos(\theta_{J/\psi})|$ use $\psi(2S)$ widths according to above dependence by default. The effect of neglecting this dependence in the J^{PC} comparisons is small. Completely fixing the width as constant in the fit function results in the same χ^2 of 15.07 for the Novikov model and a slightly worse χ^2 of 24.35 (instead of 23.50) for $J^{PC} = 1^{--}$. Besides the small dependence on $|\cos(\theta_{J/\psi})|$, no other dependences are found for the $\psi(2S)$.

A systematic source of uncertainty might be introduced by the particular selection of the parameters used in the extraction of the signal distribution. This concerns the histogram binning of the $J/\psi\pi^+\pi^-$ mass spectrum and the fit model properties. The effects of the choice of these parameters are investigated by applying numerous variations. In order to reference to the variations they are numbered, where number 1 references the default analysis.

2. Change the size of the fit window to $\pm 90\,\mathrm{MeV}/c^2$ (default $\pm 110\,\mathrm{MeV}/c^2$).

	Analysis		Check 1		Check 2		Check 3	
J^{PC}	χ^2	probability	χ^2	probability	χ^2	probability	χ^2	probability
1^{++}	13.2	0.28	14.9	0.19	12.9	0.30	18.9	0.06
2^{-+}	13.6	0.26	14.7	0.20	14.5	0.21	19.7	0.05
1^{--}	35.1	2.4×10^{-4}	25.2	0.01	32.8	5.6×10^{-4}	27.2	4.3×10^{-3}
2^{+-}	38.9	5.5×10^{-5}	27.7	3.5×10^{-3}	35.6	2.0×10^{-4}	27.7	3.6×10^{-3}
2^{--}	39.8	3.8×10^{-5}	26.9	4.8×10^{-3}	38.7	5.9×10^{-5}	34.0	3.2×10^{-4}
1^{+-}	39.8	3.8×10^{-5}	26.9	4.8×10^{-3}	38.7	5.9×10^{-5}	34.0	3.2×10^{-4}
3^{+-}	39.8	3.8×10^{-5}	26.9	4.8×10^{-3}	38.7	5.9×10^{-5}	33.0	3.2×10^{-4}
3^{--}	41.0	2.4×10^{-5}	29.2	2.1×10^{-3}	37.1	1.1×10^{-4}	28.1	3.2×10^{-3}
2^{++}	43.0	1.1×10^{-5}	29.3	2.0×10^{-3}	39.8	3.8×10^{-5}	30.2	1.5×10^{-3}
1^{-+}	45.4	4.1×10^{-6}	34.8	2.7×10^{-4}	35.1	2.4×10^{-4}	27.6	3.8×10^{-3}
0^{-+}	103.6	3.5×10^{-17}	67.5	3.7×10^{-10}	99.9	1.8×10^{-16}	59.1	1.3×10^{-8}
0^{+-}	129.2	$\leq1\times10^{-20}$	86.3	9.0×10^{-14}	108.2	4.1×10^{-18}	55.5	6.3×10^{-8}
0^{++}	163.1	$\leq1\times10^{-20}$	97.5	5.7×10^{-16}	145.8	$\leq1\times10^{-20}$	76.7	6.5×10^{-12}

	Check 4		Check 5		Check 6		Check 7	
J^{PC}	χ^2	probability	χ^2	probability	χ^2	probability	χ^2	probability
1^{++}	11.1	0.44	13.4	0.27	15.3	0.17	14.6	0.20
2^{-+}	10.8	0.46	15.2	0.17	17.0	0.11	15.7	0.15
1^{--}	24.1	0.01	31.0	1.1×10^{-3}	29.6	1.9×10^{-3}	34.7	3.1×10^{-4}
2^{+-}	27.3	4.2×10^{-3}	34.8	2.6×10^{-4}	33.2	4.8×10^{-4}	38.2	7.3×10^{-5}
2^{--}	22.6	0.02	33.4	4.6×10^{-4}	31.3	9.8×10^{-4}	39.4	4.6×10^{-5}
1^{+-}	22.6	0.02	33.4	4.6×10^{-4}	31.3	9.8×10^{-4}	39.4	4.6×10^{-5}
3^{+-}	22.6	0.02	33.4	4.6×10^{-4}	31.3	9.8×10^{-4}	39.4	4.6×10^{-5}
3^{--}	28.9	2.4×10^{-3}	36.9	1.2×10^{-4}	35.2	2.3×10^{-4}	40.1	3.5×10^{-5}
2^{++}	28.8	2.4×10^{-3}	37.7	8.9×10^{-5}	35.4	2.1×10^{-4}	42.2	1.5×10^{-5}
1^{-+}	33.7	4.0×10^{-4}	36.3	1.5×10^{-4}	35.2	2.3×10^{-3}	42.9	1.1×10^{-5}
0^{-+}	61.3	5.4×10^{-9}	107.9	4.8×10^{-18}	102.7	5.3×10^{-17}	108.9	3.0×10^{-18}
0^{+-}	87.8	4.5×10^{-14}	120.2	$\leq1\times10^{-20}$	113.0	4.3×10^{-19}	122.1	$\leq1\times10^{-20}$
0^{++}	100.7	1.3×10^{-16}	143.2	$\leq1\times10^{-20}$	130.7	$\leq1\times10^{-20}$	158.2	$\leq1\times10^{-20}$

Table 3.9: Results of the performed cross checks. Listed are the hypothesis, the obtained χ^2 and the corresponding χ^2 probability for 11 degrees of freedom. The 'default' result is given as reference. The cross-check definitions are explained in the text.

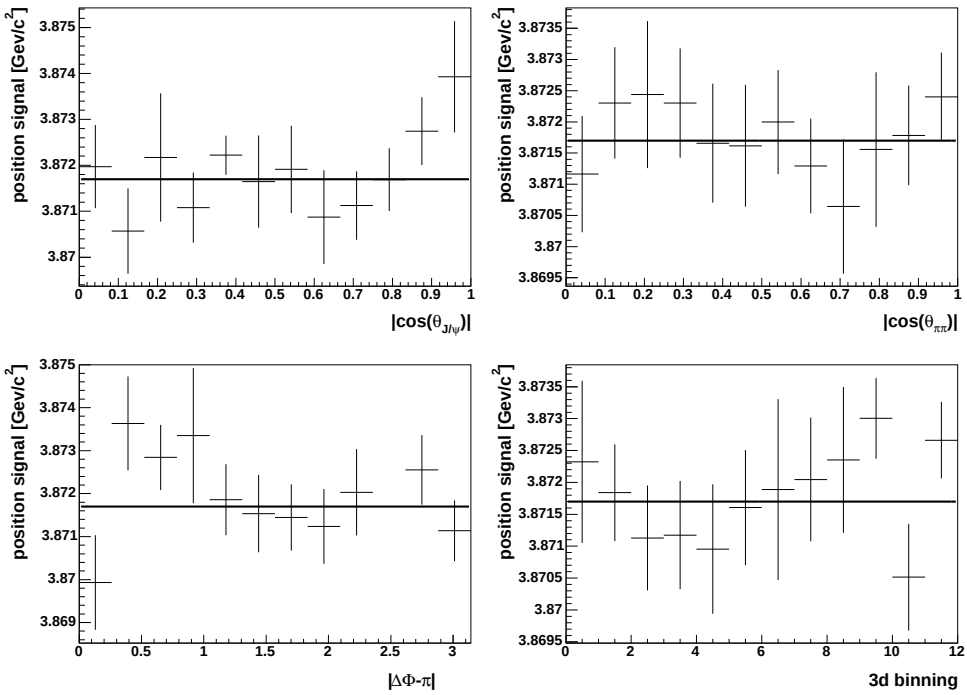

Figure 3.20: Dependence of the $X(3872)$ mass on the decay angles. Every distribution is compatible with a mean of 3.8717 GeV/c^2. In the 10th bin of the $\Delta\Phi$ plot, the fit latches onto a statistical fluctuation at $m = 3.9$ GeV/c^2 and does not return a meaningful value.

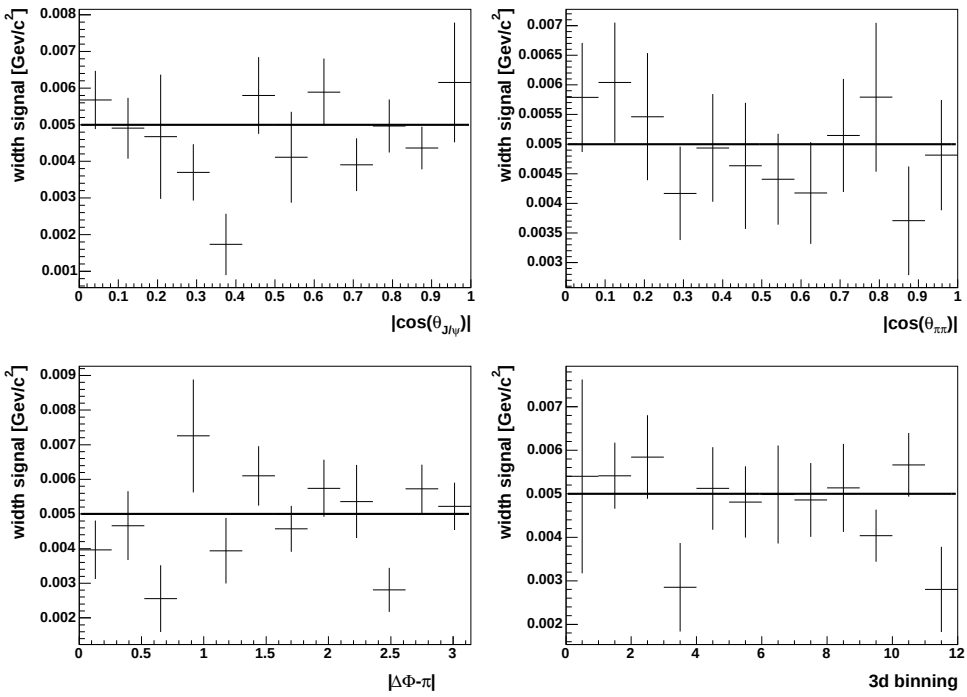

Figure 3.21: Dependence of the $X(3872)$ width on the decay angles. Every distribution is compatible with a mean of 5.0 MeV/c^2.

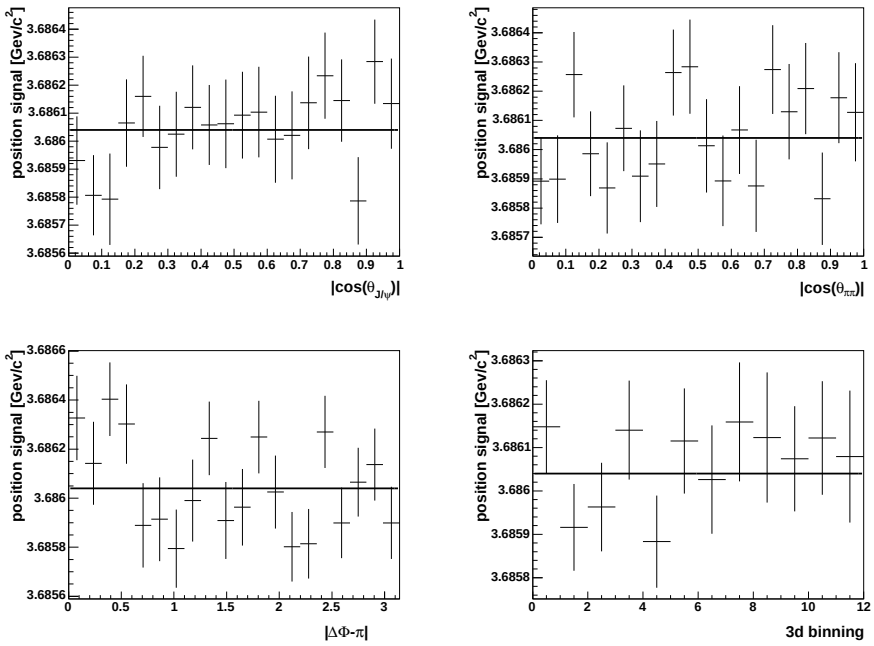

Figure 3.22: Dependence of the $\psi(2S)$ position on the decay angles. Every distribution is compatible with a mean of 3.68604 GeV/c^2.

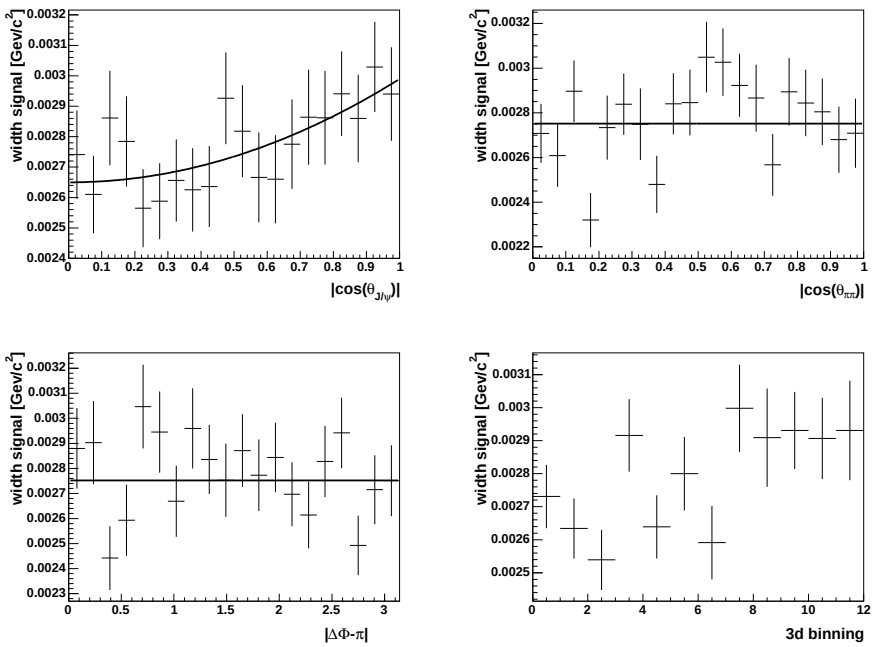

Figure 3.23: Dependence of the $\psi(2S)$ width on the decay angles. The dependence in $\cos(\theta_{J/\psi})$ is fitted by $\sigma(|\cos(\theta_{J/\psi})|) = 2.65\,\mathrm{MeV}/c^2 + 0.34\,\mathrm{MeV}/c^2\,|\cos(\theta_{J/\psi})|^2$. The other widths are compatible with a mean of 2.752 MeV/c^2.

3. Change the size of the fit window to $\pm 130\,\mathrm{MeV}/c^2$ (default $\pm 110\,\mathrm{MeV}/c^2$).
4. Change the histogram bin width to $2.86\,\mathrm{MeV}/c^2$ (default $2.5\,\mathrm{MeV}/c^2$).
5. Change the histogram bin width to $2.00\,\mathrm{MeV}/c^2$ (default $2.5\,\mathrm{MeV}/c^2$).
6. Vary fixed $X(3872)$ mass by $+1\sigma$ to $3.8720\,\mathrm{GeV}/c^2$ (default $3.8717\,\mathrm{GeV}/c^2$).
7. Vary fixed $X(3872)$ mass by -1σ to $3.8714\,\mathrm{GeV}/c^2$ (default $3.8717\,\mathrm{GeV}/c^2$).
8. Vary fixed $X(3872)$ width by $+1\sigma$ to $5.3\,\mathrm{MeV}/c^2$ (default $5.0\,\mathrm{MeV}/c^2$).
9. Vary fixed $X(3872)$ width by -1σ to $4.7\,\mathrm{MeV}/c^2$ (default $5.0\,\mathrm{MeV}/c^2$).

In the simulation of the matrix element all terms that affect the distribution of the dipion mass are fixed to a model supposed to describe the $X(3872)$ dipion mass distribution. This particular description consists of using the shape of a ρ in relative orbital angular momentum $L = 0$ with the J/ψ and using a formfactor radius of $r_{\pi\pi} = 1$ fm. Although direct correlations to the angular distributions do not exist, detector acceptance might be responsible for indirect effects. A possible influence on the angular distributions is checked by the very drastic changes of

10. fixing the formfactor radius $r_{\pi\pi}$ to 0.001 fm (default 1 fm),
11. fixing the formfactor radius $r_{\pi\pi}$ to 100.0 fm (default 1 fm),
12. using a simple phase space behavior for the dipion mass shape, instead of a resonance structure.

The simulation of the $X(3872)$ events proofs to be quite successful with a simple model as shown in section 3.3. The behavior of p_T and η is however only confirmed within a relatively large statistical uncertainty. The following checks were performed to investigate dependences under simulation changes:

13. The reweighting in $p_{T,X}$, introduced to achieve better agreement with the $\psi(2S)$, is not applied.
14. The reweighting in $|\eta_X|$, introduced to achieve better agreement with the $\psi(2S)$, is not applied.
15. The pion efficiency as a function of $p_{T,\pi}$ is not applied.
16. The COT efficiency as a function of ϕ is not applied.
17. The 'effective' η correction to smear the z-distribution of the interaction point is not applied.

The results of these checks can be found in table 3.10. Figure 3.24 shows a graphical representation of the change in χ^2 for the different variations. All values are well consistent with the results from the regular analysis and do not indicate any systematic effects which could affect the final conclusions.

J^{PC}	default	C2	C3	C4	C5	C6	C6	C8	C9
1^{++}	13.2	13.9	11.0	13.8	12.9	13.1	13.4	13.4	13.4
2^{-+}	13.6	14.5	11.5	14.1	13.0	13.4	13.7	13.7	13.7
1^{--}	35.1	33.9	33.7	37.5	35.4	34.8	35.4	35.6	35.3
2^{+-}	38.9	37.1	37.2	41.0	39.0	38.6	39.2	39.3	39.2
2^{--}	39.8	39.3	40.2	43.1	41.2	39.3	40.3	40.6	40.4
1^{+-}	39.8	39.3	40.2	43.1	41.2	39.3	40.3	40.6	40.4
3^{+-}	39.8	39.3	40.2	43.1	41.2	39.3	40.3	40.6	40.4
3^{--}	41.0	39.0	39.2	43.0	41.0	40.7	41.2	41.4	41.3
2^{++}	43.0	41.1	41.8	45.7	43.4	42.6	43.4	43.5	43.4
1^{-+}	45.4	42.5	43.4	48.5	46.2	45.2	45.5	45.8	45.7
0^{-+}	103.6	99.7	105.0	98.3	101.0	103.4	103.5	103.9	103.8
0^{+-}	129.2	119.0	127.6	128.6	127.3	129.1	128.9	129.7	129.6
0^{++}	163.1	151.6	165.4	166.8	164.0	162.3	163.4	164.4	164.0

J^{PC}	C10	C11	C12	C13	C14	C15	C16	C17
1^{++}	13.2	13.3	13.7	13.4	13.4	13.7	13.5	14.7
2^{-+}	13.5	13.6	14.3	13.6	13.7	14.0	13.7	14.8
1^{--}	35.0	35.2	36.5	35.9	35.9	35.4	34.8	38.1
2^{+-}	38.8	38.9	40.2	39.7	39.7	39.3	38.7	42.1
2^{--}	40.4	39.9	41.8	40.4	41.2	39.0	38.8	41.2
1^{+-}	40.4	39.9	41.8	40.4	41.2	39.0	38.8	41.2
3^{+-}	40.4	39.9	41.8	40.4	41.2	39.0	38.8	41.2
3^{--}	40.9	41.0	42.2	41.8	41.8	41.5	40.8	44.3
2^{++}	42.8	43.1	44.6	43.9	43.9	43.2	42.6	46.2
1^{-+}	45.4	45.4	45.8	46.2	46.1	46.0	45.8	48.6
0^{-+}	103.5	103.7	105.7	103.3	101.0	103.7	103.3	102.9
0^{+-}	130.0	129.2	129.7	130.0	127.3	130.5	129.6	133.4
0^{++}	163.9	163.1	164.7	163.9	164.0	163.4	162.4	167.3

Table 3.10: Results of the different systematic checks. Listed are the hypothesis and the χ^2 for 11 degrees of freedom for all checks. The 'default' result is given as reference.

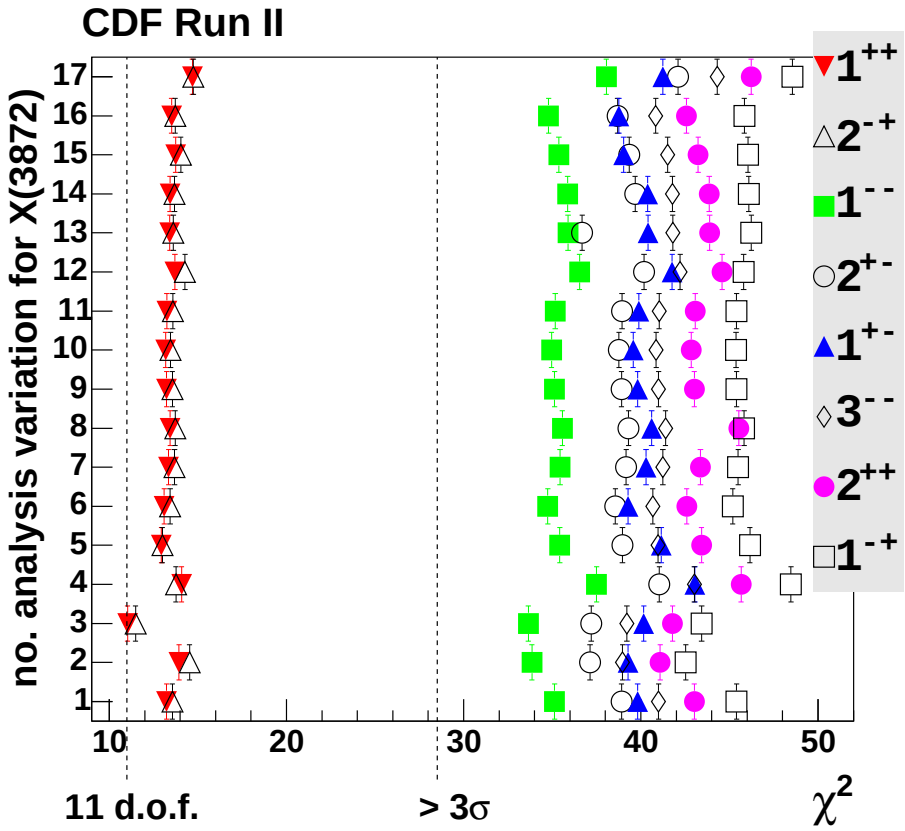

Figure 3.24: Variation of the total χ^2 for different systematic checks. Shown are the χ^2 values for the best hypotheses (all spin 0 states are not plotted because they have values larger than 100) and their variation. The lowest measurement at 1 corresponds to the standard analysis, the other variations are explained in the text.

Chapter 4

Measurement of the $X(3872)$ Mass

A very important property of the $X(3872)$ is its mass. On the one hand the value is interesting on its own because it does not agree very well with predicted charmonium masses. On the other hand and more importantly, the mass difference to the sum of the D^0 and D^{0*} masses is of interest. The picture of a bound 'molecular' state of these two mesons is very popular because of the near identity in mass between the $X(3872)$ mass and the summed D^0 and D^{0*} masses. Whether or not such a state is bound crucially depends on the question, whether the $X(3872)$ is heavier or lighter than the sum of the 'constituent' masses. In order to answer this question a precise mass determination of the $X(3872)$ is required.

Some exotic hypotheses to explain the $X(3872)$ predict a whole spectrum of exotic states out of which the $X(3872)$ is only one. The multiquark model of Maiani *et al.* [34] accommodates the $X(3872)$ as a mixture of two neutral flavor states and predicts the existence of a partner state of similar mass. This hypothesis can be tested by investigating whether the observed $X(3872)$ mass structure is compatible with two separate peaks or not.

This chapter will first describe the selection process for the measured data sample and the creation of the corresponding simulated samples in section 4.1. Section 4.2 will investigate the agreement of the observed mass spectrum with two separate signal peaks. Finally, the mass of the $X(3872)$ will be precisely measured in section 4.3.

4.1 Sample Selection

The measured data sample is obtained in the same way as the data sample for the J^{PC} measurement. Two muons are combined to a J/ψ candidate, which in turn is combined with two pions to form an $X(3872)$ candidate. While in the angular analysis a simple simulation was sufficient to model the important detector effects, a more detailed, 'realistic' simulation of the CDF detector is required to properly model the detector mass resolution.

particle candidate	requirements
pion candidate	$p_T > 0.4\,\mathrm{GeV}/c$ $\lvert\eta\rvert < 1$ ≥ 10 COT hits, ≥ 2 SVX hits
muon candidate	$p_T > 1.5\,\mathrm{GeV}/c$ $\lvert\eta\rvert < 1$ ≥ 10 COT hits, ≥ 2 SVX hits
J/ψ candidate	$2.95\,\mathrm{GeV}/c^2 < m(\mu\mu) < 3.25\,\mathrm{GeV}/c^2$ $\chi^2(\mu^+\mu^-) < 30$
$X(3872)$ candidate	$m(J/\psi\pi\pi) < 4.0\,\mathrm{GeV}/c^2$ $p_T > 3.5\,\mathrm{GeV}/c$ $\chi^2(J/\psi\pi\pi) < 40$

Table 4.1: $X(3872)$ preselection cuts.

4.1.1 Preselection of the Measured Data Sample

In the analysis of the $X(3872)$ mass all available data until August 2007 is being used. This corresponds to the run range 138425–246231. The $J/\psi \to \mu^+\mu^-$ trigger is used to select the data, stored in the datasets `jpmm0d`, `jpmm0h`, `jpmm0i`, and `jpmm0j`. The amount of measured data corresponds to an integrated luminosity of $\mathcal{L} \approx 2.4\,\mathrm{fb}^{-1}$.

As in the J^{PC} analysis, the reconstruction procedure combines a J/ψ candidate with two pion candidates to an $X(3872)$ candidate. The reconstruction code is based on the generic `BottomMods` package [98, 99], using a custom steering file to specify the reconstruction chain.

The preselection requirements are listed in table 4.1. The two pions are required to have opposite charge for the signal sample, however, also the wrong-sign combinations are stored for cross-checks. The requirements are designed to reject obvious background and to apply basic quality criteria. In comparison to the J^{PC} analysis, only tracks with at least 2 hits in the silicon layers are used in order to improve the mass resolution.

4.1.2 Signal Selection Procedure

The final $X(3872)$ signal selection procedure uses a neural network approach. A neural network combines the information from multiple variables and their correlations in a single discriminative variable. This discriminative variable can be used in different ways, here it is simply used as a cut variable. The neural network package employed in this analysis is the product `NeuroBayes`®, developed by the company Phi-T [100, 101]. One of its biggest advantages is the sophisticated preprocessing of the input variables.

#	variable	description
1	training target	known training classification, signal=1, background=0
2	$\chi^2(J/\psi\pi\pi)$	$J/\psi\pi\pi$ vertex fit quality
3	$p_{T,X(3872)}$	transverse momentum of the $X(3872)$ candidate
4	$\chi^2(\mu\mu)$	$\mu\mu$ vertex fit quality
5	$p_{T,J/\psi}$	transverse momentum of the J/ψ candidate
6	$m_{J/\psi}$	fitted mass of the J/ψ candidate
7	$\max(\mathrm{NN}_{\mu^+}, \mathrm{NN}_{\mu^-})$	larger muon network probability
8	$\min(\mathrm{NN}_{\mu^+}, \mathrm{NN}_{\mu^-})$	smaller muon network probability
9	$\max(p_{T,\mu^+}, p_{T,\mu^-})$	larger transverse muon momentum
10	$\max(\Delta R_{\pi^+}, \Delta R_{\pi^-})$	larger pion cone radius relative to $X(3872)$
11	$\max(m_{J/\psi\pi^+}, m_{J/\psi\pi^-})$	larger mass of $J/\psi\pi^+$ and $J/\psi\pi^-$ systems
12	Q	Q value of the decay
13	$\max(p_{T,\pi^+}, p_{T,\pi^-})$	larger transverse pion momentum
14	$\min(p_{T,\pi^+}, p_{T,\pi^-})$	smaller transverse pion momentum
15	$\lvert\eta_{\pi,\mathrm{mean}}\rvert$	absolute average pion pseudorapidity

Table 4.2: Input variables for the $X(3872)$ selection network. The muon network probability is the output of a dedicated neural network and gives an estimate whether a particle is a muon or not. The first variable is not a real input variable but rather denotes whether the given event is a signal or background event.

The network is trained with sample events to learn the difference between signal events and background events. Two samples are required for training, one containing signal events and one containing background events. The signal event sample is provided by a sample of simulated events, which is described in section 4.1.3. For the background event sample real events from the preselection sample are used. They are taken from the sideband mass region of the $X(3872)$. This avoids the presence of a significant amount of real signal events in the background sample while at the same time it can be confidently assumed that the sideband background events show similar properties as the background events at the true signal mass. The mass sidebands are defined as two $25\,\mathrm{MeV}/c^2$ broad mass windows: $[3816.7 - 3841.7;\ 3901.7 - 3926.7]\,\mathrm{MeV}/c^2$.

In order to be able to separate between signal and background, the network needs input variables that describe the characteristics of an event. To add to the separation power of the whole network, the input variables usually have either separation power on their own, or in connection with other variables. The variables used in the selection are listed in table 4.2.

One very important aspect must be considered. The $J/\psi\pi\pi$ mass as the most obvious separating variable is not allowed to enter the list of variables. The reason is that the signal and background samples have exclusive mass regions. As a consequence, the network training would primarily pick up the fact that any signal event is in the vicinity of the true $X(3872)$ mass, while all background events are not. Applying this training result on real measurements would reject all candidates not close to

the signal mass. This is a most undesirable effect, since it leads to the fact that the number of background entries — and with it the number of signal entries — can no longer be interpolated from the rest of the mass spectrum. The background suppression in the signal range becomes worse as well, because other discriminating information gets suppressed compared to the dominant discriminating information from the mass. It even must not be possible to obtain information about the $J/\psi\pi\pi$ mass from other variables in the list. As a consequence, all input variables which allow implicit deductions on the $J/\psi\pi\pi$ mass are transformed so that they are no longer directly correlated to the $J/\psi\pi\pi$ mass.

Two types of transformations are performed. On the one hand a variable A can be correlated to the $J/\psi\pi\pi$ mass in the regular sense, e.g. higher values of A on average correspond to higher values of $J/\psi\pi\pi$. In such a case the network is not trained with the variable A. Instead, a corrected variable $A/F(m_{J/\psi\pi\pi})$ is used, where $F(m_{J/\psi\pi\pi})$ is the mean value of A for a given value of the $J/\psi\pi\pi$ mass $m_{J/\psi\pi\pi}$. $F(m_{J/\psi\pi\pi})$ is determined from a fit to the correlation on the wrong-sign $J/\psi\pi\pi$ candidate sample. This transformation is performed for all transverse momenta, the cone size, the average pion pseudorapidity, and the Q value. On the other hand, the $J/\psi\pi\pi$ mass can be correlated to a variable B if the allowed range for B depends on the value of the $J/\psi\pi\pi$ mass. As an example the $J/\psi\pi^+$ mass is restricted to small values if the $J/\psi\pi\pi$ mass is small. This is resolved by transforming the variable B into the range between 0 and 1, where 0 means that B has the smallest possible value for a given value of the $J/\psi\pi\pi$ mass while 1 means that it has the largest possible value. This transformation is performed for the Q value and the $J/\psi\pi$ masses.

Some training control plots are shown in figure 4.1. The purity shows a linear dependence on the network output which indicates that the training did converge in its training process. It can be seen that signal and background events show a good separation. Many background events can be almost unambiguously rejected. It is however difficult to select a pure signal sample with decent efficiency. The signal network output, which is a measure of purity, peaks at 0.8 and not at 1.0. The network is not able to find events, which can unambiguously be identified as signal events. Also shown are the correlations between the input variables.

It needs to be verified that in the training of the network no dependences on the $J/\psi\pi\pi$ mass were learned. This check is performed by applying the training results on the wrong-sign sample, i.e. the sample where the two pions have the same charge. Figure 4.2 shows the mean network output as a function of the $J/\psi\pi\pi$ mass. No peaking structure is observed at the $X(3872)$ mass or at any other mass. This shows that the network did not pick up any peaking mass dependence.

The data selection is obtained by a cut on the neural network output. The cut value is chosen by optimizing the significance-like quantity K, defined by $K = N_{MC}/\sqrt{N_{data}}$. N_{MC} is the number of simulated signal events and N_{data} the number of measured data events, both counted in a mass window of $\pm 10\,\mathrm{MeV}/c^2$ around the signal mass of $m_{X(3872)} = 3871.7\,\mathrm{MeV}/c^2$. With the 'regular' significance definition $K_{reg} = S/\sqrt{S+B}$, where S and B are the number of signal and background events

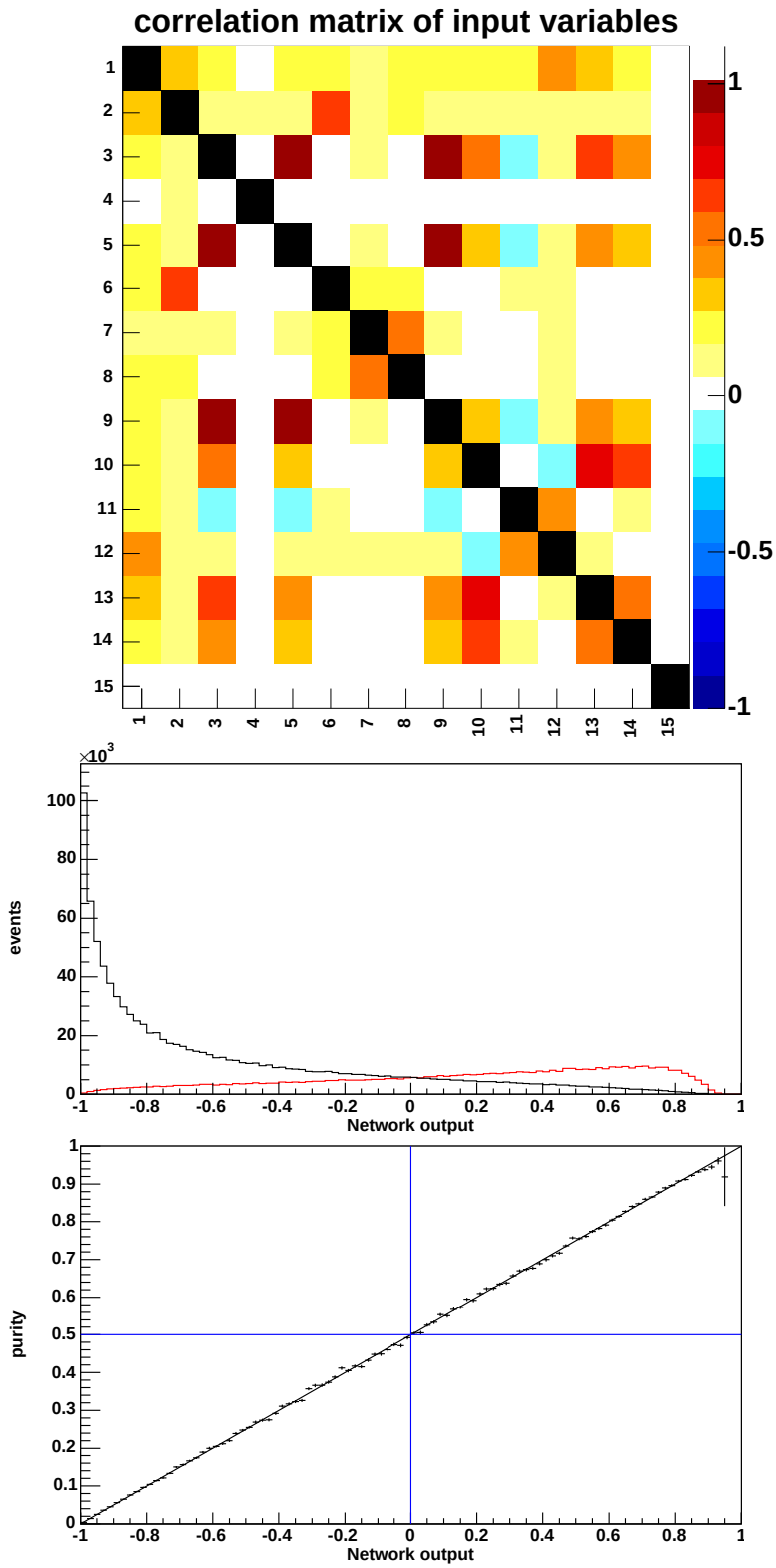

Figure 4.1: Control plots of the $X(3872)$ neural network training. The first plot illustrates the correlations between the input variables (see table **??**). The middle plot shows the network output for the background sample (black line) and the signal sample (red). The signal purity is shown in the bottom plot.

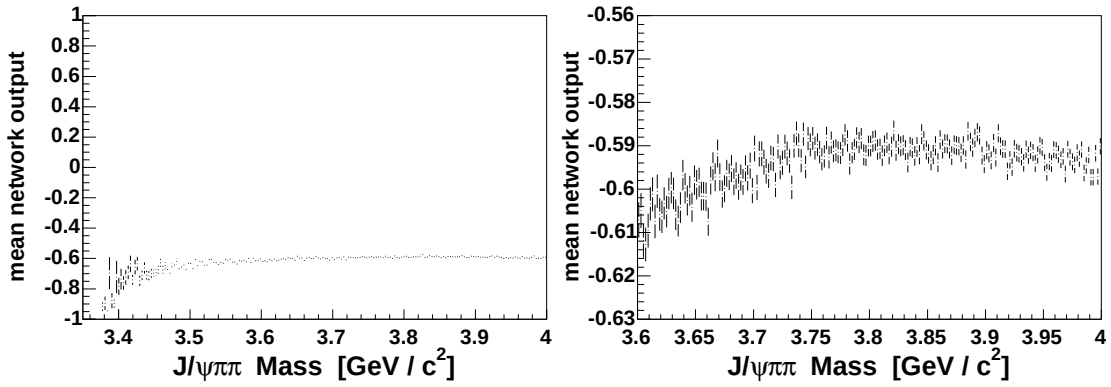

Figure 4.2: The mean value of the neural network output as a function of the wrong-sign $J/\psi\pi\pi$ candidate mass. The left plot shows the dependence in the whole range. The right plot shows the same dependence, focussing on the range between 3.6 and 4 GeV/c^2.

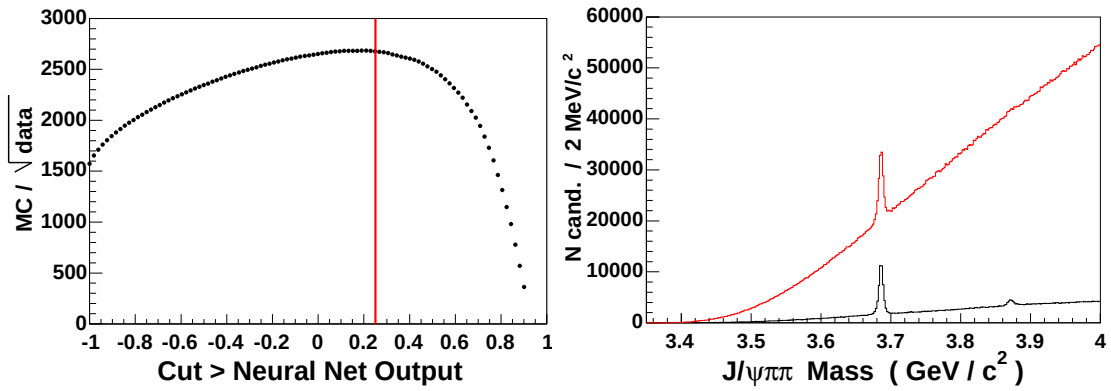

Figure 4.3: Significance scan of the neural network cut. A value of 0.25 is selected. The right plots shows the $J/\psi\pi\pi$ mass spectrum after this cut on the network output (black). The red histogram shows the distribution of the rejected events. The cut reduces the background by a factor of ≈ 10 while keeping $\approx 50\%$ of the signal.

in measured data, K is

$$K = \frac{N_{MC}}{\sqrt{N_{data}}} = \frac{nS}{\sqrt{S+B}} = nK_{reg},$$

and proportional (by an arbitrary factor n) to the regular significance. This assumes that the signal simulation behaves in the same way as real signal in measured data. The scan of K is shown in figure 4.3. From the plateau of high values a value with good signal purity is chosen. This leads to the selection of the cut on the neural network output of greater than 0.25. Also shown is the mass spectrum for the selection with a neural network output larger and smaller than 0.25. It can be seen that the background is reduced by a factor of 10. From the $\psi(2S)$ signal size it can be estimated that the signal selection efficiency is $\approx 50\%$.

In addition to the selection by the cut on the neural network output, a cut is performed on the number of $X(3872)$ candidates per detector event to increase the

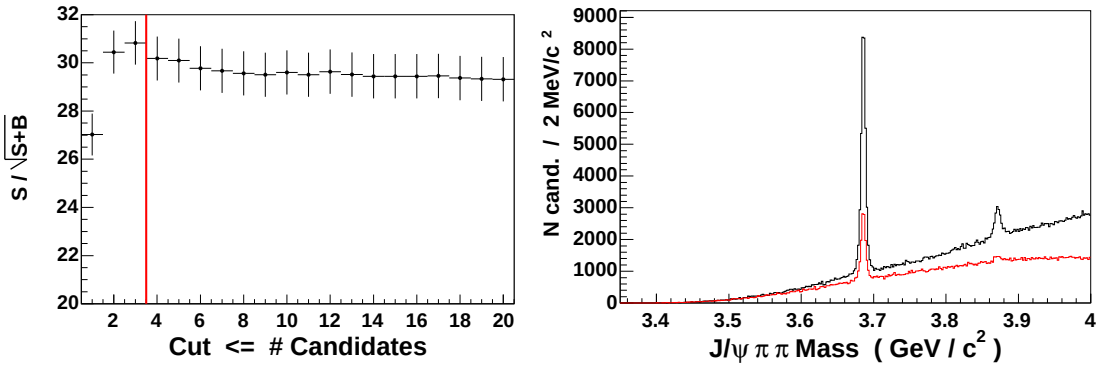

Figure 4.4: Significance scan of the cut on the number of candidates. A value of smaller or equal than three is selected. The right plots shows the $J/\psi\pi\pi$ mass spectrum after this cut on the number of candidates (black). The red histogram shows the distribution of the rejected events.

a priori signal probability in each detector event. The number of candidates per detector event is determined after the preselection. Since the number of candidates is not modelled in the simulation, the selection is performed in a data-driven way. The significance K_{reg} is determined by a fit to the mass spectrum, using a second order polynomial for the background and a Gaussian function for the signal. Signal and background yields are determined within a $\pm 10\,\mathrm{MeV}/c^2$ mass window around a signal mass of $m_{X(3872)} = 3871.5\,\mathrm{MeV}/c^2$. Figure 4.4 shows the significance scan. As a result a cut of smaller or equal than three is obtained. Also shown is the mass spectrum for the new selection with the requirement on the number of candidates.

The final selection requirement is the trigger confirmation. This rejects all events where the J/ψ in the $J/\psi\pi\pi$ candidate was not the one that triggered the recording of the event. This requirement has only very slight effects because the probability is very small to have more than one J/ψ in a detector event. It is applied to ensure the agreement between measured data and generated simulation, where only J/ψ mesons occur that also were triggered.

The selection was developed with the data available until March 2007. An increase in statistics by 20% was achieved by adding new data until August 2007. This increase did not necessitate a re-optimization of the selection, so that the same selection is applied. The mass spectrum after the final selection is shown in figure 4.5. A fit to the spectrum in the $X(3872)$ range using a second order polynomial for the background description and a Gaussian function for the signal description yields

$$m_{X(3872)} = 3871.6 \pm 0.2\,\mathrm{MeV}/c^2,$$
$$\sigma_{X(3872)} = 4.3 \pm 0.2\,\mathrm{MeV}/c^2.$$

The significance in a $\pm 10\,\mathrm{MeV}/c^2$ window is 32.9. A similar fit to the $\psi(2S)$ results

in

$$m_{\psi(2S)} = 3686.01 \pm 0.02\,\mathrm{MeV}/c^2,$$
$$\sigma_{\psi(2S)} = 3.23 \pm 0.02\,\mathrm{MeV}/c^2.$$

According to the fits, approximately 34500 $\psi(2S)$ candidates and 5800 $X(3872)$ candidates are selected.

4.1.3 Simulation Sample Generation

For the mass analysis, the simulated samples are generated with the standard CDF full simulation, release 6.1.4mc. Two high statistics samples are created, one sample for the decay $X(3872) \to J/\psi\pi^+\pi^-$ and one for the decay $\psi(2S) \to J/\psi\pi^+\pi^-$. The generation proceeds in the following steps:

1. Generation of the initial state momentum. The software generates values of transverse momentum following a distribution measured for B-mesons. The mass is fixed to the $\psi(2S)$ or $X(3872)$ mass, while the pseudorapidity and the azimuthal angle ϕ are distributed uniformly.

2. Decay into the final state. The `EvtGen` package [102] is used. Is is most convenient to consider only phase space at this stage and reweight the events later according to their decay matrix element.

3. The response of the CDF detector to the created particles is modelled by the full `GEANT`-based simulation of the CDF detector [103, 104].

4. Whether a detector event is accepted and recorded is decided in the trigger simulation.

5. The simulated event gets reconstructed in the same way as a real measured event.

The same preselection cuts as for the measured data sample are applied. As a next step the simulated samples are reweighted to account for the respective decay specifics. Three separate aspects require reweighting:

- Decay weight: The simulation assumes a phase-space decay of the initial state into the final state. Each event needs to be reweighted with a decay weight. In case of the $\psi(2S)$ the Novikov-Shifman decay weight is used. For the $X(3872)$ the same weight as in the J^{PC} analysis is used. Because of the small effect and the ambiguity in choice between 1^{++} and 2^{-+} all angular dependences are ignored, effectively resulting in a pure modelling of an intermediate ρ^0 meson for the dipion system. These weights are described in section 3.1.

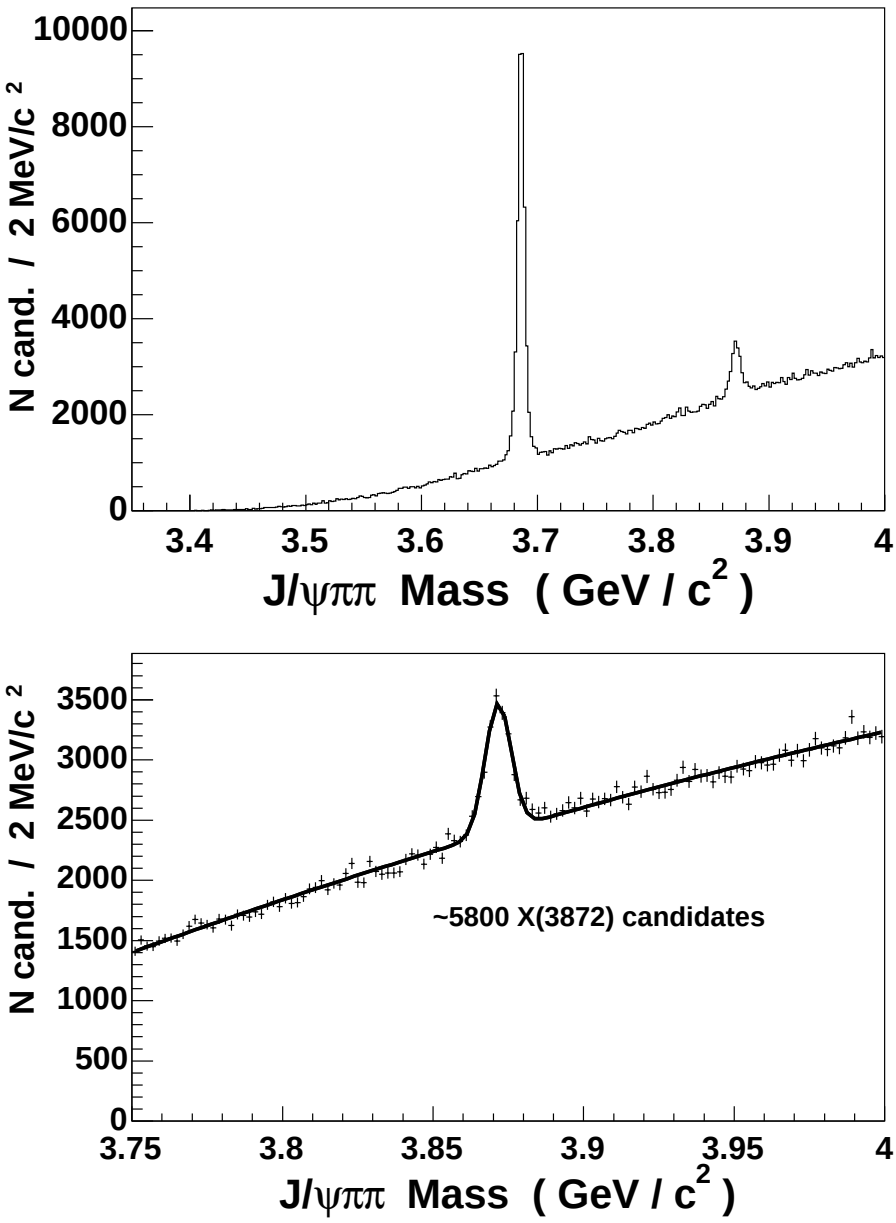

Figure 4.5: The final mass spectrum of the selection. Shown are the whole spectrum from threshold to 4.0 GeV/c^2 (top) and the range focussing on the $X(3872)$ (bottom). The bottom plot also shows a fit to the spectrum, using a second order polynomial for the background description and a Gaussian function for the signal description.

- Transverse momentum: The simulation uses a generic transverse momentum spectrum for the decaying particle, not particularly designed for the $\psi(2S)$ or the $X(3872)$. Each event is reweighted so that the total simulated transverse momentum distribution agrees with the measured transverse momentum distribution after preselection. The reweighting function is obtained by fitting the ratio between measured and simulated transverse momentum distribution.

- Trigger path: While the used trigger paths that lead to the recording of events are identical in measured and simulated data, there are slight differences in the distributions of how often a certain trigger path is used. The most important aspect is the ratio between trigger paths that only use the central muon chambers CMU/CMP to the trigger paths that also allow for muons from the CMX, because this ratio affects the muon pseudorapidity distribution. Each event is reweighted to account for the difference in simulation and real measurement.

At preselection level both the weight for the transverse momentum and for the trigger path are determined from the distributions of the $\psi(2S)$. The reason is that the measured data sample after preselection does not yet allow for a measurement of the $X(3872)$ distributions with reasonable uncertainty. The distribution measurement is performed with the 'slicing method' explained in section 3.2.4.

The generated $X(3872)$ simulated sample is used as signal sample input for the neural network training in section 4.1.2.

4.1.4 Final Reweighting of the Simulated Samples

After applying the final selection from section 4.1.2 on both measured data and simulated samples, the reweighting procedure from the previous section is repeated. The reason is that after the final selection a good signal significance has been obtained in measured data, so that the data behavior can be measured more precisely. Even more important, now it is possible to measure $X(3872)$ distributions with sufficiently small uncertainty.

The reweighting procedure is thus repeated, separate for the $\psi(2S)$ and the $X(3872)$ samples. The main steps are identical compared to the previous reweighting process, slight changes are introduced for the transverse momentum reweighting.

1. Reweight each event with the specific $X(3872)/\psi(2S)$ decay weight.

2. Reweight each event so that the overall muon trigger CMU/CMX ratio agrees between simulation and measured data.

3. Reweight each event so that the overall transverse momentum distributions of the pion and $X(3872)/\psi(2S)$ candidates agree between simulation and mea-

sured data. The reweighting uses the following functions:

$$f(p_{T,J/\psi\pi\pi}) \propto \exp(a_0\, p_{T,J/\psi\pi\pi})\, p_{T,J/\psi\pi\pi}^{a_1}\,,$$
$$f(p_{T,\pi}) \propto 1 - \frac{b_0}{p_{T,\pi} - b_1}.$$

The parameters of these functions are obtained by a simultaneous fit. This fit minimizes a combined χ^2 value which is obtained as a sum from single χ^2 values, describing the agreement between a measured distribution and a reweighted simulated distribution. The distributions of $p_{T,J/\psi\pi\pi}$, p_{T,π^+}, and p_{T,π^-} are used.

The agreement of the simulated events with the measured distributions after the final reweighting is shown in figure 4.6 for the $\psi(2S)$ and in figure 4.7 for the $X(3872)$. Both show good agreement.

4.2 Analysis of the $X(3872)$ Mass Shape

Multiquark hypotheses are among the most prominent models to explain the $X(3872)$. In most cases they do not only accommodate the $X(3872)$, but also predict a spectrum of different states. The $X(3872)$ is described by a combination of two charm quarks with two light quarks. Because multiple combinations of light quarks are possible, also multiple $X(3872)$-like states with similar mass are possible.

If the multiquark hypothesis holds for the $X(3872)$, it is thus possible that the observed $X(3872)$ enhancement in the $J/\psi\pi^+\pi^-$ mass spectrum is in reality not only one peak, but rather an unresolved structure of two peaks. This hypothesis can to some extent be valid for the earlier confirmations of the $X(3872)$ at CDF, since the mass resolution of the measurement is of the order of $5\mathrm{MeV}/c^2$. However, also the B-factories with approximately twice as good resolution only observe one peak. Maiani *et al.* explain this behavior in their multiquark model [34, 41]. It is suggested that only one of the neutral multiquark states is predominantly produced in the observed decay of a charged b-meson, i.e. in the decay $B^+ \to X(3872)K^+$. The other neutral state is produced in the decay of a neutral b-meson $B^0 \to X(3872)K_S^0$.

At the Tevatron, the $X(3872)$ production via the decay of b-mesons is small compared to the one from direct fragmentation. As a consequence, both neutral states should be observable at the same time in the decay to $J/\psi\pi^+\pi^-$. If the mass difference of two states is smaller or of the order of the detector mass resolution, they cannot be clearly separated. However, it is still possible to draw conclusions which allow to answer the question whether the description of the measured signal requires two separate states or if one state suffices.

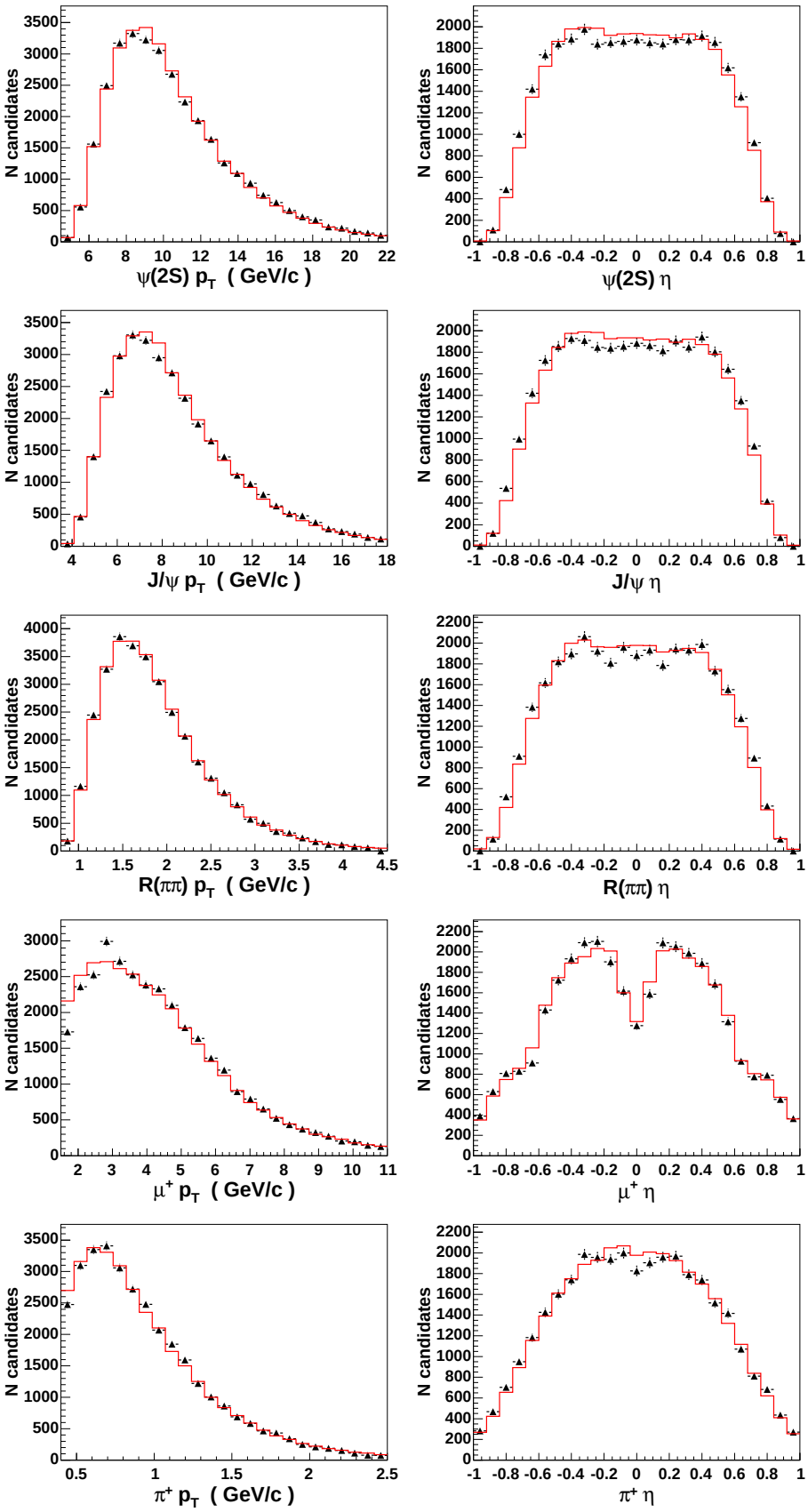

Figure 4.6: Comparison between the simulated and the measured distributions in the $\psi(2S)$ decay. Shown are the transverse momenta and pseudorapidities of the involved particles.

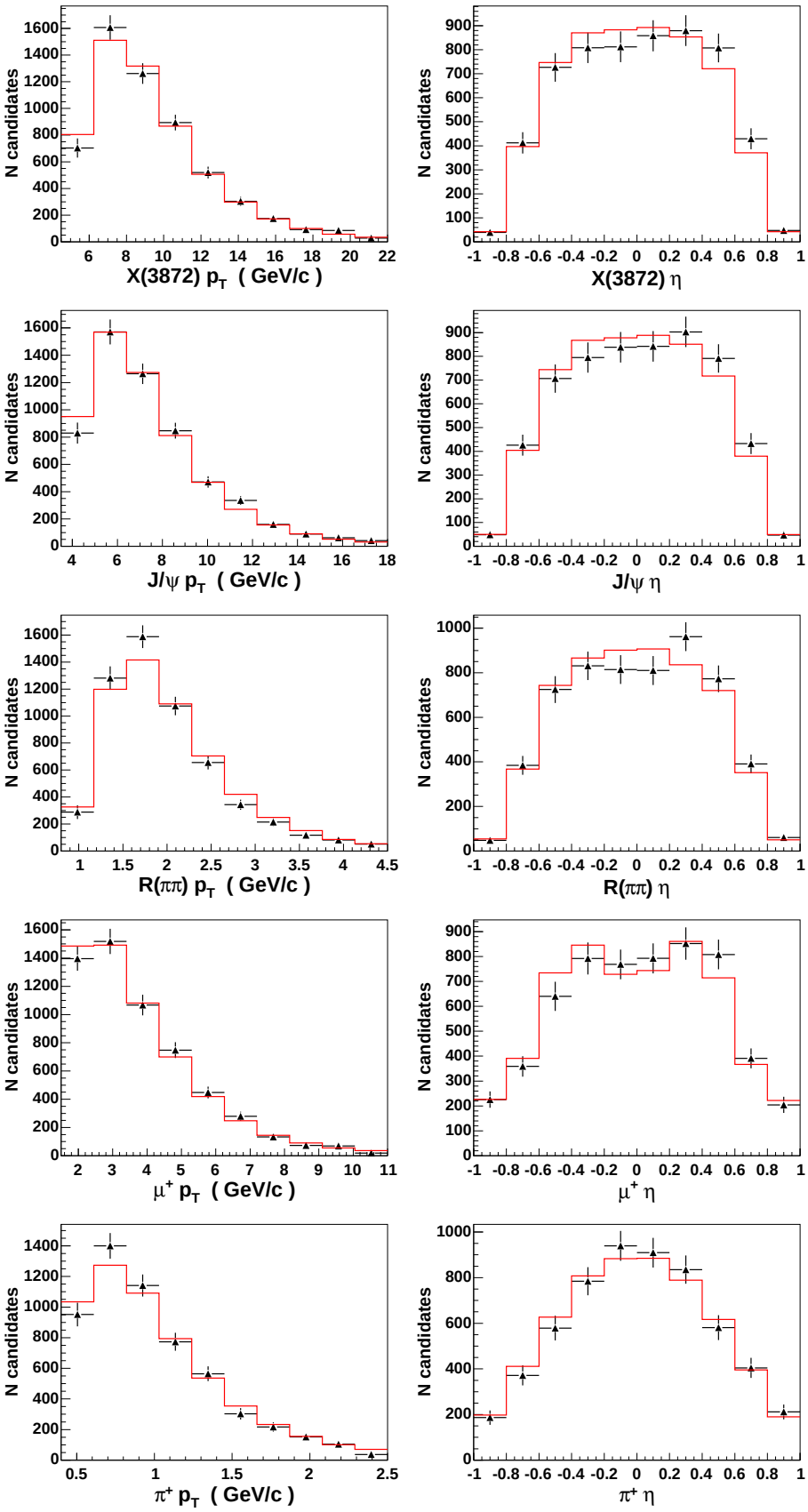

Figure 4.7: Comparison between the simulated and the measured distributions in the $X(3872)$ decay. Shown are the transverse momenta and pseudorapidities of the involved particles.

4.2.1 Hypothesis Test Procedure

The basic idea of the hypothesis test procedure is simple. Two peaks, separated in mass by a mass difference Δm, will appear as a broader structure than one peak. Any distribution that uses a dispersion parameter V to describe the width of the signal structure has to assign a larger dispersion parameter for two separated peaks than it needs to for a single peak. The further the two peaks are apart, the larger the dispersion parameter needs to get.

The hypothesis test procedure uses the following steps:

1. Create a fit model to describe the measured mass distribution.
2. Derive a test quantity from the fit model which can be used to quantify the agreement of the fitted sample with a hypothesis.
3. Measure the value of the test quantity in data.
4. Obtain the expected distribution of the test quantity for a given hypothesis by generating simulated experiments.
5. Deduce the agreement of the measurement with the two hypotheses:
   - 'Only one signal peak is present.'
   - 'Two peaks are present with mass difference Δm.'

4.2.2 Fit Model and Test Quantity

The shape of a single signal peak is modelled by a non-relativistic Breit-Wigner function of intrinsic width Γ. For the intrinsic width of the $\psi(2S)$ the world average value [5] of $\Gamma_{\psi(2S)} = 0.337$ MeV is used. While the $X(3872)$ is known to be compatible with detector resolution, both Belle and *BABAR* measure non-zero values for the central value of the width. Combining the measured value $\Gamma_X = 1.4 \pm 0.7$ MeV [1] from Belle with the measurement $\Gamma_X = 1.05 \pm 1.52 \pm 0.24$ MeV [7] from *BABAR* results in a mean value of $\Gamma_X = 1.34 \pm 0.64$ MeV, assuming uncorrelated uncertainties.

In addition, detector resolution effects will lead to further broadening of the structure. The mass resolution is modelled by two Gaussian functions with common mean

$$f_n \,\mathrm{Gauss}(m; m_0, \sigma_n) + (1 - f_n)\,\mathrm{Gauss}(m; m_0, k\,\sigma_n).$$

f_n is the contributing fraction of the narrow Gaussian function, σ_n is the width of the narrow Gaussian function, and k is a multiplicative factor that denotes the ratio between the width of the broad Gaussian function and the width of the narrow Gaussian function. Each Gaussian function is properly normalized to one.

The mass resolution effects are determined from the simulated samples with realistically modelled detector. For this purpose a binned fit to the mass deviation of

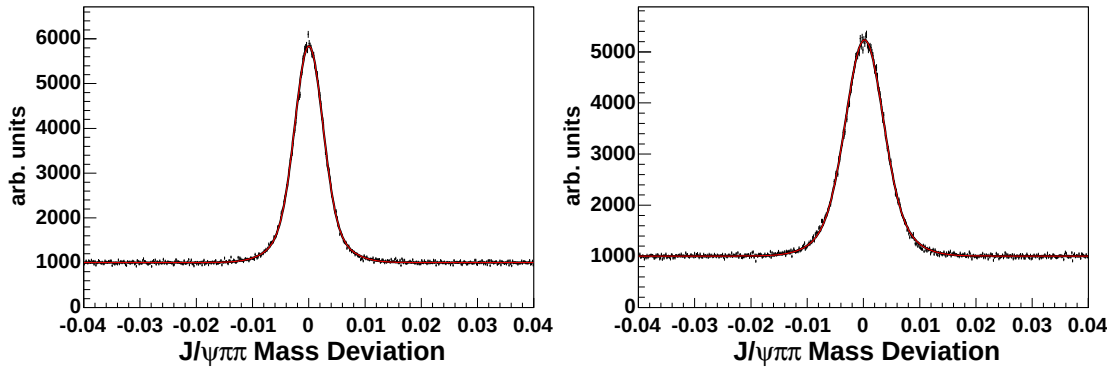

Figure 4.8: Expected mass resolution from the difference between generated and reconstructed mass for the $\psi(2S)$ (left) and the $X(3872)$ (right). Because the $X(3872)$ is heavier, the final state particles have on average higher momenta and worse resolution. The mass resolution is modelled by two Gaussian functions with common mean. Uniformly distributed background is added to the histogram to remove the effect of outliers on the fit.

the simulation is performed. This is shown in figure 4.8. Uniformly distributed background is added in order to minimize the danger that single outliers lead to an unwanted broadening of the fitted Gaussian functions. For the $\psi(2S)$, the fit results in the resolution parameters $\sigma_n = 2.43\,\mathrm{MeV}/c^2$, $f_n = 0.717$, $k = 2.04$, while in case of the $X(3872)$ the values $\sigma_n = 3.18\,\mathrm{MeV}/c^2$, $f_n = 0.675$, $k = 1.81$ are obtained.

The folded effect of the Gaussian smearing of a non-relativistic Breit-Wigner distribution is described by the Voigt function. It has three parameters: the central value m_0 of the distribution, the Gaussian width σ and the intrinsic Breit-Wigner width Γ. Since the detector resolution is described by two Gaussian functions, the total signal shape is described by a sum of two Voigt functions:

$$y_S(m; m_0, f_n, \sigma_n, k, \Gamma) = f_n\,\mathrm{Voigt}(m; m_0, \sigma_n, \Gamma) \;+\; (1 - f_n)\,\mathrm{Voigt}(m; m_0, k\sigma_n, \Gamma).$$

The background function uses a simple second order polynomial function

$$y_B(m; p_1, p_2) = \frac{1}{m_h - m_l}\left[1 + p_1 x(m) + p_2(3x(m)^2 - 1)\right],$$

where the nominal mass range $[m_l, m_h]$ is transformed into the mass range [-1,1] by

$$x(m) = -1 + \frac{2}{m_h - m_l}(m - m_l).$$

p_1 and p_2 are parameters for the slope and the curvature of the background description. By above construction, the background function is always normalized to one. Background and signal part of the fit function are combined by

$$y(m) = N\left[f_S\, y_S(m; m_0, f_n, \sigma_n, k, \Gamma) + (1 - f_S) y_B(m; p_1, p_2)\right],$$

introducing the overall normalization N and the signal fraction f_S.

The effective width of the signal distribution will be used to define the test quantity, because it is physically descriptive and robust to mismodelling of the signal shape. To scale the overall width of the signal distribution all relevant parameters for the width are scaled by the width scale t, which will be used as test quantity. With a fixed yield ratio $f_n/(1-f_n)$ between the two Voigt functions and a fixed ratio k between the broad resolution width and the narrow resolution width, only two parameters determine the overall width of the resolution: the intrinsic width Γ and the narrow resolution width σ_n. Both parameters are multiplied by the test quantity t, i.e.

$$\sigma_n \to t\,\sigma_n,$$
$$\Gamma \to t\,\Gamma.$$

With fixed values for σ_n and Γ, t is the only free parameter to scale the signal width of the fit function.

4.2.3 Width Scale Measurement

The data spectrum is fitted using the parameterization from section 4.2.2. Except for the width scale t, all parameters defining the shape of the signal are fixed to the following values:

parameter	value $\psi(2S)$	value $X(3872)$
intrinsic width Γ	0.337 MeV	1.34 MeV
narrow resolution width σ_n	2.43 MeV/c^2	3.18 MeV/c^2
narrow resolution fraction f_n	0.717	0.675
broad/narrow width ratio k	2.04	1.81

The overall normalization N, the background shape parameters p_1 and p_2, the signal fraction f_S, the central position of the signal m_0, and the width scale t remain free parameters in the fit.

A histogram in the $X(3872)$ mass range from 3.75 to 4.0 MeV/c^2 and a bin width of 0.5 MeV/c^2 is filled with the measured data mass spectrum. Using a binned likelihood ansatz to fit the total fit function $y(m)$ to the histogram returns a width scale $t_{X(3872)} = 1.052 \pm 0.047$. An analogous fit to the $\psi(2S)$ in the mass range from 3.60 to 3.75 MeV/c^2 returns a width scale $t_{\psi(2S)} = 1.049 \pm 0.008$. The measured mass distributions with the fit projections are shown in figure 4.9. It should be noted that the expected value for a one-peak hypothesis is not necessarily exactly 1.0 which will be explained in the next section.

4.2.4 Ensemble Creation

The measured value needs to be compared to the expected distribution of the width scale t for a given hypothesis. This distribution is obtained from a large amount of

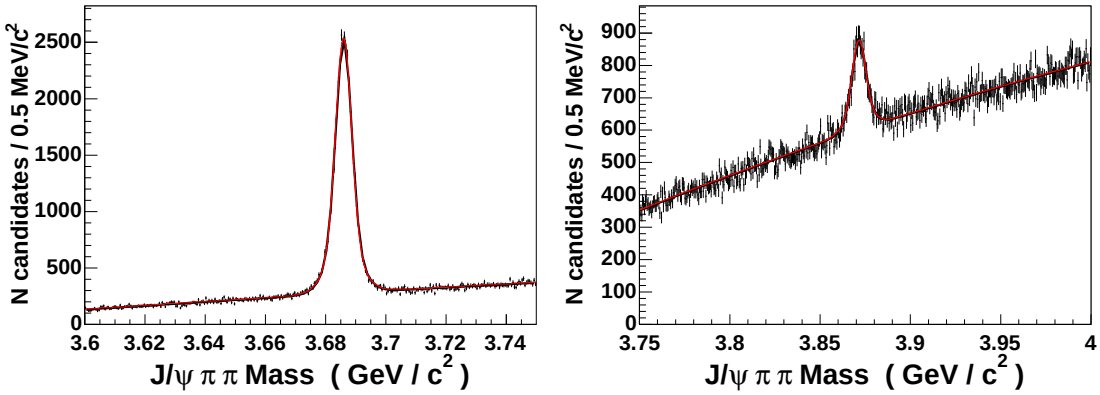

Figure 4.9: Fit to the measured mass spectrum for the $\psi(2S)$ (left) and the $X(3872)$ (right), resulting in the measured width scales.

simulated experiments, created according to the hypothesis. The tested hypotheses read 'Two peaks with signal yields N_1 and N_2 are present with mass difference Δm.' The one-peak hypothesis is obtained by setting Δm to zero.

The experiments are generated according to:

- The combinatorial background is created according to the background part of the fit to the measured data.
- Two peaks are created with mass difference Δm and signal yields N_1 and N_2. Their single shapes follow the parameterization from section 4.2.2.

This method assumes that mixing of the two states is only allowed as far as it does neither change the combined mass spectrum nor the total yield as compared to the simple incoherent addition of the two states. Furthermore the two states are assumed to have the same shape. This assumes that the two states behave similarly in their decay.

Multiple parameters that characterize the sample need to be determined. The overall number of events N_{sim} in the sample is chosen after the number N_{data} of events in the data sample and varied according to a Poisson distribution with mean N_{data}.

The background parameters and the fraction of signal events are modelled after measured data as well. Their generation is based on their measured values and correlations. The slope p_1, the curvature p_2, and the signal fraction f_S are obtained from a 3-dimensional Gaussian distribution, using the measured means and considering their covariance matrix. The number of background candidates is obtained from the signal fraction f_S and the total number of events N_{sim}.

Both the mass difference Δm between the two signal peaks and the yield fraction of the signal with lower mass f_1 are external parameters and explicitly set, since they define the hypothesis. By this, also the yield fraction of the higher mass signal is determined. The total signal yield of the two signal peaks is calculated from the

signal fraction f_S and the total number of sample events N_{sim}. With the fraction f_1 the two signal yields N_1 and N_2 are obtained. The masses are chosen in such a way that the 'mass center' equals the measured $X(3872)/\psi(2S)$ mass M, i.e.

$$\frac{N_1 m_1 + N_2 m_2}{N_1 + N_2} = M.$$

Combined with the relation $m_2 - m_1 = \Delta m$ this allows to determine the single peak positions.

The determination of the parameters for the shape of a single signal peak is the most critical and complicated aspect. Each single signal peak follows the description of the sum of two Voigt functions as described in section 4.2.2. The description of the resolution shape as a sum of two Gaussian functions is an effective description of the detector effects. The ratio k between the two Gaussian widths and the yield fraction f_n of the narrow Gaussian function are assumed to be uncritical, so that k and f_n are fixed to the values as determined from the simulation.

The situation is different for the overall resolution width, which is determined by σ_n. This value is critical for the result of the analysis, since an under- or overestimation of the detector resolution will systematically shift the predicted width scale t for any hypothesis. For example, mistakenly assuming the resolution too narrow in the creation of the simulated mass spectra will shift the expected width scales to smaller values. The opposite effect is caused by creating too broad widths. To validate the mass resolution model derived from simulation, the shape function is tested using the $\psi(2S)$. For this, a similar measurement as in section 4.2.3 is performed. However, this time only the resolution widths are allowed to scale by a factor s_r, since only the effect of the resolution is studied. The intrinsic width Γ is kept fixed, i.e.

$$\begin{aligned} \sigma_n &\rightarrow s_r\, \sigma_n, \\ \Gamma &\rightarrow \Gamma. \end{aligned}$$

This of course assumes that the world average value for the intrinsic $\psi(2S)$ decay width is correct. It is known that for the $\psi(2S)$ only one state contributes to the measured signal peak width. Any result not compatible with the value of $s_r = 1$ will thus indicate a disagreement in resolution between measured data and simulation. This is precisely checked by performing an unbinned likelihood fit[1] to the measured spectrum in the $\psi(2S)$ mass range from $3.6\,\mathrm{GeV}/c^2$ to $3.75\,\mathrm{GeV}/c^2$. The fit returns a value for the resolution scale factor of $s_r = 1.050 \pm 0.008$. This value indicates that the resolution in measured data is underestimated by the simulation by 5%.

This raises the decisive question by how much the simulated resolution is different from the real resolution in the case of the $X(3872)$. This can of course not be directly checked, since any direct measurement could both indicate a resolution mismatch

[1] In an unbinned maximum likelihood fit, extra care needs to be taken in the normalization of the signal function. Since the Breit-Wigner part of the fit function creates long tails in the distribution, the Voigt function needs to be explicitly normalized to account for the signal part which is outside the fitted range.

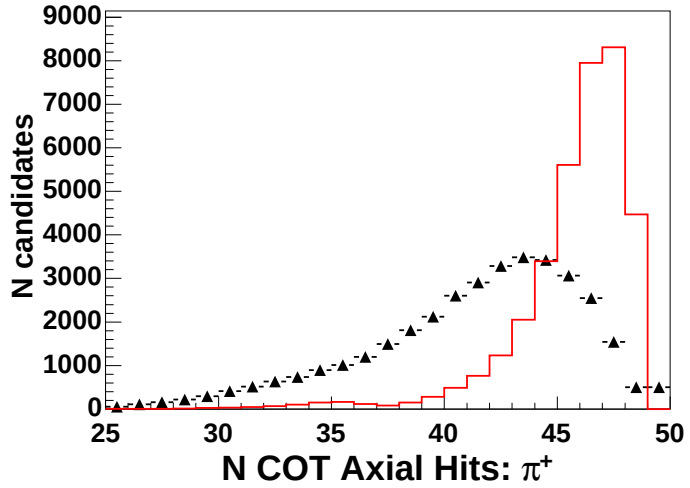

Figure 4.10: The disagreement in the number of COT hits, in this case for a π^+ from the $\psi(2S)$ decay. Shown are the distribution of the number of drift chamber hits per track, both for measured data (points) and for simulation (histogram). The simulation systematically picks up more hits, which improves the track measurement.

or the existence of two peaks. In order to understand the resolution difference, an extensive check was performed to compare event distributions between the measured data and the simulation. Only one major difference was found: all final state tracks from the simulation had significantly more hits in the drift chamber than their measured counterparts (see figure 4.10). It is probable that this effect is caused by the difference in detector occupancy in measured data and the simulation. While in real measured data events a large number of background tracks is present, the simulated event is only occupied with particles from the simulated decay. As a result, both a larger number and less ambiguous detector hits are available for the track reconstruction algorithm. No matter the cause, the effect is a slightly better momentum resolution per track, which causes an improvement in the mass resolution. In this case, it is a reasonable assumption that any difference in resolution between simulation and measured data should be similar for similar decays in a similar momentum regime.

A test was performed with measured and simulated samples of the decay $D^{+*} \to D^0\pi^+$, with $D^0 \to \pi\pi$, $D^0 \to K\pi$, or $D^0 \to KK$. In those three cases, resolution width scale factors with the values of $s_r = 1.025 - 1.055$ were obtained. This strengthens the explanation of a general simulation effect. As a consequence, the resolution of the $X(3872)$ derived from simulation will be scaled by a value of 1.05, since the $\psi(2S)$ gives the best estimate for the $X(3872)$ according to decay topology and involved momenta. However, a systematic uncertainty of 3% will be assigned based on the spread of values in the D^{+*} cases. The same treatment will be applied for the $\psi(2S)$.

The systematic uncertainty of the resolution scale needs to be accounted for in the ensemble creation. It is implemented by allowing the resolution scale s_r to vary

parameter	created according to
total number of events	Poisson-distributed with mean from measurement
background slope	3d Gaussian distr. using measured means,correlations
background curvature	3d Gaussian distr. using measured means,correlations
signal fraction	3d Gaussian distr. using measured means,correlations
yield ratio N_1, N_2	externally set, defines hypothesis
mass difference $m_2 - m_1$	externally set, defines hypothesis
masses m_1, m_2	weighted mean equals measured value
resolution narrow width σ_n	simulation value, multiplied by (1.05 ± 0.03)
res. narrow yield fraction f_n	simulation value
res. width ratio k	simulation value
intrinsic width Γ	world average value, varied by uncertainty

Table 4.3: Summary of the required parameters for the creation of the simulated experiments and the distribution these parameters are created after.

according to a Gaussian distribution with mean 1.05 and width 0.03. The resolution will thus be crated using a value of

$$\sigma_n \rightarrow s_r \, \sigma_n$$

for the width of the narrow Gaussian distribution in the resolution function. This is the main reason why the expected width scale t for the one-peak hypothesis is not 1.0.

The intrinsic width Γ is modelled after measured data. The value is also not unambiguously known, resulting in a systematic uncertainty. This is treated identically as the uncertainty for the resolution scale. For the $\psi(2S)$ the width is drawn from a Gaussian distribution, where the Gaussian mean is given by the world average value of $\Gamma_{\psi(2S)} = 0.337\,\text{MeV}$ and the Gaussian width by the uncertainty of the world average, $\sigma_\Gamma = 0.013$ MeV [5]. A similar procedure is used for the $X(3872)$. The combined measurement values of Belle and *BABAR* are used, leading to an average of $\Gamma_X = 1.34$ MeV and an uncertainty of $\sigma_\Gamma = 0.64$ MeV. The intrinsic widths, drawn from a Gaussian distribution, are required to be greater than zero. Taking the width average of Belle and *BABAR* is motivated by the assumption, that these two experiments measure only one single peak in B^0 decays, while the second signal, if existent, is suppressed. If this were not the case, Belle and *BABAR* would either have observed two separate peaks already, or the mass splitting would be unmeasurably small.

Table 4.3 summarizes the determination of the parameters, necessary to create the simulated experiments. N_B background events are created according to the background parameterization, while N_1 (N_2) signal events are created according to the signal parameterization of two Voigt functions for peak 1 (2). Systematic and statistical uncertainties are considered by varying the ensemble parameters according to their uncertainty.

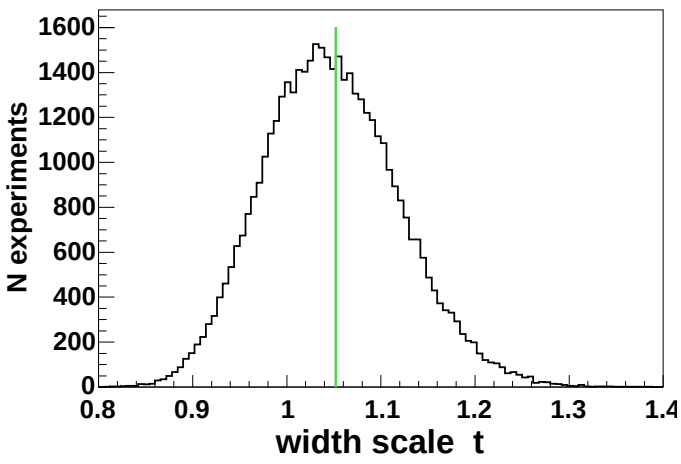

Figure 4.11: The distribution of the expected values of the width scale t for the null hypothesis 'only one signal peak'. The line at $t = 1.052$ illustrates the measured value.

4.2.5 Ensemble Test Evaluation

For each hypothesis the distribution of the width scale t is obtained with an ensemble of simulated mass spectra. The distribution of t for the hypothesis defined by the mass difference ΔM and the yield fraction f_1 is denoted by $g(t; \Delta m, f_1)$. The measured value of t is compared to distributions of different hypotheses.

The first studied hypothesis is the null hypothesis. The existence of only one peak is studied by investigating the distribution for the samples with $\Delta m = 0$. Figure 4.11 shows the expected distribution of the width scale t for the null hypothesis and the measured value of 1.052. The measured value is near the center of the distribution and thus clearly compatible with the null hypothesis.

As a next step, a limit on the allowed values of Δm is obtained under the assumption of $f_1 = 50\%$, i.e. a yield ratio of $50 : 50$ between the two signal peaks. For this fraction the width scale is most sensitive to changes in Δm. With growing Δm the distribution of t will shift to higher values, until at some point the measured value becomes too small to be compatible with the expected distribution, i.e. the measured width becomes too narrow to be compatible with the broad width expectations. This is illustrated in figures 4.11 and 4.12 where the distribution of the width scale is shown for the one-peak hypothesis and two two-peak hypotheses. It can be clearly seen that the expected widths are shifted to higher values for larger mass differences. This motivates the construction of a one-sided confidence region. The confidence region defines the region that contains the true value of t for a given hypothesis at a confidence level of $n\%$, where n is the desired confidence level. In this analysis limits are calculated using 90% and 95% confidence level regions. Since the confidence region is one-sided, the definition

$$n(\Delta m, f_1) = \int_{t(n)}^{\infty} g(t; \Delta m, f_1) dt$$

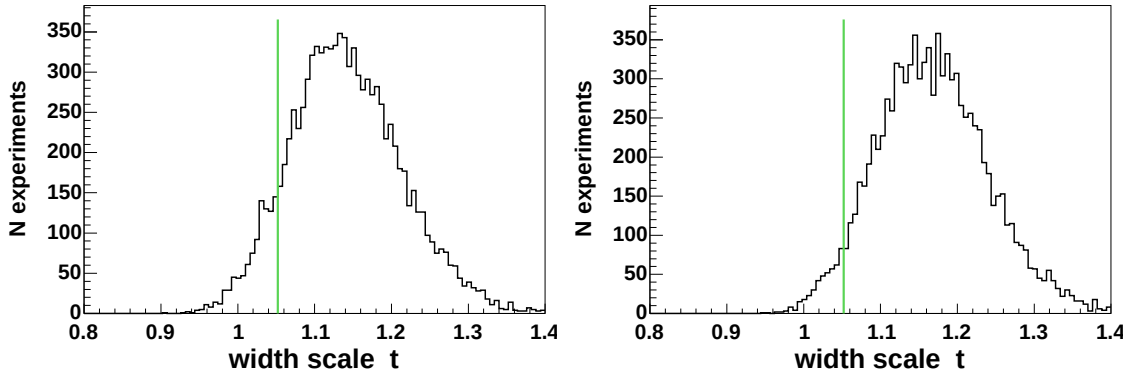

Figure 4.12: The distribution of the expected values of the width scale t for the two-peak hypotheses with mass difference $\Delta m = 3.2\,\mathrm{MeV}/c^2$ (left) and $\Delta m = 3.6\,\mathrm{MeV}/c^2$ (right). Both hypotheses use the yield ratio 50 : 50. The line at $t = 1.052$ illustrates the measured value. For these hypotheses, the measured width scale approximately equals the lower border of the 90% (left) and 95% (right) level confidence regions.

is used.

The limit determination is visualized in figure 4.13. As a function of the mass difference Δm the values of the critical width scale t for both the 90% and 95% confidence level regions are shown. The critical width scales $t(90\%)$, $t(95\%)$ mark the lower border of the confidence regions, i.e. the value for which an observed value is no longer part of the confidence region. It can be seen that the confidence region borders rise with the mass difference. For mass differences of Δm greater than $3.2\,\mathrm{MeV}/c^2$ the measured width scale is no longer within the 90% confidence level region (shown in the left part of figure 4.12). The 95% confidence level region is left for Δm greater than $3.6\,\mathrm{MeV}/c^2$ (shown in the right part of figure 4.12).

For a fraction of $f_1 = 50\%$, the upper limit on Δm thus is $3.2\,(3.6)\,\mathrm{MeV}/c^2$ at 90% (95%) confidence level. The procedure is repeated for all fractions between 20% and 80% in 10% steps. Figure 4.14 shows the obtained limits on Δm, both at 90% and 95% confidence level, as a function of Δm. The obtained limit is quite stable for values of f_1 between 30% and 70%, resulting in upper limits of $\approx 3.4\,(3.8)\,\mathrm{MeV}/c^2$ at 90%(95%) confidence level. For more unbalanced signal yield ratios the limit quickly becomes worse. For the most unbalanced tested relative yield fraction of 20% (80%), i.e. a yield ratio of 1 : 4 (4 : 1), an upper limit of $4.2\,\mathrm{MeV}/c^2$ at 90% confidence level is obtained.

4.3 Measurement of the $X(3872)$ Mass

In the previous section no evidence for the existence of more than one state was found. The mass of a single $X(3872)$ state is obtained by a fit to the $X(3872)$ mass spectrum.

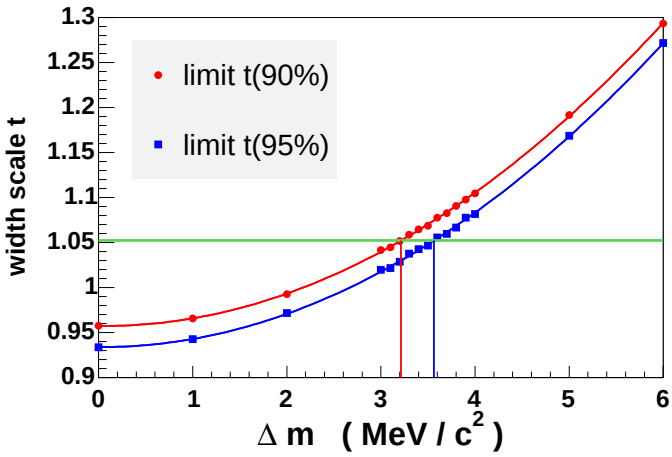

Figure 4.13: The evaluation of the upper limit on the mass difference for the case that two hypothetical signal peaks have the yield ratio 50:50. Shown are as a function of Δm the critical width scale values that define the lower border of the 90% C.L. region (red points) or the 95% C.L. region (blue points). They are connected by an interpolating line. The vertical green line indicates the measured value of $t = 1.052$. This value is no longer in the 90% C.L. region for $\Delta m \geq 3.21\,\mathrm{MeV}/c^2$ and no longer in the 95% C.L. region for $\Delta m \geq 3.57\,\mathrm{MeV}/c^2$.

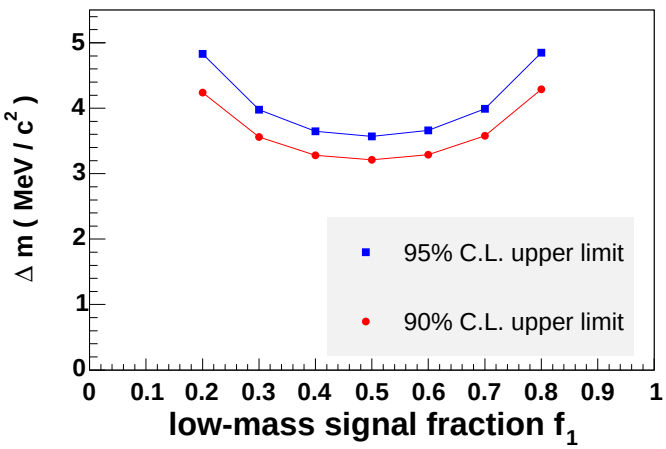

Figure 4.14: The obtained 90% C.L. (red points) and 95% C.L. (blue points) upper limits on the mass difference Δm. The limit is best for an assumed $50:50$ ratio between the signal peaks and rises for the cases of unbalanced peak ratios. The connecting lines guide the eye.

parameter	$\psi(2S)$ value	$X(3872)$ value
lower mass border m_l	3.6 GeV/c^2	3.75 GeV/c^2
upper mass border m_h	3.75 GeV/c^2	4.0 GeV/c^2
background slope p_1	free	free
background curvature p_2	free	free
signal fraction f_S	free	free
signal position m_0	free	free
intrinsic signal width Γ	0.337 MeV	1.34 MeV
narrow resolution width σ_n	2.43 MeV/c^2	3.18 MeV/c^2
narrow resolution fraction f_n	0.717	0.675
broad/narrow width ratio k	2.04	1.81
resolution scale s_r	free	free

Table 4.4: An overview of the used parameters in the fit function. For fixed parameters the value is listed.

The large available number of $X(3872)$ candidates allows for a precise measurement of the $X(3872)$ mass with small statistical uncertainty. It is expected that the systematic uncertainty is of the order of or slightly larger than the statistical uncertainty. The value of the systematic uncertainty is significantly improved by the existence of the nearby $\psi(2S)$ signal peak since any effect that may result in a systematic uncertainty of the $X(3872)$ mass should also be present for the $\psi(2S)$ at similar magnitude.

4.3.1 Fit to the Mass Spectrum

An unbinned maximum likelihood fit to the mass spectrum is performed for both the $\psi(2S)$ and the $X(3872)$. The used fit function was already introduced in section 4.2.2 and is explicitly repeated here:

$$\begin{aligned} y(m) = f_S \left[f_n \,\mathrm{Voigt}(m; m_0, s_r\sigma_n, \Gamma) \;+\; (1-f_n)\,\mathrm{Voigt}(m; m_0, s_r k\sigma_n, \Gamma) \right] \\ + (1-f_S)\frac{1}{m_h - m_l}\left[1 + p_1 x(m) + p_2(3x(m)^2 - 1)\right]. \end{aligned}$$

For the background function, the fit mass region $[m_l, m_h]$ is transformed into the interval $[-1, 1]$ by

$$x(m) = -1 + \frac{2}{m_h - m_l}(m - m_l).$$

The Voigt functions are explicitly normalized to the mass range $[m_l, m_h]$. Table 4.4 lists all fit parameters of the total fit function and, if fixed, the values they are fixed to.

Performing the fit leads to measured mass values of

$$\begin{aligned} m_{\psi(2S)} &= 3686.03 \pm 0.02\,\mathrm{MeV}/c^2, \\ m_{X(3872)} &= 3871.61 \pm 0.16\,\mathrm{MeV}/c^2. \end{aligned}$$

variation	$\psi(2S)$ mass	$X(3872)$ mass
smaller fit window	$3686.03 \pm 0.02\,\mathrm{MeV}/c^2$	$3871.61 \pm 0.16\,\mathrm{MeV}/c^2$
fix Γ to 0	$3686.03 \pm 0.02\,\mathrm{MeV}/c^2$	$3871.60 \pm 0.16\,\mathrm{MeV}/c^2$
fix $\Gamma \to 2\Gamma$	$3686.03 \pm 0.02\,\mathrm{MeV}/c^2$	$3871.61 \pm 0.16\,\mathrm{MeV}/c^2$
linear background	$3686.02 \pm 0.02\,\mathrm{MeV}/c^2$	$3871.62 \pm 0.16\,\mathrm{MeV}/c^2$
simple Gaussian function	$3686.02 \pm 0.02\,\mathrm{MeV}/c^2$	$3871.61 \pm 0.16\,\mathrm{MeV}/c^2$

Table 4.5: Mass measurements for different changes to the fit model. No effects are observed.

Projections of the fits can be seen in figure 4.15.

4.3.2 Evaluation of Systematic Uncertainties

The main contributions to the systematic uncertainty can be divided into two classes: uncertainties from the fit model and uncertainties from the overall momentum scale.

A potential source of uncertainty is the fit model. If the fit model does not reflect the true behavior of the spectrum, systematic shifts in the parameter estimates can occur. The measurement of a signal position is however very robust to changes in the fit model. If there is a prominent and symmetrical peak structure, the symmetrical behavior of the signal shape does not show strong preferences for either side of the signal position. As a consequence no significant systematic shifts should occur. The following variations are investigated:

- Reduce the mass window by 40% from $[3.6, 3.75]$ GeV/c^2 to $[3.63, 3.72]$ GeV/c^2 for the $\psi(2S)$ and from $[3.75, 4.0]$ GeV/c^2 to $[3.80, 3.95]$ GeV/c^2 for the $X(3872)$.
- Fix the intrinsic width Γ to 0.
- Fix the intrinsic width Γ to twice the default value.
- Only use a linear background description.
- The fit model is drastically changed by using a simple single Gaussian function to describe the signal distribution.

As expected, all variations lead to a negligible change in the fit result. For completeness, the fit results are listed in table 4.5.

The largest effect is found to originate from the momentum scale calibration. This describes the uncertainty in the translation from the track curvature to the momentum. Magnetic field and energy loss uncertainties can lead to a systematic over- or underestimation of the measured momenta, which will systematically affect the measured masses. It is very difficult to assign uncertainties only based on the knowledge about the $X(3872)$. It is thus of great benefit that with the $\psi(2S)$ a state exists

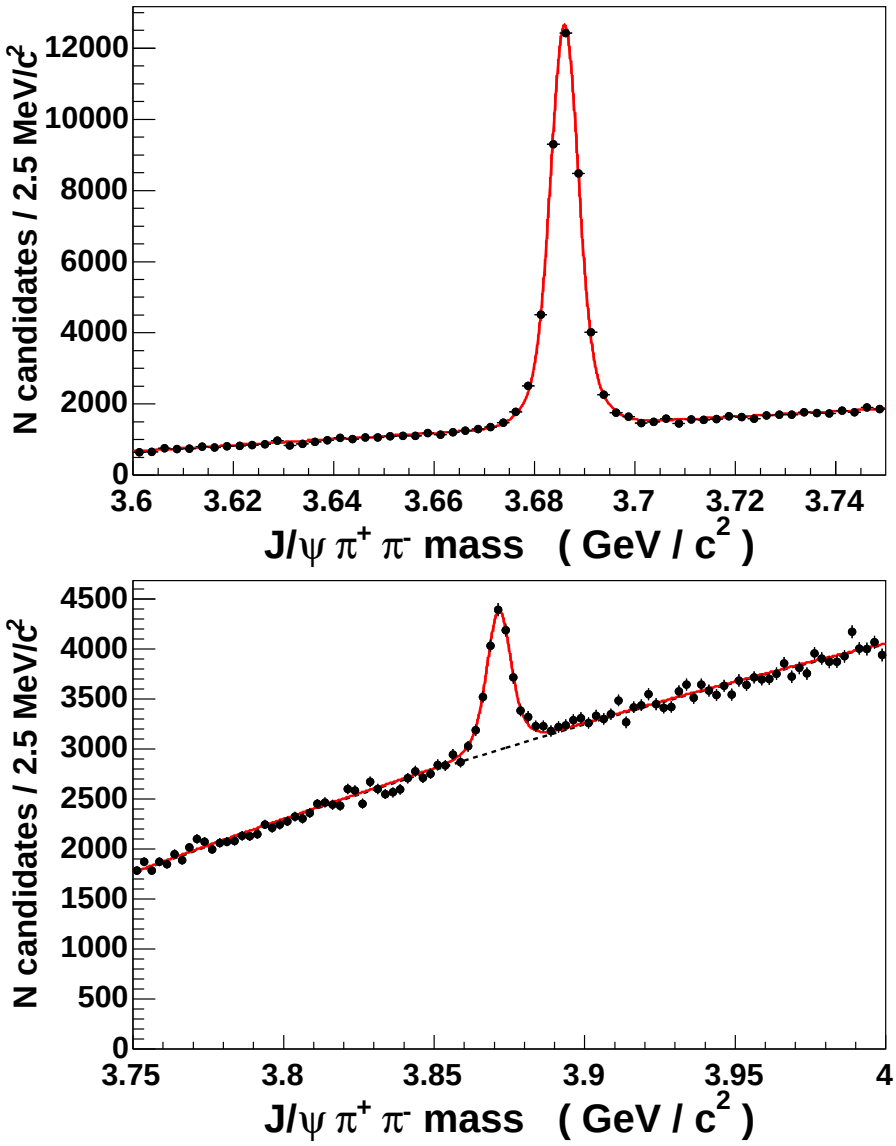

Figure 4.15: Projection of the performed unbinned fit to the mass spectrum for the $\psi(2S)$ (top) and the $X(3872)$ (bottom). The fitted values are $m_{\psi(2S)} = 3686.03 \pm 0.02\,\mathrm{MeV}/c^2$ and $m_{X(3872)} = 3871.61 \pm 0.16\,\mathrm{MeV}/c^2$.

nearby which can be used to estimate the overall effect of the momentum scale on the mass.

The measured and the world average value of the $\psi(2S)$ mass are

$$m_{\psi(2S)} = 3686.03 \pm 0.02\,(\text{stat})\,\text{MeV}/c^2,$$
$$m_{PDG} = 3686.09 \pm 0.03\,\text{MeV}/c^2.$$

This is an extraordinary agreement with a difference of only 60 keV. Part of the reason for the good agreement might be that at CDF the $\psi(2S)$ was used together with other particles to gauge the experimental momentum scale. However, the gauge is usually performed on the dimuon decay mode of the $\psi(2S)$. No matter the reason, the agreement is very good but it can change slightly with different momenta involved, so that the heavier $X(3872)$ might have a slightly worse difference to its true mass. Also studied is the $\psi(2S)$ mass as a function of the momenta. This can be seen in figures 4.16 and 4.17. The value of the $\psi(2S)$ mass varied over p_T and η is quite stable. No major effects are observed. From the $\psi(2S)$ mass deviation to the world average and the good agreement in transverse momenta and pseudorapidities, the systematic uncertainty in the $\psi(2S)$ case is estimated to be $0.1\,\text{MeV}/c^2$. Conservatively multiplying this number by a factor 2 to account for possible differences due to the increase in available energy in the $X(3872)$ case leads to a systematic uncertainty of $0.2\,\text{MeV}/c^2$ for the $X(3872)$.

As a further check the decay length in the transverse plane L_{xy} is investigated. Mismeasurements of L_{xy} causes systematically smaller or larger track curvatures, depending on the facts whether the shift occurs towards larger or smaller values of L_{xy} with respect to the true value and whether the fitted tracks are curving away from ('sailors') or towards each other ('cowboys'). Although the integrated effect should cancel, both small asymmetries in L_{xy}-shifts and the presence of $X(3872)/\psi(2S)$ from b-meson decays could cause a net shift. This is checked by cutting on $|L_{xy}| < 0.01\,\text{cm}$ and $|L_{xy}| < 0.005\,\text{cm}$ to test for a systematic effect. The results are:

cut	$\psi(2S)$ mass	$X(3872)$ mass
no cut	$3686.03 \pm 0.02\,\text{MeV}/c^2$	$3871.61 \pm 0.16\,\text{MeV}/c^2$
$\lvert L_{xy}\rvert < 0.01$ cm	$3686.01 \pm 0.02\,\text{MeV}/c^2$	$3871.65 \pm 0.17\,\text{MeV}/c^2$
$\lvert L_{xy}\rvert < 0.005$ cm	$3686.00 \pm 0.03\,\text{MeV}/c^2$	$3871.59 \pm 0.19\,\text{MeV}/c^2$

A miniscule shift towards lower values is observed for the $\psi(2S)$, while for the $X(3872)$ no conclusive effect can be observed. If an effect exists, it is negligible to the assigned uncertainty of $0.2\,\text{MeV}/c^2$ from the momentum scale.

Possible effects from the selection process are cross-checked by investigating the stability of the measured $\psi(2S)$ mass as a function of the variables, used in the selection. Considered are the neural network output and the number of candidates. Figure 4.18 illustrates the stability of the $\psi(2S)$ mass in both cases. No systematic uncertainty is assigned.

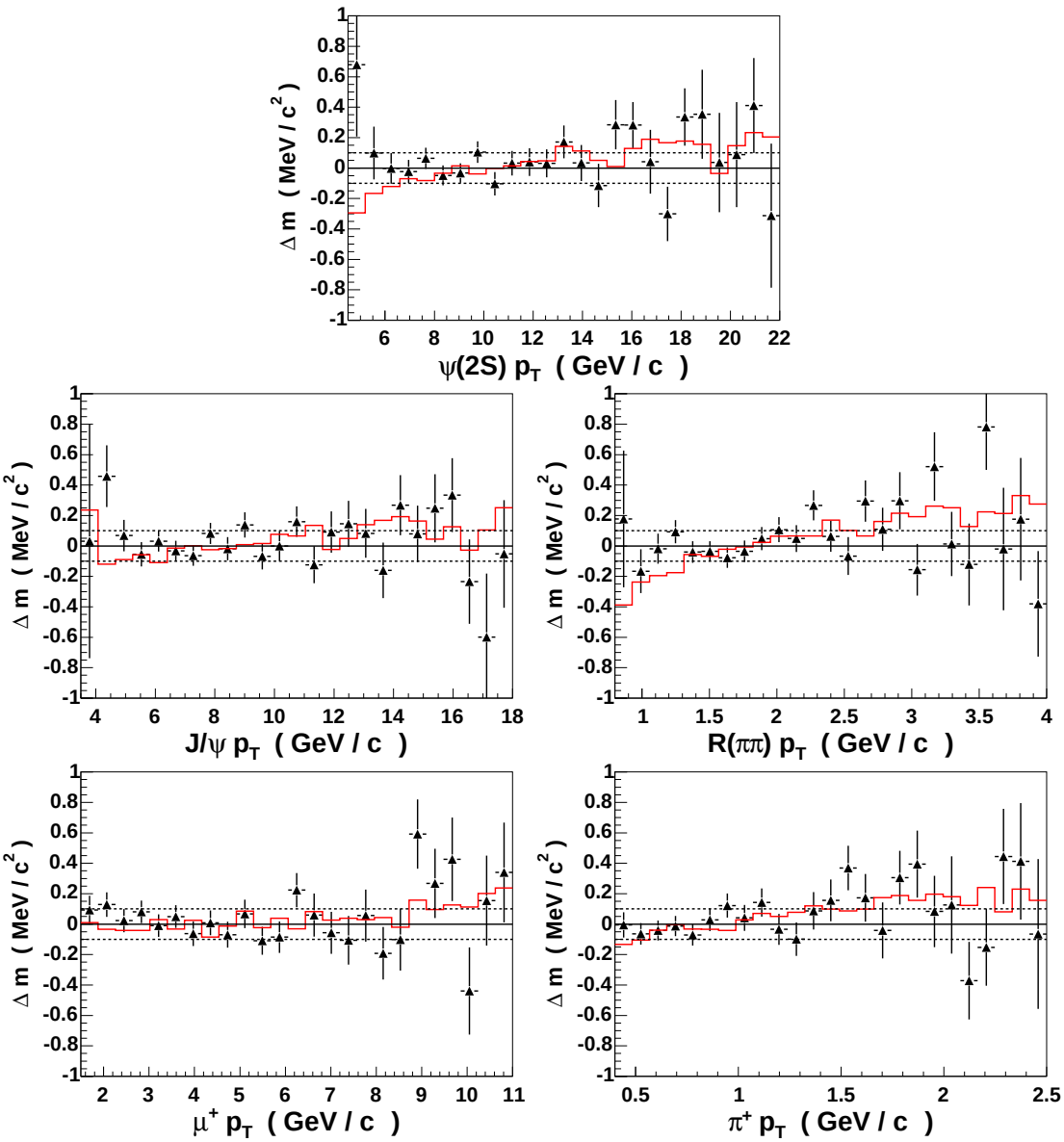

Figure 4.16: Dependence of the measured $\psi(2S)$ mass as a function of the transverse momenta of the involved particles. Also shown (histogram) are the expected position changes from simulation, which show a slightly stronger dependence than the measured data. The lines are added to 'guide the eye'.

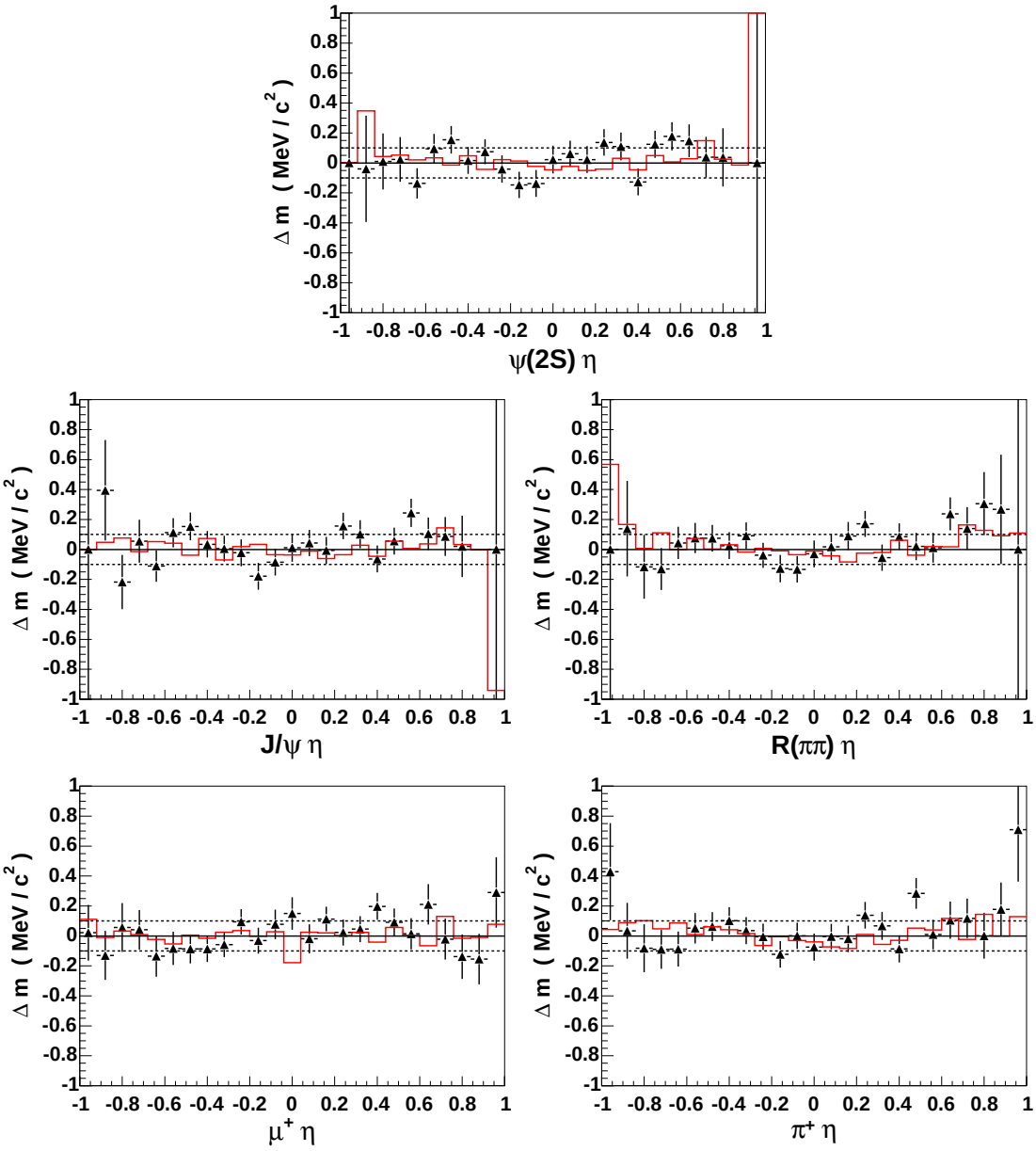

Figure 4.17: Dependence of the measured $\psi(2S)$ mass as a function of the pseudorapidities of the involved particles. Also shown (histogram) are the expected position changes from simulation. The lines are added to 'guide the eye'.

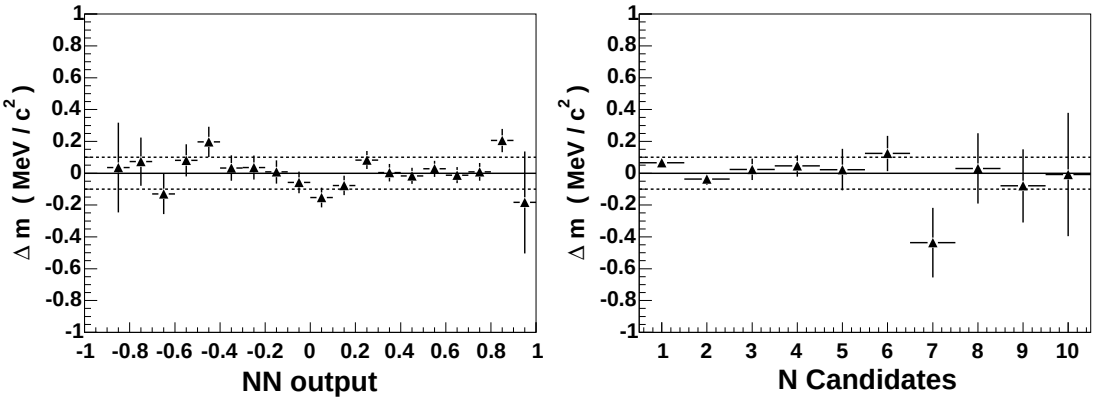

Figure 4.18: Dependence of the measured $\psi(2S)$ mass on the selection variables. The left plot shows the dependence on the neural network output, which is the main selection variable. A low-statistics fluctuation at -0.9 ($\Delta m = -1.99 \pm 0.96$) is outside the shown range. The right plot shows the dependence on the number of candidates after preselection per detector event. In both cases no dependence is observed.

In total, a systematic uncertainty of $0.2\,\mathrm{MeV}/c^2$ is assigned to the $X(3872)$ mass. The final mass measurement of the $X(3872)$ is

$$m_{X(3872)} = 3871.61 \pm 0.16\,(\mathrm{stat}) \pm 0.20\,(\mathrm{syst})\,\mathrm{MeV}/c^2.$$

Chapter 5

Discussion and Outlook

5.1 Summary

The discovery of the $X(3872)$ in 2003 caused a resurgence of interest for charm spectroscopy. To the present day the nature of the $X(3872)$ is unknown. From the variety of possible conventional charmonium states, none is able to give a fitting description of the observed properties of the $X(3872)$. The exceptional agreement between the $X(3872)$ mass and the sum of the D^0 and D^{0*} meson masses quickly prompted the attempt to explain the $X(3872)$ by a molecule-like bound meson state. Also multiquark states, quark-gluon hybrids or glueballs were proposed as possible explanations.

The CDF experiment is well suited to measure the $X(3872)$ in its decay to $J/\psi\pi^+\pi^-$. A dedicated trigger system for clean J/ψ selection and a large tracking volume for precise momentum measurement allow a high-yield and precise reconstruction of $X(3872)$ candidates. The main challenge is the suppression of the vast background due to random track combinations. The measurement of $X(3872)$ properties strongly benefits from the existence of the well-known charmonium state $\psi(2S)$ in the same decay channel at a similar momentum regime. This allows for an independent verification of the involved methods.

Of primary interest for the interpretation of the $X(3872)$ are its quantum numbers J^{PC}, i.e. the spin J and the parity and charge-parity eigenvalues P and C. A data sample corresponding to an integrated luminosity of $\approx 780\ \mathrm{pb}^{-1}$ is used to measure the angular distributions and correlations in the decay X(3872)$\rightarrow$ $J/\psi\pi^+\pi^-$. The measured distribution is compared to expected distributions for different J^{PC} hypotheses and evaluated with a χ^2 approach. The determination of the expected distributions involves the construction of decay matrix elements for the decay X(3872)$\rightarrow$ $J/\psi\pi^+\pi^-$ and a simulation of the CDF detector and trigger system. Table 5.1 lists all tested J^{PC} hypotheses and their agreement with the measurement. From 15 tested J^{PC} hypotheses only the assignments $J^{PC} = 1^{++}$ and $J^{PC} = 2^{-+}$ are able to describe the measured data. All other hypotheses are excluded by at least 3σ. The results of this analysis have been published in reference [60].

hypothesis	χ^2 (11 d.o.f.)	χ^2 probability
1^{++}	13.23	0.28
2^{-+}	13.56	0.26
1^{--}	35.13	2.4×10^{-4}
2^{+-}	38.91	5.49×10^{-5}
2^{--}	39.82	3.84×10^{-5}
1^{+-}	39.82	3.84×10^{-5}
3^{+-}	39.82	3.84×10^{-5}
3^{--}	41.00	2.41×10^{-5}
2^{++}	43.02	1.08×10^{-5}
1^{-+}	45.40	4.13×10^{-6}
0^{-+}	103.59	3.46×10^{-17}
0^{+-}	129.21	$\leq1\times10^{-20}$
0^{++}	163.07	$\leq1\times10^{-20}$

Table 5.1: Result of the angular analysis. Listed are the J^{PC} hypothesis, the obtained χ^2 and the corresponding χ^2 probability for 11 degrees of freedom.

The analysis of the $X(3872)$ mass is important to evaluate the validity of non-conventional $X(3872)$ models. For this purpose, a data sample corresponding to an integrated luminosity of $\approx 2.4\,\mathrm{fb}^{-1}$ is analyzed. The possibility of two separate, nearby $X(3872)$ states which appear as one state because of resolution effects is studied by comparing the observed $X(3872)$ width to predictions for various two-state scenarios and the one-state scenario. The one-state scenario is found to be very well compatible with the observed mass spectrum, not indicating any evidence for two separate states. Under the assumption of two states contributing to the observed signal, 90% and 95% confidence level upper limits on the mass difference between the two signals are set as a function of the fractional contribution of the lower mass signal peak (see figure 5.1). For the most sensitive case when both states contribute equally, the upper limit on Δm is 3.2 (3.6) MeV/c^2 at 90% (95%) confidence level. Assuming a single state, the precise measurement of the $X(3872)$ mass results in

$$m_{X(3872)} = 3871.61 \pm 0.16\,(\mathrm{stat}) \pm 0.20\,(\mathrm{syst})\ \mathrm{MeV}/c^2.$$

5.2 Discussion

5.2.1 Comparison to Previous Results

These measurements significantly and consistently add to the known facts about the $X(3872)$. Both the remaining possibilities for the quantum numbers, $J^{PC} = 1^{++}$ and $J^{PC} = 2^{-+}$, have positive C-parity, supporting the pieces of evidence for

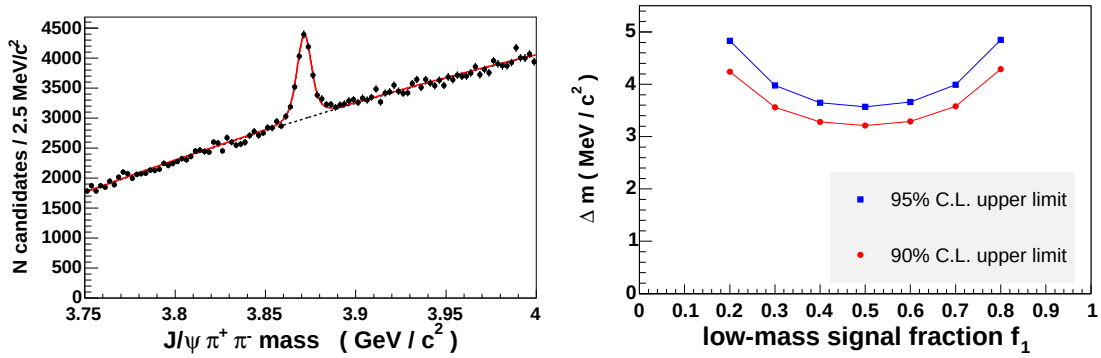

Figure 5.1: The results of the analysis of the measured $J/\psi\pi^+\pi^-$ mass spectrum. The left plot shows the distribution of the measured $J/\psi\pi^+\pi^-$ mass spectrum and a projection of the fit used to determine the mass. The right plot shows the obtained 90% C.L. (red points) and 95% C.L. (blue points) upper limits on the mass difference Δm.

the decay X(3872) $\rightarrow$ $J/\psi\gamma$ [57, 56] and the evidence for the decay X(3872) $\rightarrow$ $J/\psi\omega$ [56]. It also supports the interpretation of the intermediate dipion system as a ρ^0-resonance [59].

The observed peak structure agrees well with the expectations for only one state. This confirms the results from Belle and *BABAR* [7, 61] with high statistical power. They measure the $X(3872)$ mass both in B^+ and B^0 decays. While the statistically very weak result from *BABAR* indicates a 2σ mass deviation in the B^0 decay (also see figure 5.2), the Belle result shows essentially no deviation, but also with low statistical power.

The measured mass of $m_{X(3872)} = 3871.61 \pm 0.16\,(\text{stat}) \pm 0.20\,(\text{syst})\,\text{MeV}/c^2$ is well consistent with the current world average value $m_{PDG} = 3871.4 \pm 0.6\,\text{MeV}/c^2$ [6]. This new measurement has by far the lowest measurement uncertainty of all single $X(3872)$ mass measurements and will dominate the world average $X(3872)$ mass for a long time. In the foreseeable future only LHCb or Super-Belle might be able to measure the $X(3872)$ with equally high statistical power. Figure 5.2 shows the impact of the measured $X(3872)$ mass. Shown are the most recent mass measurements from the single experiments, combined to a world average. Compared to the world average from the Particle Data Group the mass measurement of the $X(3875)$ is omitted, since it is not clear whether this state is connected to the $X(3872)$ or not. This results in a world average mass of $3871.20 \pm 0.39\,\text{MeV}/c^2$ without the new measurement of this thesis. Replacing the old CDF measurement with the new one results in an average of $m = 3871.50 \pm 0.22\,\text{MeV}/c^2$, shifting the value by $0.3\,\text{MeV}/c^2$ to higher masses and reducing the uncertainty of the world average mass by almost a factor of 2.

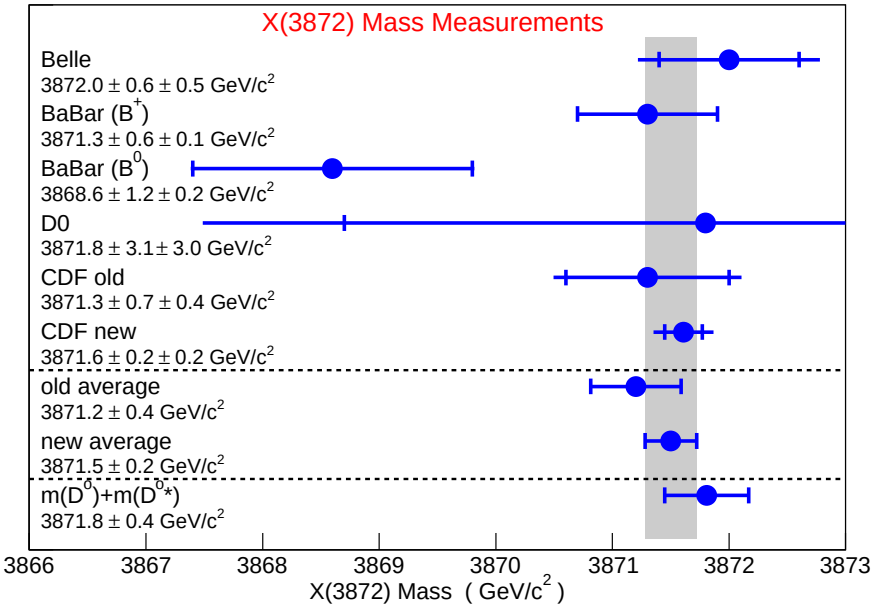

Figure 5.2: An overview of the measured $X(3872)$ masses from the experiments observing the $X(3872)$. Shown are the measurement from Belle [1], *BABAR* (from both B^+ and B^0 decays) [7], DØ [3], and the first CDF measurement [2]. The result from this thesis is shown as the last single measurement entry. Additionally shown is the change in the world average mass due to the new measurement. The current value for the D^0D^{0*} threshold is shown as the last entry. Shown are the statistical and combined errors on each measurement.

5.2.2 Impact on $X(3872)$ Models

The impact of the quantum number analysis result on the charmonium hypothesis is severe. Only two possible states in the $X(3872)$ mass vicinity remain: the 2^3P_1 state χ'_{c1} with $J^{PC} = 1^{++}$ and the 1^1D_2 state η_{c2} with $J^{PC} = 2^{-+}$. For both χ'_{c1} and η_{c2} the observed decay to $J/\psi\rho$ should be suppressed by isospin conservation. Furthermore charmonium models predict $55-200\,\mathrm{MeV}/c^2$ higher masses for the χ'_{c1} and $35-110\,\mathrm{MeV}/c^2$ lower masses for the η_{c2} [19, 20]. It remains to be seen if model changes can satisfactorily and coherently explain these discrepancies. At any rate the charmonium hypothesis is even weaker than before, while its firm exclusion is still not possible.

The hypothesis $J^{PC} = 1^{++}$ agrees with the ground state prediction of 'molecular' $D^0\bar{D}^{0*}$ bound state models. The performed precise mass measurement of the $X(3872)$ adds crucial information to this hypothesis. By comparing the central value of the average to the world average value of the sum of the 'molecular constituents', $m_{D^0D^{0*}} = 3871.81\,\mathrm{MeV}/c^2$, it can be seen that the $X(3872)$ is lighter by $0.3 \pm 0.4\,\mathrm{MeV}/c^2$. This still allows for a simple bound state. Unfortunately, the involved uncertainty does not allow to firmly determine the heavier system. With the new $X(3872)$ mass measurement, this uncertainty is now dominated by the

uncertainties on the D masses.

The quantum numbers $J^{PC} = 1^{++}$ agree with the prediction of various multiquark models. The model of Maiani *et al.* is however disfavored, since there is no evidence for two separate states. The proposed mass difference of (8 ± 3) MeV/c^2 is beyond the obtained upper limits for the mass difference. This either means that there simply is no prominent second neutral state decaying into $J/\psi\pi^+\pi^-$ or that the two possible states are so close in mass that they cannot be resolved by experiment. While multiquark hypotheses remain an interesting field, no model with verifiable predictions has so far turned out to be correct.

All hypotheses predicting other quantum numbers than $J^{PC} = 1^{++}$ or $J^{PC} = 2^{-+}$ are excluded. This includes the glueball hypothesis, predicting $J^{PC} = 1^{--}$.

The bottom line is that the nature of the $X(3872)$ remains to be unclear. While the results from this thesis considerably add to the available information about the $X(3872)$, they unfortunately do not suffice to draw firm conclusions, neither about the question 'Is the conventional charmonium hypothesis for the $X(3872)$ excluded?' nor about the less interesting question 'Are the main alternatives excluded?' It should however be noted that all results are in agreement with the molecular interpretation of the $X(3872)$.

5.3 Outlook

The observation of the $X(3872)$ and the challenges to explain its properties in a consistent way lead to newfound interest in particle spectroscopy. Experimental interest in the $X(3872)$ has in the meantime decreased to some degree, since no new properties are left to study that are easily measurable. However, a reinvestigation of some properties might be of interest, like the study of the possible decay channels X(3872)$\rightarrow J/\psi\pi^0\pi^0$ or X(3872)$\rightarrow J/\psi\omega$, or a measurement of the dipion system.

The possibility of the $X(3872)$ being an unconventional state has in the meantime been strengthened by the observation of further charmonium-like particles. To the present day, nine further new particles have been observed. They are listed in table 5.2. These states can not all be explained by one model. They cannot all be charmonium states since the number of states overpopulate the expected charmonium spectrum. As for the $X(3872)$, various explanations are available for most of the states and the picture is completely unclear how the entirety of all states can fit into a given picture. A nice overview for the new XYZ states can be found in references [18, 105]. One state is particularly interesting. The $Z(4430)$, observed by Belle [106] in the decay mode to $\psi(2S)\pi^+$, is a charged particle. This cannot be achieved by a regular, neutral $c\bar{c}$ charmonium state. If confirmed as a real particle, this would unambiguously proof the existence of an exotic state. All of the observed states are observed with a significance of more than 5σ. Still, the statistical basis for the single observations is quite low, so that independent confirmations and more data are welcome to clarify the picture. All the combined information, even allowing

state	mass (MeV/c^2)	Γ (MeV)	decay mode	experiment
$Z(3930)$	3929 ± 5	29 ± 10	$D\bar{D}$	Belle
$X(3940)$	3942 ± 9	37 ± 17	$D\bar{D}^*$	Belle
$Y(3940)$	3943 ± 17	87 ± 34	$J/\psi\omega$	*BABAR*, Belle
$Y(4008)$	4008^{+82}_{-49}	226^{+97}_{-80}	$J/\psi\pi^+\pi^-$	Belle
$X(4160)$	4156 ± 29	139^{+113}_{-65}	$D^*\bar{D}^*$	Belle
$Y(4260)$	4264 ± 12	83 ± 22	$J/\psi\pi^+\pi^-$	*BABAR*, Belle, CLEO
$Y(4350)$	4361 ± 13	74 ± 18	$\psi(2S)\pi^+\pi^-$	*BABAR*, Belle
$Z(4430)$	4433 ± 5	45^{+35}_{-18}	$\psi(2S)\pi^+$	Belle
$Y(4660)$	4664 ± 12	48 ± 15	$\psi(2S)\pi^+\pi^-$	Belle

Table 5.2: Overview of the observed XYZ states (from reference [18]). Listed are the state, its mass and width, the decay mode and the observing experiments.

for wrongly claimed signals, quite clearly suggest that the regular quark model is not able to satisfactorily describe the experimental observations.

So far, all observations were made in the c-quark sector. Most exotic interpretations should equally well hold in the b-quark sector. So a complete range of states potentially awaits observation in the b-quark sector, where so far only the radial excitations of the quark model $b\bar{b}$ Υ states are known. However, low statistics will be an enormous challenge, both at the Tevatron and even more at the B-factories. This challenge could be met at the Tevatron or the B-factories if the production cross section of these yet unknown states is sufficiently high. In fact, recent observations by Belle indicate the existence of a state at the $\Upsilon(5S)$ mass, which does not agree with the known $\Upsilon(5S)$ properties [107]. If searches remain however unsuccessful, the LHCb experiment with its large event rate should be able to make firm statements about the existence of such states in the foreseeable future.

Spectroscopy analyses are at the moment reaping the benefits of continuous and successful data collection. While the $X(3872)$ might turn out to be a conventional charmonium state, it is still clear from the $X(3872)$ and the zoo of unaccounted states that we do not yet understand the physics of bound states at low energies. This sector will thus be a continuous field of interest in the future, awaiting breakthroughs both experimentally and theoretically. It is not only of interest to look for new physics at the highest available energies — we learned from the $X(3872)$ that unexpected phenomena are still to be found in seemingly well-understood energy ranges.

5.4 Conclusion

This thesis studied properties of the charmonium-like $X(3872)$ state, which is an exotic matter candidate. The measurements are performed using a data sample collected with the CDF experiment. This sample features the world's largest amount

of $X(3872)$ particles. Constraints on spin, parity, and charge conjugation parity of the $X(3872)$ are obtained by studying the angular distributions and correlations in the exclusive decay mode $X(3872) \to J/\psi\pi^+\pi^-$. The assignments $J^{PC} = 1^{++}$ and $J^{PC} = 2^{-+}$ are the only hypotheses consistent with the measured data. All other tested hypotheses are excluded by more than 3σ confidence level. To test the hypothesis of two separate states with similar mass, the signal mass distribution of the $X(3872)$ is investigated. It is concluded that the measured spectrum is very well compatible with only one state. Assuming equal production and decay rates between two possible states, an upper limit on their mass difference Δm is set to be 3.2 (3.6) MeV/c^2 at 90% (95%) confidence level. A precise $X(3872)$ mass measurement is performed, resulting in $m_{X(3872)} = 3871.61 \pm 0.16$ (stat)± 0.20 (syst) MeV/c^2. This is the most precise single measurement to date, reducing the world average mass uncertainty by nearly 50%. All measurements are crucial inputs for the developing understanding of the $X(3872)$.

Appendix A

Reference Distributions for the J^{PC} Analysis

A.1 Angular Distributions of All Tested J^{PC} Hypotheses

On the following pages the angular distributions used for the discrimination between different J^{PC} hypotheses are shown. The histograms show the distributions with and without the effects of detector acceptance (dotted line). Also shown is the distribution using the three-dimensional binning, employed to determine the χ^2 value in the analysis.

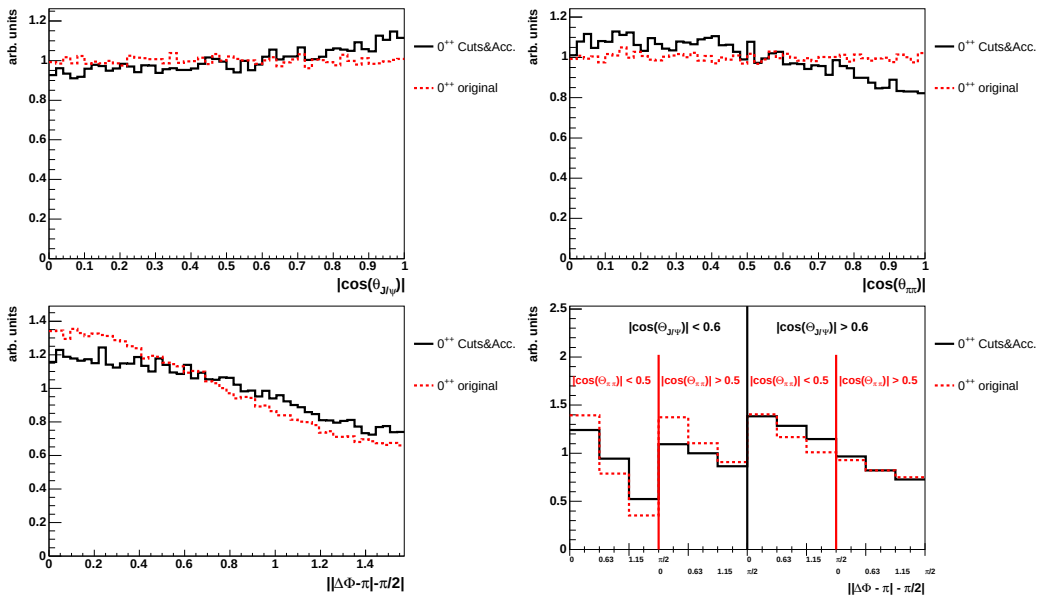

Figure A.1: Angular distributions for the hypothesis $J^{PC} = 0^{++}$.

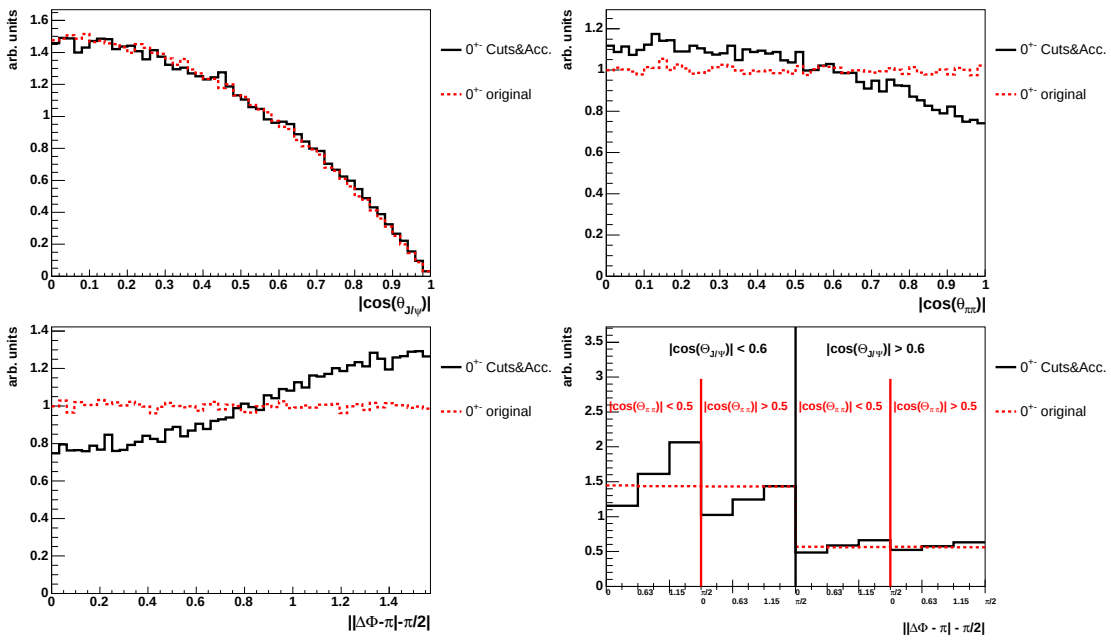

Figure A.2: Angular distributions for the hypothesis $J^{PC} = 0^{+-}$.

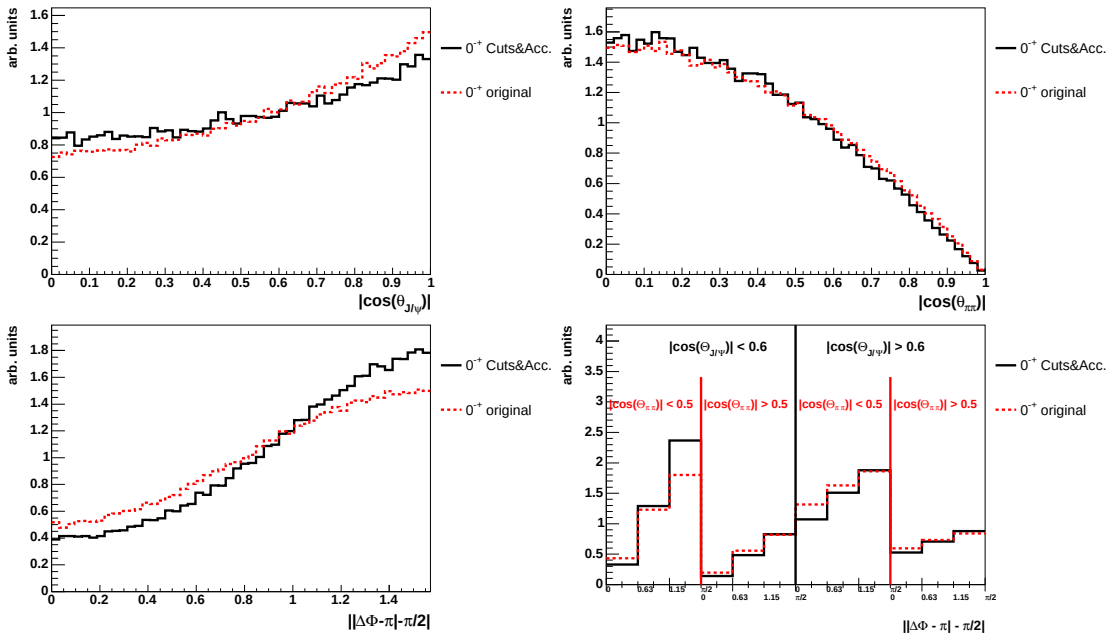

Figure A.3: Angular distributions for the hypothesis $J^{PC} = 0^{-+}$.

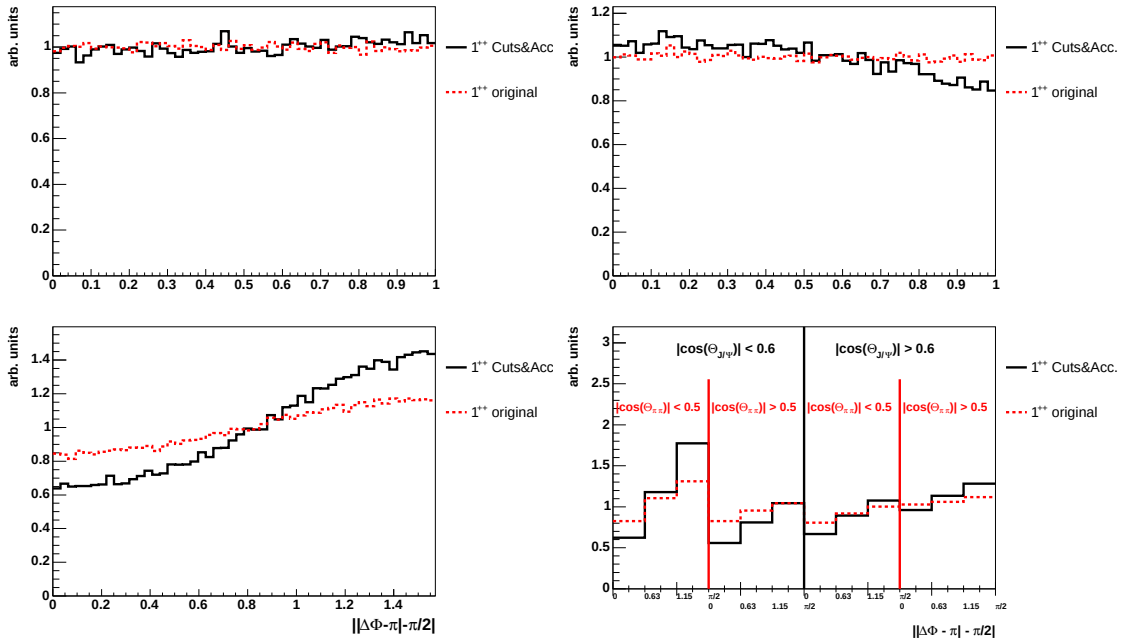

Figure A.4: Angular distributions for the hypothesis $J^{PC} = 1^{++}$.

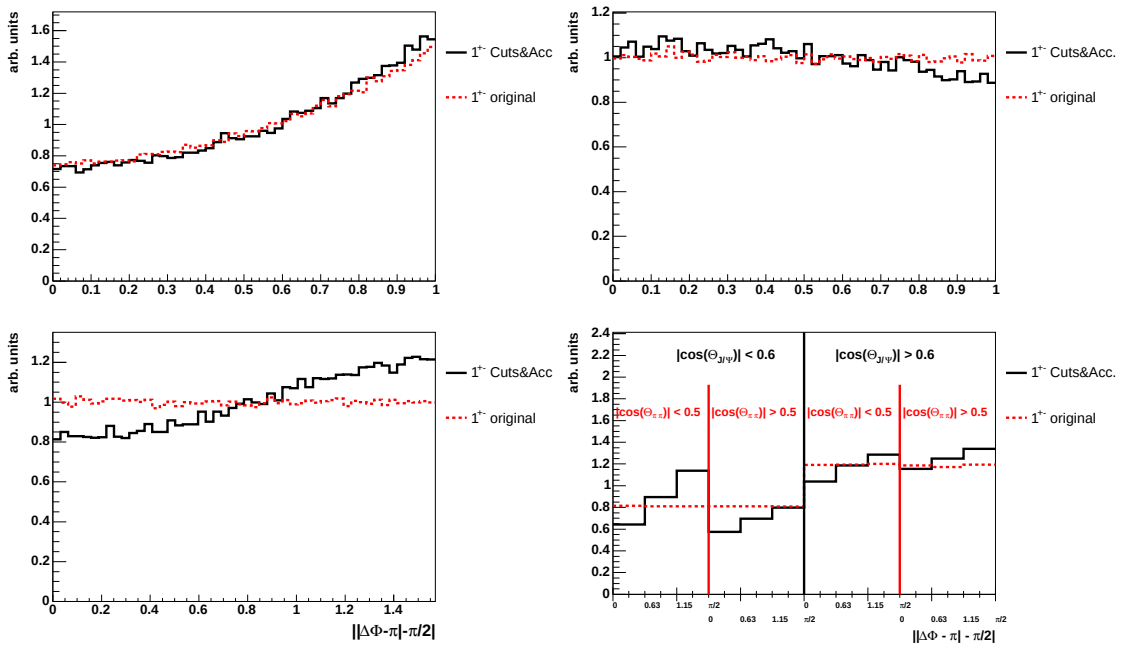

Figure A.5: Angular distributions for the hypothesis $J^{PC} = 1^{+-}$.

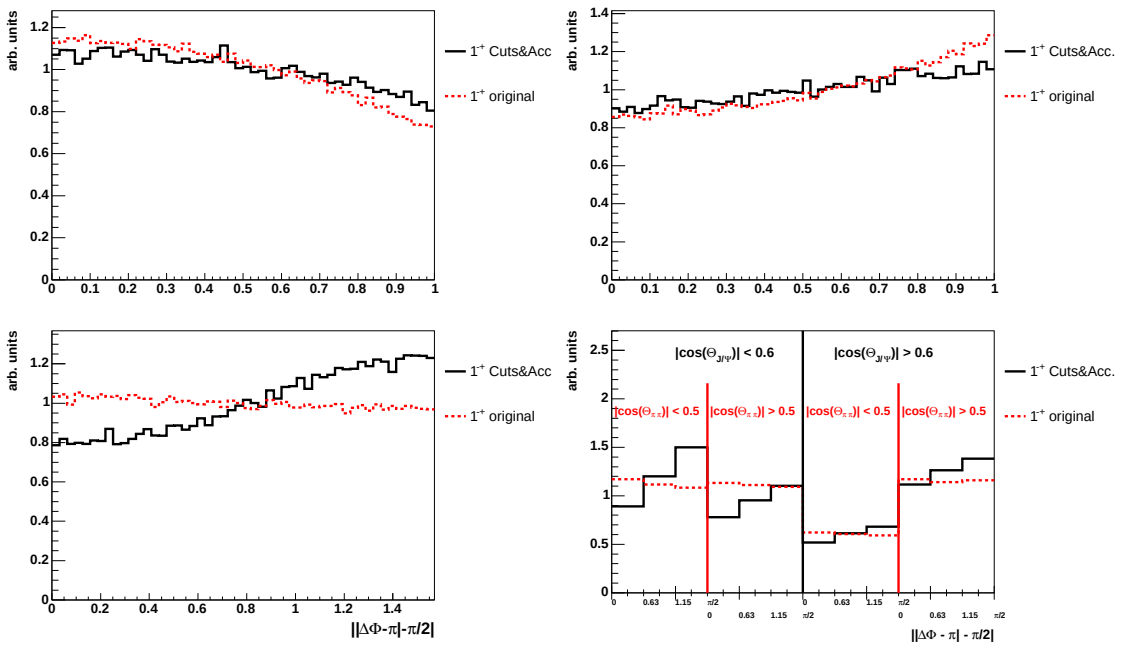

Figure A.6: Angular distributions for the hypothesis $J^{PC} = 1^{-+}$.

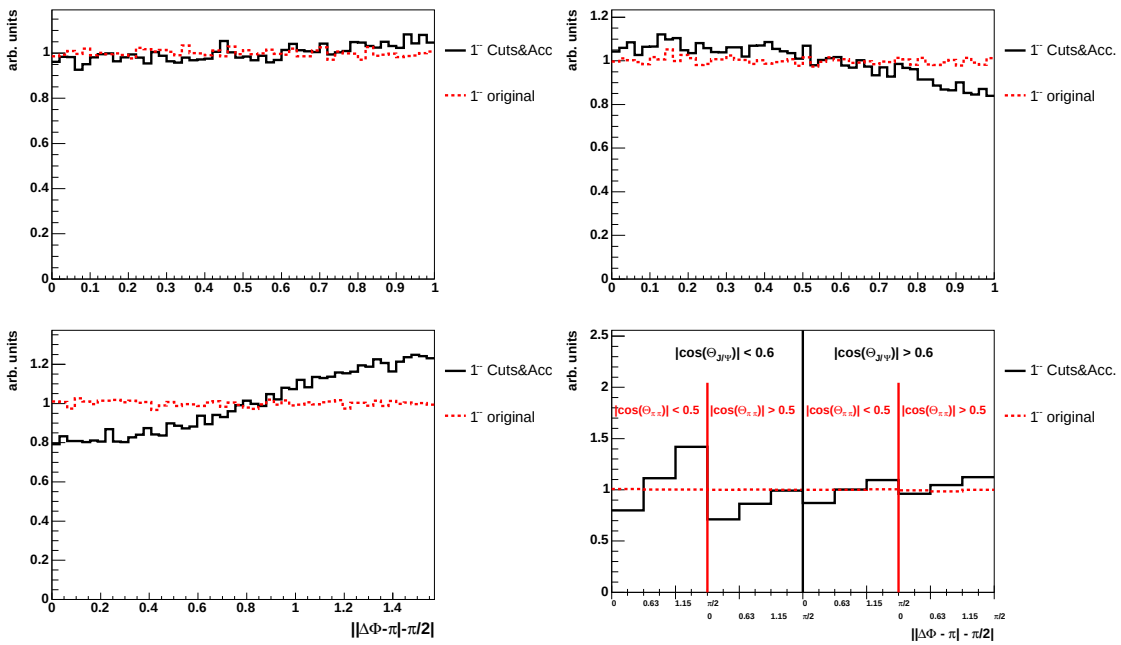

Figure A.7: Angular distributions for the hypothesis $J^{PC} = 1^{--}$.

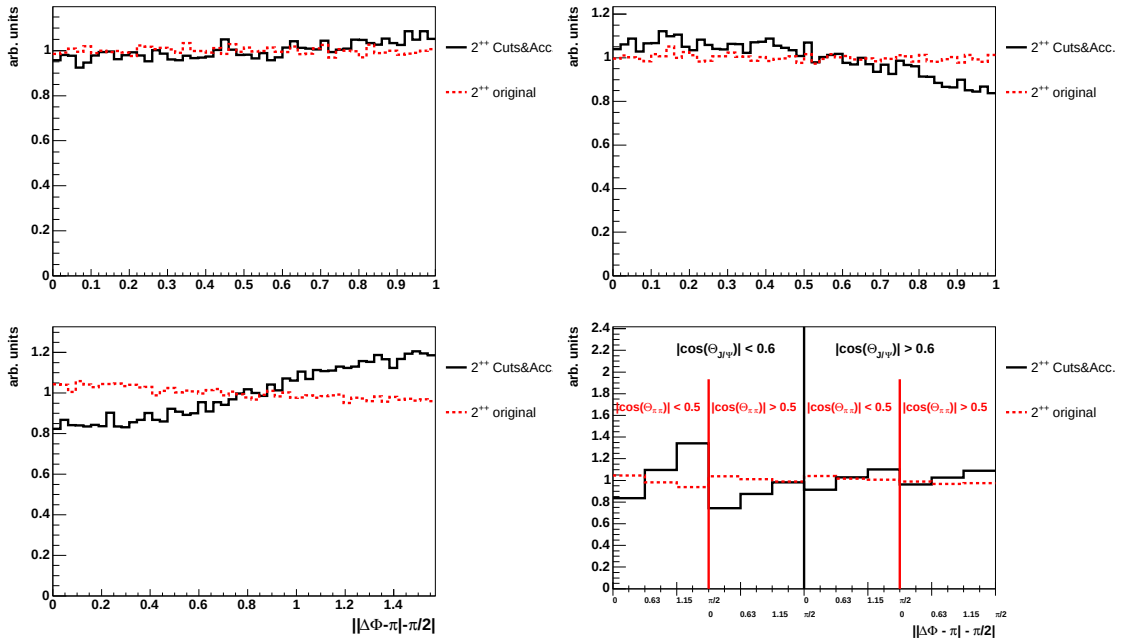

Figure A.8: Angular distributions for the hypothesis $J^{PC} = 2^{++}$.

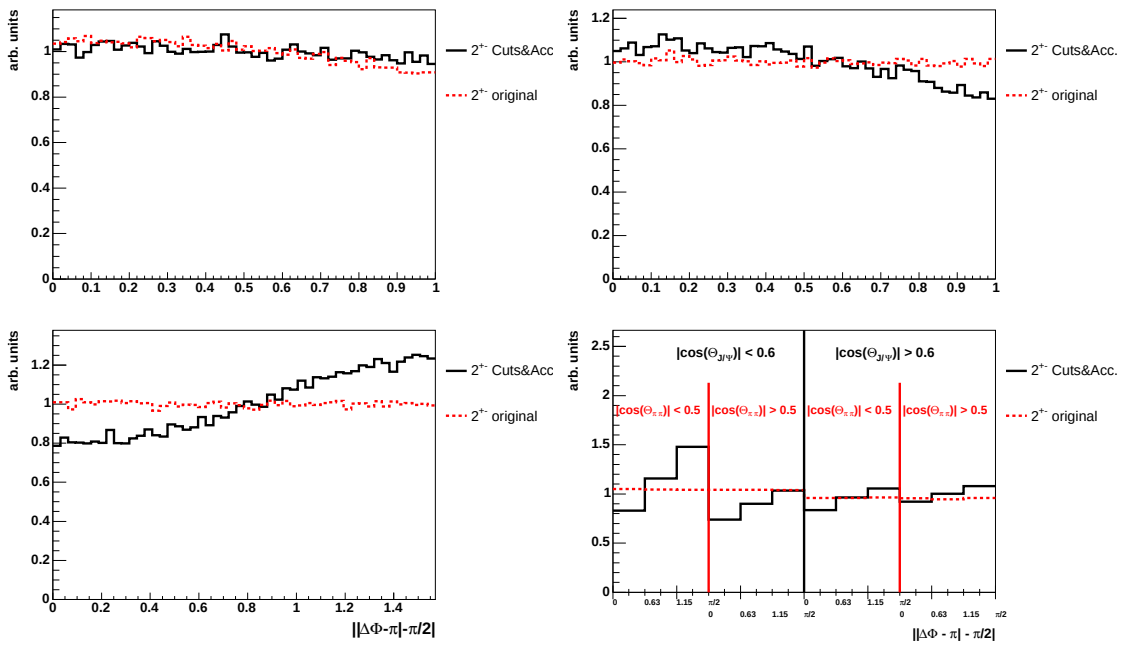

Figure A.9: Angular distributions for the hypothesis $J^{PC} = 2^{+-}$.

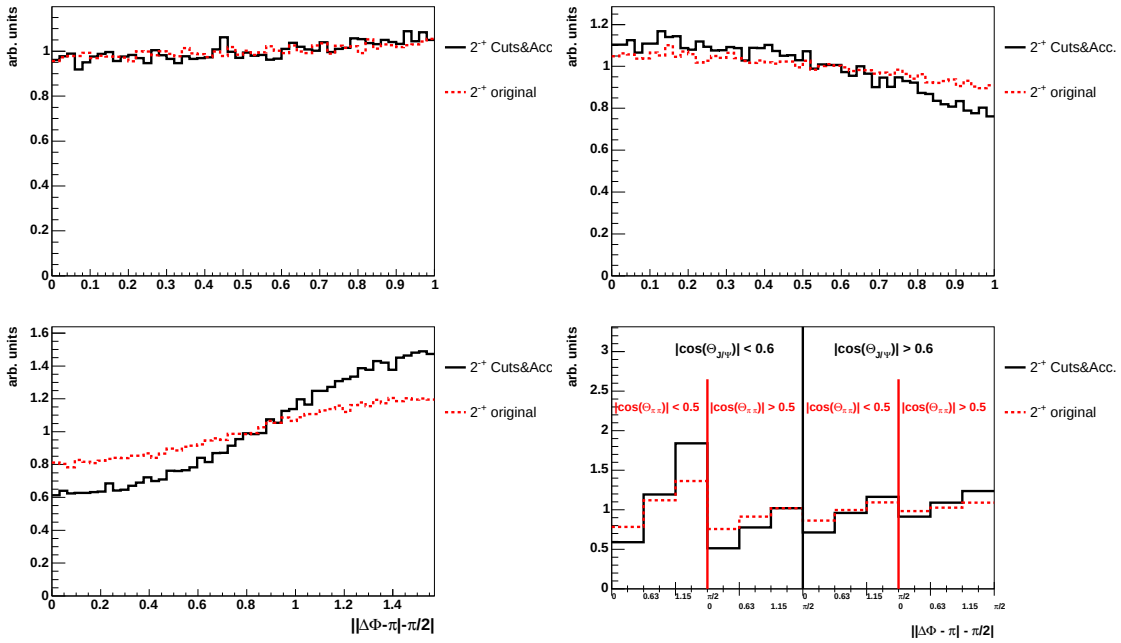

Figure A.10: Angular distributions for the hypothesis $J^{PC} = 2^{-+}$.

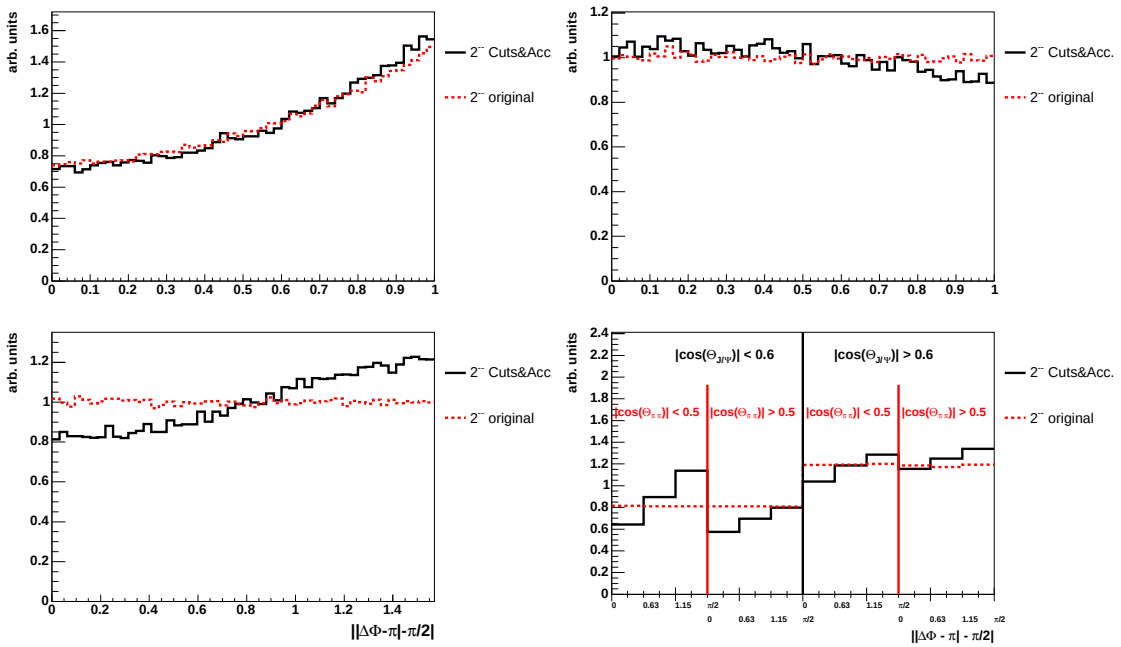

Figure A.11: Angular distributions for the hypothesis $J^{PC} = 2^{--}$.

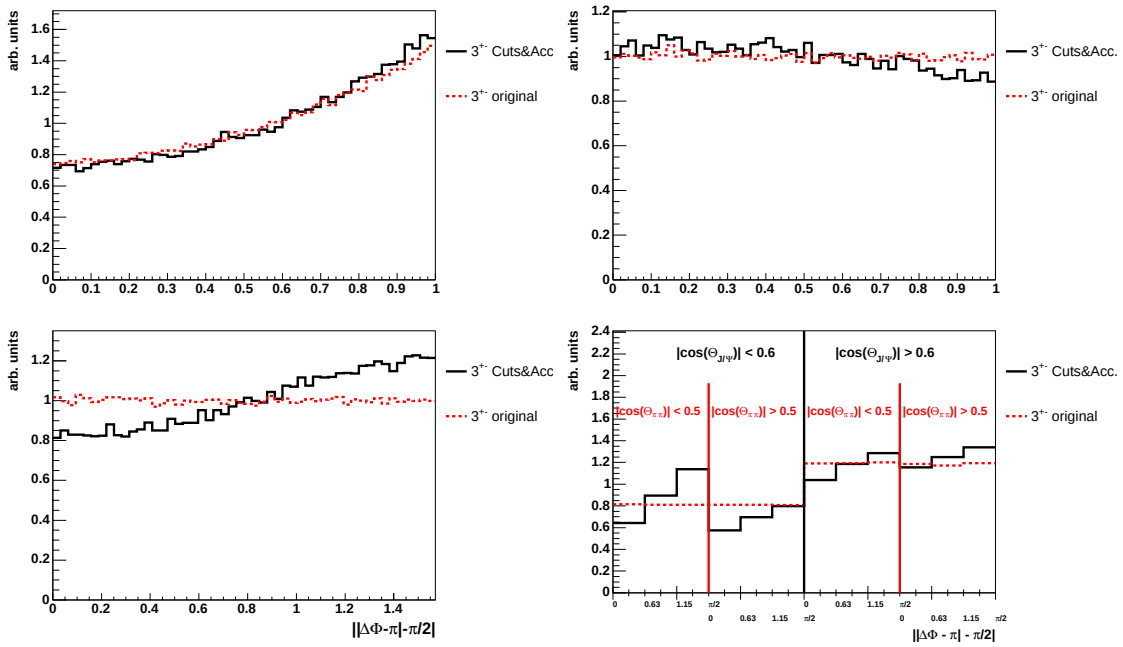

Figure A.12: Angular distributions for the hypothesis $J^{PC} = 3^{+-}$.

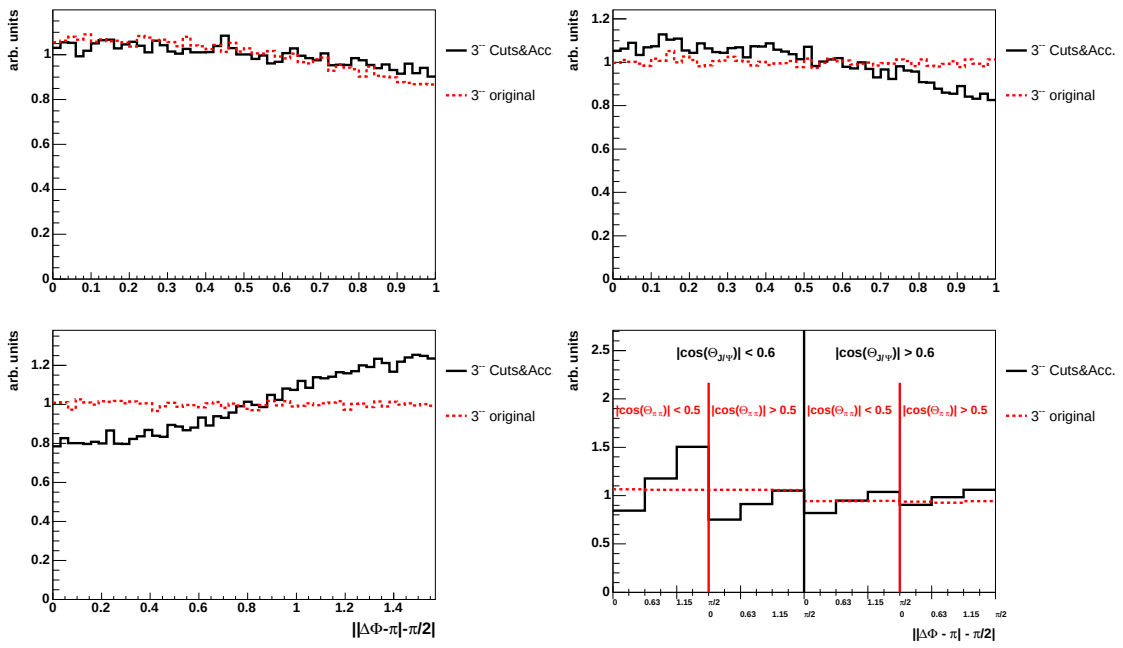

Figure A.13: Angular distributions for the hypothesis $J^{PC} = 3^{--}$.

A.2 Fits to the $J/\psi\pi\pi$ Mass Spectrum

In this section all fits to the measured data $J/\psi\pi^+\pi^-$ mass spectrum are shown, which are performed to obtain the distribution of the three-dimensional angular distribution. The fit function is parameterized by a second-order polynomial for the combinatorial background, and a Gaussian function with position $m = 3871.7\ \mathrm{MeV}/c^2$ and width $\sigma = 5.0\ \mathrm{MeV}/c^2$.

In the following figures, the upper left plot shows the fit result in the fitted mass window. The upper right plot shows the same spectrum and the same fit in a narrower mass window for a closer look at the signal peak. The lower left plot shows the residuals between fit value and histogram value, i.e. the difference between measured value and fitted value, divided by the square root of the measured data value. In the lower right plot the values from the lower left plot are filled into a histogram and fitted with a Gaussian function. The fit must be compatible with a width of $\sigma = 1$ and and a mean value of 0, if the fit-model is correct.

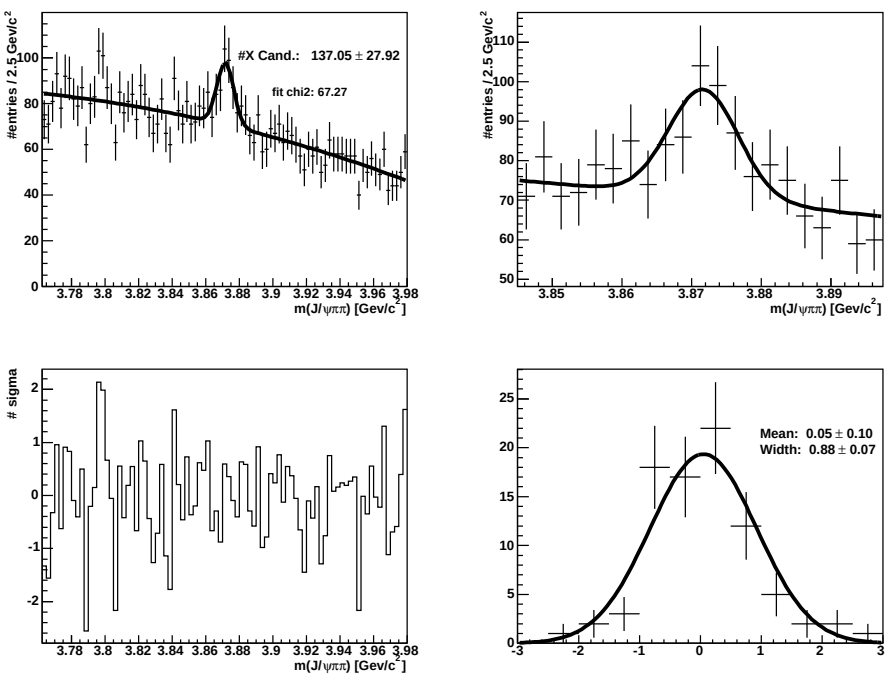

Figure A.14: Fit to the mass spectrum in the angular bin: $|\cos(\theta_{J/\psi})| < 0.6$, $|\cos(\theta_{\pi\pi})| < 0.5$, $0 < ||\Delta\Phi - \pi| - \frac{\pi}{2}| < 0.63$.

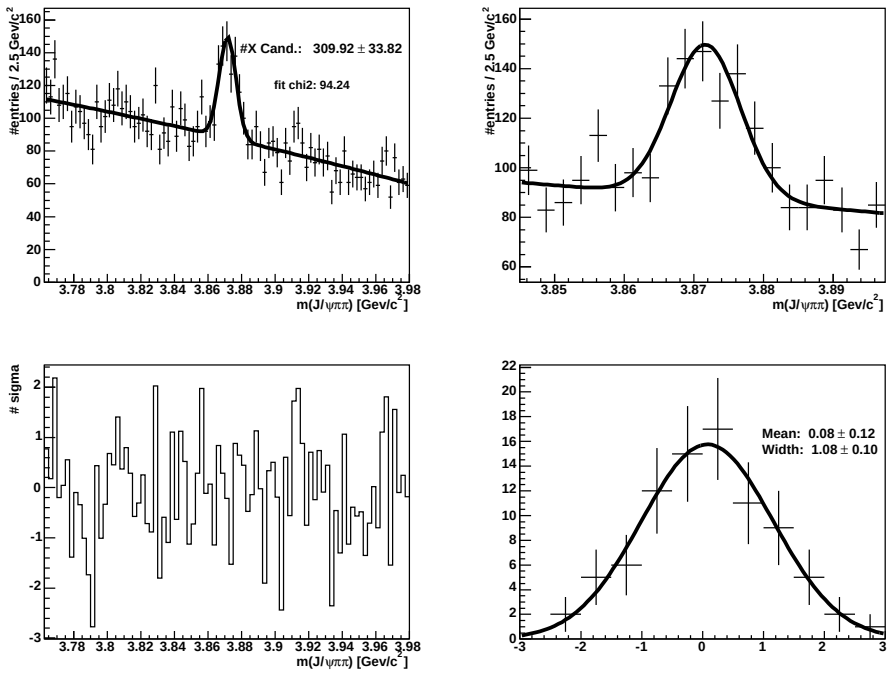

Figure A.15: Fit to the mass spectrum in the angular bin: $|\cos(\theta_{J/\psi})| < 0.6$, $|\cos(\theta_{\pi\pi})| < 0.5$, $0.63 < ||\Delta\Phi - \pi| - \frac{\pi}{2}| < 1.15$.

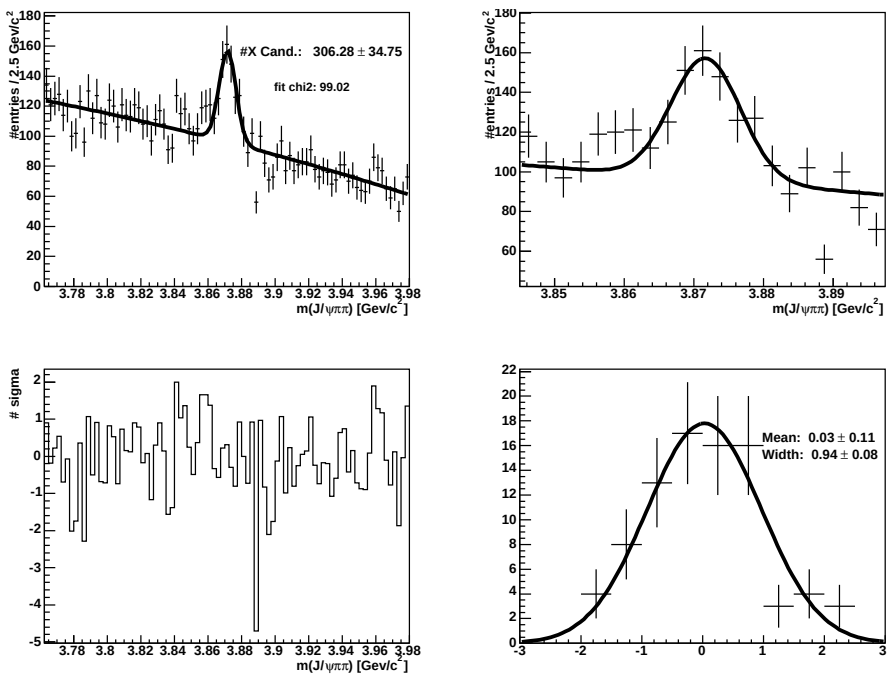

Figure A.16: Fit to the mass spectrum in the angular bin: $|\cos(\theta_{J/\psi})| < 0.6$, $|\cos(\theta_{\pi\pi})| < 0.5$, $1.15 < ||\Delta\Phi - \pi| - \frac{\pi}{2}| < \pi/2$.

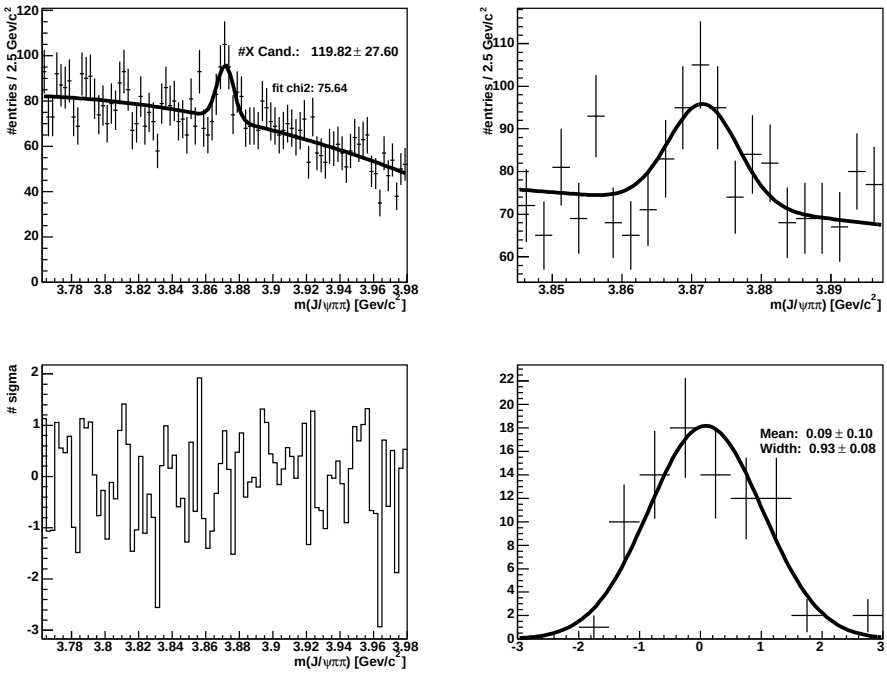

Figure A.17: Fit to the mass spectrum in the angular bin: $|\cos(\theta_{J/\psi})| < 0.6$, $|\cos(\theta_{\pi\pi})| > 0.5$, $0 < ||\Delta\Phi - \pi| - \frac{\pi}{2}| < 0.63$.

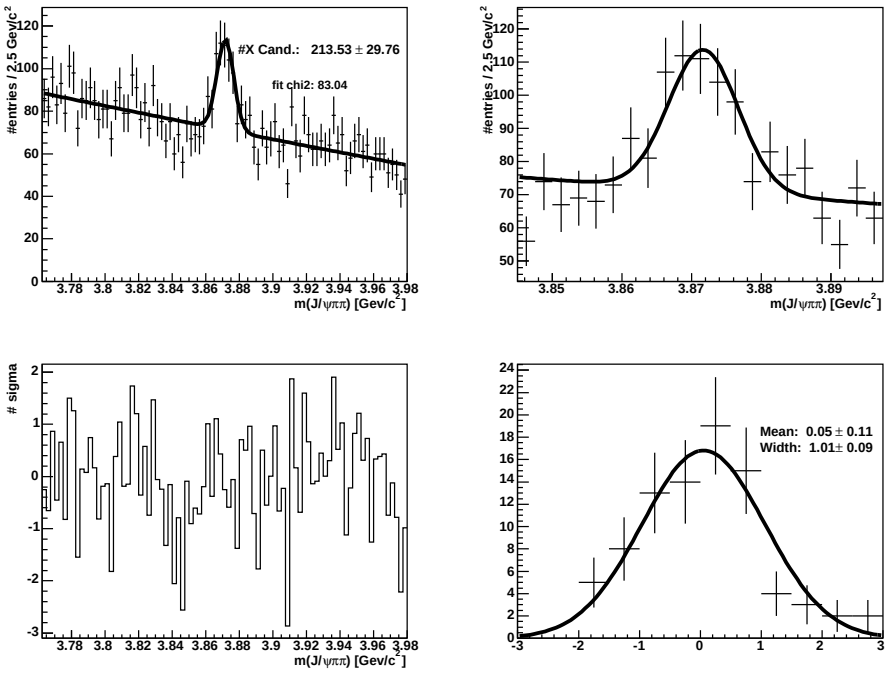

Figure A.18: Fit to the mass spectrum in the angular bin: $|\cos(\theta_{J/\psi})| < 0.6$, $|\cos(\theta_{\pi\pi})| > 0.5$, $0.63 < ||\Delta\Phi - \pi| - \frac{\pi}{2}| < 1.15$.

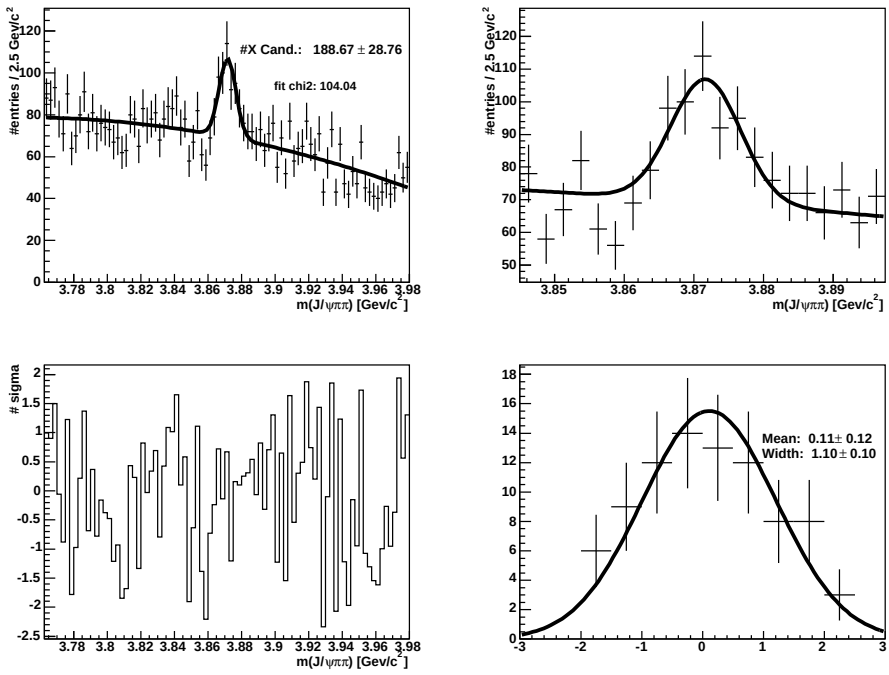

Figure A.19: Fit to the mass spectrum in the angular bin: $|\cos(\theta_{J/\psi})| < 0.6$, $|\cos(\theta_{\pi\pi})| > 0.5$, $1.15 < ||\Delta\Phi - \pi| - \frac{\pi}{2}| < \pi/2$.

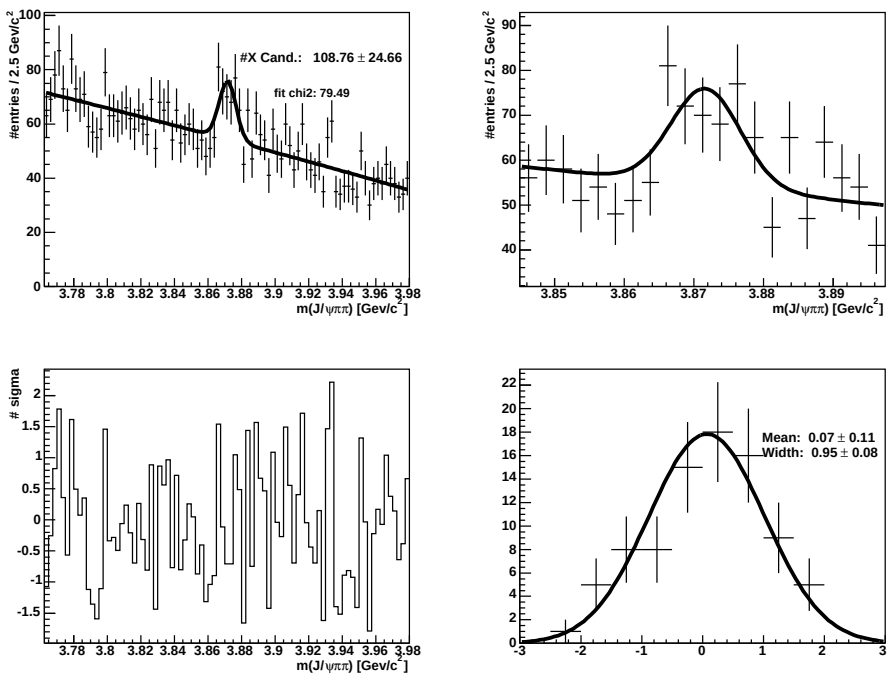

Figure A.20: Fit to the mass spectrum in the angular bin: $|\cos(\theta_{J/\psi})| > 0.6$, $|\cos(\theta_{\pi\pi})| < 0.5$, $0 < ||\Delta\Phi - \pi| - \frac{\pi}{2}| < 0.63$.

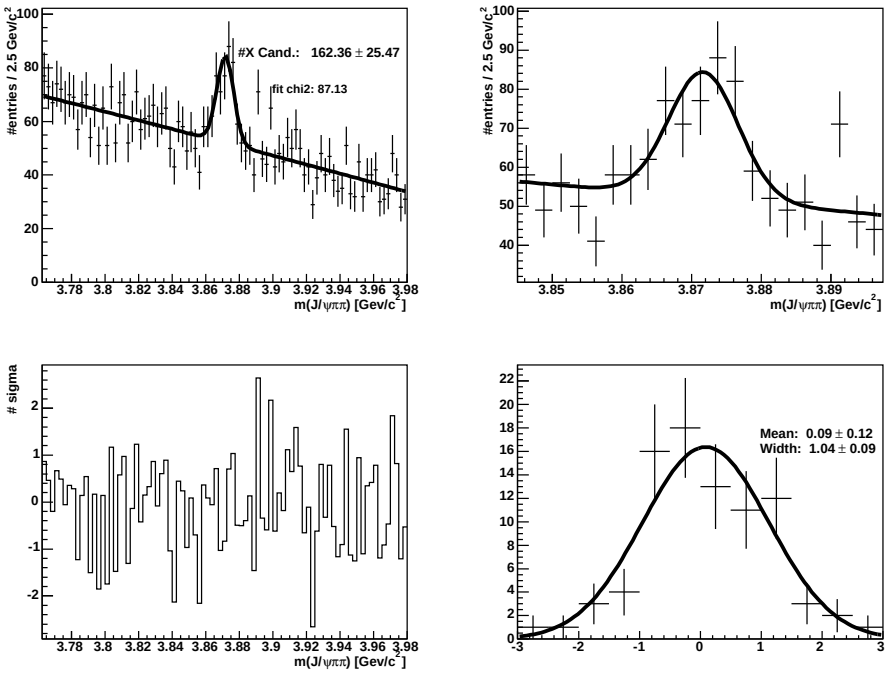

Figure A.21: Fit to the mass spectrum in the angular bin: $|\cos(\theta_{J/\psi})| > 0.6$, $|\cos(\theta_{\pi\pi})| < 0.5$, $0.63 < ||\Delta\Phi - \pi| - \frac{\pi}{2}| < 1.15$.

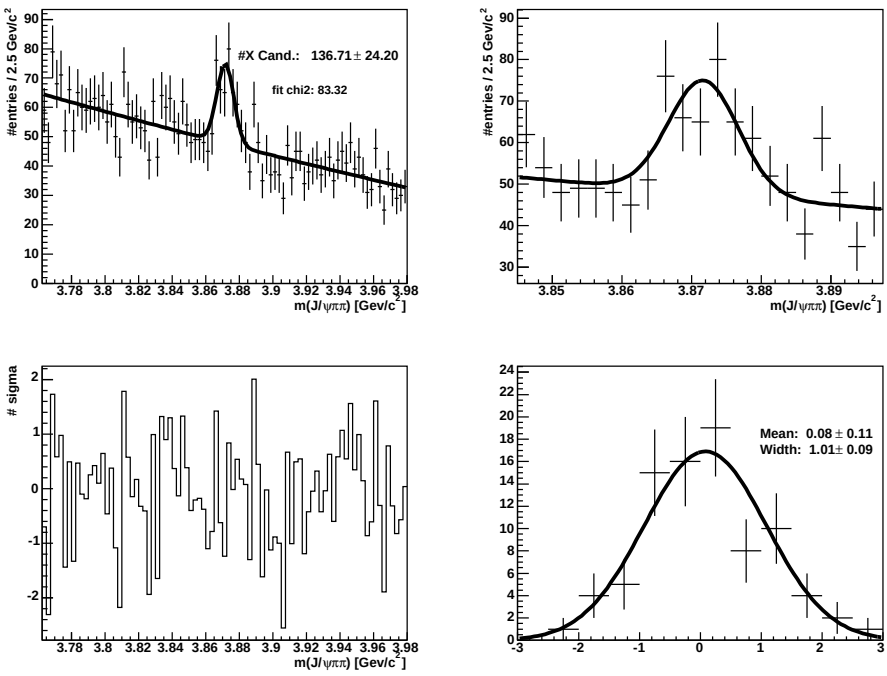

Figure A.22: Fit to the mass spectrum in the angular bin: $|\cos(\theta_{J/\psi})| > 0.6$, $|\cos(\theta_{\pi\pi})| < 0.5$, $1.15 < ||\Delta\Phi - \pi| - \frac{\pi}{2}| < \pi/2$.

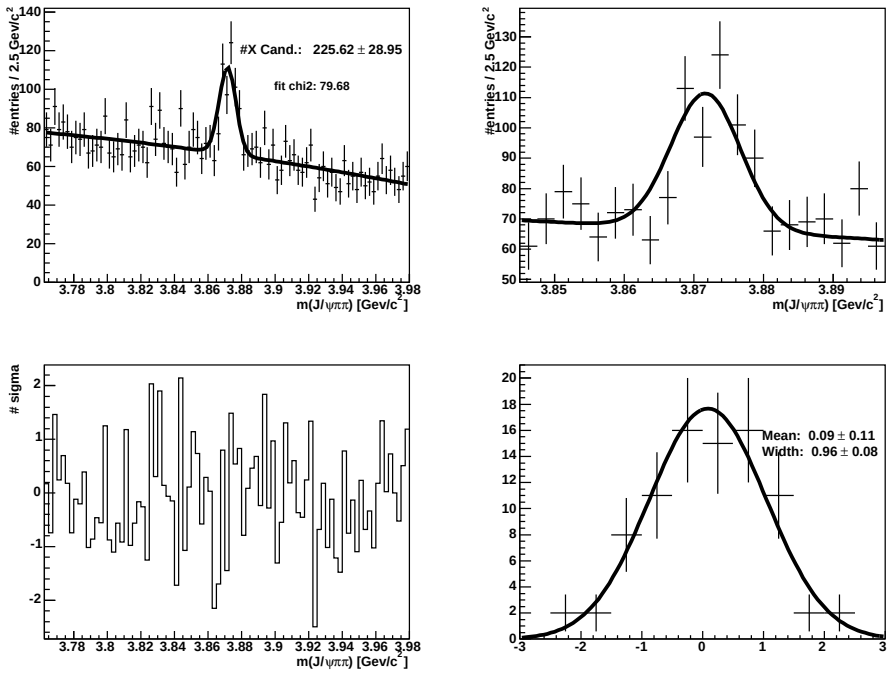

Figure A.23: Fit to the mass spectrum in the angular bin: $|\cos(\theta_{J/\psi})| > 0.6$, $|\cos(\theta_{\pi\pi})| > 0.5$, $0 < ||\Delta\Phi - \pi| - \frac{\pi}{2}| < 0.63$.

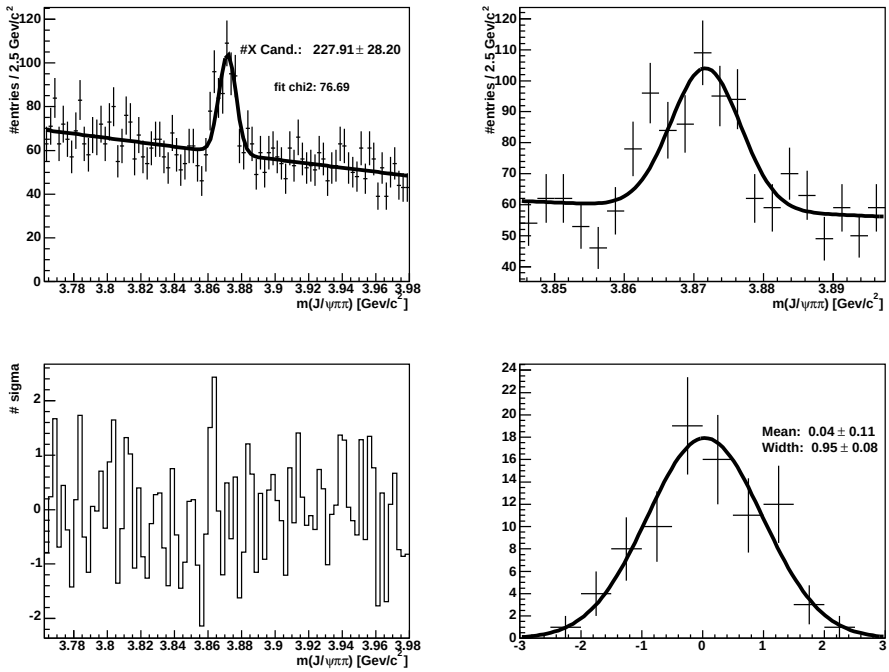

Figure A.24: Fit to the mass spectrum in the angular bin: $|\cos(\theta_{J/\psi})| > 0.6$, $|\cos(\theta_{\pi\pi})| > 0.5$, $0.63 < ||\Delta\Phi - \pi| - \frac{\pi}{2}| < 1.15$.

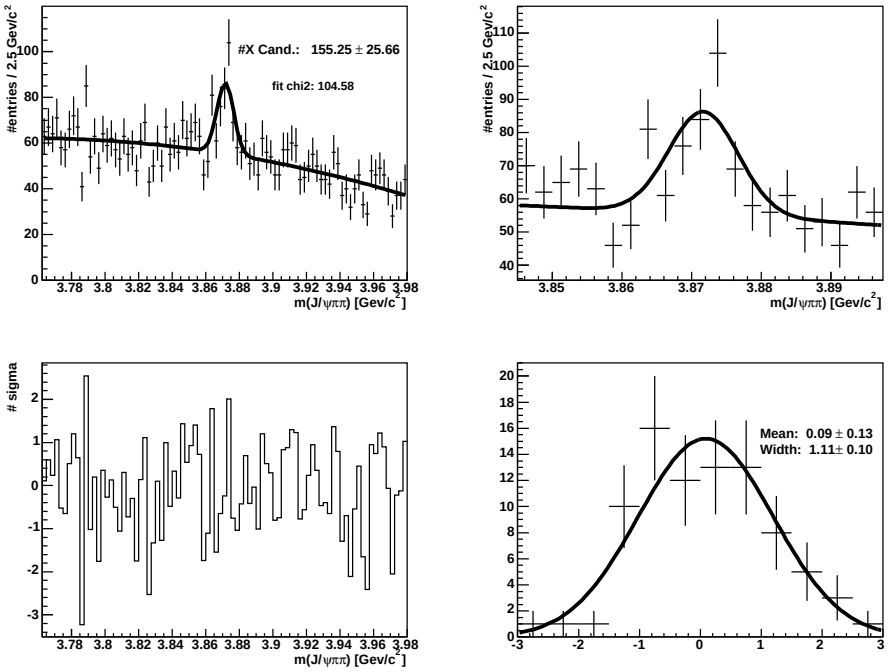

Figure A.25: Fit to the mass spectrum in the angular bin: $|\cos(\theta_{J/\psi})| > 0.6$, $|\cos(\theta_{\pi\pi})| > 0.5$, $1.15 \leq ||\Delta\Phi - \pi| - \frac{\pi}{2}| \leq \pi/2$.

A.3 Angular Comparison for All Tested J^{PC} Hypotheses

This section shows the comparison plots between measured angular distributions and expectations for different J^{PC} hypotheses. Shown are the graphical representation and a table of the residuals for each angular interval. The numbering of the intervals in the table uses interval 1 as the leftmost bin in the histogram and interval 12 as the rightmost bin. The numbers in the table have a slight mismatch between residual and squared value because of rounding inaccuracies.

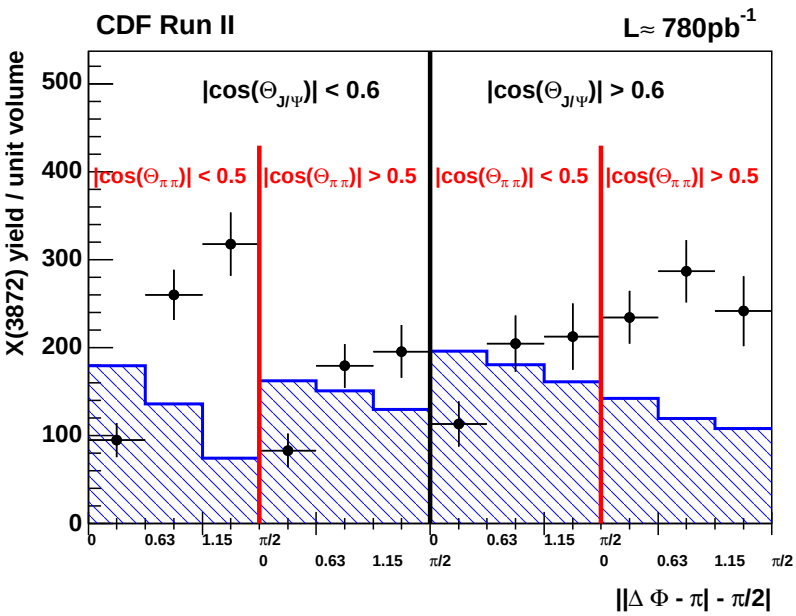

Bin	Resid.	χ_i^2
1	-4.4	19.2
2	4.4	19.2
3	6.8	45.6
4	-4.2	17.3
5	1.1	1.3
6	2.2	4.9
7	-3.2	10.5
8	0.8	0.6
9	1.4	1.9
10	3.1	9.4
11	4.7	22.2
12	3.4	11.2
total		163.1

Figure A.26: Comparison of measurement and prediction for $J^{PC} = 0^{++}$.

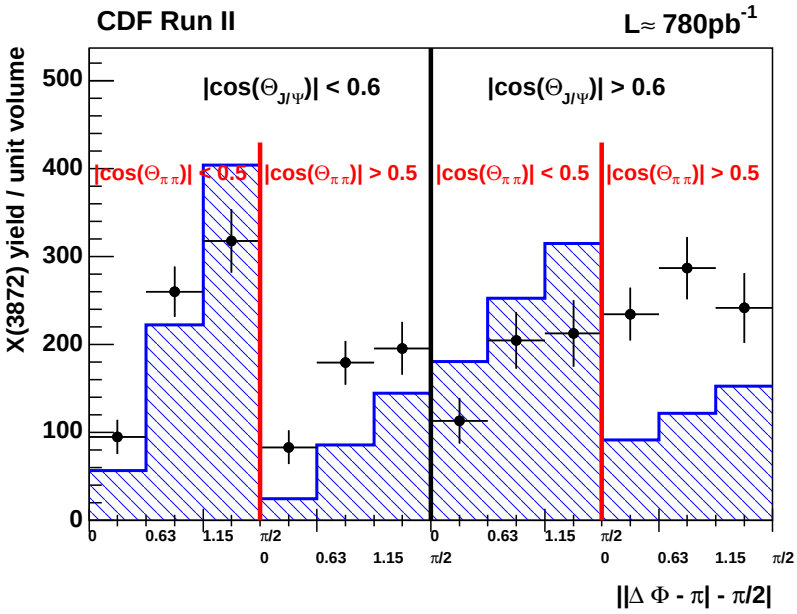

Bin	Resid.	χ_i^2
1	2.0	4.0
2	1.3	1.7
3	-2.4	5.8
4	3.1	9.4
5	3.7	13.9
6	1.7	2.9
7	-2.6	7.0
8	-1.5	2.2
9	-2.7	7.4
10	4.8	22.6
11	4.7	21.7
12	2.2	5.0
total		103.6

Figure A.27: Comparison of measurement and prediction for $J^{PC} = 0^{-+}$.

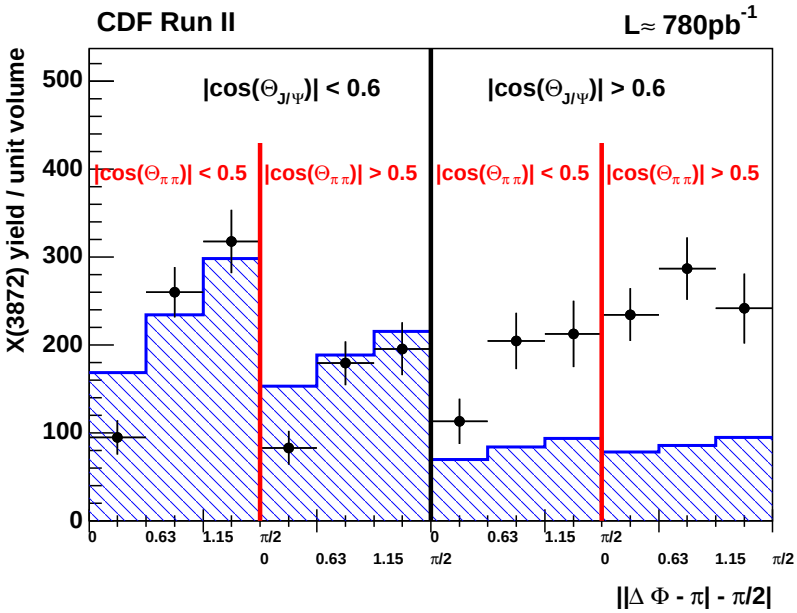

Bin	Resid.	χ_i^2
1	-3.8	14.4
2	0.9	0.8
3	0.5	0.3
4	-3.7	13.5
5	-0.4	0.2
6	-0.7	0.4
7	1.7	2.9
8	3.8	14.1
9	3.1	9.9
10	5.2	26.9
11	5.7	32.1
12	3.7	13.5
total		129.2

Figure A.28: Comparison of measurement and prediction for $J^{PC} = 0^{+-}$.

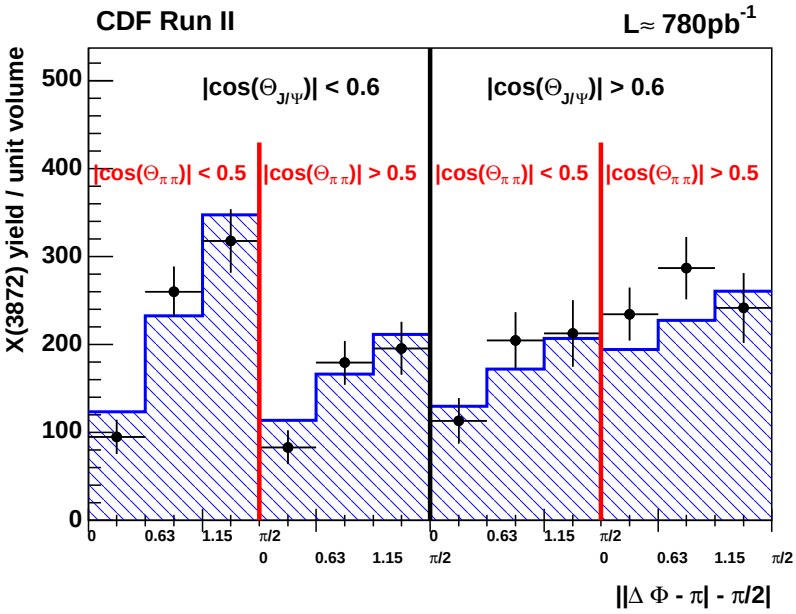

Bin	Resid.	χ_i^2
1	-1.5	2.1
2	1.0	0.9
3	-0.8	0.7
4	-1.6	2.6
5	0.5	0.3
6	-0.5	0.3
7	-0.7	0.4
8	1.0	1.0
9	0.1	0.0
10	1.3	1.8
11	1.7	2.8
12	-0.5	0.2
total		13.2

Figure A.29: Comparison of measurement and prediction for $J^{PC} = 1^{++}$.

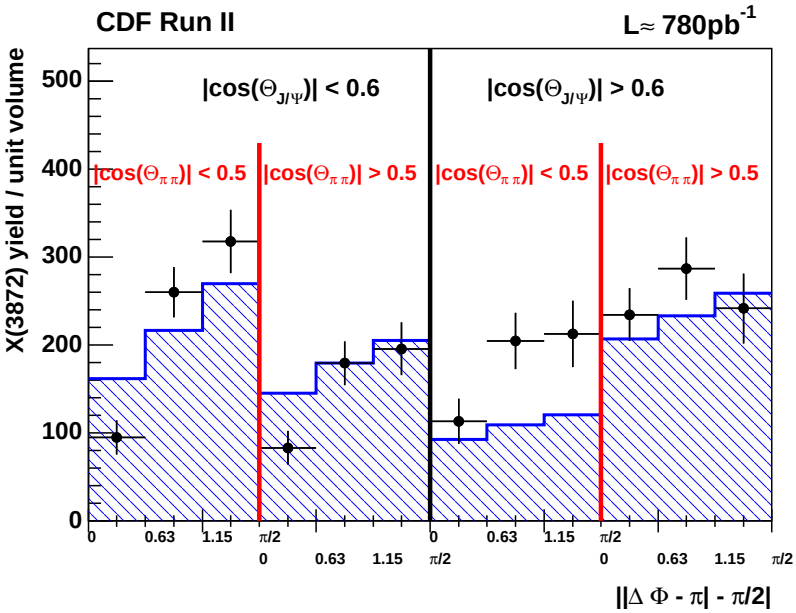

Bin	Resid.	χ_i^2
1	-3.4	11.8
2	1.5	2.3
3	1.3	1.8
4	-3.2	10.6
5	-0.0	0.0
6	-0.3	0.1
7	0.8	0.6
8	3.0	8.8
9	2.5	6.0
10	0.9	0.8
11	1.5	2.3
12	-0.4	0.2
total		45.3

Figure A.30: Comparison of measurement and prediction for $J^{PC} = 1^{-+}$.

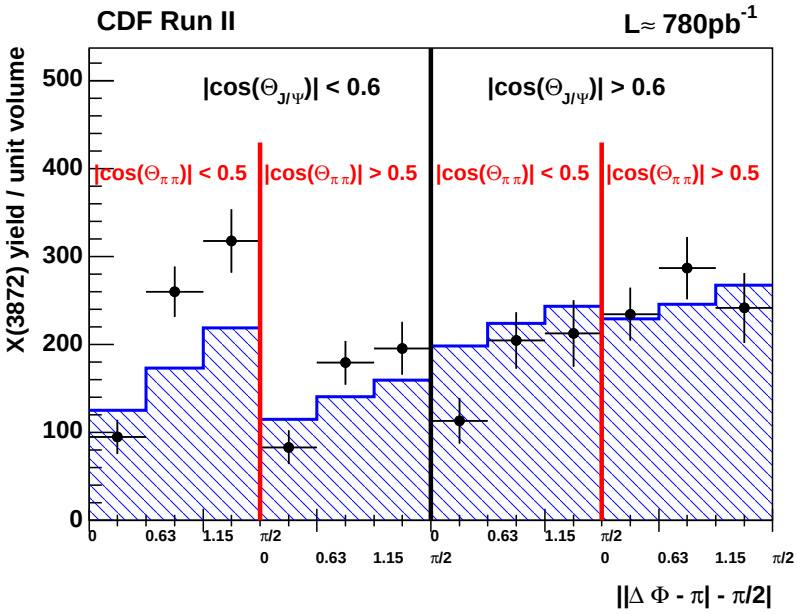

Bin	Resid.	χ_i^2
1	-1.6	2.4
2	3.0	9.3
3	2.7	7.5
4	-1.7	2.8
5	1.5	2.4
6	1.2	1.5
7	-3.3	11.1
8	-0.6	0.4
9	-0.8	0.7
10	0.2	0.0
11	1.2	1.3
12	-0.7	0.4
total		39.8

Figure A.31: Comparison of measurement and prediction for $J^{PC} = 1^{+-}$.

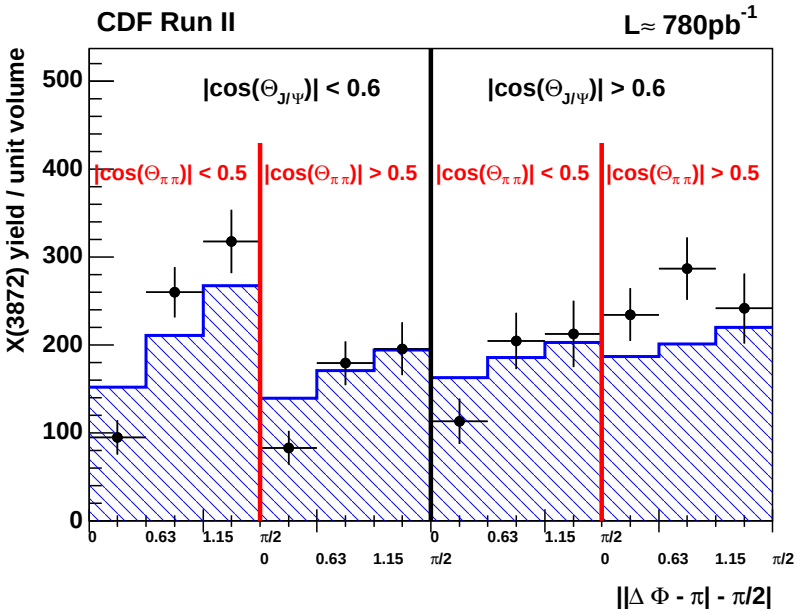

Bin	Resid.	χ_i^2
1	-3.0	8.7
2	1.7	3.0
3	1.4	1.9
4	-2.9	8.6
5	0.3	0.1
6	0.1	0.0
7	-1.9	3.8
8	0.6	0.3
9	0.3	0.1
10	1.6	2.5
11	2.4	5.8
12	0.5	0.3
total		35.1

Figure A.32: Comparison of measurement and prediction for $J^{PC} = 1^{--}$.

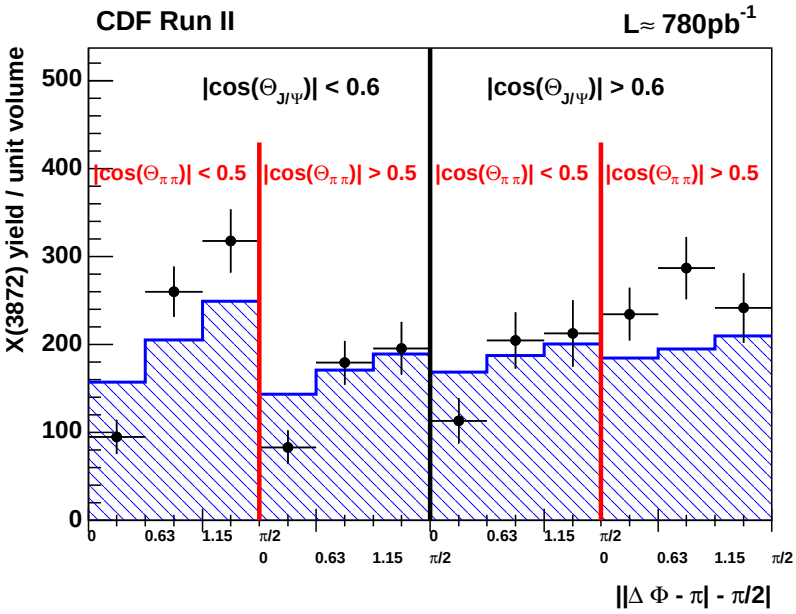

Bin	Resid.	χ^2_i
1	-3.2	10.3
2	1.9	3.7
3	1.9	3.6
4	-3.2	10.0
5	0.3	0.1
6	0.2	0.0
7	-2.2	4.7
8	0.5	0.3
9	0.3	0.1
10	1.7	2.8
11	2.6	6.8
12	0.8	0.6
total		43.1

Figure A.33: Comparison of measurement and prediction for $J^{PC} = 2^{++}$.

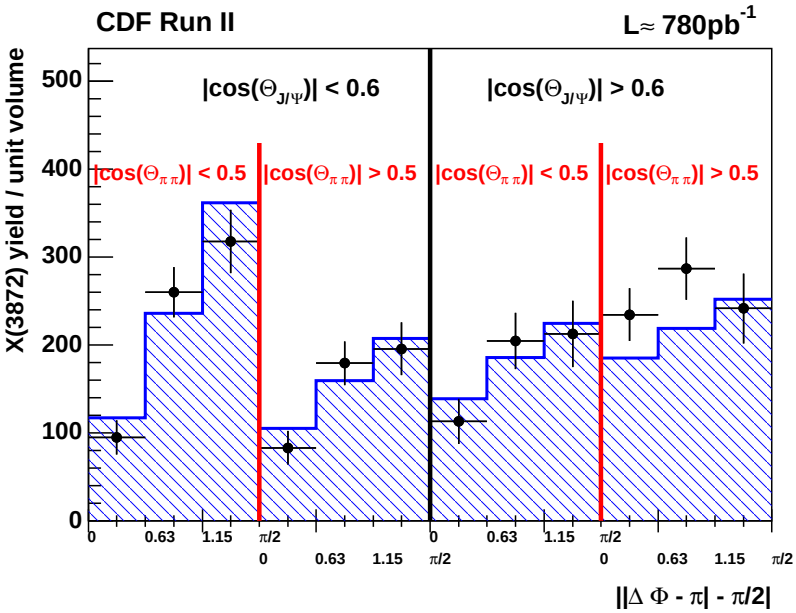

Bin	Resid.	χ^2_i
1	-1.2	1.3
2	0.8	0.7
3	-1.2	1.5
4	-1.1	1.3
5	0.8	0.6
6	-0.4	0.2
7	-1.0	1.0
8	0.6	0.3
9	-0.3	0.1
10	1.6	2.7
11	1.9	3.7
12	-0.3	0.1
total		13.6

Figure A.34: Comparison of measurement and prediction for $J^{PC} = 2^{-+}$.

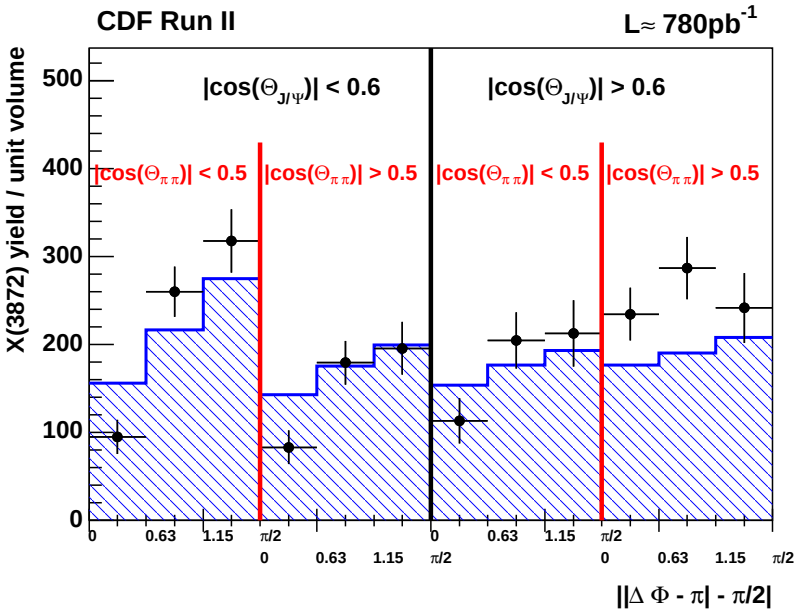

Bin	Resid.	χ_i^2
1	-3.2	10.0
2	1.5	2.3
3	1.2	1.4
4	-3.1	9.8
5	0.1	0.0
6	-0.1	0.0
7	-1.6	2.6
8	0.9	0.8
9	0.5	0.3
10	1.9	3.7
11	2.7	7.3
12	0.8	0.7
total		38.9

Figure A.35: Comparison of measurement and prediction for $J^{PC} = 2^{+-}$.

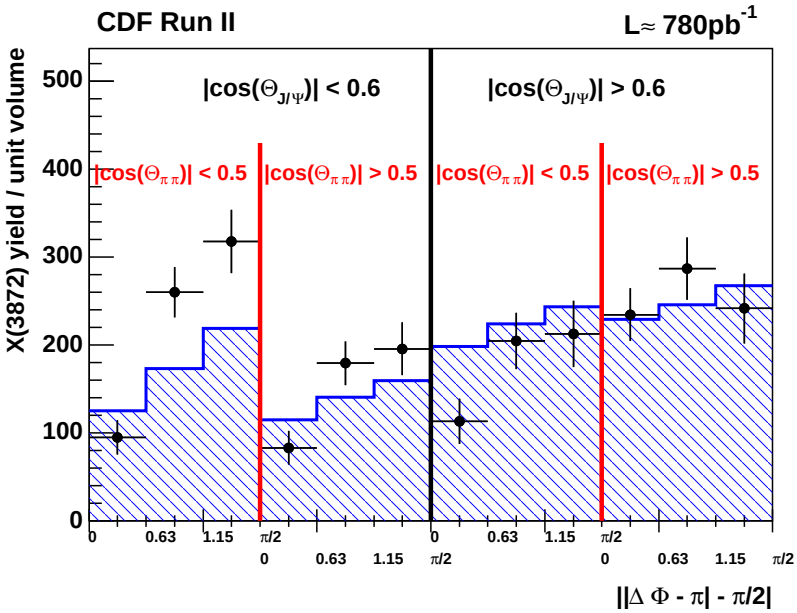

Bin	Resid.	χ_i^2
1	-1.6	2.4
2	3.0	9.3
3	2.7	7.5
4	-1.7	2.8
5	1.5	2.4
6	1.2	1.5
7	-3.3	11.1
8	-0.6	0.4
9	-0.8	0.7
10	0.2	0.0
11	1.2	1.3
12	-0.7	0.4
total		39.8

Figure A.36: Comparison of measurement and prediction for $J^{PC} = 2^{--}$.

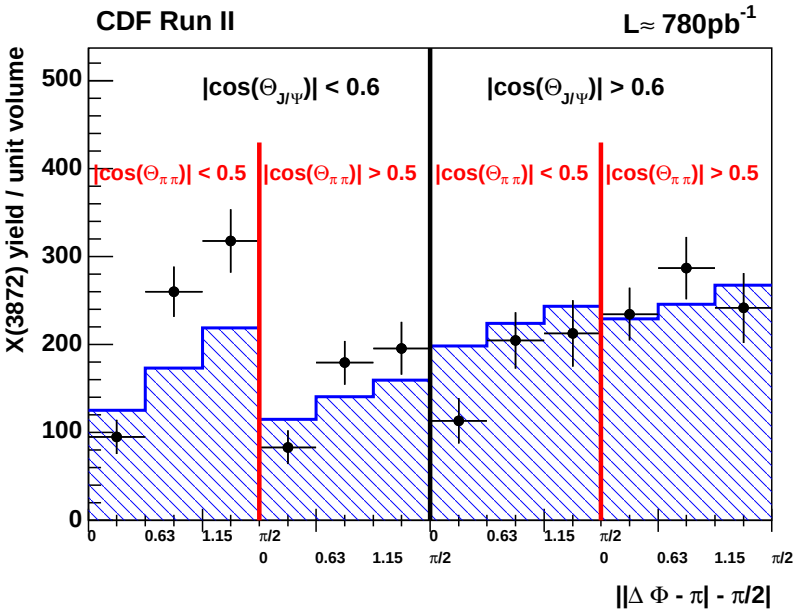

Bin	Resid.	χ_i^2
1	-1.6	2.4
2	3.0	9.3
3	2.7	7.5
4	-1.7	2.8
5	1.5	2.4
6	1.2	1.5
7	-3.3	11.1
8	-0.6	0.4
9	-0.8	0.7
10	0.2	0.0
11	1.2	1.3
12	-0.7	0.4
total		39.8

Figure A.37: Comparison of measurement and prediction for $J^{PC} = 3^{+-}$.

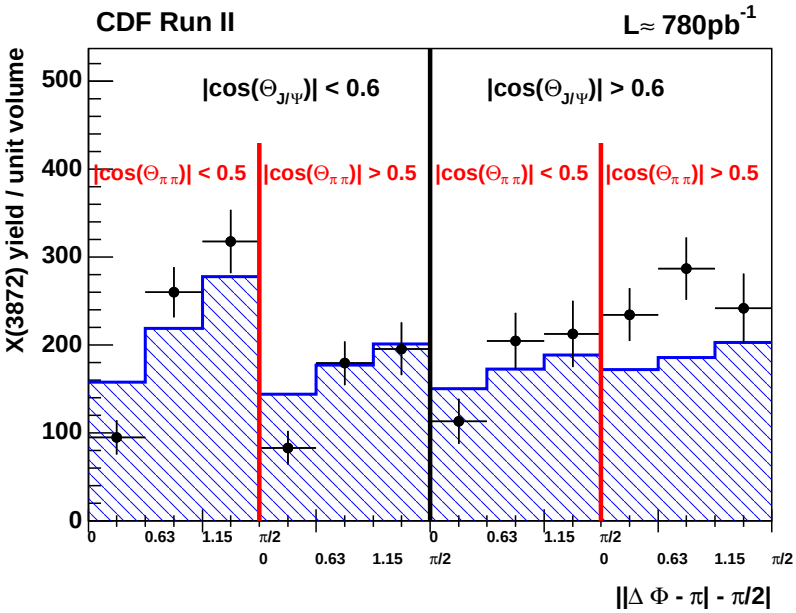

Bin	Resid.	χ_i^2
1	-3.2	10.6
2	1.4	2.1
3	1.1	1.2
4	-3.2	10.2
5	0.1	0.0
6	-0.2	0.0
7	-1.4	2.1
8	1.0	1.0
9	0.6	0.4
10	2.1	4.3
11	2.9	8.1
12	1.0	0.9
total		41.0

Figure A.38: Comparison of measurement and prediction for $J^{PC} = 3^{--}$.

List of Figures

1.1 $X(3872)$ Observation: Mass Spectrum 6
1.2 $X(3872) - \psi(2S)$ Comparison 10
1.3 Charmonium Spectrum 11
1.4 Evidence for the Decay Mode $X(3872) \to J/\psi\gamma$ 19
1.5 Indication for the Decay Mode $X(3872) \to J/\psi\pi^+\pi^-\pi^0$ 19
1.6 $m(\pi\pi)$ Spectrum in $X(3872) \to J/\psi\pi^+\pi^-$ 20
1.7 Decay $X(3875) \to D^0\bar{D}^0\pi^0$ 22

2.1 Tevatron: Aerial View 26
2.2 Tevatron: Accelerator Chain 27
2.3 CDF: Initial Luminosities 30
2.4 CDF: Integrated Luminosities 30
2.5 CDF: Cutaway View 31
2.6 CDF: Elevation View 32
2.7 CDF: Silicon Layers 33
2.8 CDF: Tracking System 34
2.9 CDF: COT Wire Scheme 35
2.10 CDF: Muon System $\eta - \phi$ Coverage 37
2.11 CDF: Trigger Scheme 39

3.1 $X(3872)$ Decay Topology 42
3.2 Decay Angle Definition 43
3.3 Illustration: Vertex Decay Matrix Element 47
3.4 Data Selection: Dimuon Trigger 56
3.5 Dimuon Mass Distribution After Preselection 58
3.6 Cut Selection: Fluctuation Cross-check 61

3.7 Mass Spectrum After Final Selection 62
3.8 MC Simulation: Acceptance 66
3.9 MC Simulation: Correction Functions 68
3.10 Simulation Verification: Transverse Momenta $\psi(2S)$ Decay 69
3.11 Simulation Verification: Pseudorapidities $\psi(2S)$ Decay 70
3.12 Simulation Verification: Angular Distributions $\psi(2S)$ Decay 71
3.13 Simulation Verification: Transverse Momenta $X(3872)$ Decay 72
3.14 Simulation Verification: Pseudorapidities $X(3872)$ Decay 73
3.15 Illustration of Angular Correlations 75
3.16 $X(3872)$ Angular Distribution: Measurement 76
3.17 $X(3872)$ Angular Distribution: Measurement and Expectations 82
3.18 $\psi(2S)$ Angular Distribution: Measurement and Expectations 84
3.19 Cross-check: Working Point Cut Scan 86
3.20 Angular Signal Parameter Dependence: Mass $X(3872)$ 91
3.21 Angular Signal Parameter Dependence: Width $X(3872)$ 91
3.22 Angular Signal Parameter Dependence: Position $\psi(2S)$ 92
3.23 Angular Signal Parameter Dependence: Width $\psi(2S)$ 92
3.24 Systematic Check Overview: Measurement and Simulation 95

4.1 $X(3872)$ Neural Network Training 101
4.2 $X(3872)$ Neural Network Mass Dependence Check 102
4.3 $X(3872)$ Neural Network Cut 102
4.4 $X(3872)$ Cut on Number of Candidates 103
4.5 $X(3872)$ Final Mass Spectrum 105
4.6 Comparison $\psi(2S)$ Measurement vs. Simulation 108
4.7 Comparison $X(3872)$ Measurement vs. Simulation 109
4.8 Expected Mass Resolution 111
4.9 Measurement of $\psi(2S)/X(3872)$ Width Scale 113
4.10 Data-Simulation: Disagreement in Number of COT Hits 115
4.11 Evaluation of the Null Hypothesis 117
4.12 Width Scale Distribution for 90%, 95% Limits 118
4.13 Evaluation of the Limit on the Mass Difference for $f_1 = 50 : 50$ 119
4.14 Limit on the Mass Difference for all tested f_1 119

4.15 Mass Fit: $X(3872)/\psi(2S)$ 122
4.16 $\psi(2S)$ Mass Dependence: Transverse Momenta 124
4.17 $\psi(2S)$ Mass Dependence: Pseudorapidities 125
4.18 $\psi(2S)$ Mass Dependence: Selection Variables 126

5.2 $X(3872)$ Mass Measurement Overview 130

A.1 Angular Distributions for $J^{PC} = 0^{++}$ 135
A.2 Angular Distributions for $J^{PC} = 0^{+-}$ 136
A.3 Angular Distributions for $J^{PC} = 0^{-+}$ 136
A.4 Angular Distributions for $J^{PC} = 1^{++}$ 137
A.5 Angular Distributions for $J^{PC} = 1^{+-}$ 137
A.6 Angular Distributions for $J^{PC} = 1^{-+}$ 138
A.7 Angular Distributions for $J^{PC} = 1^{--}$ 138
A.8 Angular Distributions for $J^{PC} = 2^{++}$ 139
A.9 Angular Distributions for $J^{PC} = 2^{+-}$ 139
A.10 Angular Distributions for $J^{PC} = 2^{-+}$ 140
A.11 Angular Distributions for $J^{PC} = 2^{--}$ 140
A.12 Angular Distributions for $J^{PC} = 3_s^{+-}$ 141
A.13 Angular Distributions for $J^{PC} = 3^{--}$ 141
A.14 Fit to the Mass Spectrum in Angular Bin 1 142
A.15 Fit to the Mass Spectrum in Angular Bin 2 143
A.16 Fit to the Mass Spectrum in Angular Bin 3 143
A.17 Fit to the Mass Spectrum in Angular Bin 4 144
A.18 Fit to the Mass Spectrum in Angular Bin 5 144
A.19 Fit to the Mass Spectrum in Angular Bin 6 145
A.20 Fit to the Mass Spectrum in Angular Bin 7 145
A.21 Fit to the Mass Spectrum in Angular Bin 8 146
A.22 Fit to the Mass Spectrum in Angular Bin 9 146
A.23 Fit to the Mass Spectrum in Angular Bin 10 147
A.24 Fit to the Mass Spectrum in Angular Bin 11 147
A.25 Fit to the Mass Spectrum in Angular Bin 12 148
A.26 Comparison of Measurement and Prediction for $J^{PC} = 0^{++}$ 149

A.27 Comparison of Measurement and Prediction for $J^{PC} = 0^{-+}$ 150
A.28 Comparison of Measurement and Prediction for $J^{PC} = 0^{+-}$ 150
A.29 Comparison of Measurement and Prediction for $J^{PC} = 1^{++}$ 151
A.30 Comparison of Measurement and Prediction for $J^{PC} = 1^{-+}$ 151
A.31 Comparison of Measurement and Prediction for $J^{PC} = 1^{+-}$ 152
A.32 Comparison of Measurement and Prediction for $J^{PC} = 1^{--}$ 152
A.33 Comparison of Measurement and Prediction for $J^{PC} = 2^{++}$ 153
A.34 Comparison of Measurement and Prediction for $J^{PC} = 2^{-+}$ 153
A.35 Comparison of Measurement and Prediction for $J^{PC} = 2^{+-}$ 154
A.36 Comparison of Measurement and Prediction for $J^{PC} = 2^{--}$ 154
A.37 Comparison of Measurement and Prediction for $J^{PC} = 3^{+-}$ 155
A.38 Comparison of Measurement and Prediction for $J^{PC} = 3^{--}$ 155

List of Tables

1.1 Standard Model: Gauge Bosons 3
1.2 Standard Model: Leptons 4
1.3 Standard Model: Quarks 4
1.4 $X(3872)$: Experimental Knowledge 24
1.5 $X(3875)$: Experimental Knowledge 24

2.1 CDF: Muon System Summary 37
2.2 CDF: Calorimeter System Summary 38

3.1 Definition of Angles 43
3.2 Allowed LS combinations in the $X(3872)$ decay 46
3.3 $X(3872)$ Measured Yield Values of Angular Distribution 77
3.4 $X(3872)$ χ^2 Comparison: Unambiguous Hypotheses 78
3.5 $X(3872)$ χ^2 Comparison: All Hypotheses 81
3.6 $\psi(2S)$ χ^2 Comparison 83
3.7 Cross-check: Different Working Points 85
3.8 Overview: Polarization Effects 87
3.9 Cross-Check Overview: Various Sources 90
3.10 Systematic Check Overview: Measurement and Simulation Effects . . 94

4.1 Mass Analysis: Preselection Cuts 98
4.2 Mass Analysis: Neural Network Input Variables 99
4.3 Choice of Ensemble Parameters 116
4.4 Fit Function: Parameter Overview 120
4.5 Systematic Mass Uncertainties: Fit Model 121

5.2 XYZ States: Overview 132

Bibliography

[1] S. K. Choi et al. Observation of a New Narrow Charmonium State in Exclusive $B^{\pm} \to K^{\pm}\pi^{+}\pi^{-}J/\psi$ Decays. *Phys. Rev. Lett.*, 91:262001, 2003.

[2] Darin E. Acosta et al. Observation of the Narrow State $X(3872) \to J/\psi\pi^{+}\pi^{-}$ in $\bar{p}p$ Collisions at $\sqrt{s} = 1.96$ TeV. *Phys. Rev. Lett.*, 93:072001, 2004.

[3] V. M. Abazov et al. Observation and Properties of the $X(3872)$ Decaying to $J/\psi\pi^{+}\pi^{-}$ in $p\bar{p}$ Collisions at $\sqrt{s} = 1.96$ TeV. *Phys. Rev. Lett.*, 93:162002, 2004.

[4] B. Aubert et al. Study of the $B \to J/\psi K^{-}\pi^{+}\pi^{-}$ Decay and Measurement of the $B \to X(3872)K^{-}$ Branching fraction. *Phys. Rev.*, D71:071103, 2005.

[5] W. M. Yao et al. Review of Particle physics. *J. Phys.*, G33:1–1232, 2006.

[6] W. M. Yao et al. Review of Particle Physics. *J. Phys.*, G33:1–1232, 2006. And 2007 Partial Update for the 2008 edition.

[7] B. Aubert et al. A study of $B \to X(3872)K$, with $X(3872) - > J/\psi pi^{+}pi^{-}$. 2008.

[8] S. K. Choi. Properties of the $X(3872)$. 2004.

[9] K. Abe et al. Observation of $B^{+} \to \psi(3770)K^{+}$. *Phys. Rev. Lett.*, 93:051803, 2004.

[10] B. Aubert et al. Observation of the Decay $B \to J/\psi\eta K$ and Search for $X(3872) \to J/\psi\eta$. *Phys. Rev. Lett.*, 93:041801, 2004.

[11] B. Aubert et al. Search for a Charged Partner of the $X(3872)$ in the B Meson Decay $B \to X^{-}K$, $X^{-} \to J/\psi\pi^{-}\pi^{0}$. *Phys. Rev.*, D71:031501, 2005.

[12] K. Abe et al. Properties of the $X(3872)$ at Belle. 2004.

[13] S. Dobbs et al. Search for $X(3872)$ in $\gamma\gamma$ Fusion and ISR at CLEO. *Phys. Rev. Lett.*, 94:032004, 2005.

[14] C. Z. Yuan, X. H. Mo, and P. Wang. The Upper Limit of the $e^{+}e^{-}$ Partial Width of $X(3872)$. *Phys. Lett.*, B579:74–78, 2004.

[15] B. Aubert et al. The $e^+e^- \to \pi^+\pi^-\pi^+\pi^-$, $K^+K^-\pi^+\pi^-$, and $K^+K^-K^+K^-$ Cross Sections at Center-of- mass Energies $0.5\,\mathrm{GeV} - 4.5\,\mathrm{GeV}$ Measured with Initial-state Radiation. *Phys. Rev.*, D71:052001, 2005.

[16] G. Bauer. The $X(3872)$ at CDF II. *Int. J. Mod. Phys.*, A20:3765–3767, 2005.

[17] S. Godfrey and Nathan Isgur. Mesons in a Relativized Quark Model with Chromodynamics. *Phys. Rev.*, D32:189–231, 1985.

[18] Stephen Godfrey and Stephen L. Olsen. The Exotic XYZ Charmonium-like Mesons. 2008.

[19] T. Barnes, S. Godfrey, and E. S. Swanson. Higher Charmonia. *Phys. Rev.*, D72:054026, 2005.

[20] Eric S. Swanson. The New Heavy Mesons: A Status Report. *Phys. Rept.*, 429:243–305, 2006.

[21] Stephen L. Olsen. Search for a Charmonium Assignment for the $X(3872)$. *Int. J. Mod. Phys.*, A20:240–249, 2005.

[22] C. Cawlfield et al. A Precision Determination of the D^0 Mass. *Phys. Rev. Lett.*, 98:092002, 2007.

[23] John D. Weinstein and Nathan Isgur. $K\bar{K}$ Molecules. *Phys. Rev.*, D41:2236, 1990.

[24] M. B. Voloshin and L. B. Okun. Hadron Molecules and Charmonium Atom. *JETP Lett.*, 23:333–336, 1976.

[25] A. De Rujula, Howard Georgi, and S. L. Glashow. Molecular Charmonium: A New Spectroscopy? *Phys. Rev. Lett.*, 38:317, 1977.

[26] Nils A. Tornqvist. Isospin Breaking of the Narrow Charmonium State of Belle at 3872 MeV as a Deuson. *Phys. Lett.*, B590:209–215, 2004.

[27] Yan-Rui Liu, Xiang Liu, Wei-Zhen Deng, and Shi-Lin Zhu. Is $X(3872)$ *Really* a Molecular State? 2008.

[28] Eric S. Swanson. Short Range Structure in the $X(3872)$. *Phys. Lett.*, B588:189–195, 2004.

[29] M. B. Voloshin. Interference and Binding Effects in Decays of Possible Molecular Component of $X(3872)$. *Phys. Lett.*, B579:316–320, 2004.

[30] Frank E. Close and Philip R. Page. The $D^{*0}\bar{D}^0$ Threshold Resonance. *Phys. Lett.*, B578:119–123, 2004.

[31] Cheuk-Yin Wong. Molecular States of Heavy Quark Mesons. *Phys. Rev.*, C69:055202, 2004.

[32] Eric Braaten and Masaoki Kusunoki. Production of the $X(3870)$ at the $\Upsilon(4S)$ by the Coalescence of Charm Mesons from B Decays. *Phys. Rev.*, D69:114012, 2004.

[33] Robert L. Jaffe. Multi-Quark Hadrons. 2. Methods. *Phys. Rev.*, D15:281, 1977.

[34] L. Maiani, F. Piccinini, A. D. Polosa, and V. Riquer. Diquark-antidiquarks with Hidden or Open Charm and the Nature of $X(3872)$. *Phys. Rev.*, D71:014028, 2005.

[35] H. Hogaasen, J. M. Richard, and P. Sorba. A Chromomagnetic Mechanism for the $X(3872)$ Resonance. *Phys. Rev.*, D73:054013, 2006.

[36] D. Ebert, R. N. Faustov, and V. O. Galkin. Masses of Heavy Tetraquarks in the Relativistic Quark Model. *Phys. Lett.*, B634:214–219, 2006.

[37] N. Barnea, J. Vijande, and A. Valcarce. Four-quark Spectroscopy Within the Hyperspherical Formalism. *Phys. Rev.*, D73:054004, 2006.

[38] Ying Cui, Xiao-Lin Chen, Wei-Zhen Deng, and Shi-Lin Zhu. The Possible Heavy Tetraquarks $qQ\bar{q}\bar{q}$, $qq\bar{Q}\bar{Q}$ and $qQ\bar{Q}\bar{Q}$. *High Energy Phys. Nucl. Phys.*, 31:7–13, 2007.

[39] R. D. Matheus, S. Narison, M. Nielsen, and J. M. Richard. Can the $X(3872)$ be a 1^{++} Four-quark State? *Phys. Rev.*, D75:014005, 2007.

[40] Ting-Wai Chiu and Tung-Han Hsieh. Pseudovector Meson with Strangeness and Closed-charm. *Phys. Rev.*, D73:111503, 2006.

[41] L. Maiani, A. D. Polosa, and V. Riquer. Indications of a Four-Quark Structure for the $X(3872)$ and $X(3876)$ Particles from Recent Belle and *BABAR* Data. *Phys. Rev. Lett.*, 99:182003, 2007.

[42] D. Horn and J. Mandula. A Model of Mesons with Constituent Gluons. *Phys. Rev.*, D17:898, 1978.

[43] F. E. Close and Stephen Godfrey. Charmonium Hybrid Production in Exclusive B Meson Decays. *Phys. Lett.*, B574:210–216, 2003.

[44] Nathan Isgur and Jack E. Paton. A Flux Tube Model for Hadrons in QCD. *Phys. Rev.*, D31:2910, 1985.

[45] Ted Barnes, F. E. Close, and E. S. Swanson. Hybrid and Conventional Mesons in the Flux Tube Model: Numerical Studies and Their Phenomenological Implications. *Phys. Rev.*, D52:5242–5256, 1995.

[46] John Merlin and Jack E. Paton. Spin Interactions in the Flux Tube Model and Hybrid Meson Masses. *Phys. Rev.*, D35:1668, 1987.

[47] X. Liao and T. Manke. Excited Charmonium Spectrum from Anisotropic Lattices. 2002.

[48] Bing An Li. Is $X(3872)$ a Possible Candidate of Hybrid Meson. *Phys. Lett.*, B605:306–310, 2005.

[49] D. V. Bugg. Reinterpreting Several Narrow 'Resonances' as Threshold Cusps. *Phys. Lett.*, B598:8–14, 2004.

[50] D. V. Bugg. The $X(3872)$ and the 3941 MeV Peak in $\omega J/\psi$. *Phys. Rev.*, D71:016006, 2005.

[51] D. V. Bugg. How Resonances Can Synchronise with Thresholds. 2008.

[52] Yu. S. Kalashnikova. Coupled-channel Model for Charmonium Levels and an Option for (3872). *Phys. Rev.*, D72:034010, 2005.

[53] C Hanhart, Yu. S Kalashnikova, Alexander E. Kudryavtsev, and A. V Nefediev. Reconciling the $X(3872)$ with the Near-threshold Enhancement in the $D^0\bar{D}^{*0}$ Final State. *Phys. Rev.*, D76:034007, 2007.

[54] Kamal K. Seth. An Alternative Interpretation of $X(3872)$. *Phys. Lett.*, B612:1–4, 2005.

[55] Colin J. Morningstar and Mike J. Peardon. The Glueball Spectrum from an Anisotropic Lattice Study. *Phys. Rev.*, D60:034509, 1999.

[56] K. Abe et al. Evidence for $X(3872) \to \gamma J/\psi$ and the Sub-threshold Decay $X(3872) \to \omega J/\psi$. 2005.

[57] B. Aubert et al. Search for $B^+ \to X(3872)K^+$, $X(3872) \to J/\psi\gamma$. *Phys. Rev.*, D74:071101, 2006.

[58] K. Abe et al. Experimental Constraints on the Possible J^{PC} Quantum Numbers of the $X(3872)$. 2005.

[59] A. Abulencia et al. Measurement of the Dipion Mass Spectrum in $X(3872) \to J/\psi\pi^+\pi^-$ Decays. *Phys. Rev. Lett.*, 96:102002, 2006.

[60] A. Abulencia et al. Analysis of the Quantum Numbers J^{PC} of the $X(3872)$. *Phys. Rev. Lett.*, 98:132002, 2007.

[61] BELLE-CONF-0711, First Conference Mention of the Result is: Faccini, R., Heavy Quarkonium Spectroscopy, Lepton Photon 2007, Daegu, Korea.

[62] G. Gokhroo et al. Observation of a Near-threshold $D^0\bar{D}^0\pi^0$ Enhancement in $B \to D^0\bar{D}^0\pi^0K$ Decays. *Phys. Rev. Lett.*, 97:162002, 2006.

[63] B. Aubert et al. Study of Resonances in Exclusive B Decays to $\bar{D}^*D^*K$. *Phys. Rev.*, D77:011102, 2008.

[64] W. Dunwoodie and V. Ziegler. A Simple Explanation for the $X(3872)$ Mass Shift Observed for Decay to $D^{*0}\bar{D}^0$. *Phys. Rev. Lett.*, 100:062006, 2008.

[65] M. B. Voloshin. Isospin Properties of the X State Near the $D\bar{D}^*$ Threshold. *Phys. Rev.*, D76:014007, 2007.

[66] Eric Braaten and Meng Lu. The Effects of Charged Charm Mesons on the Line Shapes of the $X(3872)$. *Phys. Rev.*, D77:014029, 2008.

[67] B. Aubert et al. Study of $J/\psi\pi^+\pi^-$ States Produced in $B^0 \to J/\psi\pi^+\pi^-K^0$ and $B^- \to J/\psi\pi^+\pi^-K^-$. *Phys. Rev.*, D73:011101, 2006.

[68] R. Blair et al. The CDF II detector: Technical Design Report. FERMILAB-PUB-96-390-E.

[69] Darin E. Acosta et al. Measurement of the J/ψ Meson and $b-$hadron Production Cross Sections in $p\bar{p}$ Collisions at $\sqrt{s} = 1960$ GeV. *Phys. Rev.*, D71:032001, 2005.

[70] Darin E. Acosta et al. Measurement of the $t\bar{t}$ Production Cross Section in $p\bar{p}$ Collisions at $\sqrt{s} = 1.96$ TeV Using Lepton + Jets Events with Secondary Vertex $b-$tagging. *Phys. Rev.*, D71:052003, 2005.

[71] A. Abulencia et al. Measurements of Inclusive W and Z Cross Sections in p-pbar Collisions at $\sqrt{s} = 1.96$ TeV. *J. Phys.*, G34:2457–2544, 2007.

[72] A. Sill. CDF Run II Silicon Tracking Projects. *Nucl. Instrum. Meth.*, A447:1–8, 2000.

[73] Christopher S. Hill. Operational Experience and Performance of the CDF II Silicon Detector. *Nucl. Instrum. Meth.*, A530:1–6, 2004.

[74] Anthony A. Affolder et al. Intermediate Silicon Layers Detector for the CDF Experiment. *Nucl. Instrum. Meth.*, A453:84–88, 2000.

[75] Anthony Allen Affolder et al. CDF Central Outer Tracker. *Nucl. Instrum. Meth.*, A526:249–299, 2004.

[76] G. Ascoli et al. CDF Central Muon Detector. *Nucl. Instrum. Meth.*, A268:33, 1988.

[77] D. Acosta et al. A Time-of-flight Detector in CDF II. *Nucl. Instrum. Meth.*, A518:605–608, 2004.

[78] L. Balka et al. The CDF Central Electromagnetic Calorimeter. *Nucl. Instrum. Meth.*, A267:272, 1988.

[79] S. Bertolucci et al. The CDF Central and Endwall Hadron Calorimeter. *Nucl. Instrum. Meth.*, A267:301, 1988.

[80] M. G. Albrow et al. The CDF Plug Upgrade Electromagnetic Calorimeter: Test Beam Results. *Nucl. Instrum. Meth.*, A480:524–546, 2002.

[81] A. Bhatti et al. Determination of the Jet Energy Scale at the Collider Detector at Fermilab. *Nucl. Instrum. Meth.*, A566:375–412, 2006.

[82] D. Acosta et al. The Performance of the CDF Luminosity Monitor. *Nucl. Instrum. Meth.*, A494:57–62, 2002.

[83] Evelyn J. Thomson et al. Online Track Processor for the CDF Upgrade. *IEEE Trans. Nucl. Sci.*, 49:1063–1070, 2002.

[84] Jeffrey D. Richman. An Experimenter's Guide to the Helicity Formalism. CALT-68-1148.

[85] D. A. Varshalovich, A. N. Moskalev, and V. K. Khersonsky. Quantum Theory of Angular Momentum: Irreducible Tensors, Spherical Harmonics, Vector Coupling Coefficients, 3NJ Symbols. Singapore, Singapore: World Scientific (1988) 514p.

[86] John David Jackson. Remarks on the Phenomenological Analysis of Resonances. *Nuovo Cim.*, 34:1644–1666, 1964.

[87] J. M. Blatt and V. F. Weisskopf. Theoretical Nuclear Physics. New York, John Wiley, 1952.

[88] Michael Feindt. An Amplitude Construction Primer for Experimentalists. (unpublished).

[89] M. Nikolic. Analysis of Scattering and Decay. New York, USA: Gordan and Breach (1968) 332p.

[90] H. Albrecht et al. A Partial Wave Analysis of the Decay $D^0 \to K^0(s)\pi^+\pi^-$. *Phys. Lett.*, B308:435–443, 1993.

[91] V. A. Novikov and Mikhail A. Shifman. Comment on the $\psi(2S) \to J/\psi\pi\pi$ Decay. *Zeit. Phys.*, C8:43, 1981.

[92] J. Z. Bai et al. $\psi(2S) \to \pi^+\pi^- J/\psi$ Decay Distributions. *Phys. Rev.*, D62:032002, 2000.

[93] Mikhail B. Voloshin and Valentin I. Zakharov. Measuring QCD Anomalies in Hadronic Transitions Between Onium States. *Phys. Rev. Lett.*, 45:688, 1980.

[94] Ulrich Kerzel. *CDF Grid Computing and the Decay $X(3872) \to J/\psi\pi^+\pi^-$ with $J/\psi \to e^+e^-$*. PhD thesis, Universität Karlsruhe, 2005. (unpublished).

[95] G. Bauer, C. Paus, and K. Sumorok. Observation of the Charmonium State $\psi(3870)$ in $J/\psi\pi^+\pi^-$ with Run II Data. Public CDF Note 6669 (unpublished), 2004.

[96] J. Marriner. Secondary Vertex Fit with Mass and Pointing Constraints `CTVMFT`. Public CDF Note 1996 (unpublished), 1993.

[97] `http://root.cern.ch/root/html/TGenPhaseSpace.html`.

[98] C. Blocker, J. Boudreau, and Ch. Paus. Common Tools for B Physics Analyses in Run II at CDF. Public CDF Note 5735 (unpublished), 2002.

[99] Ch. Paus. `http://cdfkits.fnal.gov/CdfCode/source/BottomMods/`.

[100] M. Feindt and U. Kerzel. The NeuroBayes Neural Network Package. *Nucl. Instrum. Meth.*, A559:190–194, 2006.

[101] M. Feindt. A Neural Bayesian Estimator for Conditional Probability Densities, 2004.

[102] D. J. Lange. The EvtGen Particle Decay Simulation Package. *Nucl. Instrum. Meth.*, A462:152–155, 2001.

[103] `http://www-cdf.fnal.gov/cdfsim/cdfsim_main.html`.

[104] E. Gerchtein and M. Paulini. CDF Detector Simulation Framework and Performance. 2003.

[105] Estia Eichten, Stephen Godfrey, Hanna Mahlke, and Jonathan L. Rosner. Quarkonia and Their Transitions. 2007.

[106] K. Abe et al. Observation of a Resonance-like Structure in the $\pi^{\pm}\psi'$ Mass Distribution in Exclusive $B \to K\pi^{\pm}\psi'$ Decays. *Phys. Rev. Lett.*, 100:142001, 2008.

[107] K. F. Chen et al. Observation of Anomalous $\Upsilon(1S)\pi^+\pi^-$ and $\Upsilon(2S)\pi^+\pi^-$ Production Near the $\Upsilon(5S)$ Resonance. *Phys. Rev. Lett.*, 100:112001, 2008.

Acknowledgments

First and foremost I would like to thank my supervisor Prof. Dr. Michael Feindt for the guidance throughout the course of this thesis. His deep knowledge about particle physics and many fruitful discussions were essential pillars for the success of the work.

I would also like to thank Prof. Dr. Günter Quast for both co-supervising this thesis and his continuous dedication in providing computing power for every student. I as well would like to thank Prof. Dr. Thomas Müller for his work for everybody in his function as head of the institute.

Dr. Michal Kreps and Dr. Thomas Kuhr deserve special mention. Without their work and advice this thesis would not have been possible. For this I am deeply grateful. I also would like to thank Dr. Ulrich Kerzel for his support and sacrifices during the course of the analysis.

I would like to thank Dr. Michal Kreps for carefully reading and commenting on this manuscript. Additional thanks goes to Dr. Thomas Kuhr, Iris Gebauer, Claudia Marino, and Martin Heck.

For all their work to keep everything running i would like to thank our secretaries Mrs Weißmann, Mrs Schorn, Mrs Gerstner, Mrs Schulz, and Mrs Marusev. I especially would like to thank all members of the EKP admin team.

Each member of the B group and of the institute in general added to the great working atmosphere. This really made for a worthwhile experience. From the many persons I especially want to mention Dr. Christian Piasecki, Claudia Marino, Dr. Dominic Hirschbühl, Volker Büge, Iris Gebauer, Philipp Sturm, Armin Scheurer, and Philipp Mack.

Last, but of course not least, I would like to thank my parents for their help and support.